UNCLOAKING GLOBULAR CLUSTERS IN THE INNER GALAXY

by

Javier Alonso García

A dissertation submitted in partial fulfillment
of the requirements for the degree of
Doctor of Philosophy
(Astronomy and Astrophysics)
in The University of Michigan
2010

Doctoral Committee:

Professor Mario L. Mateo, Chair
Professor Joel N. Bregman
Associate Professor Moulinath Banerjee
Associate Professor Rebecca A. Bernstein, U. of California
Assistant Professor Fabian Heitsch, U. of North Carolina

Copyright © Javier Alonso García
All Rights Reserved 2010

Dedicado, con todo cariño, a mi abuelo Andrés

ACKNOWLEDGMENTS

I am indebted to a lot of people for making this thesis possible, and my life in the U.S. an unforgettable experience.

I will always have the biggest professional debt with my advisor Mario Mateo. Thanks for your insight, for your guidance, and for having your door always open for me. I will always appreciate the extra time spent in our "five minutes meetings", and your giving me the time to do my work and never push too soft or too hard on me.

Thanks to the other members of my committee, Joel Bregman, Rebecca Bernstein, Mouli Banerjee, and Fabian Heitsch for enriching this thesis with their suggestions.

Thanks to Antonio Aparicio, for introducing me into the world of astronomical research during my first year after graduation, and for supporting my idea of pursuing a doctoral degree in the States.

Thanks to Michael Woodroofe, Mouli Banerjee, and especially Bodhi Sen, for their big help with the statistical part of this thesis.

I thank all the people in the Astronomy department for creating such a great job environment and good atmosphere to begin my professional life. And all the people in this country that have supported this research through their taxes .

I thank my fellow graduate students for being always available when some help was needed. I would like to especially thank Joe Bernstein for sharing his office and giving me his friendship, Matt Walker for being a good friend and great companion in all the lunches and conferences we have shared together, Tom Brink for being able to talk about Astronomy, life and sports with great passion, and Sarah Ragan, for being such a great friend and housemate, and for her support in difficult times for me.

Debo agradecer también a todos mis amigos de la colonia española y sudamericana

de Ann Arbor haber hecho mi estancia especialmente agradable y enriquecedora. Algunos habéis estado poco, y otros lleváis aquí tantos años como yo o más incluso, pero quiero que sepáis que siempre guardaré vuestra amistad como un gran regalo. Gracias especialmente a Roberto y Carlos por vuestras llamadas y correos de apoyo durante los últimos días de escritura e intenso trabajo, y por estar siempre dispuestos a acompañarme a tomar una copa y charlar un rato en cualquier momento que lo he necesitado; a Luís, Alberto y Ricardo, por haber estado a mi lado en momentos buenos y malos; de nuevo a Alberto, Carlos, Luís, Ricardo, y Roberto, y también a Carlos, Sebastián, Dio, Chad, Isaac, Andy, Mikel y a todos los miembros del "31 con duples" por haber compartido inquietudes, charlas, bromas, pizza y cartas una noche a la semana durante mucho tiempo; a Aurora, Aurelia, y Raquel, por haber sido las mejores vecinas en Marshall Court; y a Susana, Marisa, Noelia, Cristina, Rashmi y Esther por haber compartido sábados, fiestas, y bailes.

También quiero agradecer a mis amigos de siempre, Jose, Juanma, José Angel, Guille y Alvaro, y a Vero, Anna y Elena, por hacerme sentir en casa, como si no me hubiese ido, cada vez que puedo pasar unos días en España.

Por último, quiero mencionar aquí a mi familia, que no importa la distancia, siempre han estado cerca de mí, y han comprendido, guiado, y apoyado todas mis decisiones. Ellos son los principales artífices de que haya sido capaz de llevar esta tesis a buen puerto, gracias a su cariño y afecto, que nunca me han dejado sentirme solo.

CONTENTS

LIST OF FIGURES

Figure

LIST OF TABLES

Table

CHAPTER 1

Introduction

Spiral galaxies can be divided into three components: a flat disk with spiral arms, a central bulge, and a diffuse halo (figure 1.1). The central bulge becomes smaller, less prominent and less massive as we move to later-type galaxies in the Hubble sequence.

Bulges can be classified in three different types with different formation scenarios and different morphological, photometrical and kinematical characteristics (Freeman, 2008; Athanassoula, 2005, 2008)

- Classical bulges, which follow the characteristic $r^{1/4}$ law light distribution of elliptical galaxies, sharing with them also their kinematical and morphological characteristics. They are formed by gravitational collapse or hierarchical merging of smaller objects.

- Boxy/peanut (B/P) bulges, with near exponential surface brightness profiles, and mainly constitute by inner disk stars. They are believed to come from bar-buckling instabilities in the disks.

- Disc-like bulges, with an enhancement over the exponential disk light distribution, with a Sérsic law (Sérsic, 1968) with index ~ 1 form, but appearing to be disk-like from its shape and kinematics. They form from the inflow of gas material and from the ensuing enhanced star formation, and by this reason they are mainly constituted by gas and young stars.

These last two scenarios are two cases of pseudo-bulges.

The bulge of our own Galaxy (figure 1.1) is a very interesting study case, being the only bulge that can be resolved into stars. It is now generally accepted that

Figure 1.1. Representation of the different components of the Milky Way

there is a stellar bar in the Milky Way, but the morphology of the inner Galaxy is still controversial. In some papers the inner Galaxy in shown as a thick bar, around ~ 3.5 kpc long, with position angle of $15° - 30°$ from the Sun-Galactic center direction (Bissantz & Gerhard, 2002; Rattenbury et al., 2007), while some other papers present a longer, thinner bar, ~ 8 kpc long, and position angle $\sim 45°$ (Picaud et al., 2003; Benjamin et al, 2005). This controversy has led to some authors to study the possibility of two structures in the inner Galaxy: an inner thin bar, with half length of ~ 4 kpc and a position angle of $\sim 43°$, or $-14° < l < +30°$, $|b| < 1.5°$, and a thicker triaxial bulge, with position angle of $\sim 25°$, or $|l| < 15°$, $|b| < 10°$ (Hammersley et al., 2000; López-Corredoira et al., 2007; Cabrera-Lavers et al., 2008). There are also conflicting views about the inner Milky Way formation (Barbuy, 2008): It appears as a classical bulge from stellar populations studies, whereas dynamical simulation modelers predict it to be a pseudobulge resulting from disk dynamical instabilities and secular evolution of the bar.

1.1 Inner Galactic Globular Clusters

The study of the inner Galactic globular clusters (GGCs) can help in the resolution of the dilemmas previously mentioned, and help also to better constraint the characteristics of the Galactic bulge, since inner GGCs can be used as tracers of the spatial distribution, metallicity and ages of the inner Milky Way old stellar population.

A globular cluster is a spherical collection of stars that orbits a galactic core (figure 1.2). It may contain between 10^4 and 10^6 stars and have central densities of $\sim 10^4 M_\odot pc^{-3}$ (Binney & Tremaine, 1994). Due to the inhomogeneity in the their stellar distributions, it is difficult to describe their sizes. Usually three radii are quoted: a core radius r_c, where the surface brightness falls to half its central value; a half-light radius r_h, the radius of a sphere that contains half of all the light from the cluster; and a tidal radius r_t, the outer limit where the density drops to zero. Average values for these three parameters are $r_c = 1.5$ pc, $r_h = 10$ pc, and $r_t = 50$ pc (Binney & Tremaine, 1994). The Milky Way contains ~ 150 globular clusters, and the GGC system is bimodal (at least) in its chemical, kinematic and spatial properties. Stars

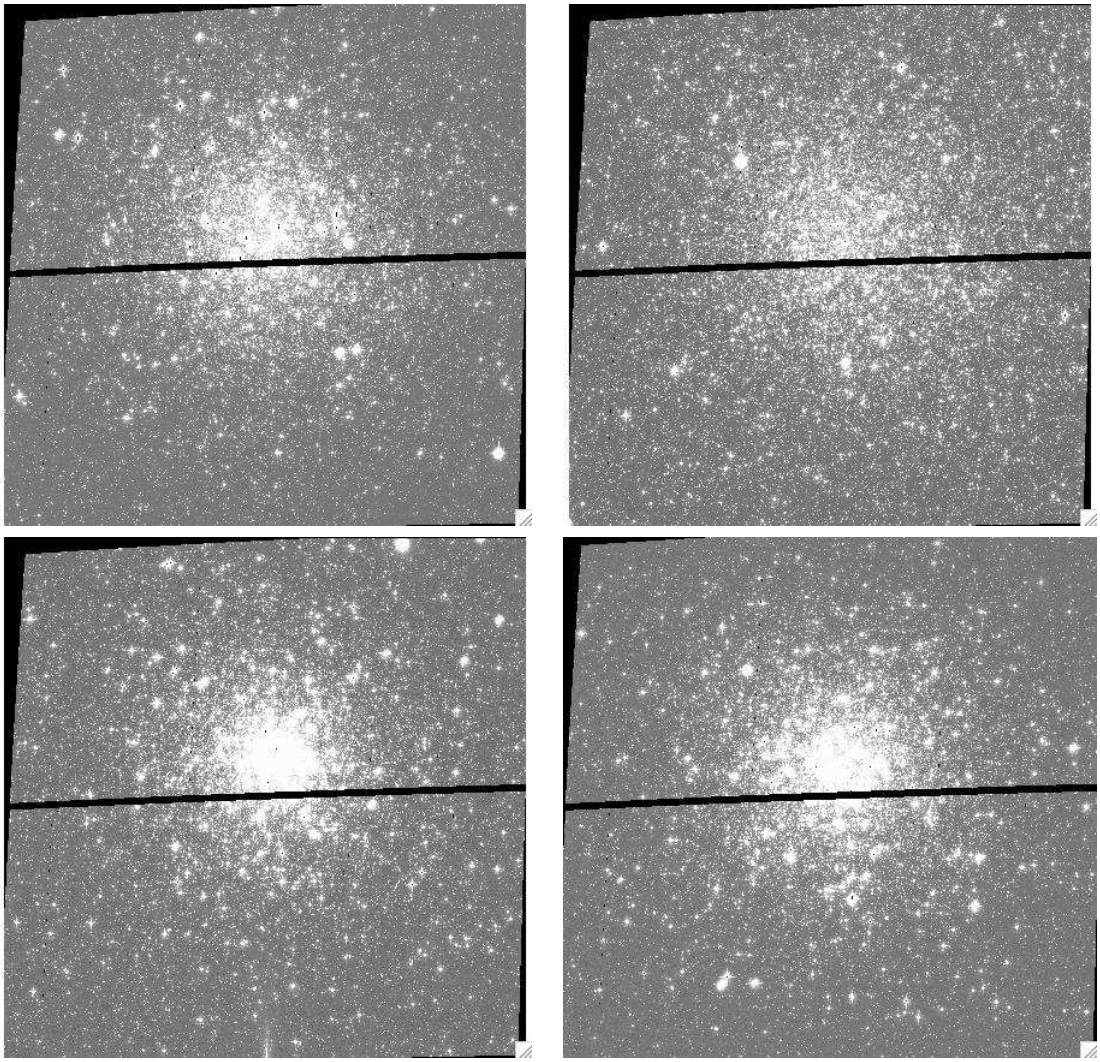

Figure 1.2. NGC 6333 - M 9 (top left), NGC 6553 (top right), NGC 6624 (bottom left), and NGC 6637 - M 69 (bottom right), some of the inner Milky Way globular clusters in our sample, as seen by the ACS camera on the HST.

in individual GGCs have been characterized as old and coeval, created all in a single burst of star formation and sharing the same chemical history. Recent studies tend to suggest that this is not true, especially in the most massive GGCs (Bedin et al., 2004; Piotto et al., 2007). In the cases discovered, it is conjectured that the spread in helium content between stars in the cluster is important, but the spread in age and metallicity seems to be small (D'Antona & Caloi, 2008).

Since inner GGCs provide a means to determine spatial, chemical and age distributions of the old component of the Galactic bulge in detail, they complement what

we can learn from bulge field stars. This is partly due to the reasonably large number of GGCs in the inner Galaxy –most GGCs are interior to the solar circle–, allowing us to sample much of the volume of the Galactic bulge, and partly due to the fact that the stars in individual clusters are coeval, and spatially and kinematically distinct. As we shall show in this thesis, the clusters also provide a unique means of determining the differential extinction along their lines of sight, giving us the opportunity to improve the precision with which we can determine the properties of their stellar populations.

1.2 Color-Magnitude Diagram

One of the more extensively used tools to study the characteristics of the GGCs and their stellar populations is the Color-Magnitude Diagram (CMD). Stars in the CMDs follow a well determined evolutionary path (figure 1.3). They spend most of their lives in the main sequence (MS) burning hydrogen in their core. They leave the MS at the turn-off point (TO) growing in size and burning hydrogen in a shell as they move across the subgiant branch (SGB) and the red giant branch (RGB). Then they move to the HB where they burn helium in the core and hydrogen in a shell. They leave the HB moving across the asymptotic giant branch (AGB) burning helium and hydrogen in a shell. And finally, if they are not very massive, like the stars still alive in the GGCs, they move rapidly across the post AGB phases to finish their lives as white dwarfs (WD). Stars spend different times in the different evolutionary sequences depending on their initial masses: less massive stars evolve slowlier along the CMD sequences than more massive stars. Since stars in GGCs are coeval and located at approximately the same distance, the most important difference between them is their initial mass. As these objects are old, they have stars in all the different evolutionary sequences that we have mentioned.

The analysis of the CMD can give us information about the distance, metallicity and age of the cluster we are studying (Recio-Blanco et al., 2005; de Angeli et al., 2005; Marín-Franch et al., 2009). However, the presence of significant differential extinction in low-latitude fields, particularly near the Galactic Center, greatly

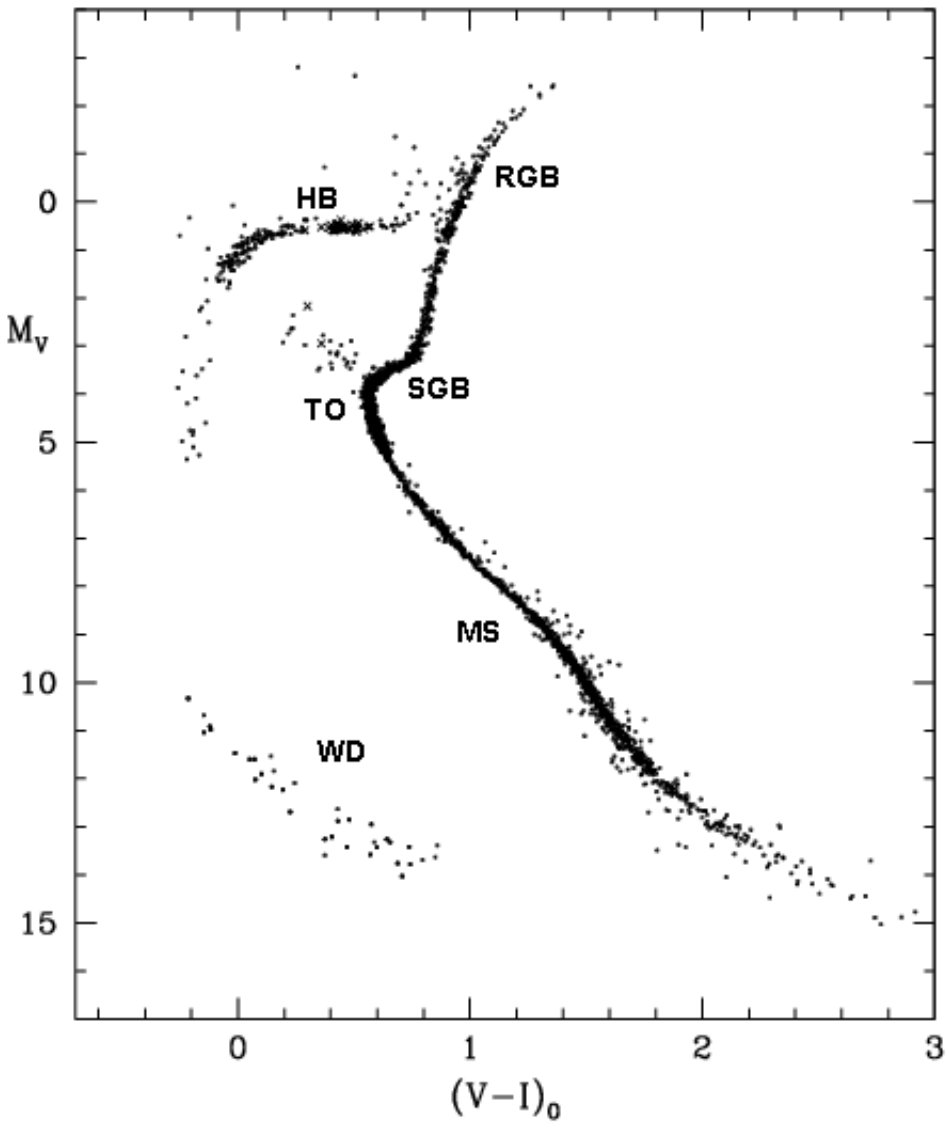

Figure 1.3. Different evolutionary sequences in the CMD, with used abbreviations: MS - Main Sequence, TO - Turn-Off point, RGB - Red Giant Branch, HB - Horizontal Branch, AGB - Asymptotic Giant Branch, and WD - White Dwarfs

complicates traditional CMD analysis. As a result, the study of many GGCs located towards the inner Galaxy has been historically neglected. Various recent studies have tried to overcome the difficulties associated with the study of inner GGCs to better exploit them as probes of the stellar populations near the Galactic Center. One obvious approach is to use infrared photometry to study these clusters (Davidge, 2000; Valenti et al., 2007) to take advantage of the smaller extinction in these bands. But to extract precise information about the ages of the GGCs, an accurate location of the MS turn-off (TO) is crucial in most methods of cluster dating (Stetson et al., 1996; Sarajedini et al., 1997; Gratton et al., 2003). Infrared photometry sufficiently deep to reach the MS with enough precision to accurately locate the TO point is difficult to achieve, and only now are we starting to see the first results after the careful application of new adaptive optics techniques on big telescopes (Moretti et al., 2009). Deep photometry is much more easily obtained in the optical, but at the cost of increased extinction. Several authors have used different methods to try to map differential optical extinction in GGCs before: Piotto et al. (2002) have used colors of variable RRLyrae stars to create the reddening maps; Melbourne & Guhathakurta (2004) and Heitsch & Richtler (1999) have used photometric studies of the stars in the HB; von Braun & Mateo (2001) and Piotto et al. (1999b) have used photometric studies of MS, SGB, and RGB stars. In general, the resolution and accuracy of optical extinction maps are not adequate to fully eliminate the effects of differential reddening at a level of precision to produce deep CMDs of similar high quality now typical for high-latitude clusters with little or no differential extinction (Rosenberg et al., 2000a; Piotto et al., 2002). In the course of this thesis, we have developed a new technique that allow us to map the ISM across a cluster with a high precision, and used it to clean the CMDs of a sample of inner GGCs. Those high-quality CMDs are used to obtain the kind of information about the distances, reddenings and ages for these inner GGCs that can be useful to address questions about the structure, formation and evolution of the central regions of the Milky way.

1.3 Outline of Dissertation

This thesis is divided in five more chapters. Chapter 2 presents a new optical photometric database consisting of a sample of 25 GGCs, located towards the center of the Milky Way, which were suspected to be affected by differential extinction. The criteria used to define our sample of GGCs are given, along with an explanation of the steps followed to obtain precise astrometry and optical photometry of the stars in these clusters. An overview of the un-dereddened CMDs of the clusters in our sample is provided, along with descriptions of characteristic features of the environments in which they are located. Previous optical and infrared photometric studies are also briefly summarized. Chapter 3 describes the new technique that we have developed to map the differential extinction along the field of the clusters in our sample. The different iterative steps that this technique is composed of are detailed in this chapter, along the powerful non-parametric statistics that allow to apply them. Chapter 4 shows the extinction maps produced by the dereddening technique, and the high-quality, cleaner, differentially dereddened CMDs produced when using this information. Chapter 5 provides an analysis of the stellar populations of the clusters based on the differentially dereddened CMDs, inferring information about the distances, absolute reddenings, and ages of the clusters from comparisons with the latest models. Finally, chapter 6 summarizes our results and outlines future work.

CHAPTER 2

The Catalog

2.1 Selection of our sample members

The cluster sample presented in this study consists of 25 GGCs located in the direction of the inner Galaxy. The target selection was restricted to clusters located within 30 deg of the Galactic center. Because the precision of our dereddening technique (see chapter 3) requires good sampling and photometry down to a few magnitudes below the MSTO, and also depends on the density of stars and the spatial variations in the extinction, the clusters in our sample were chosen to also satisfy the following criteria:

- Exhibit moderate mean extinction, implying that they may suffer from extinction variations. We explicitly restricted our sample to clusters with a mean reddening of $E(B-V) \geq 0.07$ mag.

- Be sufficiently luminous to possess a well-defined MS. Our analysis requires a significant number of stars (at least a few hundreds) to calculate the extinction in a region. We therefore chose clusters with a luminosity satisfying $M_{\rm V} \leq -6$.

- Be relatively nearby. With our dereddening technique, the stars that provide most of the information about the differential extinction are those located in the CMD sequences most nearly orthogonal to the reddening vector (SGB and upper MS). Since one of the goals of this project is to accurately calculate the relative ages of this clusters, we must also reach the MS with good precision at the TO in order to carry out a reliable age/metallicity analysis. Hence, we chose clusters with an apparent distance modulus of $(m-M)_{\rm V} \leq 16.6$.

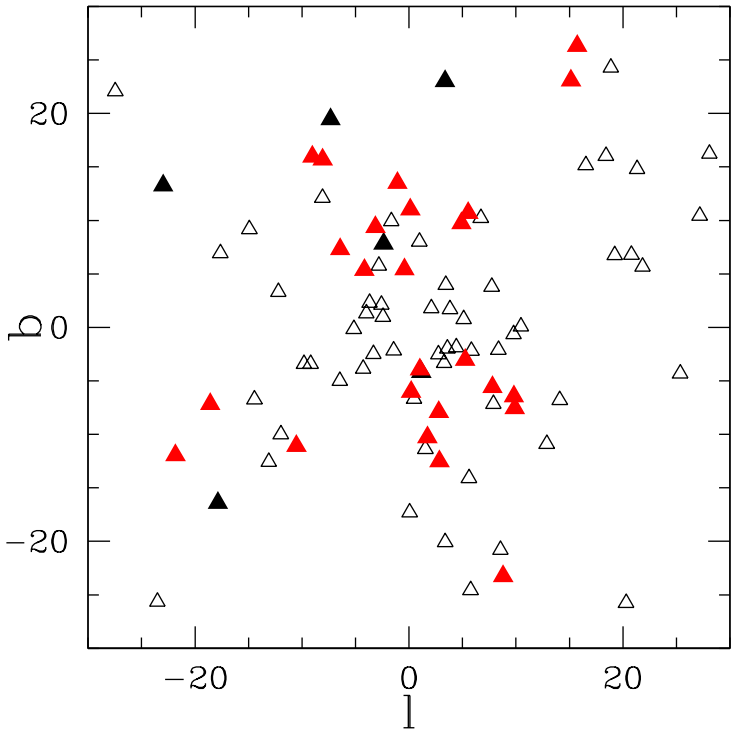

Figure 2.1. .
Location of the clusters that follow the criteria to belong to our sample (solid triangles), and the rest of the inner Galactic globular clusters (open triangles). The position of the 25 GGCs that we were able to observe and made our sample is in red.

- Be sufficiently extended so that we can define maps that cover a significant solid angle around the clusters. We therefore chose clusters with a tidal radius $r_t \geq 7.5$ arcmin.

We were able to observe 25 of the 31 GGCs that fulfill these requirements, according to the 2005 version of Harris catalog (Harris, 1996). Their positions are shown in figure 2.1 along with the rest of the clusters located in the inner Galaxy. Their characteristics, according to the most recent 2009 version of Harris catalog (Harris, 1996), are given in figure 2.7. Note that according to this updated version of the catalog, two of the clusters in our sample, NGC 6287 and NGC 6355, do not fulfill anymore the apparent distance modulus requirement to belong to our sample.

2.2 Observations and data reduction

We obtained optical photometric data for our sample of GGCs using two telescopes, the Magellan 6.5m Baade Telescope located at the Las Campanas Observatory (LCO) in Chile, and the *Hubble Space Telescope* (*HST*). In this section we provide a complete summary of these observations and explain in detail the steps followed for the reduction and calibration of the data. The final photometry has an absolute precision of $\sigma \sim 0.02 - 0.03$ magnitudes in most cases. The internal precision is around $\sigma \sim 0.01 - 0.02$, sufficient to achieve the precise extinction maps that will allow us to produce clean CMDs. From these we will aim to derive the cluster characteristics with an accuracy similar to those derived from high-latitude clusters CMDs that suffer little or no differential extinction.

2.2.1 Observations

The GGCs in our sample were observed from the ground over four nights, May, 30th to June, 2nd 2005, with the LCO 6.5 m Magellan Baade Telescope, using the Inamori Magellan Areal Camera and Spectrograph (IMACS) in imaging mode. We used the f/4 camera to image a field of view (FOV) of $15.46' \times 15.46'$, with a pixel size of $0.11''$. All fields were observed using standard Johnson-Cousins B,V, and I filters (Bessell, 1990). Two sets of observations with different exposure times (short and long) were taken in B and V filter, and three (extra-short, short, and long) in I, for every cluster. Although the nights during our observing run were not all completely photometric, the seeing conditions were very good, with average values of $\sim 0.6''$ in V for the whole run. Table 2.1 lists the details of these ground-based photometry observations.

In order to obtain useful photometry of the inner regions of the more centrally crowded clusters, we supplemented our Magellan images with the Advanced Camera for Surveys (ACS) aboard *HST*. These data were obtained in Snapshot program 10573. The ACS has a FOV of $3.37' \times 3.37'$, with a pixel size of $0.05''$. Five clusters of our sample were observed using the $f435w(B_{435})$, $f555w(V_{555})$, and $f814w(I_{814})$ filters. Table 2.2 lists the details of these new *HST* observations.

Table 2.1. Summary of the observations with the Magellan telescope

Cluster	α_{2000} [a]	δ_{2000} [b]	UT Date	Filter	Exp. Time [c]	Airmass
NGC 6121	16 23 40.0	-26 30 29.8	2005 Jun 2	B	$3\times1, 3\times25$	1.37-1.42
...	...	...	...	V	$3\times1, 3\times20$	1.43-1.48
...	...	...	...	I	$3\times1, 3\times15$	1.50-1.57
NGC 6144	16 27 18.7	-26 00 28.4	2005 May 31	B	$3\times5, 3\times120$	1.38-1.52
...	...	...	...	V	$3\times5, 3\times120$	1.55-1.65
...	...	...	...	I	$1\times1, 3\times3, 3\times75$	1.77-1.92
NGC 6218	16 47 18.6	-01 55 51.6	2005 Jun 1	B	$3\times5, 3\times120$	1.34-1.44
...	...	...	...	V	$3\times5, 3\times120$	1.46-1.55
...	...	...	...	I	$1\times1, 3\times3, 3\times75$	1.56-1.66
NGC 6235	16 53 29.8	-22 09 37.8	2005 May 31	B	$3\times5, 3\times120$	1.19-1.27
...	...	...	...	V	$3\times5, 3\times120$	1.28-1.34
...	...	...	...	I	$1\times1, 3\times3, 3\times75$	1.36-1.44
NGC 6254	16 57 13.0	-04 04 58.3	2005 Jun 1	B	$3\times5, 3\times120$	1.14-1.16
...	...	...	...	V	$3\times5, 3\times120$	1.17-1.20
...	...	...	...	I	$1\times1, 3\times3, 3\times75$	1.21-1.25
NGC 6266	17 01 17.2	-30 05 42.8	2005 May 30	B	$3\times5, 3\times120$	1.01-1.02
...	...	...	...	V	$3\times5, 3\times120$	1.02-1.03
...	...	...	...	I	$1\times1, 3\times3, 3\times75$	1.03-1.04
NGC 6273	17 02 41.5	-26 15 17.8	2005 May 30	B	$3\times5, 3\times120$	1.00
...	...	...	...	V	$3\times5, 3\times120$	1.00-1.01
...	...	...	...	I	$1\times1, 3\times3, 3\times75$	1.01
NGC 6287	17 05 13.8	-22 41 28.2	2005 Jun 2	B	$3\times5, 3\times120$	1.24-1.32
...	...	...	...	V	$3\times5, 3\times120$	1.33-1.42
...	...	...	...	I	$1\times1, 3\times3, 3\times75$	1.44-1.53
NGC 6304	17 14 37.1	-29 26 43.2	2005 May 31	B	$3\times5, 3\times120$	1.06-1.08
...	...	...	...	V	$3\times5, 3\times120$	1.09-1.11
...	...	...	...	I	$1\times1, 3\times3, 3\times75$	1.12-1.15
NGC 6333	17 19 16.1	-18 30 00.0	2005 Jun 2	B	$3\times5, 3\times120$	1.02-1.03
...	...	...	...	V	$3\times5, 3\times120$	1.02
...	...	...	...	I	$1\times1, 3\times3, 3\times75$	1.02
NGC 6342	17 21 14.5	-19 34 13.1	2005 May 31	B	$3\times5, 3\times120$	1.04-1.06
...	...	...	...	V	$3\times5, 3\times120$	1.02-1.04
...	...	...	...	I	$1\times1, 3\times3, 3\times75$	1.02
NGC 6355	17 24 03.1	-26 20 12.2	2005 Jun 2	B	$3\times5, 3\times120$	1.03-1.06
...	...	...	...	V	$3\times5, 3\times120$	1.06-1.09
...	...	...	...	I	$1\times1, 3\times3, 3\times75$	1.09-1.12
NGC 6352	17 25 35.1	-48 24 20.40	2005 Jun 1	B	$3\times5, 3\times120$	1.06
...	...	...	...	V	$3\times5, 3\times120$	1.06-1.07
...	...	...	...	I	$1\times1, 3\times3, 3\times75$	1.08
NGC 6397	17 40 48.2	-53 39 23.4	2005 May 31	B	$3\times1, 3\times25$	1.11
...	...	...	...	V	$3\times1, 3\times20$	1.10
...	...	...	...	I	$3\times1, 3\times15$	1.10
...	...	...	2006 Apr 20	B	3×15	1.10
...	...	...	...	V	3×15	1.10
...	...	...	...	I	3×15	1.10
NGC 6522	18 03 38.5	-30 00 59.6	2005 May 30	B	$3\times5, 3\times120$	1.01-1.02
...	...	...	...	V	$3\times5, 3\times120$	1.02-1.03
...	...	...	...	I	$1\times1, 3\times3, 3\times75$	1.04-1.05
NGC 6541	18 08 07.8	-43 41 20.7	2005 May 31	B	$3\times5, 3\times120$	1.15-1.18
...	...	...	...	V	$3\times5, 3\times120$	1.18-1.22
...	...	...	...	I	$1\times1, 3\times3, 3\times75$	1.23-1.26
NGC 6553	18 09 20.1	-25 53 26.6	2005 May 31	B	$3\times5, 3\times120$	1.02-1.03
...	...	...	...	V	$3\times5, 3\times120$	1.03-1.06
...	...	...	...	I	$1\times1, 3\times3, 3\times75$	1.07-1.09
NGC 6558	18 10 23.1	-31 44 48.0	2005 May 30	B	$3\times5, 3\times120$	1.07-1.10
...	...	...	...	V	$3\times5, 3\times120$	1.11-1.13
...	...	...	...	I	$1\times1, 3\times3, 3\times75$	1.14-1.18
NGC 6624	18 23 45.2	-30 20 39.7	2005 May 30	B	$3\times5, 3\times100$	1.21-1.24
...	...	...	...	V	$3\times5, 3\times100$	1.25-1.30
...	...	...	...	I	$1\times1, 3\times3, 3\times60$	1.31-1.36

continued on next page

continued from previous page						
NGC 6626	18 24 37.3	-24 51 10.8	2005 Jun 2	B	$3\times5, 3\times120$	1.02-1.04
...	...	...	...	V	$3\times5, 3\times120$	1.04-1.05
...	...	...	...	I	$1\times1, 3\times3, 3\times75$	1.06-1.07
NGC 6637	18 31 28.0	-32 19 55.6	2005 Jun 2	B	$3\times5, 3\times120$	1.20-1.24
...	...	...	...	V	$3\times5, 3\times120$	1.25-1.30
...	...	...	...	I	$1\times1, 3\times3, 3\times75$	1.17-1.19
NGC 6642	18 31 58.7	-23 27 36.0	2005 Jun 2	B	$3\times5, 3\times120$	1.36-1.43
...	...	...	...	V	$3\times5, 3\times120$	1.45-1.53
...	...	...	...	I	$1\times1, 3\times3, 3\times75$	1.56-1.67
NGC 6656	18 36 28.6	-23 53 13.5	2005 May 31	B	$3\times1, 3\times35$	1.52-1.58
...	...	...	...	V	$3\times1, 3\times30$	1.45-1.51
...	...	...	...	I	$3\times1, 3\times20$	1.38-1.43
NGC 6681	18 43 17.4	-32 16 29.7	2005 Jun 2	B	$3\times5, 3\times120$	1.00-1.01
...	...	...	...	V	$3\times5, 3\times120$	1.01-1.02
...	...	...	...	I	$1\times1, 3\times3, 3\times75$	1.02-1.03
NGC 6809	19 40 04.1	-30 56 43.8	2005 May 31	B	$3\times1, 3\times35$	1.07-1.08
...	...	...	...	V	$3\times1, 3\times30$	1.09-1.10
...	...	...	...	I	$3\times1, 3\times20$	1.11-1.12

[a] Units of right ascension are hours, minutes, and seconds.
[b] Units of declination are degrees, arcminutes, and arcseconds.
[c] Number of exposures × exposure time, in seconds.

Table 2.2. Summary of ACS observations from Snapshot program 10573

Cluster	α_{2000} [a]	δ_{2000} [b]	UT Date	Filter	Exp. Time [c]
NGC 6218	16 47 14.50	-01 56 52.0	2006 Feb 1	B_{435}	120
...	...	...	...	V_{555}	50
...	...	...	...	I_{814}	20
NGC 6333	17 19 11.80	-18 30 59.0	2006 May 31	B_{435}	2×340
...	...	...	...	V_{555}	240
...	...	...	...	I_{814}	90
NGC 6553	18 09 17.50	-25 54 28.0	2006 Apr 4	B_{435}	3×340
...	...	...	...	V_{555}	300
...	...	...	...	I_{814}	60
NGC 6624	18 23 40.70	-30 21 39.0	2006 Jun 5	B_{435}	360
...	...	...	...	V_{555}	160
...	...	...	...	I_{814}	65
NGC 6637	18 31 23.20	-32 20 53.0	2006 Jun 6	B_{435}	300
...	...	...	...	V_{555}	120
...	...	...	...	I_{814}	50

[a] Units of right ascension are hours, minutes, and seconds.
[b] Units of declination are degrees, arcminutes, and arcseconds.
[c] Number of exposures × exposure time, in seconds.

To better calibrate our photometry, we also used images available through the *HST* data archive for all the clusters in our sample. The data taken from the *HST* data archive are comprised of $f439w(B_{439})$, $f555w(V_{555})$, $f606w(V_{606})$, and $f814w(I_{814})$ images obtained with the Wide Field Planetary Camera 2 (WFPC2), and of $f435w(B_{435})$, $f606w(V_{606})$, and $f814w(I_{814})$ images taken with the ACS. Table 2.3 lists the different *HST* programs that we use data from.

2.2.2 Data reduction and photometry derivation

For the ground-based data, the initial processing of the raw CCD images was done with the routines in the **ccdred** package of the Image Reduction and Analysis Facility (IRAF). The images were first corrected for bias, then flatfielded using a combination of dome and twilight flats. Afterward, since different frames for every cluster were taken with different exposure times in the B, V, and I filters (see table 2.1), and they had small spatial offsets between them, the frames of every individual cluster were aligned, using the IRAF task **imalign**, and average combined for every exposure time and filter, with the IRAF task **imcombine**.

Stellar photometry was carried out on the ground-based processed images using an updated version of DoPHOT (Schechter et al., 1993). This version works on any platform and accept images consisting of real data values. It also provides better aperture corrections than previous versions, allowing for variations in aperture corrections as a function of field position and stellar magnitude.

We also carried out an astrometric analysis of our cluster fields. We derived coordinates (right ascension α and declination δ) for all stars detected in our photometric study by comparison with bright reference stars obtained in each field from the Naval Observatory Merged Astrometric Dataset (NOMAD) catalog stars available through the United States Naval Observatory (USNO) website. In practice, more than 100 stars were available as astrometric references within the fields of every chip of our CCD camera. A fourth order polynomial fit, done with the IRAF task **mscpeak**, produced dispersions of $\sigma \sim 0.25''$, consistent with the catalog precision. This polynomial provides the correction for the geometric distortion of IMACS, which is a

Table 2.3. Summary of *HST* programs whose archival data have been used in our analysis.

Cluster	Camera	Program	PI	Filters
NGC 6121	WFPC2	6116	C. Bailyn	$V_{555}I_{814}$
···	ACS	10775	A. Sarajedini	$V_{606}I_{814}$
NGC 6144	WFPC2	···	···	···
···	ACS	10775	A. Sarajedini	$V_{606}I_{814}$
NGC 6218	WFPC2	8118	G. Piotto	$B_{439}V_{555}$
···	ACS	10775	A. Sarajedini	$V_{606}I_{814}$
NGC 6235	WFPC2	7470	I. King	$B_{439}V_{555}$
···	ACS	···	···	···
NGC 6254	WFPC2	6113	F. Paresce	$V_{606}I_{814}$
···	ACS	10775	A. Sarajedini	$V_{606}I_{814}$
NGC 6266	WFPC2	8118	G. Piotto	$B_{439}V_{555}$
···	WFPC2	8709	F. Ferraro	$V_{555}I_{814}$
···	ACS	···	···	···
NGC 6273	WFPC2	7470	I. King	$B_{439}V_{555}$
···	ACS	···	···	···
NGC 6287	WFPC2	6561	L. Fullton	$B_{439}V_{555}I_{814}$
···	ACS	···	···	···
NGC 6304	WFPC2	7470	I. King	$B_{439}V_{555}$
···	ACS	10775	A. Sarajedini	$V_{606}I_{814}$
NGC 6333	WFPC2	5366	R. Zinn	$V_{555}I_{814}$
···	ACS	···	···	···
NGC 6342	WFPC2	7470	I. King	$B_{439}V_{555}$
···	ACS	···	···	···
NGC 6352	WFPC2	5366	R. Zinn	$V_{555}I_{814}$
···	ACS	10775	A. Sarajedini	$V_{606}I_{814}$
NGC 6355	WFPC2	7470	I. King	$B_{439}V_{555}$
···	ACS	···	···	···
NGC 6397	WFPC2	5929	I. King	$B_{439}V_{555}$
···	WFPC2	7335	J. Grindlay	$V_{555}I_{814}$
···	ACS	10775	A. Sarajedini	$V_{606}I_{814}$
NGC 6522	WFPC2	6095	S. Djorgovski	$B_{439}V_{555}$
···	ACS	···	···	···
NGC 6541	WFPC2	5366	R. Zinn	$V_{555}I_{814}$
···	ACS	10775	A. Sarajedini	$V_{606}I_{814}$
NGC 6553	WFPC2	7307	G. Gilmore	$V_{555}I_{814}$
···	ACS	···	···	···
NGC 6558	WFPC2	···	···	···
···	ACS	9799	R. Rich	$V_{606}I_{814}$
NGC 6624	WFPC2	5324	B. Yanny	$B_{439}V_{555}$
···	WFPC2	5366	R. Zinn	$V_{555}I_{814}$
···	ACS	10775	A. Sarajedini	$V_{606}I_{814}$
NGC 6626	WFPC2	6779	K. Gebhardt	$V_{555}I_{814}$
···	ACS	···	···	···
NGC 6637	WFPC2	8118	G. Piotto	$B_{439}V_{555}$
···	WFPC2	5366	R. Zinn	$V_{555}I_{814}$
···	ACS	10775	A. Sarajedini	$V_{606}I_{814}$
NGC 6642	WFPC2	8118	G. Piotto	$B_{439}V_{555}$
···	ACS	9799	R. Rich	$V_{606}I_{814}$
NGC 6656	WFPC2	5344	C. Bailyn	$B_{439}R_{675}$
···	WFPC2	7615	K. Sahu	$V_{606}I_{814}$
···	ACS	10775	A. Sarajedini	$V_{606}I_{814}$
NGC 6681	WFPC2	8723	G.Piotto	$B_{439}V_{555}$
···	ACS	10775	A. Sarajedini	$V_{606}I_{814}$
NGC 6809	WFPC2	···	···	···
···	ACS	10775	A. Sarajedini	$V_{606}I_{814}$

function of position for every filter and every chip. From the geometric distortion coefficients, we calculated the effective pixel area and used it to make an area correction to the photometry.

To calibrate our ground-based data, we first transformed the photometry from each of the individual eight CCDs in the camera in IMACS to a common zero point (see section 2.2.3), and then transformed this system to a standard system (see section 2.2.4)–in our case, the Johnson-Cousins system (Bessell, 1990). Since all of the nights were not completely photometric we used Stetson photometric standard stars (Stetson, 2000) and the photometry from the clusters obtained with the *HST* to fine-tune the calibration of our ground-based data (see section 2.2.4).

The photometry of the clusters from the *HST* observations was obtained using the programs HSTPHOT for the WFPC2 data (Dolphin, 2000) and DolPHOT for the ACS data (Dolphin, 2000). These programs have been specifically tailored to analyze data from these cameras. They take the images for every cluster retrieved from the HST in the different filters, and analyze them all at the same time. The programs align the images, combined them and provide the final combined-frame and individual-frame photometry, both in the HST filter system and in the Johnson-Cousins system. We follow the author's prescriptions to give the input parameters for the analysis to both programs. Photometric goodness-of-fit parameters were employed to select only objects with high-quality measurements. Only measurements for which an object was classified as stellar (HSTPHOT and DolPHOT types 1 and 2), and for which $-0.1 \leq sharpness \leq 0.1$, $crowding \leq 0.5$, and errors in all measured magnitudes $\sigma \leq 0.1$ were retained.

2.2.3 Instrumental calibration

The camera in IMACS consists of eight CCDs, each with its own slightly different mean quantum efficiency and color sensitivity. To calibrate our data, we must first transform the photometry from each of the individual CCDs to a common zero point, then transform this system to a standard system–in our case, the Johnson-Cousins system (Bessell, 1990). In this section, we shall focus on the first step of transforming

the individual CCDs to a common instrumental system.

For this purpose, we arbitrarily chose one of the CCDs, chip 2 (see figure 2.2), as the one defining the instrumental system. The goal was to tie all the other CCDs to this chip's photometric zero point. We attempted to do this in two ways. First, we observed one Landolt field (Landolt (1992); PG 1047+003) in every one of the CCDs and in all three filters (BVI) in rapid succession on every night of our run. There were very few stars in this field, and the scatter we found in the mean photometric offsets – about 0.05 mag between CCDs – was too large given our need to bring all our photometry to a common system to 1-2% precision.

We tried a second approach during a sequence of observations during a 2006 Magellan run (see table 2.1) in which we tried to auto-calibrate the IMACS CCD array using stars from the cluster NGC 6397. The basic idea was to obtain a minimal number of exposures in each filter so that at least part of all CCDs overlapped with CCD 2, the chip defining our instrumental photometric system. We found that a sequence of three exposures could achieve the desired overlap. Figure 2.2 illustrates the approach. In the left panel, the darker outline of the IMACS CCD shows the location of a first exposure, in this case at the same location as the actual field we observed in 2005 for the cluster NGC 6397. The second exposure, shown as a lighter (red) outline is offset in both RA and Dec so that four of its CCDs (1, 2, 5 and 6) overlap with the position of CCD 2 in the first exposure. The right panel again shows the initial pointing in the darker outline, with a third pointing as a lighter (green) outline. Now, CCDs 3, 4, 7 and 8 of the last exposure overlap with CCD 2 from the first exposure. This sequence, repeated for each filter, generated a large list of stars that have been observed on CCD2 *and* on every other CCD in the array. Because only three exposures were required and because we took these in rapid succession, we can safely ignore airmass variations as we calculate the offsets from a given chip to the system defined by CCD 2. In addition, we have exposures from the 2005 and 2006 runs of the *same* fields (the dark outlines in figure 2.2) that allow us to determine any possible variations in CCD sensitivities between runs.

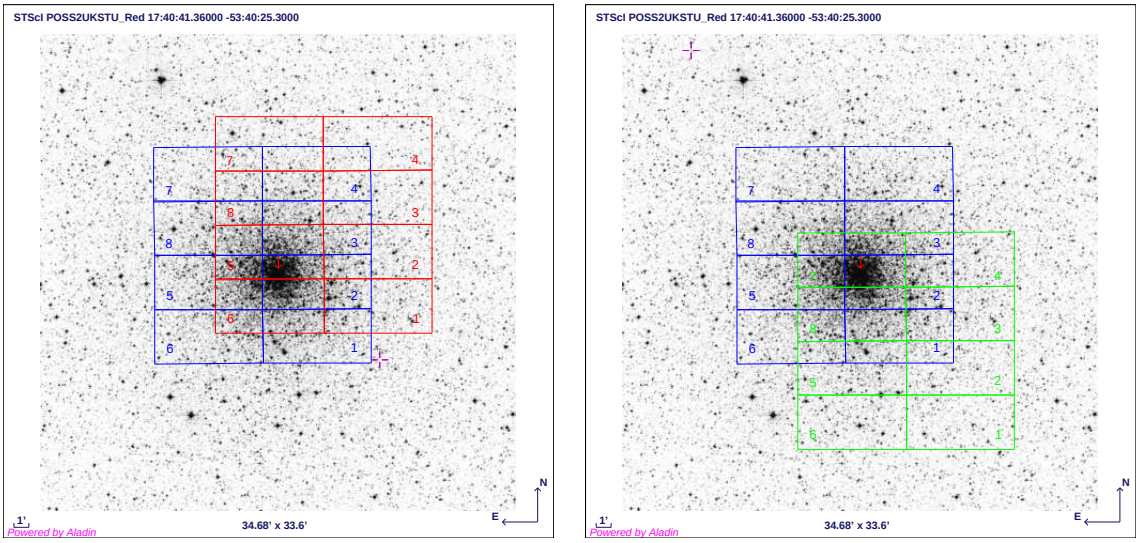

Figure 2.2. Pointings used to make the instrumental calibration, bringing the photometry from the different chips to the chip2 system. We chose these configurations because they allowed us to observe stars in common between chip2 and all the other chips in just 3 pointings (chips 1, 5 and 6 have stars in common with chip 2 in the left configuration and chips 3, 4, 7, and 8 have stars in common with chip2 in the right configuration). We used stars from the cluster NGC 6397, one of the clusters in our sample, to do this calibration. The blue pointing was the same as the one originally used in our observing run. That way we were able to compare the photometries of our original observing run and the calibrating run for all the chips in the camera and take care of any effect produced by a change in the sensitivity of the CCDs (see text).

The model we used to transform each CCD to the chip 2 system has the form

$$m_2 = m_i + Z_i + \gamma_i c_i \tag{2.1}$$

where m_i is the instrumental magnitude of chip i (excluding $i = 2$), Z_i is the zero-point offset from chip i to chip 2, and γ_i is the color coefficient for instrumental color c_i. In practice, we carried out this analysis separately for each filter, B, V, and I, with the colors defined appropriately for each filters ($(B-V)$ for the B-band transformation and $(V-I)$ for the V and I-band transformations). We found that the color terms are all negligibly small in the chip-to-chip transformations for each filter, so the final model adopts $\gamma_i = 0$ for all CCDs and all colors. Thus we only had to determine the mean values of the Z_i coefficients as the weighted mean of the differences of the instrumental magnitudes, $m_i - m_2$ for all stars in common between chip i and chip 2. Weights for each measurement were assigned according to the

photometric errors and the dispersion in the offset distribution. A first application of this approach, to the calibration sequence of NGC 6397 obtained in 2006 (figure 2.2), allowed us to place all the data from that run on the 2006 chip 2 instrumental system.

Since the relative sensitivities of the CCDs might have changed between the 2005 and 2006 runs, we then took an additional step to define the chip-to-chip offsets for the 2005 run from which all our ground-based cluster photometry is defined. This process involves the observations of NGC 6397 from our 2006 run (described above) and the observations of the same field for the same cluster obtained in 2005.

For this purpose we adopted the following transformation,

$$m_{i,06} = m_{i,05} + Y_i + \delta_i c_i + k_{05} X_{05} - k_{06} X_{06} \tag{2.2}$$

The zero-point offset from the 2005 observations required to place them on the 2006 system for CCD i is given by Y_i (this now includes the case $i = 2$), for a color term δ_i, and an instrumental color on the 2005 system of c_i. The final two terms account for the different airmasses and possibly different extinction coefficients for each run and each observation. We do not know this product (extinction coefficient k times airmass X) for the 2006 run, because we did not observe standard stars on that run. But we know that the sum of these products is constant when comparing the 2005 and 2006 NGC 6397 observations. Thus, we can rewrite the equation above as

$$m_{i,06} = m_{i,05} + Y_i' + \delta_i c_i \tag{2.3}$$

in close analogy to equation 1. Note that the new zero point offset now implicitly includes the airmass terms:

$$Y_i' = Y_i + k_{05} X_{05} - k_{06} X_{06} \tag{2.4}$$

We can simplify this due to the fact that we found that the color terms in equation 3 are all negligibly small. Thus we only had to determine the mean values of the Y_i'

Table 2.4. Zero-points to bring the photometry to the chip2 system

Chip	Z_B	$\Delta Y'_B$	Z_V	$\Delta Y'_V$	Z_I	$\Delta Y'_I$
1	-0.160	0.065	-0.159	0.075	-0.038	0.077
2	0.0	0.0	0.0	0.0	0.0	0.0
3	-0.106	0.009	-0.117	0.008	-0.020	0.014
4	-0.755	0.052	-0.711	0.042	-0.442	0.078
5	-0.009	0.016	0.010	0.012	0.078	0.007
6	-0.137	0.005	-0.175	0.004	-0.132	0.021
7	-0.262	0.023	-0.263	0.012	-0.191	0.054
8	-0.230	0.052	-0.169	0.040	-0.033	0.046

coefficients as the weighted mean of the differences of the instrumental magnitudes, $m_{i,06} - m_{i,05}$ for all stars from chip i. As before, weights for each measurement were assigned according to the photometric errors and the dispersion in the offset distribution.

At this stage, we can transform the 2005 NGC 6397 data to a common instrumental system defined by the chip 2 from the 2006 observations of this same cluster. But what we really require are the offsets in the 2005 system that bring all data from the IMACS CCDs obtained in 2005 to a common system. That is, the final chip-to-chip offsets for the 2005 data are simply

$$\Delta Y'_i = Y'_i - Y'_2 \tag{2.5}$$

The values of Z and $\Delta Y'$ required to tie the various chips systems to a common system defined by chip 2 are listed in table 2.4. The errors in the values of Z and $\Delta Y'$ are $\sigma \sim 0.001$, the error of the mean of the distributions used to obtain them (see figure 2.3). The dispersions of the distributions from which these Z and $\Delta Y'$ are derived, a measure of the internal precision of our photometry, are $\sigma \sim 0.01$.

2.2.4 Absolute calibration

We placed our photometry in the Johnson-Cousins photometric system by observing Landolt fields (Landolt, 1992) over a range of airmasses during the nights of our 2005 observing run. Since the first two nights were the most photometric of our run, we only used the standard fields observed those two nights to obtain the following

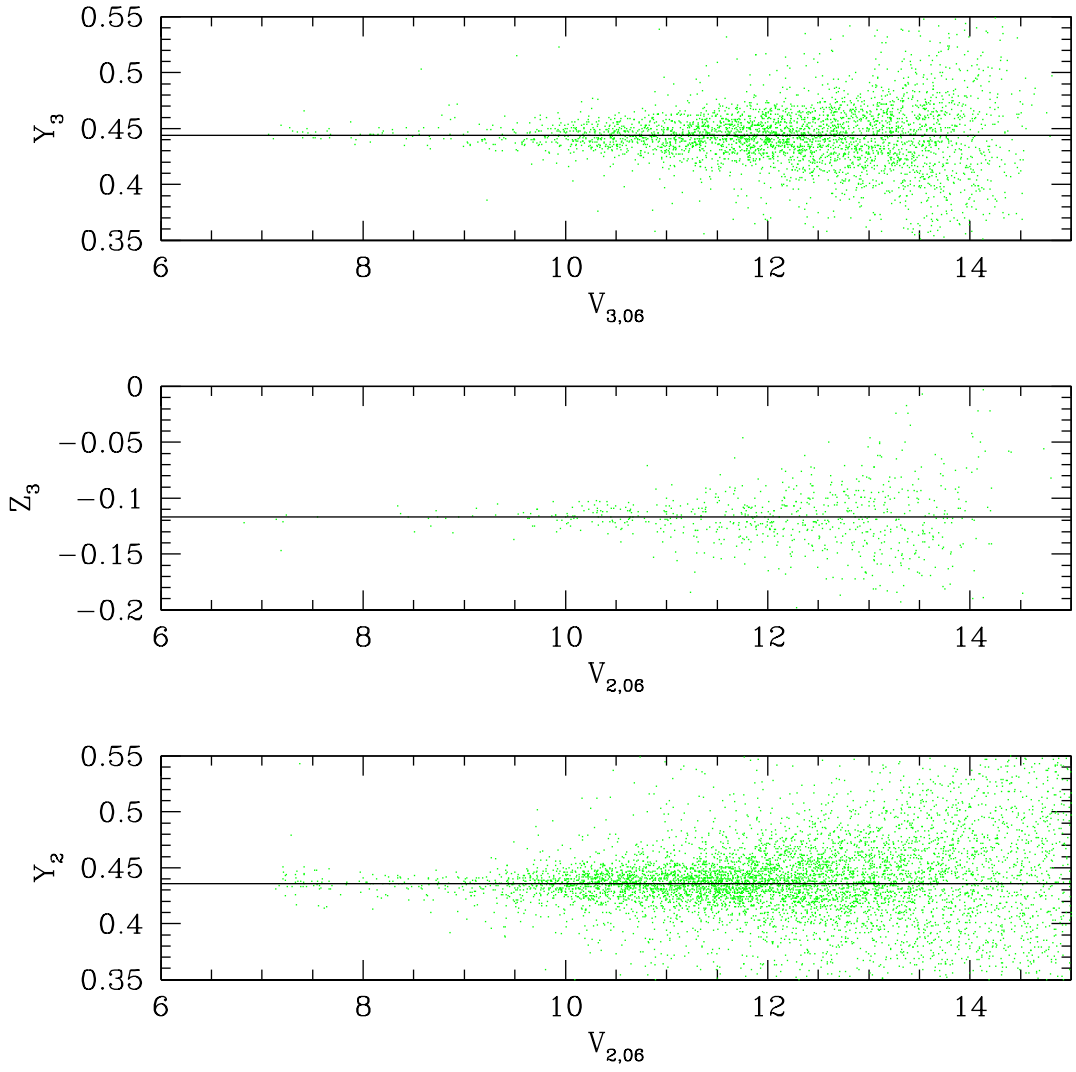

Figure 2.3. Calculation of the zero-points to bring the photometry to the chip2 system. In this figure we have plotted, as an example of the technique, the different zero-points that we have to obtain to move the V photometry from the chip3 to the chip2 reference system (see equations in the text). The solid lines show the final average values adopted.

transformations:

$$V = 3.699 + v - 0.169X - 0.0106(b - v) \tag{2.6}$$

$$B - V = -0.286 - 0.080X + 1.127(b - v) \tag{2.7}$$

$$V - I = 0.589 - 0.097X + 1.030(v - i) \tag{2.8}$$

where X is the airmass, b, v, and i are the instrumental magnitudes in the instrumental system and B, V, and I the corresponding magnitudes in the Johnson-Cousins photometric system.

To fine-tune our calibration we decided to compare our photometry with Stetson photometric standard stars (Stetson, 2000). We found in some cases significant absolute offsets between Stetson's and our photometry. These zero-points could be easily calculated (see figure 2.4 and table 2.6). However, only ten of our clusters had stars in common with Stetson's catalog, and only eight had stars calibrated in all three filters (see table 2.5).

To extend the comparison to more clusters, we looked for members of our sample already observed with at least one of the two *HST*'s optical wide-field imaging instruments, WFPC2 and ACS. We found that all of the clusters have already been observed at least in two of our filters, and most of them in all three (see table 2.5). The comparison between the *HST* and ground-based data is complicated by the large resolution difference in the datasets and the highly crowded values of the fields. When the offsets in the photometries of individual stars of a cluster are plotted, there is a clear, asymmetric spread in the data (see figure 2.5). Due to the higher resolution of the *HST*, individual stars in the *HST* data are blends in the ground-based data. To obtain the absolute offset between the two systems eliminating the blended stars effect we calculated a weighted mean of the offsets of the stars in common (see figure 2.5), where the weights were assigned according to the photometric errors and the dispersion in the offset distribution. The weighted mean was iteratively calculated, giving a zero weight to all stars 2σ away from the mean value at each iteration. Whenever we have zero-points calculated separately from independent WFPC2 and

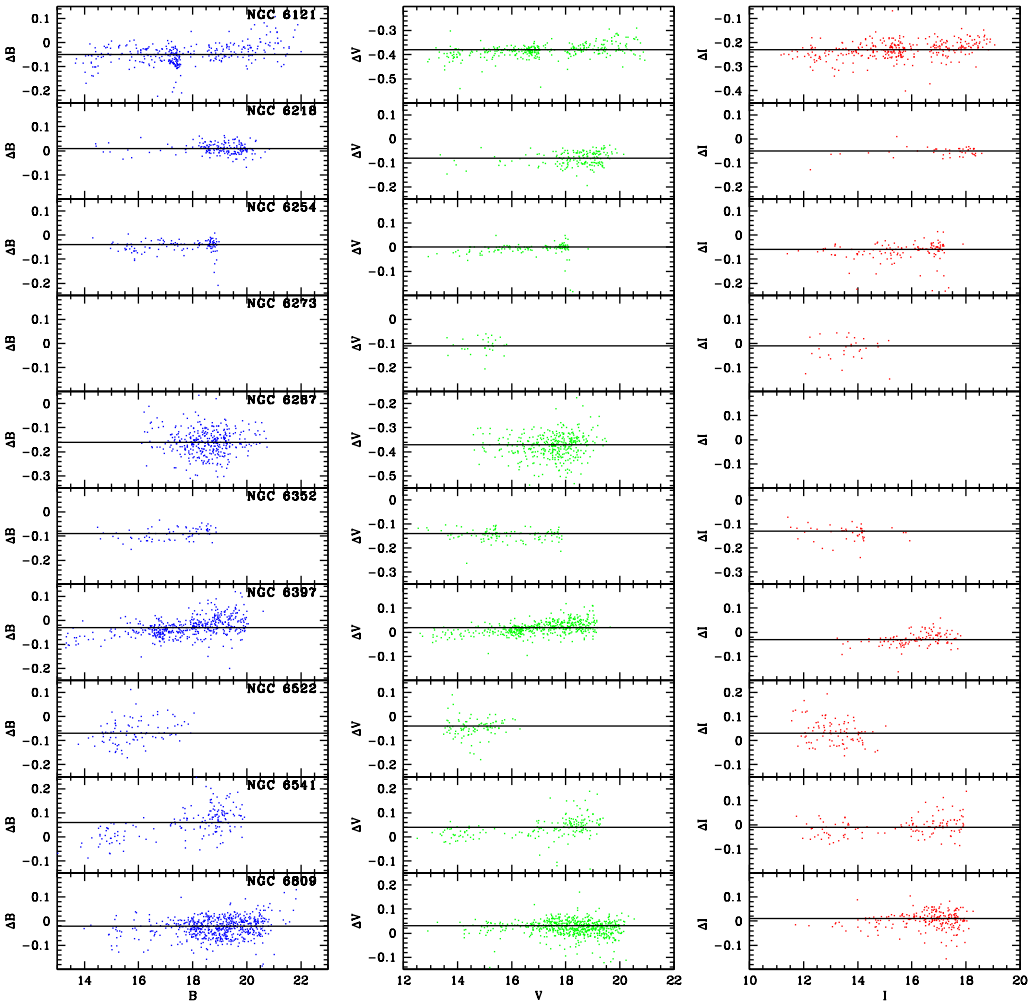

Figure 2.4. Comparison of our raw ground-based photometry with the Stetson calibrating stars for the clusters and filters available. We plot the magnitudes of the stars in our photometry for the different filters versus the differences of Stetson's values minus ours. The lines show where the average offsets lie.

Table 2.5. Calibrating stars for the clusters.

Cluster	Stetson [a]	WFPC2 [b]	ACS [c]	ACS-10573 [d]	*HST* missing[e]	Missing [f]
NGC 6121	BVI	VI	VI	···	B	···
NGC 6144	···	···	VI	···	B	B
NGC 6218	BVI	BV	VI	BVI	···	···
NGC 6235	···	BV	···	···	I	I
NGC 6254	BVI	VI	VI	···	B	···
NGC 6266	···	BVI	···	···	···	···
NGC 6273	VI	BV	···	···	I	···
NGC 6287	BV	BVI	···	···	···	···
NGC 6304	···	BV	VI	···	···	···
NGC 6333	···	VI	···	BVI	···	···
NGC 6342	···	BV	···	···	I	I
NGC 6355	···	BV	···	···	I	I
NGC 6352	BVI	VI	VI	···	B	···
NGC 6397	BVI	BVI	VI	···	···	···
NGC 6522	BVI	BV	···	···	I	···
NGC 6541	BVI	VI	VI	···	B	···
NGC 6553	···	VI	···	BVI	···	···
NGC 6558	···	···	VI	···	B	B
NGC 6624	···	BVI	VI	BVI	···	···
NGC 6626	···	VI	···	···	B	B
NGC 6637	···	BVI	VI	BVI	···	···
NGC 6642	···	BV	VI	···	···	···
NGC 6656	···	BVI	VI	···	···	···
NGC 6681	···	BV	VI	···	···	···
NGC 6809	BVI	···	VI	···	B	···

[a] Stetson calibrating stars observed in these specific Johnson-Cousin filters.

[b] WFPC2 photometry from archival data available in the specified filters. The filters are $f439w$, $f555w$, $f606w$, and $f814w$, and they are transformed by HSTPHOT to the Johnson-Cousins B, V, and I.

[c] ACS photometry from archival data available in the specified filters. The filters are $f435w$, $f606w$, and $f814w$, and they are transformed by DolPHOT to the Johnson-Cousins B, V, and I.

[d] *HST* ACS photometry from our project (SNAP 10573) available in the specified filters. The filters are $f435w$, $f555w$, and $f814w$, and they are transformed by DolPHOT to the Johnson-Cousins B, V, and I.

[e] Lack of *HST* photometry for the cluster in the filter specified.

[f] Lack of *HST* photometry and Stetson calibrating stars for the cluster in the filter specified.

Table 2.6. Offsets applied to transform to Johnson-Cousins system photometry.

Cluster	Offset in B	Offset in V	Offset in I
NIGHT 1			
NGC 6266	-0.49 ± 0.02	-0.39 ± 0.02	-0.27 ± 0.02
NGC 6273	0.01 ± 0.03	$\mathbf{-0.11 \pm 0.03}$	$\mathbf{-0.01 \pm 0.03}$
NGC 6522	$\mathbf{-0.07 \pm 0.04}$	$\mathbf{-0.04 \pm 0.02}$	$\mathbf{0.03 \pm 0.04}$
NGC 6558	...	-0.06 ± 0.02	-0.07 ± 0.02
NGC 6624	-0.03 ± 0.02	-0.02 ± 0.01	-0.05 ± 0.01
NIGHT 2			
NGC 6144	...	-0.12 ± 0.02	-0.12 ± 0.01
NGC 6235	-0.14 ± 0.02	-0.05 ± 0.02	...
NGC 6304	-0.02 ± 0.02	-0.02 ± 0.01	0.01 ± 0.02
NGC 6342	-0.03 ± 0.02	-0.12 ± 0.03	...
NGC 6397	$\mathbf{-0.03 \pm 0.02}$	$\mathbf{0.02 \pm 0.02}$	$\mathbf{-0.03 \pm 0.01}$
NGC 6541	$\mathbf{0.06 \pm 0.04}$	$\mathbf{0.04 \pm 0.02}$	$\mathbf{-0.01 \pm 0.02}$
NGC 6553	0.14 ± 0.07	0.05 ± 0.03	0.06 ± 0.02
NGC 6656	-0.02 ± 0.03	0.05 ± 0.02	0.01 ± 0.02
NGC 6809	$\mathbf{-0.02 \pm 0.03}$	$\mathbf{0.03 \pm 0.02}$	$\mathbf{0.01 \pm 0.02}$
NIGHT 3			
NGC 6218	$\mathbf{0.01 \pm 0.02}$	$\mathbf{-0.08 \pm 0.02}$	$\mathbf{-0.05 \pm 0.01}$
NGC 6254	$\mathbf{-0.04 \pm 0.01}$	$\mathbf{0.00 \pm 0.01}$	$\mathbf{-0.06 \pm 0.01}$
NGC 6352	$\mathbf{-0.09 \pm 0.02}$	$\mathbf{-0.14 \pm 0.01}$	$\mathbf{-0.13 \pm 0.01}$
NIGHT 4			
NGC 6121	$\mathbf{-0.05 \pm 0.03}$	$\mathbf{-0.38 \pm 0.01}$	$\mathbf{-0.23 \pm 0.02}$
NGC 6287	$\mathbf{-0.16 \pm 0.03}$	$\mathbf{-0.37 \pm 0.03}$	-0.05 ± 0.02
NGC 6333	-0.08 ± 0.03	-0.05 ± 0.02	-0.18 ± 0.02
NGC 6355	-0.20 ± 0.02	-0.09 ± 0.02	...
NGC 6626	...	-0.21 ± 0.03	-0.48 ± 0.02
NGC 6637	-0.31 ± 0.02	-0.45 ± 0.02	-0.20 ± 0.02
NGC 6642	-0.67 ± 0.04	-1.24 ± 0.02	-1.44 ± 0.02
NGC 6681	-0.11 ± 0.02	-0.19 ± 0.03	-0.02 ± 0.02

The numbers in bold correspond to the straight comparison between the data from Stetson and our data. The numbers in standard type correspond to the comparison between our data and the *HST* data, plus the offset between *HST* data and Stetson's data. The errors reported are the dispersions of the distributions from which the offsets were calculated, which inform about the absolute precision of the photometry of individual stars.

ACS data, a mean value was adopted.

The results were then compared with the ones we found from the Stetson comparison, since our aim is putting all the photometry in the Stetson system (see figure 2.6). A small offset for each filter was found and added to the individual cluster zero-points ($B = -0.062 \pm 0.013$, $V = -0.059 \pm 0.007$, and $I = -0.032 \pm 0.007$). These offsets may be due to the fact that the *HST* observations used in our absolute calibration are located closer to the center of the cluster than the Stetson stars used, or they may reflect small system zero-point differences. The final offsets applied to the individual clusters can be seen in table 2.6.

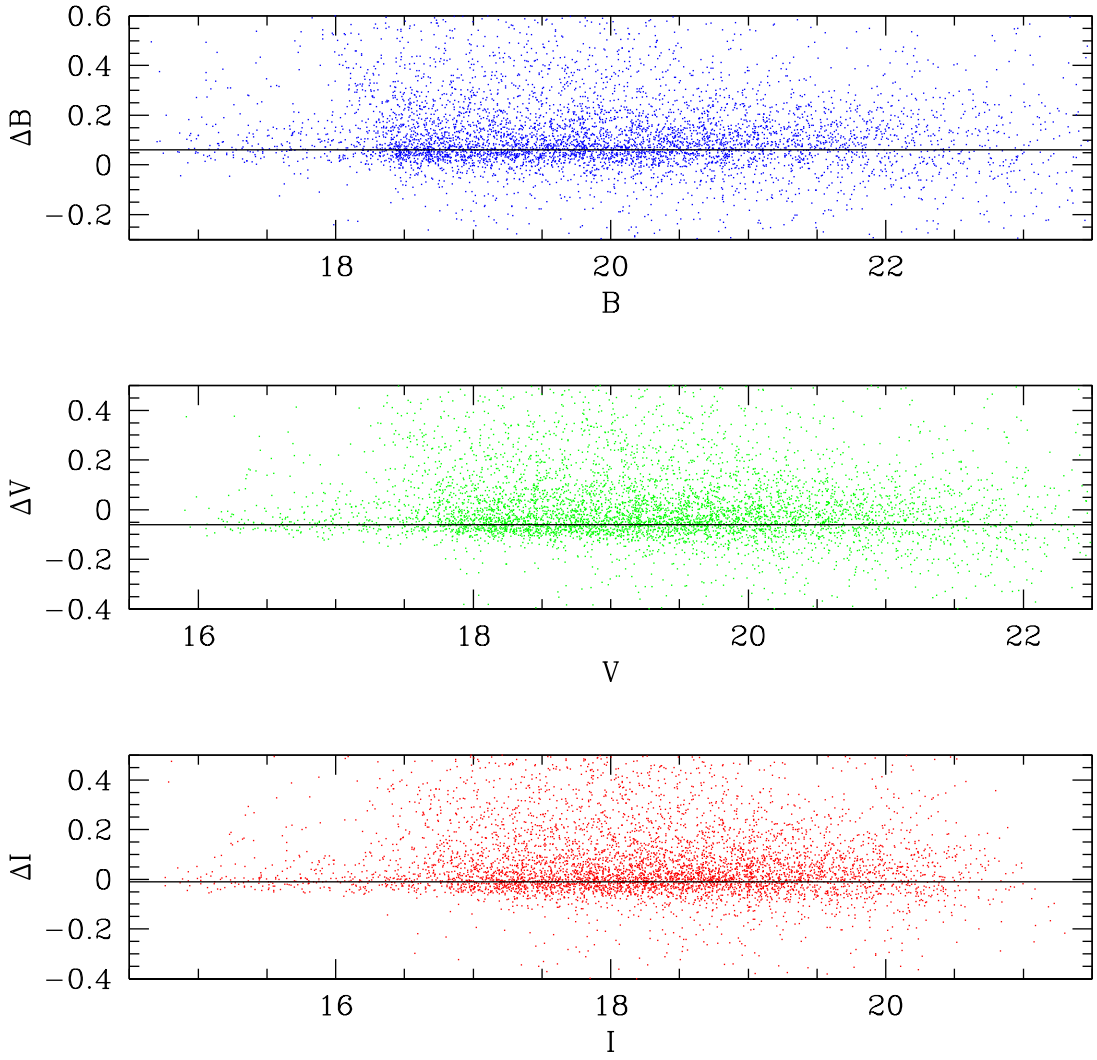

Figure 2.5. Comparison of our raw ground-based photometry with the *HST* photometry. In this figure we show the steps to calculate the offsets in NGC 6218, as an example of the technique. We plot the magnitudes obtained from our ground-based observations versus the differences of the *HST* photometry minus our ground-based photometry. We can observe the existence of the spread mentioned and explained in the text. The average offsets, shown by the lines, are calculated using a clipped weighted average (see text).

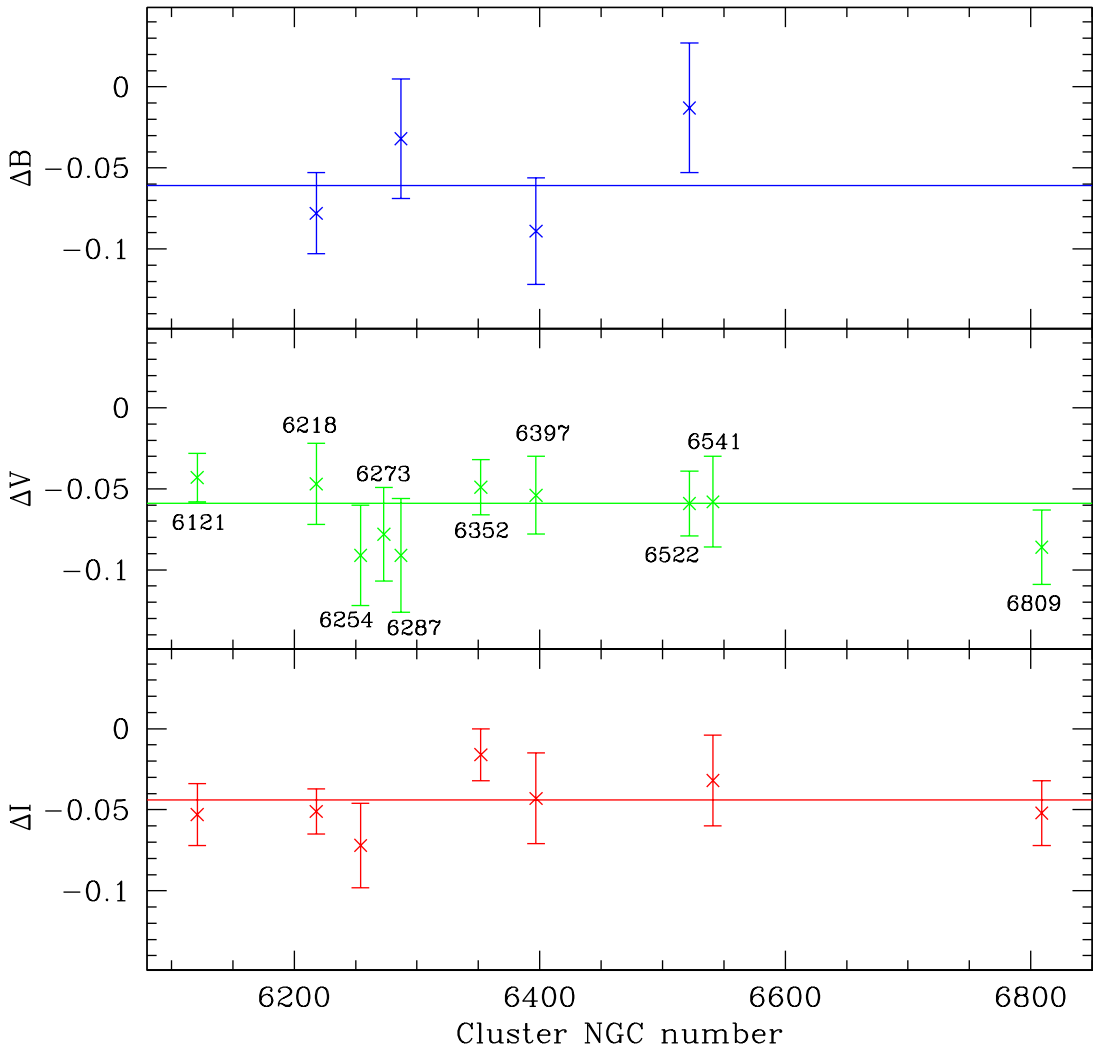

Figure 2.6. Comparison of our photometry corrected with the available *HST* offsets, with the Stetson calibrating stars. We plot the average differences of Stetson's values minus ours, for every cluster and filter. The lines show the weighted average offsets for every filter.

2.3 The Color-Magnitude Diagrams

The CMDs of the clusters in our sample, obtained from the observations with the Magellan telescope, are shown in figure 2.7, along the main characteristics of the cluster, according to the most recent 2009 version of Harris catalog (Harris, 1996). The CMDs obtained from our snapshot program *HST*/ACS observations are shown in figure 2.8, and the CMDs obtained from ACS data from the *HST* archive are shown in figures 2.9. Most of the CMDs from *HST*/ACS archival data are shown here for the first time. Since all of the CMDs obtained from WFPC2 data from the *HST* archive have previously been published or are superseded by the ACS CMDs, we decided to include here only the two WFPC2 CMDs (figure 2.10) that reach deeper magnitudes than our ground-based observations, and that will be used later in the calculation of the extinction variations in next chapters.

In the next paragraphs, we present the un-dereddened CMDs of our sample of inner GGCs and qualitatively describe the main characteristics of these CMDs. For the purpose of clarity in the present chapter, we arbitrarily divide the GGCs in a metal-poor group ($[Fe/H] < -1$) and a metal-rich group ($[Fe/H] > -1$), and use the HB morphology to assign each cluster in our sample to one of these two groups [1]. We also provide a description of the field star contamination present in each field based on a comparison with the Besançon model of the Galaxy (Robin et al., 2003). We will describe in detail in chapter 3 how this comparison is carried out. Finally, we provide references to the more recent –not necessarily all– optical and infrared photometric studies for each cluster in our sample.

NGC 6121 or M 4 (l=350.97°, b=15.97°, (m-M)$_V$=12.83, R$_\odot$=2.2 kpc, [Fe/H]=-1.20) This cluster is likely the closest to the Sun. Because of this, stars in the upper RGB are saturated in our images, even in the shortest exposures, and they do not appear in our CMDs of this cluster. The most noticeable feature in the raw CMDs of this cluster is the presence of an extended HB, with both red and blue components, though the blue HB (BHB) is not very extended. Due to its location

[1]Note that this assignation does not take in consideration any second parameter effects, and should be consider as a first guess from the visual inspection of the CMDs.

behind the Ophiuchus dust complex, about 120 pc away from us, the cluster shows substantial differential reddening noticeable by the broadening in the evolutionary sequences in the CMD. Due to its proximity, most of the field stars ($< 20\%$ of the stars in our CMD) are located behind the cluster. They are generally dimmer than the cluster stars, and the evolutionary sequences of the field stars are easily differentiable from the sequences of the cluster. Some recent ground-based optical photometric studies of this cluster include Rosenberg et al. (2000a) in VI, Mochejska et al. (2002) in UBV, and Anderson et al. (2006) in BV. Recent *HST* deep optical photometric CMDs of this cluster have been presented in $U_{336}V_{555}I_{814}$ by Bassa et al. (2004), in $V_{555}I_{814}$ by Richer et al. (2004), and in $V_{606}I_{814}$ by Ferdman et al. (2004) and Hansen et al. (2004). This cluster is also a member of the ACS survey of GGCs obtained in the $V_{606}I_{814}$ bands (Anderson et al., 2008a). Recent infrared photometric studies of this cluster are by Cho & Lee (2002) in JK, and by Ferraro et al. (2000) in VJK. Pulone et al. (1999) also used the *HST* for an optical and infrared study of the stellar mass function of this cluster in $V_{555}I_{814}J_{110}H_{160}$. The presence of significant differential reddening in this cluster has been pointed out in many studies, and a map of the differential extinction was provided by Mochejska et al. (2002). Recently, Marino et al. (2008) has suggested the presence of two distinct populations with different metal content from a spectroscopic and photometric study of stars in the RGB.

NGC 6144 (l=351.93°, b=15.70°, $(m\text{-}M)_V$=15.76, $R_\odot$=8.5 kpc, [Fe/H]=-1.75) A BHB implies that this cluster is a member of the metal-poor group of GGCs in our sample. NGC 6144 is also located behind the ρ Ophiuchi dust cloud and very close ($\sim 40'$ northeast) to NGC 6121 (M 4). Unsurprisingly, NGC 6144 also suffers from high and differential reddening, clearly visible from the broadened sequences in its CMD. The field star contamination is moderate ($\sim 50\%$ of the stars in our CMD), although the field stars are redder in average than the stars in the cluster whose different evolutionary sequences are clearly distinguishable in the CMD. This is one of the least studied clusters in our sample. The only previous ground-based optical photometric work was done in BVI by Neely et al. (2000) for the RGB and HB stars. From *HST* data, the first CMD of this cluster was published by Sarajedini et al. (2007)

as a part of their $V_{606}I_{814}$ ACS survey of GGCs. Infrared upper RGB photometry has been presented for this cluster by Davidge (2000) in $JHK2.2\mu mcontinuumCO$, and by Minniti et al. (1995) in JK.

NGC 6218 or M 12 (l=15.72°, b=26.31°, $(m\text{-}M)_V$=14.02, $R_\odot$=4.9 kpc, [Fe/H]=-1.48) This clusters shows an extended BHB, placing it also in the metal-poor group of GGCs in our sample. The well-defined regions in the CMD suggest a lack of significant differential reddening across the field. Also the number of field stars in the CMD is small ($< 10\%$) compared with the number of cluster stars in our FOV. Ground-based VI photometric data on M12 down to a few magnitudes under the TO have most recently been presented by von Braun et al. (2002) and Rosenberg et al. (2000b), BV data by Brocato et al. (1996), BVI data by Hargis et al. (2004) and deeper VR data by de Marchi et al. (2006). *HST* $B_{439}V_{555}$ data on M12 were published by Piotto et al. (2002) using the WFPC2. This cluster is also a member of the ACS survey of GGCs in $V_{606}I_{814}$ (Anderson et al., 2008a). There is no infrared photometric study of this cluster. von Braun et al. (2002) mapped the extinction in this location, finding little differential reddening in the field. Recently, Carretta et al. (2007) has suggested the presence of two distinct populations with different helium content from a spectroscopic study of stars in the RGB bump.

NGC 6235 (l=358.92°, b=13.52°, $(m\text{-}M)_V$=16.41, $R_\odot$=11.4 kpc, [Fe/H]=-1.40) This cluster shows a BHB, indicating it is a member of the metal-poor population of clusters in our sample. The narrow evolutionary sequences in its CMD suggest the absence of significant differential extinction in the field, despite its projected position, close to the Ophiuchus dust complex. The field star contamination is high ($\sim 85\%$ of the stars in our CMD), although, as with NGC 6144, the field stars are redder in average than the cluster stars. This allow us to easily differentiate the cluster and field evolutionary sequences. There is only one previous ground-based optical photometric work done in BV for RGB and HB stars by Howland et al. (2003), who found a differential extinction relation along the X axis of their data and use it to correct their photometry. This cluster has also been observed with the WFPC2 aboard the *HST* and its $B_{439}V_{555}$ CMD has been published in the GGC survey by

Piotto et al. (2002). Infrared upper RGB photometry has been presented for this cluster by Davidge (2000) in $JHK2.2\mu mcontinuumCO$ and by Minniti et al. (1995) in JK.

NGC 6254 or M 10 (l=15.14°, b=23.08°, (m-M)$_V$=14.08, R$_\odot$=4.4 kpc, [Fe/H]=-1.52) The CMD of this cluster, with an extended BHB, and its distance to the center of the Galaxy are very similar to those of M 12. The field star population is also similar in both cases. The evolutionary sequences in the CMD appear broader, suggesting the presence of a more significant amount of differential extinction in the field of this cluster. NGC 6254 has previously been studied using ground-based facilities by Rosenberg et al. (2000b) and von Braun et al. (2002) in VI and by Pollard et al. (2005) in BVI. Piotto & Zoccali (1999) used both ground-based facilities and *HST* for their study of this cluster in the VI bands. This cluster is also a member of the ACS survey of GGCs in $V_{606}I_{814}$ (Anderson et al., 2008a). Valenti et al. (2004a) studied this cluster in the infrared JK bands. The presence of differential reddening has been previously noted, and von Braun et al. (2002) mapped the extinction in the cluster field, finding a higher differential extinction than in M 12.

NGC 6266 or M 62 (l=353.57°, b=7.32°, (m-M)$_V$=15.64, R$_\odot$= 6.9 kpc, [Fe/H]=-1.29) The most striking feature in the CMD of this cluster is the presence of an extended and well populated HB, with both red and blue components. The BHB in particular, is very extended. Differential reddening across the face of this cluster is apparent, as revealed by the very broadened sequences in its CMD. The field star contamination is moderate ($\sim$ 50% of the stars in our CMD). Previous work using ground-based data includes that of Rosenberg et al. (2000a) in VI, and Brocato et al. (1996) and Contreras et al. (2005) in BV. Beccari et al. (2006) studied this cluster using a combination of BVI (ground) and $U_{255}U_{336}V_{555}$ (space) bands to study this cluster. Cocozza et al. (2008) studied a pulsar in M 62 and used their *HST* data to show the $B-R$ vs. R CMD of the cluster. NGC 6266 is included in the *HST* GGCs survey in $B_{439}V_{555}$ published by Piotto et al. (2002). Valenti et al. (2007) studied this cluster in the infrared JHK bands.

NGC 6273 or M 19 (l=356.87°, b=9.38°, (m-M)$_V$=15.95, R$_\odot$=8.6 kpc,

[Fe/H]=-1.68) This cluster possesses an extended BHB, making it a member of the metal-poor group of GGCs in our sample. The HB, along with the other evolutionary sequences, look very broadened in the CMDs, revealing significant differential reddening. The field star contamination is moderate ($\sim$ 40% of the stars in our CMD). The only previous optical photometric study is one by Piotto et al. (1999b) in $B_{439}V_{555}$ from *HST* images. As part of their study, they obtained a map of the differential reddening of the central region of the cluster. Piotto et al. (2002) included the CMD from this work in their *HST* GGCs survey in $B_{439}V_{555}$. In the infrared Davidge (2000) studied this cluster in $JHK2.2\mu mcontinuumCO$. Deeper infrared photometry was used in the studies by Valenti et al. (2007) and by Davidge (2001) in JHK.

NGC 6287 (l=0.13°, b=11.02°, (m-M)$_V$=16.71, R$_\odot$=9.3 kpc, [Fe/H]=-2.05) The BHB observed in the CMD of this cluster is a signature of a metal-poor population. The significant broadening of the HB and the other evolutionary sequences along its projected proximity to the Ophiuchus dust complex suggests substantial differential extinction in the field. This, along with the significant number of field stars ($\sim$ 75% of the stars in our CMD), makes it difficult to differentiate the cluster and field evolutionary sequences. The only previous photometric studies in the optical were done in BV by Stetson & West (1994) from ground-based observations and in VI by Fullton et al. (1999) from space-based observations. NGC 6287 is included in the *HST* GGCs survey in $B_{439}V_{555}$ published by Piotto et al. (2002). In the infrared Davidge (2000) studied this cluster in $JHK2.2\mu mcontinuumCO$, and Minniti et al. (1995) in JK. Deeper infrared photometry was used in the studies by Davidge (2001) in JHK, and by Lee et al. (2001) in $J_{110}H_{160}$ using the *HST*.

NGC 6304 (l=355.83°, b=5.38°, (m-M)$_V$=15.54, R$_\odot$=6.0 kpc, [Fe/H]=-0.59) The CMD of this cluster shows a very short, red HB (RHB), suggesting that NGC 6304 is in the metal-rich group of GGCs of our sample. The evolutionary sequences in the CMD are moderately broadened, implying differential extinction in the field. The high number of field stars ($\sim$ 80% of the stars in our CMD), along their broad range of colors, makes it difficult to identify cluster sequences away from the central regions. This cluster has been previously observed and study using ground-

based facilities by Ortolani et al. (2000) in BV and Rosenberg et al. (2000a) in VI. It is one of the clusters in the GGCs survey by Piotto et al. (2002) in $B_{439}V_{555}$ and in the ACS GGCs survey in $V_{606}I_{814}$ (Anderson et al., 2008a) done using *HST* data. Valenti et al. (2005) studied this cluster in the infrared JHK bands. Valenti et al. (2007) include results from this study in their infrared compilation of Bulge GGCs.

NGC 6333 or M 9 (l=5.54°, b=10.70°, (m-M)$_V$=15.66, R$_\odot$=7.9 kpc, [Fe/H]=-1.75) An extended BHB places M 9 in the metal-poor group of GGCs in our sample. The broadening in the HB and in the other evolutionary sequences points to a significant differential reddening in the field. The field star contamination is moderate ($\sim$ 40% of the stars in our CMD). The only previous optical photometric study of this cluster is that of Janes & Heasley (1991) in BV for stars brighter than the TO point. Although this cluster has been previously observed with the *HST* (see table 2.3), the first CMD of M 9 using space data is published in this paper in BVI. In the infrared Davidge (2000) studied this cluster in $JHK2.2\mu mcontinuumCO$, and Minniti et al. (1995) in JK. Deeper infrared photometry was used in the study by Davidge (2001) in JHK.

NGC 6342 (l=4.90°, b=9.73°, (m-M)$_V$=16.10, R$_\odot$=8.6 kpc, [Fe/H]=-0.65) If we concentrate our attention in the inner region of this cluster, its CMD reveals a short RHB, clear indication that this cluster is a member of the metal-rich group of GGCs in our sample. The inclination of the stars in the HB, along the broadening in this branch and the other evolutionary sequences imply substantial differential extinction in the field. The field star contamination is significant ($\sim$ 70% of the stars in our CMD). This cluster was first studied photometrically in the optical by Armandroff (1988) in VRI for stars in the RGB and HB. The only other optical photometric studies are those of Heitsch & Richtler (1999) in VI using ground-based facilities and that of Piotto et al. (2002) in $B_{439}V_{555}$ using the *HST*. In the infrared Valenti et al. (2004b) studied this cluster in $VJHK$. Valenti et al. (2007) include results from this study in their infrared compilation of Bulge GGCs. A map of the differential reddening was produced by Heitsch & Richtler (1999).

NGC 6352 (l=341.42°, b=−7.17°, (m-M)$_V$=14.44, R$_\odot$=5.7 kpc, [Fe/H]=-

0.70) The RHB in this cluster implies it is a member of the metal-rich population of our sample. From the broadened evolutionary sequences of the cluster in the CMD, we infer the presence of differential extinction in the field. The high number of field stars ($> 90\%$ of the stars in our CMD), along their broad range of colors, makes it difficult to identify cluster stars away from its very central regions. This cluster was studied by Sarajedini & Norris (1994) in BV and Rosenberg et al. (2000a) in VI from the ground, and from space by Fullton, et al. (1995) in VI_C, using pre-COSTAR data, and by Faria & Feltzing (2002) in $V_{555}I_{814}$ and by Pulone et al. (2003) in $V_{606}I_{814}$. It is also a member of the ACS survey of GGCs in $V_{606}I_{814}$ (Anderson et al., 2008a). There is no infrared photometric study of this cluster.

NGC 6355 (l=359.58°, b=5.43°, $(m\text{-}M)_V$=17.22, $R_\odot$=9.5 kpc, [Fe/H]=-1.50) This cluster has a BHB, indicative of a metal-poor population. The broadening of the HB indicates significant differential reddening. The high number of field stars ($> 90\%$ of the stars in our CMD), along their broad range of colors, makes it difficult to identify cluster stars away from its very central regions. The only previous optical photometric studies are those by Ortolani et al. (2003) in BVI using ground-based facilities, and that by Piotto et al. (2002) in $B_{439}V_{555}$ using the *HST*. In the infrared Davidge (2000) studied this cluster in $JHK2.2\mu mcontinuumCO$. Deeper infrared photometry was used in the studies by Valenti et al. (2007) and by Davidge (2001) in JHK.

NGC 6397 (l=338.17°, b=−11.96°, $(m\text{-}M)_V$=12.36, $R_\odot$=2.3 kpc, [Fe/H]=-1.95) This is the cluster with the smallest apparent distance modulus, though it is not the closest to the Sun. As for M 4, stars in the upper RGB saturated in our images, even in the shortest exposures, and they do not appear in or CMD of this cluster. We do observe a clear BHB, placing this cluster in the metal-poor group of GGCs in our sample. The evolutionary sequences in the CMD are quite narrow, suggesting little differential reddening across the face of the cluster. The contamination from field stars is moderate ($\sim 30\%$ of the stars in our CMD), mainly affecting MS stars in the cluster. Some of the most recent studies of this cluster done with ground-based facilities are those by Rosenberg et al. (2000a) in the VI, Anderson et

al. (2006) in $UBVI$, and Kaluzny et al. (2006) in the BV. This cluster has also been observed with the *HST*. A series of papers has been published dedicated to the study of the characteristics of this cluster using very deep photometry obtained with the ACS (Anderson et al., 2008b; Hurley et al., 2008; Richer et al., 2008; Davis et al., 2008). NGC 6397 also is a member of the GGC survey from Piotto et al. (2002) in $B_{439}V_{555}$ and of the ACS GGC survey in $V_{606}I_{814}$ (Anderson et al., 2008a). de Marchi et al. (2000) also used the *HST* for an optical and infrared study of the stellar mass function of this cluster in $V_{606}I_{814}J_{110}H_{160}$.

NGC 6522 (l=1.02°, b=−3.93°, (m-M)$_V$=15.94, R$_\odot$=7.8 kpc, [Fe/H]=-1.44) This cluster is located in Baade's Window. An extended BHB places this cluster in the metal-poor group of GGCs in our sample. The broadened HB suggest that this cluster suffers considerable differential reddening. The high number of field stars ($> 90\%$ of the stars in our CMD), along their broad range of colors, makes it difficult to identify cluster stars away from its very central regions. The most recent optical photometric studies done with ground-based data are those by Barbuy et al. (1994) in BV, and Terndrup & Walker (1994) in BVI. Terndrup et al. (1998) show a differential extinction relation with respect to the center of the cluster and use it to correct their previous photometry. Using the *HST*, the cluster was studied by Shara et al (1998) in the $U_{336}B_{439}$ bands using pre-COSTAR data. It is also one of the clusters in Piotto et al. (2002) GCs survey in $B_{439}V_{555}$. In the infrared Davidge (2000) studied this cluster in $JHK2.2\mu mcontinuumCO$, and Minniti et al. (1995) in JK. Deeper infrared photometry was used in the study by Davidge (2001) in JHK.

NGC 6541 (l=349.48°, b=−11.09°, (m-M)$_V$=14.67, R$_\odot$=7.0 kpc, [Fe/H]=-1.83) An extended BHB is a clear signature of the metal-poor character of this cluster. Its CMD shows well defined evolutionary sequences, slightly broadened, suggesting the presence of some differential extinction. A moderate field star contamination ($\sim 30\%$ of the stars in our CMD), along with stars redder in average than the cluster stars, lets us distinguish NGC 6541 evolutionary sequences unambiguously. The only ground-based studies of this cluster are by Alcaino et al. (1997) in $BVRI$ and by Rosenberg et al. (2000a) in VI. It has been studied using *HST* WFPC2 data

by Lee & Carney (2006) in VI. It is also one of the cluster in the ACS GGC survey observed in $V_{606}I_{814}$ (Anderson et al., 2008a). In the infrared Davidge (2000) studied this cluster in $JHK2.2\mu mcontinuumCO$. Deeper infrared photometry was used in the study by Kim et al. (2006) in JHK.

NGC 6553 (l=5.25°, b=−3.03°, (m-M)$_V$=15.83, R$_\odot$=6.0 kpc, [Fe/H]=-0.21) This cluster has a RHB, placing it in the metal-rich group of GGCs in our sample. The CMD shows broadened evolutionary sequences and the RHB is quite tilted and extended. These are clear signs of significant differential reddening in the field. The field star contamination is high (> 90% of the stars in a big color range in our CMD), which makes it difficult to identify cluster stars away from its very central regions. Some of the most recent optical photometric studies of this cluster are that by Sagar et al. (1999) in VI using ground-based data and those by Beaulieu et al. (2001) and Zoccali et al. (2001) in $V_{555}I_{814}$ using *HST* data. Zoccali et al. (2001) calculated the extinction map, not shown in their paper, and applied it to get a clean CMD. Heitsch & Richtler (1999) show an extinction map calculated with data from Sagar et al. (1999). Guarnieri et al. (1998) in $VIJK$, and Ferraro et al. (2000) in VJK studied this cluster in the optical and in the infrared. Valenti et al. (2007) include results from this last study in their infrared compilation of Bulge GGCs.

NGC 6558 (l=0.20°, b=−6.02°, (m-M)$_V$=15.72, R$_\odot$=7.4 kpc, [Fe/H]=-1.44) A BHB places this cluster in the metal-poor group of GGCs in our sample. The broadened sequences in the CMD suggest the presence of substantial differential reddening in the field. The CMD of this cluster is also strongly contaminated by field stars (> 90% of the stars in a big color range in our CMD), which makes it difficult to identify cluster stars away from its very central regions. There are only two previous optical photometric studies using ground-based data, those by Rich et al. (1998) and by Barbuy et al. (2007), both in VI. Although this cluster has been previously observed with the *HST*, the first CMD of the deep MS stars using space-based data is published in this paper in VI. In the infrared Davidge (2000) studied this cluster in the $JHK2.2\mu mcontinuumCO$ bands.

NGC 6624 (l=2.79°, b=−7.91°, (m-M)$_V$=15.36, R$_\odot$=7.9 kpc, [Fe/H]=-

0.44) This cluster possesses a RHB, characteristic of the metal-rich population. The CMD of the core of this cluster shows well defined sequences, indicating the lack of very significant differential reddening in the inner region. This is another cluster strongly contaminated by field stars ($> 90\%$ of the stars in a big color range in our CMD), making it quite difficult to identify cluster stars away from its very central regions. This cluster has been studied using ground-based data by Sarajedini & Norris (1994), who presented a photometric study of the RGB and HB stars in BV. Richtler et al. (1994) and Rosenberg et al. (2000a) obtained deeper photometry, reaching a few magnitudes below the TO in BV and VI, respectively. Using *HST* data, studies of this cluster were published by Sosin & King (1995) in BV using pre-COSTAR data, and by Guhathakurta et al. (1996) in $U_{336}B_{439}V_{555}$ and Heasley et al. (2000) in VI. This cluster is also a member of Piotto et al. (2002) $B_{439}V_{555}$ GGCs survey, and of the $V_{606}I_{814}$ ACS GGCs survey (Anderson et al., 2008a). In the infrared Valenti et al. (2004b) studied this cluster in $VJHK$. Valenti et al. (2007) include results from this study in their infrared compilation of Bulge GGCs.

NGC 6626 or M 28 (l=7.80°, b=−5.58°, (m-M)$_V$=14.97, R$_\odot$=5.6 kpc, [Fe/H]=-1.45) NGC 6626 is a metal-poor cluster, as inferred from its extended BHB. The CMD of the central region of the cluster shows broadened sequences, which indicates the presence of differential extinction in the field. The field contamination is high ($\sim 90\%$ of the stars in a big color range in our CMD), but due to its proximity the cluster's brightest stars are brighter on average than the field's, and we can identify without much difficulty stars from the RGB. This cluster has been studied in the optical using ground-based data by Rosenberg et al. (2000a) in VI, and using *HST* data by Testa et al. (2001) and by Golden et al. (2001) in VI. Davidge et al. (1996) used a combination of optical and infrared bands ($BVJK$) to study this cluster. In the infrared Davidge (2000) studied this cluster in the $JHK2.2\mu mcontinuumCO$ bands.

NGC 6637 or M 69 (l=1.72°, b=−10.27°, (m-M)$_V$=15.28, R$_\odot$=9.1 kpc, [Fe/H]=-0.70) The RHB of this cluster places it in the metal-rich group of GGCs in our sample. The slightly broadened evolutionary sequences suggest the presence

of moderate differential reddening in its field. The field contamination is significant ($\sim$ 75% of the stars in a big color range in our CMD). This clusters has been the subject of several studies, usually along with the also metal-rich NGC 6624. Using ground-based data Ferraro et al. (1994), in $BVJK$, and Sarajedini & Norris (1994), in BV, present a photometric study of the RGB and HB stars of this cluster, and Richtler et al. (1994) and Rosenberg et al. (2000a) got deeper photometry, arriving to a few magnitudes below the TO, in BV and VI respectively. Using *HST* data, Heasley et al. (2000) studied this cluster in VI. This cluster is also a member of Piotto et al. (2002) $B_{439}V_{555}$ GGCs survey, and of the $V_{606}I_{814}$ ACS GGCs survey (Anderson et al., 2008a). In the infrared this cluster was studied by Ferraro et al. (2000) in VJK and by Valenti et al. (2005) in JHK. Valenti et al. (2007) include results from these studies in their infrared compilation of Bulge GGCs.

NGC 6642 (l=9.81°, b=−6.44°, (m-M)$_V$=15.90, R$_\odot$=8.4 kpc, [Fe/H]=-1.35) During the observation of this cluster, we had the least photometric conditions of our run (see table 2.6). This resulted in the shallowest CMD of our study, reaching only stars down to the very upper parts of the MS. The most prominent feature in its CMD is the presence of an extended HB, with both red and blue components. The broadening in the HB suggests differential extinction is present in the field. This is yet another cluster strongly contaminated by the field ($>$ 90% of the stars in a big color range in our CMD), making it difficult to identify cluster stars away from its central regions. NGC 6642 has only one previous but recent optical photometric study done using ground-based data by Barbuy et al. (2006) in BVI. Using *HST* data, its $B_{439}V_{555}$ CMD appears in the Piotto et al. (2002) GGCs survey. In the infrared Davidge (2000) studied this cluster in $JHK2.2\mu mcontinuumCO$, and Minniti et al. (1995) in JK. Deeper infrared photometry was used in the studies by Davidge (2001), Kim et al. (2006), and Valenti et al. (2007) in JHK

NGC 6656 or M 22 (l=9.89°, b=−7.55°, (m-M)$_V$=13.60, R$_\odot$=3.2 kpc, [Fe/H]=-1.64) The relative proximity of M22 explains why the upper RGB stars are saturated in our observations and are excluded from the CMDs of this cluster. An extended BHB identifies NGC 6656 as a member of the metal-poor group of

clusters in our sample, although there are some studies claiming a metallicity spread in this cluster (Lehnert et al., 1991; Brown & Wallerstein, 1992). Its CMD shows broadening in its evolutionary sequences that can be a sign of metallicity dispersion or differential reddening. The contamination from field stars is moderate ($\sim 25\%$ of the stars in our CMD). There are several optical photometric studies for this cluster. Using ground-based data, it was studied by Monaco et al. (2004) in BVI, by Webb et al. (2004) in UV, by Kaluzny & Thompson (2001) in BV, by Rosenberg et al. (2000a) in VI, and by Anthony-Twarog et al. (1995) and by Richter et al. (1999) in Stromgrem $uvbyCa$ and vby bands, respectively. Piotto & Zoccali (1999) used both ground facilities and the *HST* for their study of this cluster in VI, and Anderson et al. (2003) shows CMDs for the cluster in $B_{435}V_{606}R_{675}I_{814}$ bands. This cluster is also a member of the ACS survey of GGCs in $V_{606}I_{814}$ (Anderson et al., 2008a). In the infrared Minniti et al. (1995), Davidge & Harris (1996) and Cho & Lee (2002) studied this cluster in JK.

NGC 6681 or M 70 (l=2.85°, b=−12.51°, (m-M)$_V$=14.98, R$_\odot$=9.0 kpc, [Fe/H]=-1.51) The extended BHB of M70 indicates that this cluster possesses a metal-poor population. The evolutionary sequences in this cluster show little broadening, suggesting moderate differential reddening in the field. The field star contamination is significant ($\sim 60\%$ of the stars in our CMD), although the field stars are redder in average than the cluster stars, which allows us to easily distinguish the different evolutionary sequences. There are also some dim blue field stars in our CMD that belong to the Sagittarius dwarf galaxy. Stars from this galaxy's MS are easily observed in the CMD at magnitudes dimmer than $V \sim 21$ and colors bluer than $(V-I) \sim 0.8$. The only available optical photometric studies using ground-based data are those by Brocato et al. (1996) in BV, and by Rosenberg et al. (2000a) in VI. Using *HST* data, Piotto et al. (2002) included it in its GGCs survey in $B_{435}V_{555}$. This cluster is also a member of the $V_{606}I_{814}$ ACS survey of GGCs (Anderson et al., 2008a). In the infrared Davidge (2000) studied this cluster in $JHK2.2\mu mcontinuumCO$. Deeper infrared photometry was used in the study by Kim et al. (2006) in JHK.

NGC 6809 or M 55 (l=8.8°, b=−23.27°, (m-M)$_V$=13.87, R$_\odot$=5.3 kpc,

[Fe/H]=-1.81) The tip of the RGB is saturated in our CMDs of this cluster, due to the small apparent distance modulus of M 55. The BHB places this cluster in the metal-poor group of GGCs in our sample. The CMD shows well-defined evolutionary sequences, implying little differential extinction in the field. The contamination from Galactic field stars in the CMD is small ($< 10\%$ of the stars in our CMD), though there is clear contamination from stars in the background Sagittarius dwarf galaxy. Stars from its MS are easily observed in the CMD at magnitudes dimmer than $V \sim 21$ and colors bluer than $(V - I) \sim 0.8$. The latest optical photometric studies of this cluster done using ground-based data are by Kaluzny et al. (2005) in $UBVI$, by Pych et al. (2001) in BV and by Rosenberg et al. (2000a) in VI. Using a combination of ground-based and *HST* data, this cluster was studied by Lanzoni et al. (2007) in BVI, and by Bassa et al. (2008) in $BVRIH_{\alpha}$. The ACS VI photometry used by Bassa et al. (2008) comes from Anderson et al. (2008a), since this cluster is one of the members of the ACS GGC survey. In the infrared this cluster was studied by Ferraro et al. (2000) in VJK.

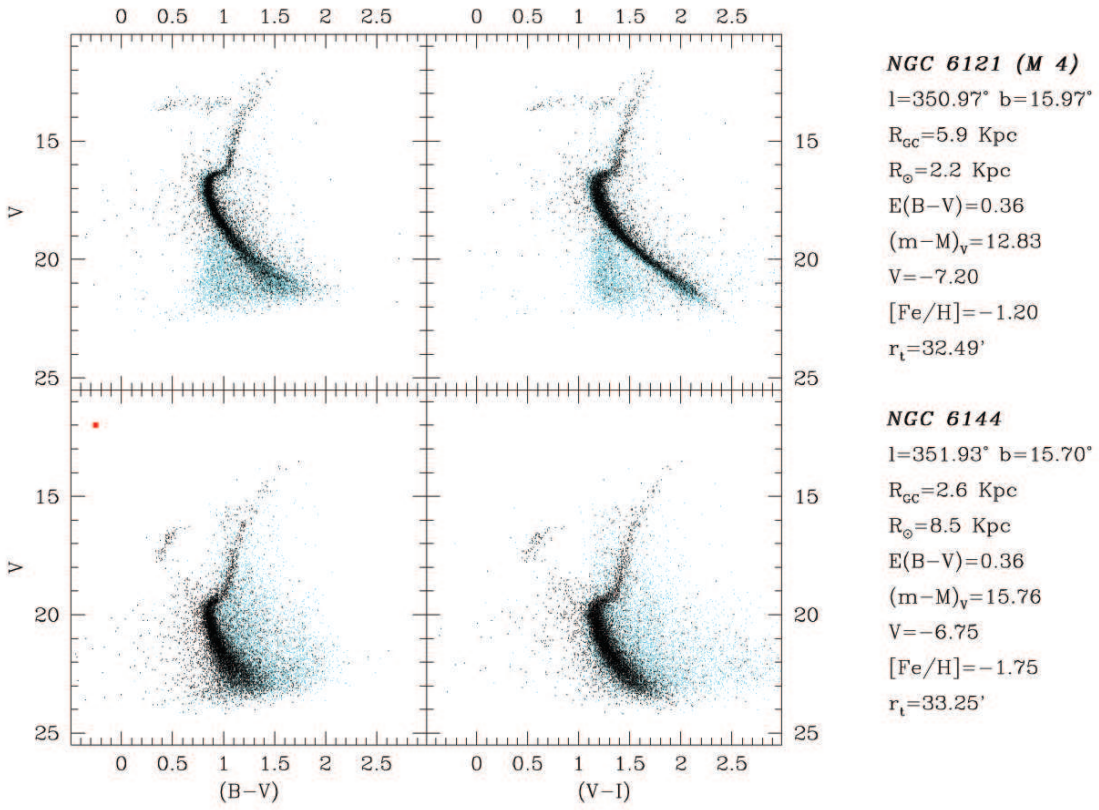

Figure 2.7. $B-V$ vs. V (left) and $V-I$ vs. I (right) color-magnitude diagrams of the 25 clusters in our sample observed with the 6.5m Magellan telescope. The same color and magnitude scale has been used in plotting the CMDs. Stars closer to the center of the cluster ($r < 2.5'$) are plotted with darker dots, so we can better observe the CMD of the stars in the cluster over the sometimes very populated field. CMDs showing a red square in the upper right corner are those that could not be correctly calibrated in color using the method described in the text because of the lack of calibrating data in one of the filters. The legend on the right of the CMDs described the characteristics of the GCs according to the 2009 version of Harris GGC catalog (Harris, 1996): galactic latitude and longitude, galactocentric distance, distance from the Sun, foreground reddening, apparent visual distance modulus, cluster luminosity, metallicity, and tidal radius.

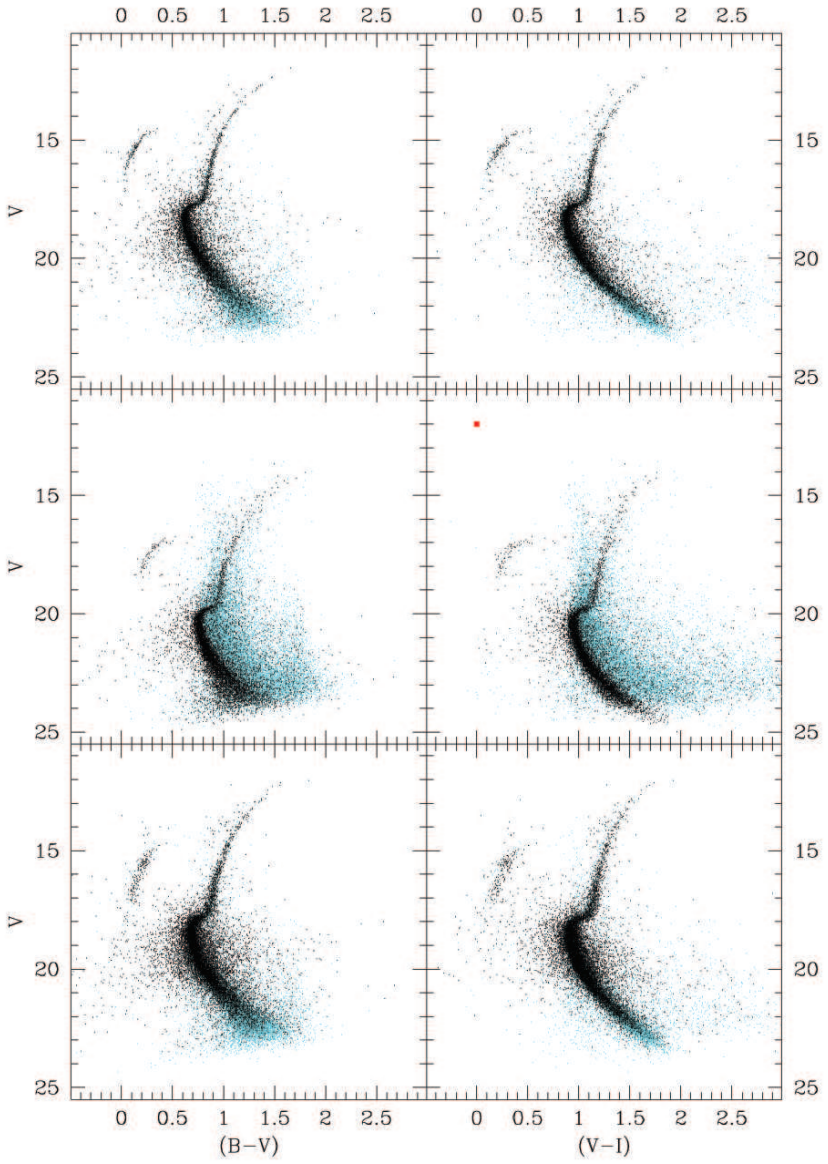

NGC 6218 (M 12)

l=15.72° b=26.31°

R_{gc}=4.5 Kpc

$R_{\odot}$=4.9 Kpc

E(B−V)=0.19

$(m-M)_v$=14.02

V=−7.32

[Fe/H]=−1.48

r_t=17.60'

NGC 6235

l=358.92° b=13.52°

R_{gc}=4.1 Kpc

$R_{\odot}$=11.4 Kpc

E(B−V)=0.36

$(m-M)_v$=16.41

V=−6.44

[Fe/H]=−1.40

r_t=7.61'

NGC 6254 (M 10)

l=15.14° b=23.08°

R_{gc}=4.6 Kpc

$R_{\odot}$=4.4 Kpc

E(B−V)=0.28

$(m-M)_v$=14.08

V=−7.48

[Fe/H]=−1.52

r_t=21.48'

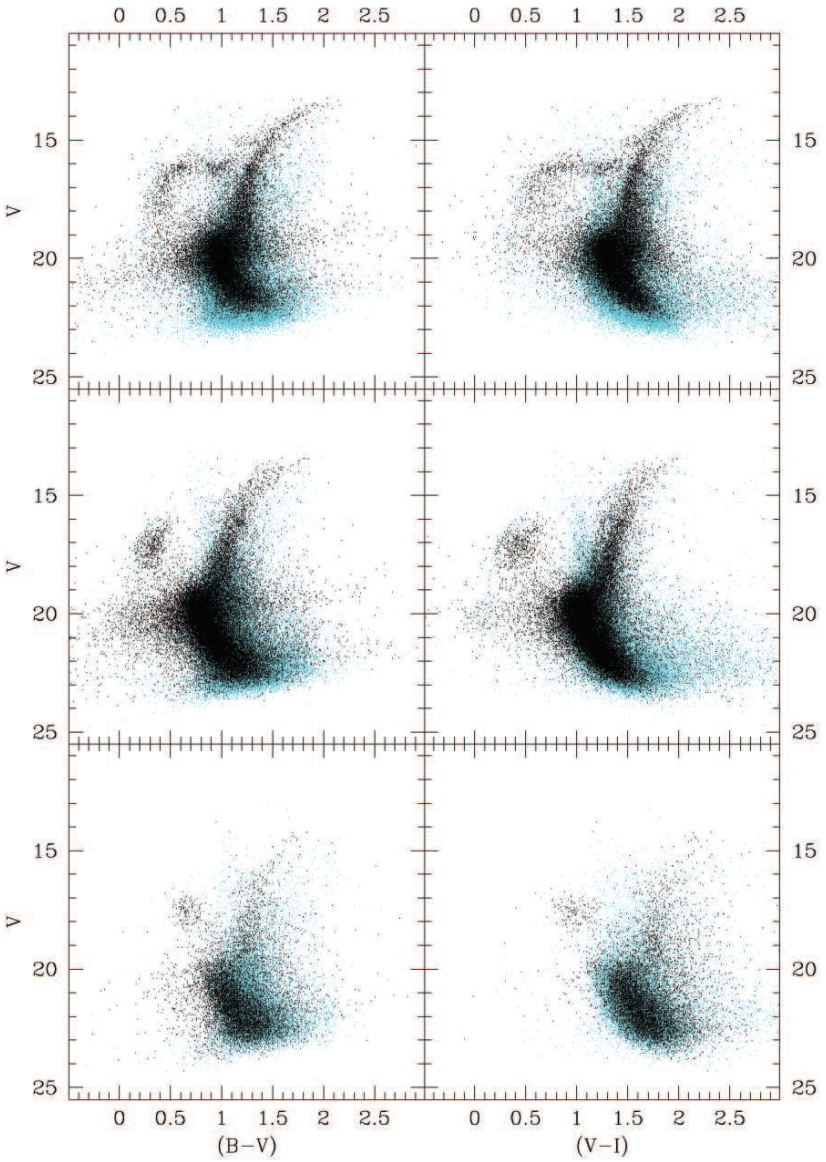

NGC 6266 (M 62)

l=353.57° b=7.32°

R_{gc}=1.7 Kpc

$R_{\odot}$=6.9 Kpc

E(B−V)=0.47

$(m-M)_V$=15.64

V=−9.19

[Fe/H]=−1.29

r_t=8.97'

NGC 6273 (M 19)

l=356.87° b=9.38°

R_{gc}=1.6 Kpc

$R_{\odot}$=8.6 Kpc

E(B−V)=0.41

$(m-M)_V$=15.95

V=−9.18

[Fe/H]=−1.68

r_t=14.50'

NGC 6287

l=0.13° b=11.02°

R_{gc}=2.1 Kpc

$R_{\odot}$=9.3 Kpc

E(B−V)=0.60

$(m-M)_V$=16.71

V=−7.36

[Fe/H]=−2.05

r_t=10.51'

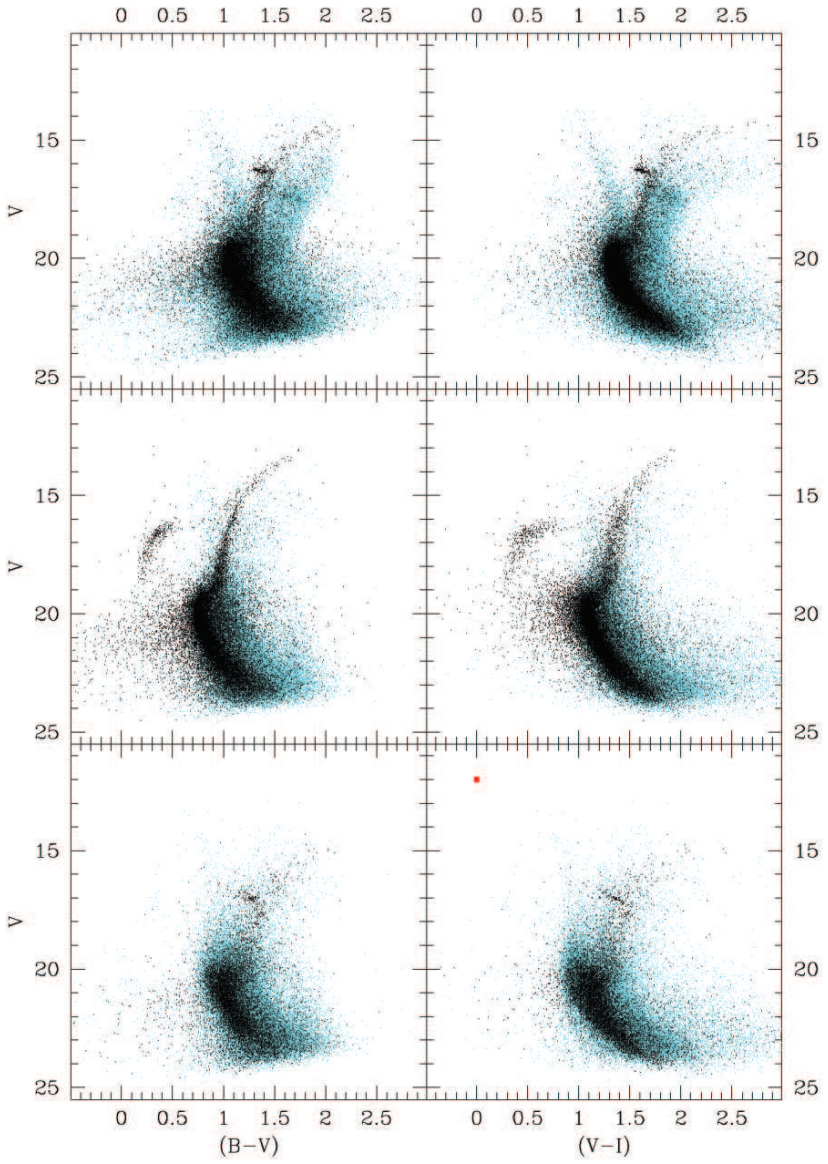

NGC 6304
l=355.83° b=5.38°
R_{gc}=2.2 Kpc
$R_{\odot}$=6.0 Kpc
E(B−V)=0.53
$(m-M)_v$=15.54
V=−7.32
[Fe/H]=−0.59
r_t=13.25'

NGC 6333 (M 9)
l=5.54° b=10.7°
R_{gc}=1.7 Kpc
$R_{\odot}$=7.9 Kpc
E(B−V)=0.38
$(m-M)_v$=15.66
V=−7.94
[Fe/H]=−1.75
r_t=8.16'

NGC 6342
l=4.90° b=9.73°
R_{gc}=1.7 Kpc
$R_{\odot}$=8.6 Kpc
E(B−V)=0.46
$(m-M)_v$=16.10
V=−6.44
[Fe/H]=−0.65
r_t=14.86'

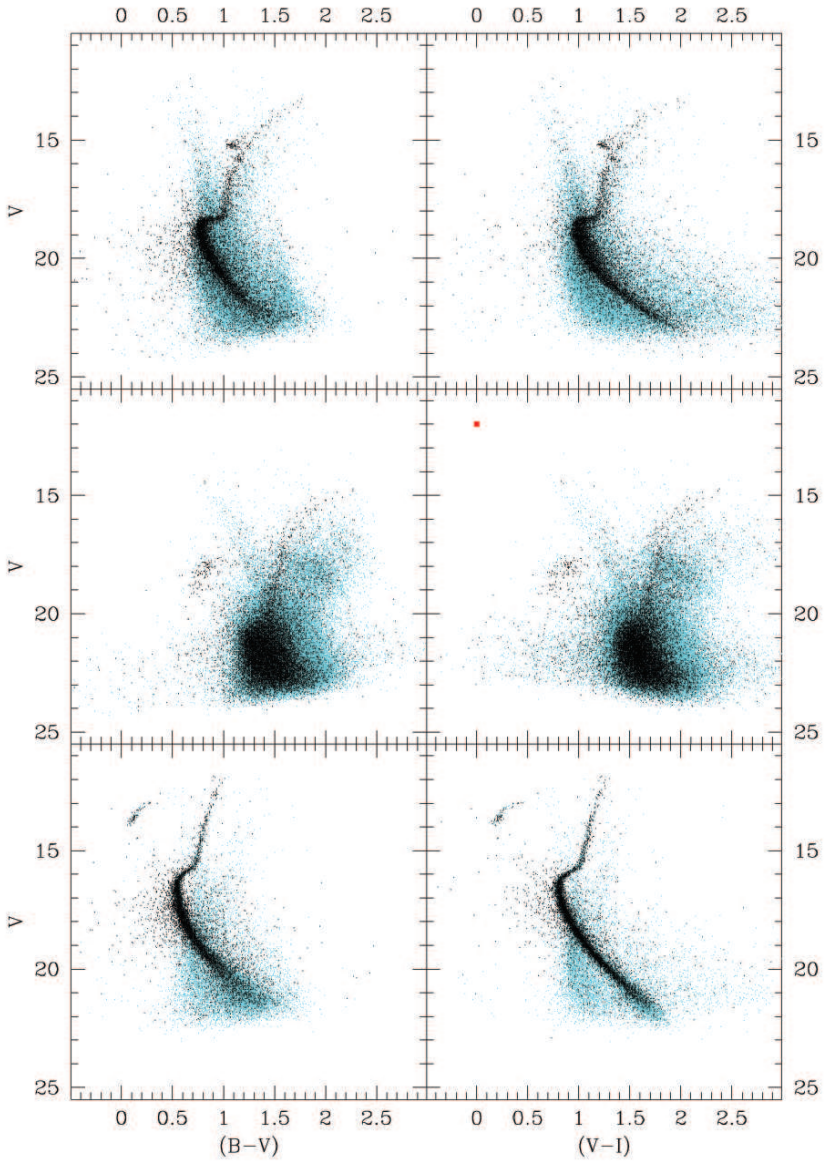

NGC 6352

l=341.42° b=−7.17°

R_{gc}=3.3 Kpc

$R_{\odot}$=5.7 Kpc

E(B−V)=0.21

$(m-M)_V$=14.44

V=−6.48

[Fe/H]=−0.70

r_t=10.51'

NGC 6355

l=359.58° b=5.43°

R_{gc}=1.8 Kpc

$R_{\odot}$=9.5 Kpc

E(B−V)=0.75

$(m-M)_V$=17.22

V=−8.08

[Fe/H]=−1.50

r_t=15.18'

NGC 6397

l=338.17° b=−11.96°

R_{gc}=6.0 Kpc

$R_{\odot}$=2.3 Kpc

E(B−V)=0.18

$(m-M)_V$=12.36

V=−6.63

[Fe/H]=−1.95

r_t=15.81'

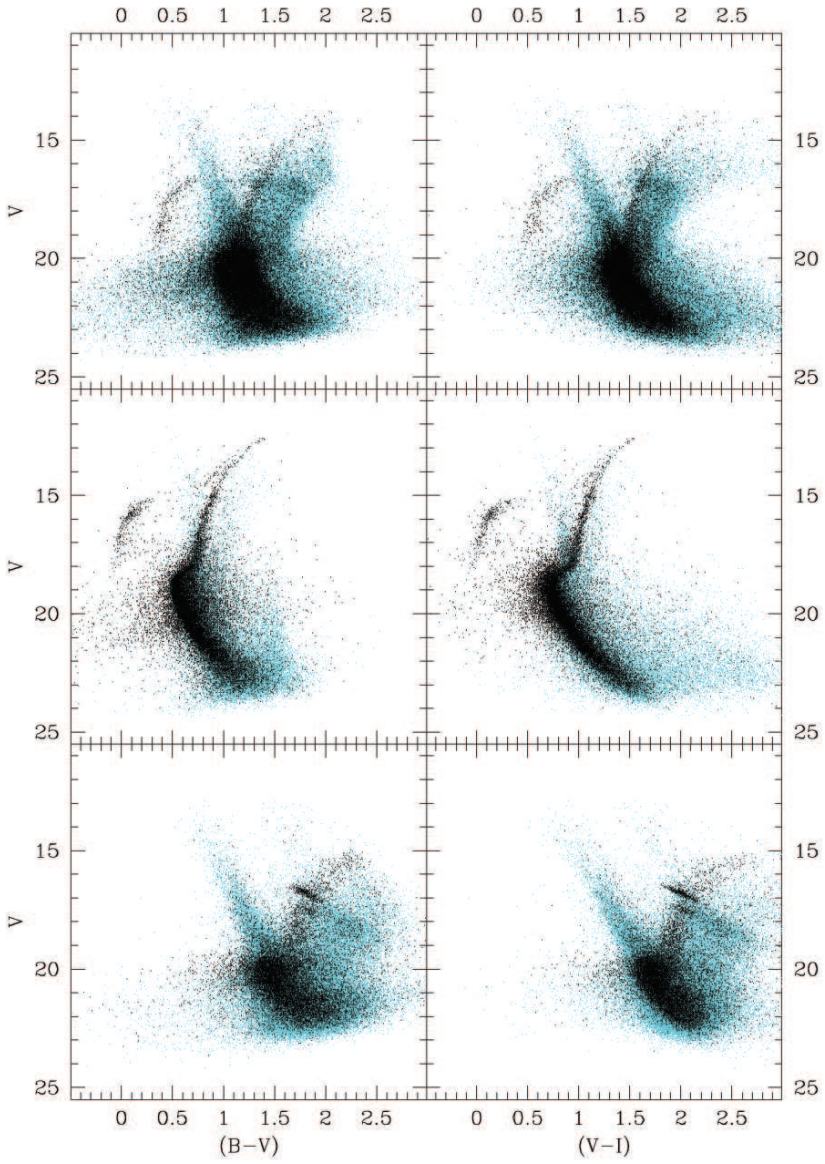

NGC 6522

l=1.02° b=−3.93°

R_{gc}=0.6 Kpc

$R_{\odot}$=7.8 Kpc

E(B−V)=0.48

$(m-M)_V$=15.94

V=−7.67

[Fe/H]=−1.44

r_t=16.44'

NGC 6541

l=349.48° b=−11.09°

R_{gc}=2.2 Kpc

$R_{\odot}$=7.0 Kpc

E(B−V)=0.14

$(m-M)_V$=14.67

V=−8.37

[Fe/H]=−1.83

r_t=29.6'

NGC 6553

l=5.25° b=−3.03°

R_{gc}=2.2 Kpc

$R_{\odot}$=6.0 Kpc

E(B−V)=0.63

$(m-M)_V$=15.83

V=−7.77

[Fe/H]=−0.21

r_t=8.16'

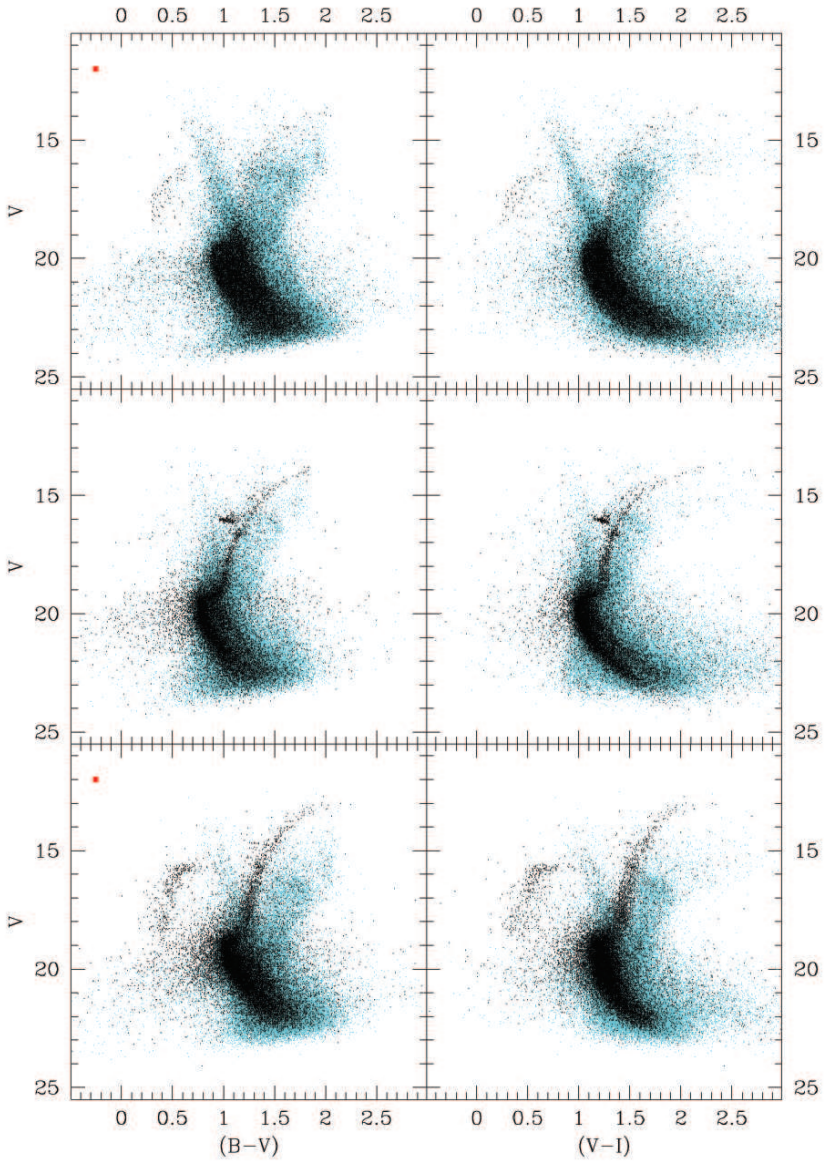

NGC 6558

l=0.20° b=−6.03°

R_{GC}=1.0 Kpc

$R_{\odot}$=7.4 Kpc

E(B−V)=0.44

$(m-M)_V$=15.72

V=−6.46

[Fe/H]=−1.44

r_t=10.44'

NGC 6624

l=2.79° b=−7.91°

R_{GC}=1.2 Kpc

$R_{\odot}$=7.9 Kpc

E(B−V)=0.28

$(m-M)_V$=15.36

V=−7.49

[Fe/H]=−0.44

r_t=20.55'

NGC 6626 (M 28)

l=7.80° b=−5.58°

R_{GC}=2.7 Kpc

$R_{\odot}$=5.6 Kpc

E(B−V)=0.40

$(m-M)_V$=14.97

V=−8.18

[Fe/H]=−1.45

r_t=11.27'

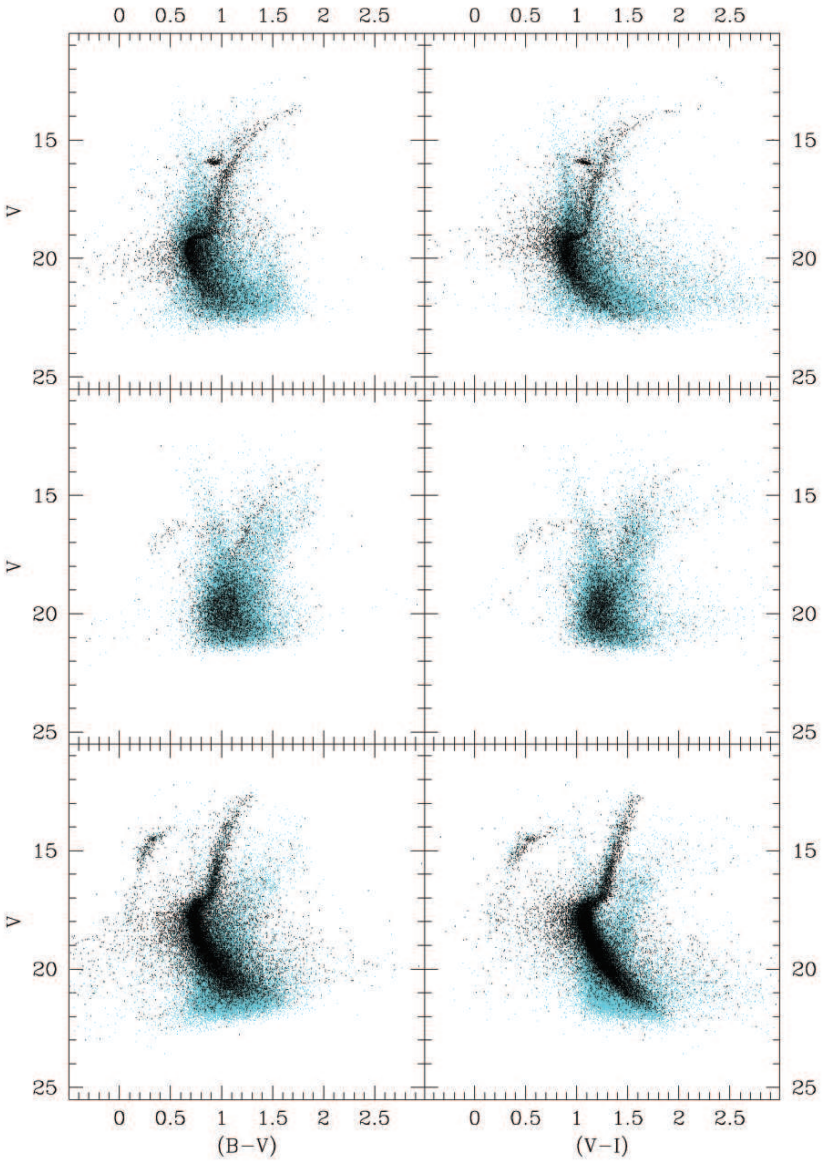

NGC 6637 (M 69)

l=1.72° b=−10.27°

R_{GC}=1.9 Kpc

$R_{\odot}$=9.1 Kpc

E(B−V)=0.16

$(m-M)_V$=15.28

V=−7.64

[Fe/H]=−0.70

r_t=8.35'

NGC 6642

l=9.81° b=−6.44°

R_{GC}=1.7 Kpc

$R_{\odot}$=8.4 Kpc

E(B−V)=0.41

$(m-M)_V$=15.90

V=−6.77

[Fe/H]=−1.35

r_t=10.07'

NGC 6656 (M 22)

l=9.89° b=−7.55°

R_{GC}=4.9 Kpc

$R_{\odot}$=3.2 Kpc

E(B−V)=0.34

$(m-M)_V$=13.60

V=−8.50

[Fe/H]=−1.64

r_t=28.97'

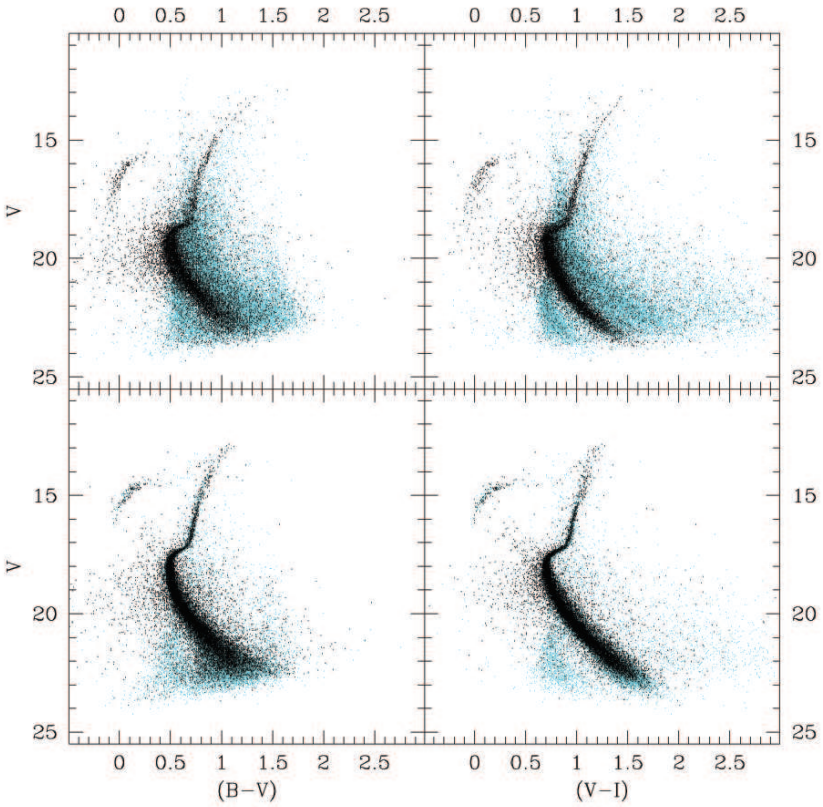

NGC 6681 (M 70)

l=2.85° b=−12.51°

R_{GC}=2.1 Kpc

$R_{\odot}$=9.0 Kpc

E(B−V)=0.07

$(m-M)_V$=14.98

V=−7.11

[Fe/H]=−1.51

r_t=7.91'

NGC 6809 (M 55)

l=8.80° b=−23.27°

R_{GC}=3.9 Kpc

$R_{\odot}$=5.3 Kpc

E(B−V)=0.08

$(m-M)_V$=13.87

V=−7.55

[Fe/H]=−1.81

r_t=16.28'

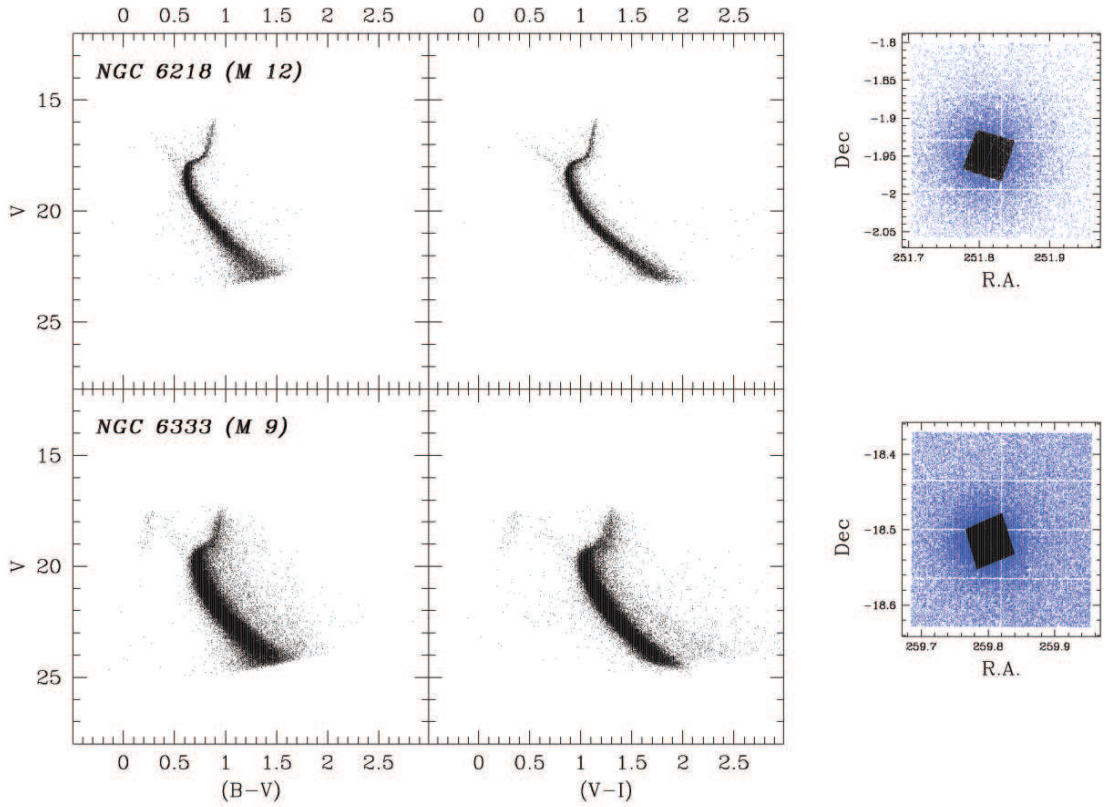

Figure 2.8. $B-V$ vs. V (left) and $V-I$ vs. I (right) color-magnitude diagrams of the central region of the 5 clusters observed with the *HST*/ACS in our proposal 10573. The same color and magnitude scale has been used in plotting the CMDs. The colors and magnitudes have been transformed to the Johnson-Cousins system, so CMDs from the ground and from space can be compared more easily. On the right, the positions of the stars obtained from the *HST* observation are plotted against the position of the stars obtained from the ground to give an idea of the field covered by both observations.

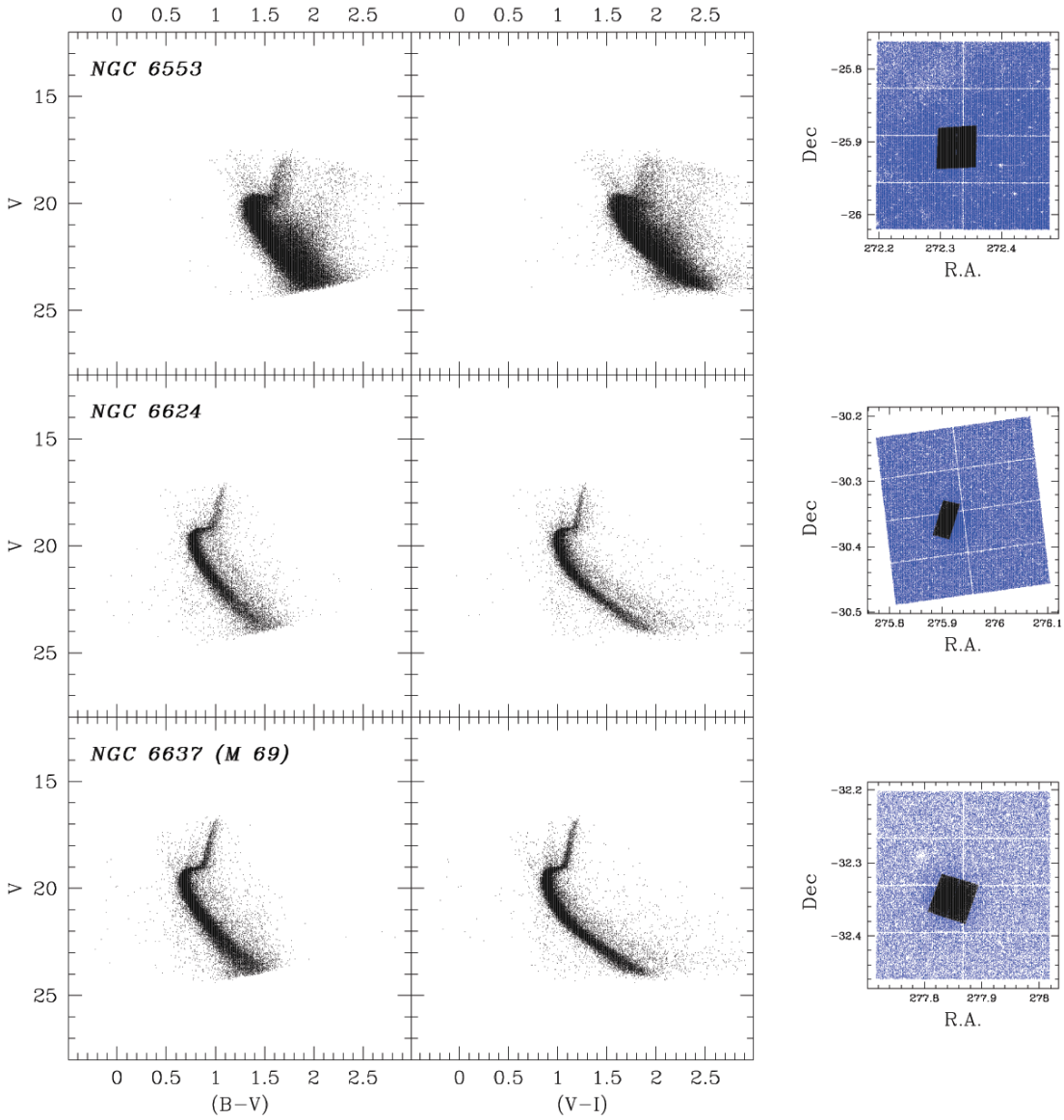
NGC 6553
NGC 6624
NGC 6637 (M 69)
V
(B−V)
(V−I)
Dec
R.A.

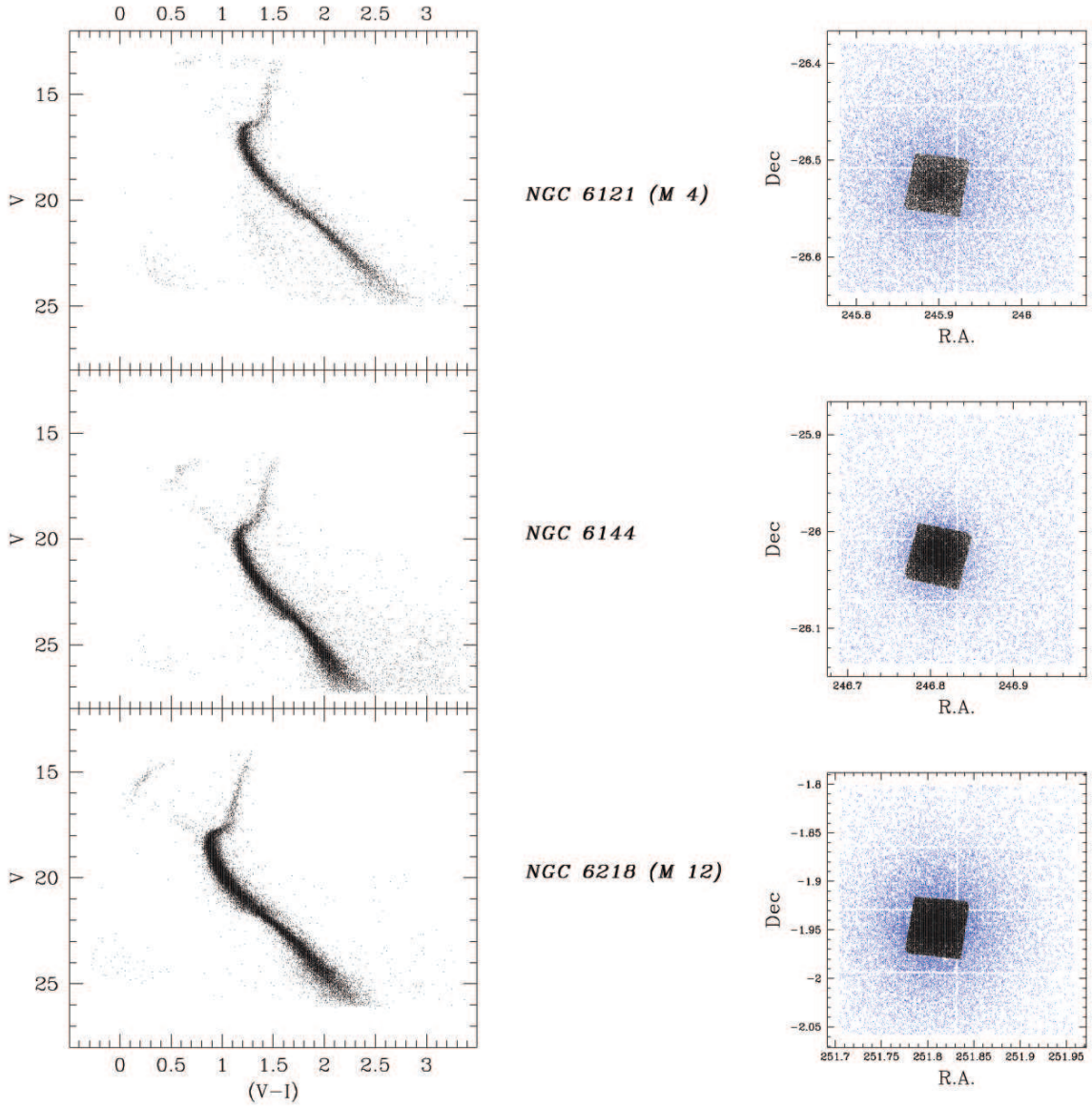

Figure 2.9. $V - I$ vs. I color-magnitude diagrams of the 15 clusters in our sample observed with the *HST*/ACS available in the *HST* data archive. All of the clusters were observed in program 10775, except NGC 6558 and NGC 6642, observed in program 9799. The same color and magnitude scale has been used in plotting the CMDs. The colors and magnitudes have been transformed to the Johnson-Cousins system, so CMDs from the ground and from space can be compared more easily. On the right, the positions of the stars obtained from the *HST* observation are plotted against the position of the stars obtained from the ground to give an idea of the field covered by both observations.

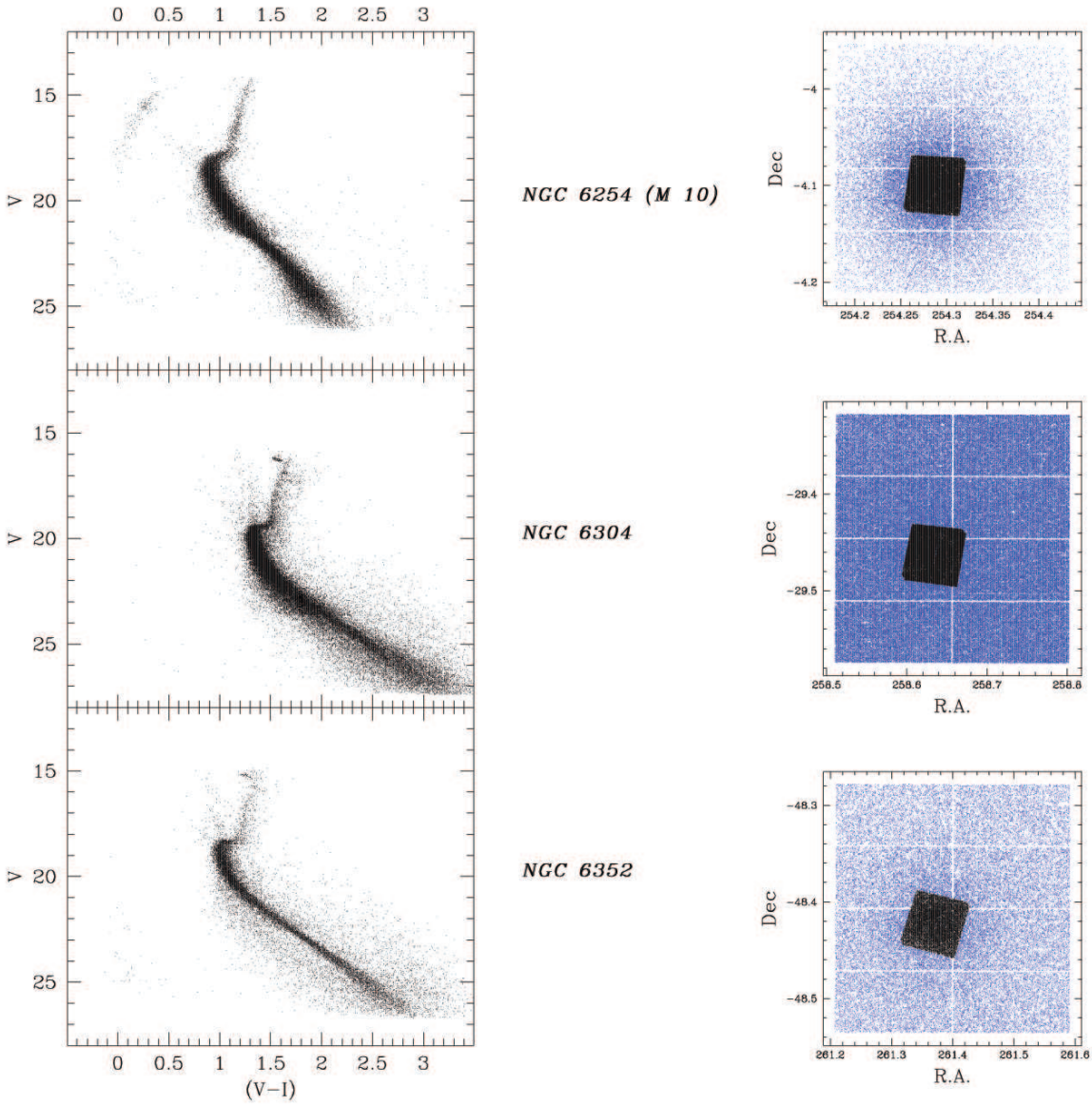
0 0.5 1 1.5 2 2.5 3
15
20
25
V
(V−I)
NGC 6254 (M 10)
NGC 6304
NGC 6352
Dec
R.A.
−4
−4.1
−4.2
254.2 254.25 254.3 254.35 254.4
−29.4
−29.5
258.5 258.6 258.7 258.8
−48.3
−48.4
−48.5
261.2 261.3 261.4 261.5 261.6

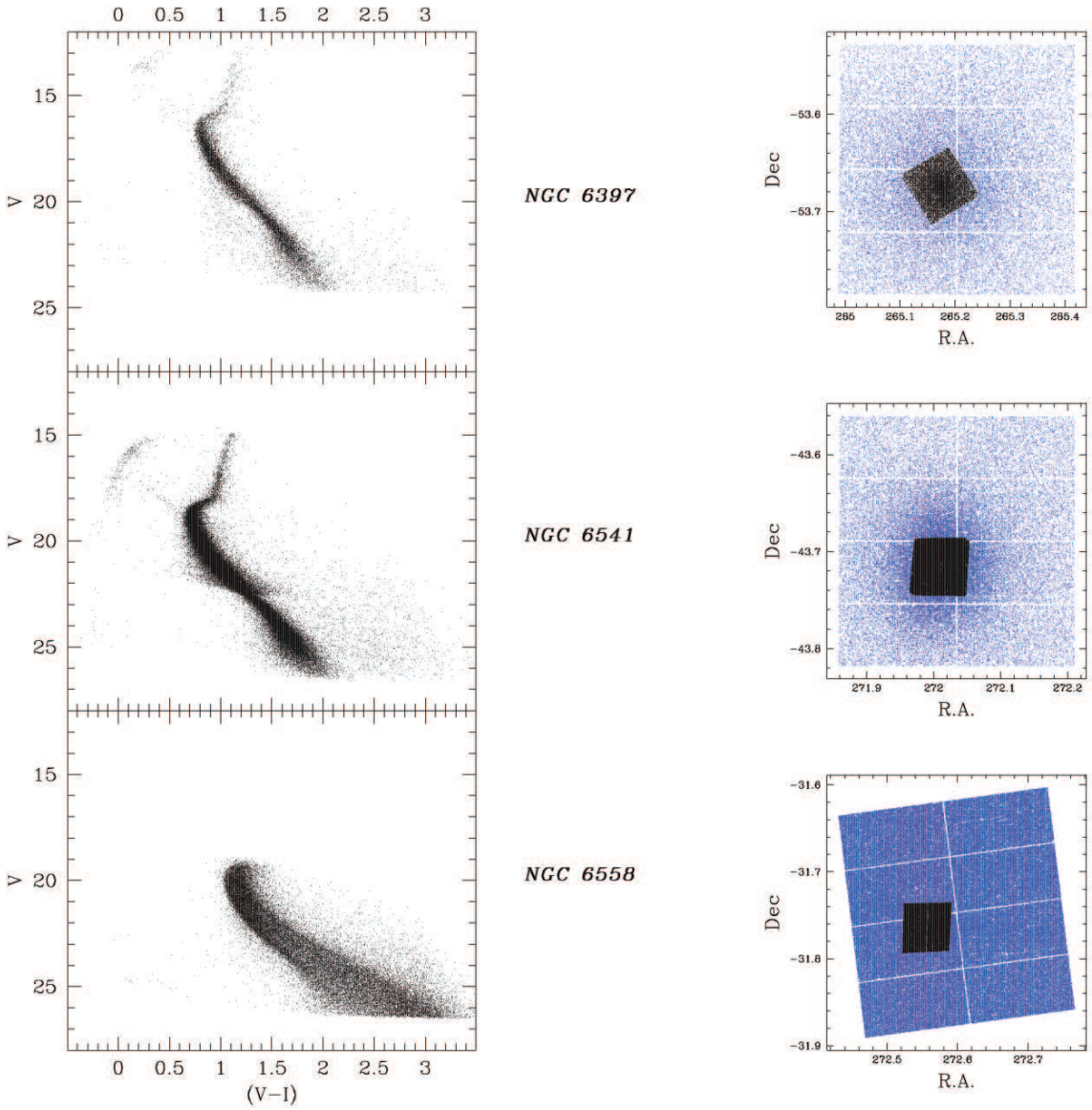
0 0.5 1 1.5 2 2.5 3
15
20
25
V
(V−I)
NGC 6397
NGC 6541
NGC 6558
Dec
R.A.
−53.6
−53.7
265 265.1 265.2 265.3 265.4
−43.6
−43.7
−43.8
271.9 272 272.1 272.2
−31.6
−31.7
−31.8
−31.9
272.5 272.6 272.7

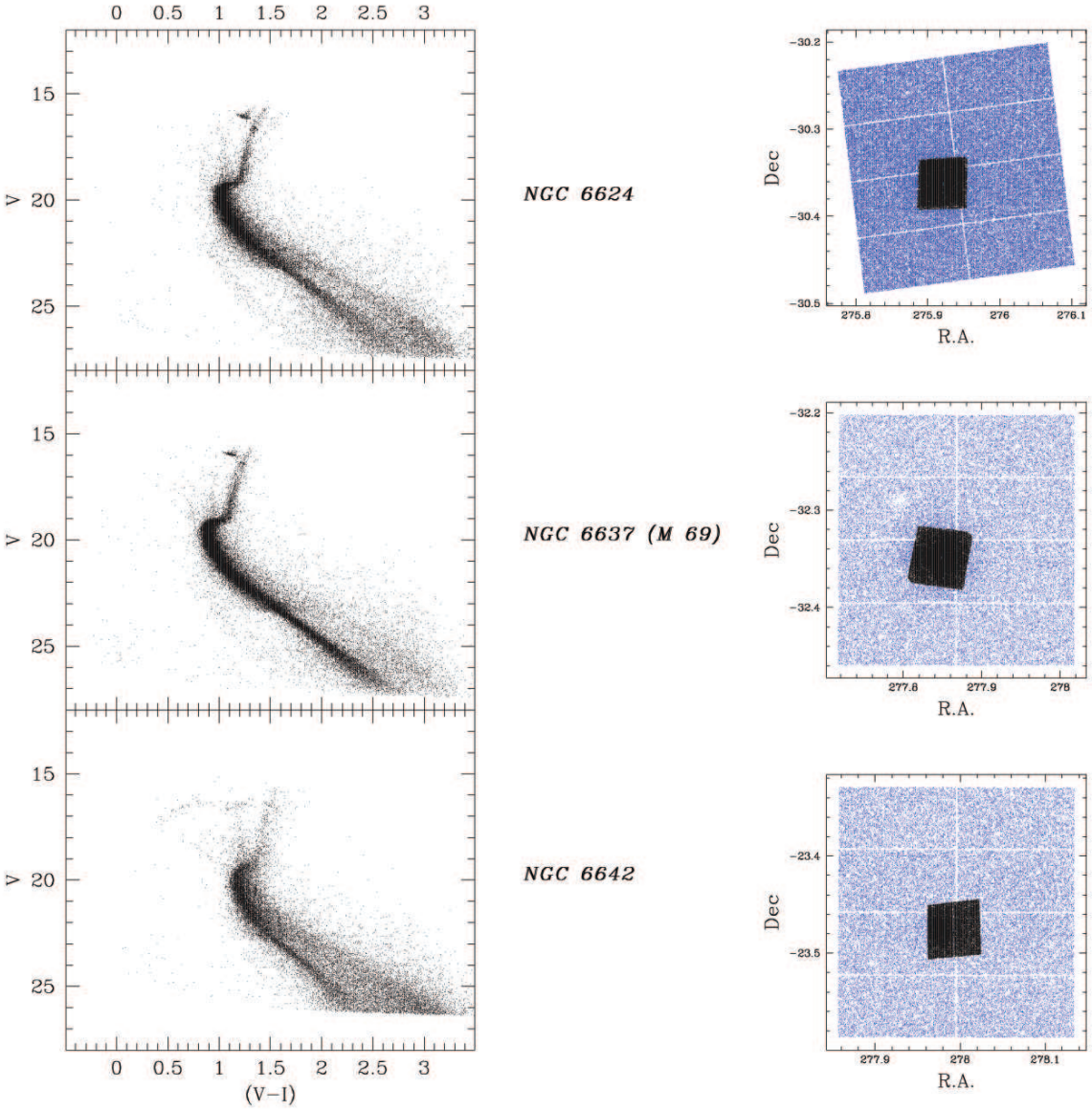
0 0.5 1 1.5 2 2.5 3
15
20
25
V
(V−I)
NGC 6624
NGC 6637 (M 69)
NGC 6642
−30.2
−30.3
−30.4
−30.5
275.8
275.9
276
276.1
Dec
R.A.
−32.2
−32.3
−32.4
277.8
277.9
278
Dec
R.A.
−23.4
−23.5
277.9
278
278.1
Dec
R.A.

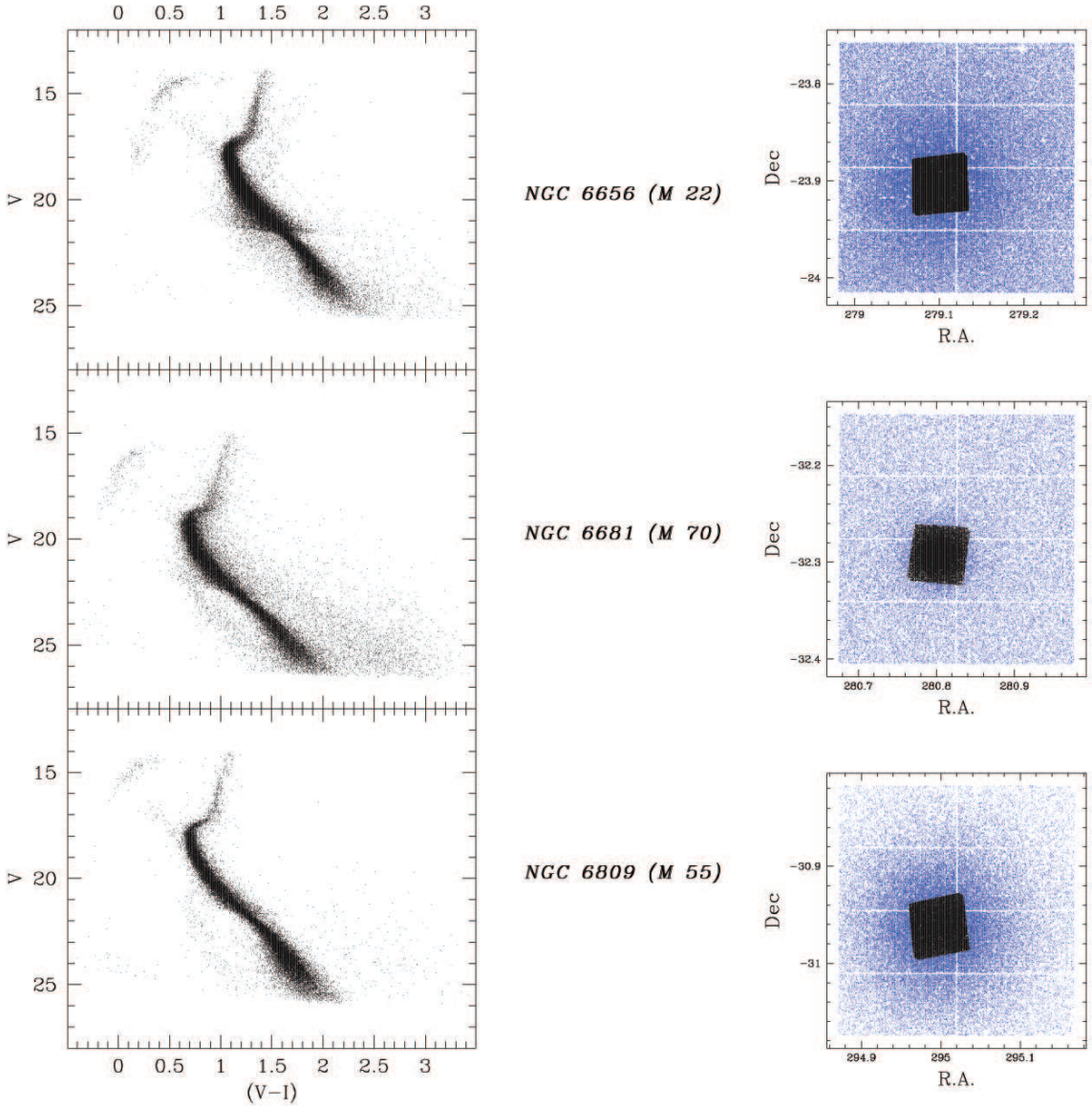
0 0.5 1 1.5 2 2.5 3
15
20
25
V
(V−I)
NGC 6656 (M 22)
NGC 6681 (M 70)
NGC 6809 (M 55)
Dec
R.A.
−23.8
−23.9
−24
279
279.1
279.2
−32.2
−32.3
−32.4
280.7
280.8
280.9
−30.9
−31
294.9
295
295.1

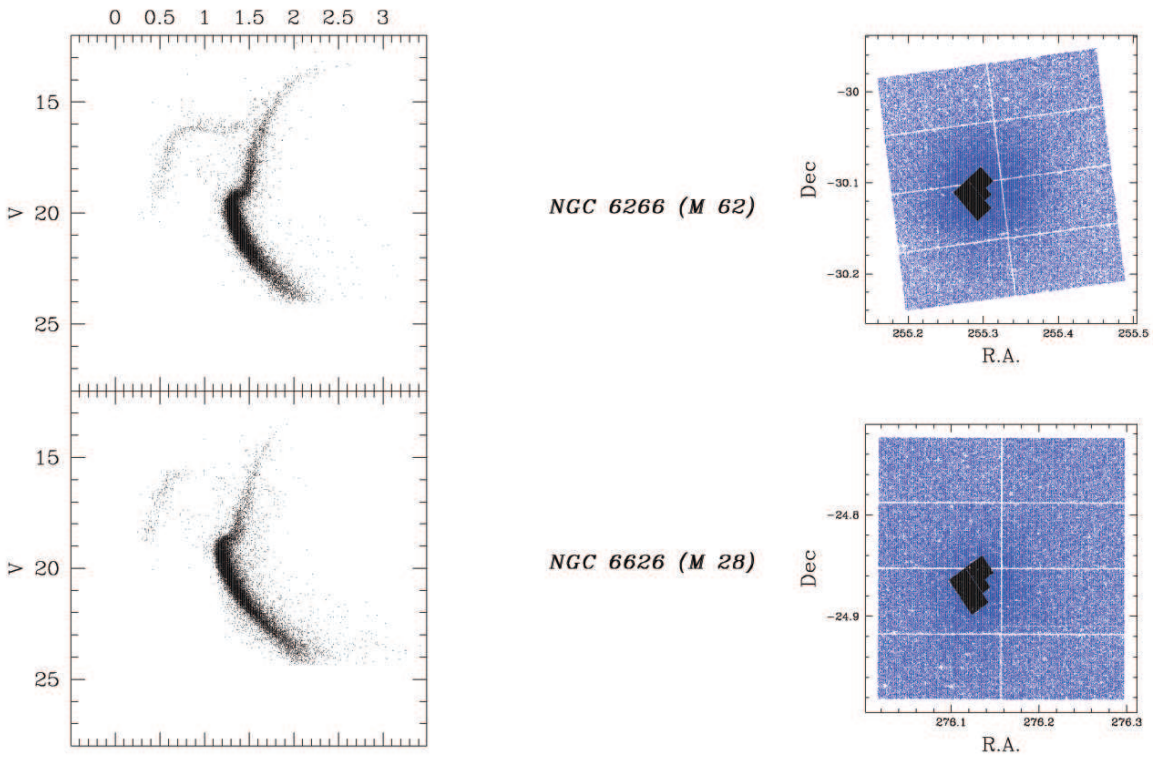

Figure 2.10. $V - I$ vs. V color-magnitude diagrams of the 2 clusters in our sample observed with the *HST*/WFPC2 available from the *HST* data archive that reach deeper magnitudes than our ground-based observations, and that will be used later to calculate extinction variations in the field. NGC 6266 was observed in program 8709, and NGC 6626 in program 6779. The same color and magnitude scale has been used in plotting the CMDs. The colors and magnitudes have been transformed to the Johnson-Cousins system, so CMDs from the ground and from space can be compared more easily. On the right, the positions of the stars obtained from the *HST* observation are plotted against the position of the stars obtained from the ground to give an idea of the field covered by both observations.

CHAPTER 3

The dereddening technique

Our dereddening technique is composed of five iterative steps (see figure 3.1):

- We assign a probability to the stars in our observed regions to belong to the cluster or to the Galactic field depending on their positions in the sky and in the CMD (section 3.1).
- We build a ridgeline for the stellar population of the observed cluster (section 3.2).
- We assign an individual extinction value to every star, based on its displacement from the ridgeline along the reddening vector (section 3.3).
- We smooth the different color excesses over the observed field to generate an extinction map (section 3.4).
- We apply the extinction values from the map to the stars in our observations to construct a dereddened CMD (section 3.5).

We repeat these steps iteratively until they converge.

This technique is based on work by von Braun & Mateo (2001) and Piotto et al. (1999b), and pioneered by Kaluzny & Krzeminski (1993), but unlike them, we do not divide the field in a grid of well established subregions a priori, but use a non-parametric approximation to smooth the information about the reddening in the field provided by every star, without such hard edges.

The success of this analysis depends critically on the assumption that the stellar populations are uniform within individual GCs. Recent studies tend to suggest that

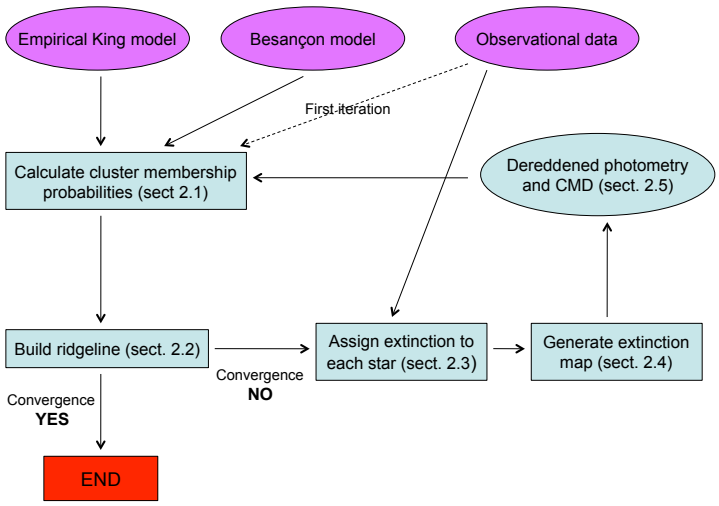

Figure 3.1. Flow chart describing our technique to map the differential extinction.

this is not strictly true, especially in the most massive GGCs (Bedin et al., 2004; Piotto et al., 2007). In the cases discovered, it is conjectured that the spread in helium content between stars in the cluster is important, but the spread in age and metallicity seems to be small (D'Antona & Caloi, 2008), making the spread of the stars in the SGB and upper RGB regions of the CMD to be also small. Since most of the information in our method comes from stars in these regions of the CMDs, our technique should not be significantly affected. What is more, in our method variations in the reddening must be spatially related, which should not be the case if there are multiple helium enriched populations within the cluster. Because of these reasons and since our sample only includes a few massive clusters, we expect the differential populations effects to be comparatively minor and not significantly affect our dereddening approach.

Also it is important to realize that our dereddening method does not establish the absolute extinction toward a target cluster, so we need to use other methods to estimate the absolute extinction in each case.

3.1 Field-cluster probability assignment

From our photometric studies we can assign probabilities to the stars in our observations to belong to the clusters, based on its position (x, y) on the field, i.e., how close to the center of the cluster the star is, and also on its position ($color, c$ and $magnitude, m$) on the CMD. These probabilities will be used in the next steps of our technique to give higher weight to the information provided by stars with high probabilities of being cluster members.

Before going any further, it is convenient to explain the notation that we are going to use, and to remember the basic rules of probability calculation. The marginal or unconditional probability of an event A happening is expressed P(A). The joint probability of an event A and an event B happening at the same time is expressed $P(A, B)$. Finally, the conditional probability of an event A happening given the occurrence of some other event B is expressed $P(A|B)$, and can be written as

$$P(A|B) = \frac{P(A, B)}{P(B)} \tag{3.1}$$

or, using the Bayes theorem, as

$$P(A|B) = \frac{P(B|A)P(A)}{P(B)} \tag{3.2}$$

Also, notice that in many parts of our analysis it is going to be more convenient to use probability density functions, $\rho(x)$, to express the probability. These functions describe the relative likelihood for a random variable X to occur at a given point in the sampled space Ω and satisfy

$$P(a \leq X \leq b) = \int_a^b \rho(x)dx \tag{3.3}$$

$$\forall x : \rho(x) \geq 0 \tag{3.4}$$

$$\int_\Omega \rho(x)dx = 1 \tag{3.5}$$

Whenever needed in this work, the probability density functions are calculated non-

parametrically using *locfit*. *Locfit* (Loader, 1999) is a local likelihood estimation software implemented in the R statistical programming language (see appendix). The main parameter input that *locfit* requires is a smoothing factor given by the maximum of two elements: a bandwidth generated by a nearest neighbor fraction, and a constant bandwidth (see appendix).

Now, if we suppose the variable X indicates membership to the cluster ($X = 1$ indicates observation of a member, and $X = 0$ indicates observation of a non-member), in the next paragraphs we calculate the conditional probability of the stars of being members of the cluster, given their position in the sky ($P(X = 1|x, y)$), and given their position in the color magnitude diagram ($P(X = 1|c, m)$) [1].

- If we assume an empirical King profile (King, 1962) for the cluster, we can write $f_{mem}(r)$, the surface density of member stars, as a function of r, the distance to its center

$$f_{mem}(r) = kK(r) = k \begin{cases} \left(\frac{1}{[1+(r/r_c)^2]^{1/2}} - \frac{1}{[1+(r_t/r_c)^2]^{1/2}}\right)^2 & \text{if} \quad r \leq r_t \\ 0 & \text{if} \quad r > r_t \end{cases} \tag{3.6}$$

  where r_c and r_t are the core radius and the tidal radius of the cluster. If we make another assumption and consider a constant surface density of stars for the non-member population, which is reasonable due to the small size of our field, then

$$f_{non}(r) = c \tag{3.7}$$

  and we have the following functional form for the total surface density distribution of stars observed in our field of view (FOV)

$$f_t(r) = kK(r) + c \tag{3.8}$$

[1] Notice than in our analysis we do not take into account all the information that we have available for every star at the same time, but we choose to calculate the probabilities as we only know the position in the sky r or the position in the CMD c, m of the stars. This is all right, since we are only using the calculated probabilities to assign weights for the next steps.

and we can write

$$P(X = 1|x, y) = P(X = 1|r) = \frac{kK(r)}{kK(r) + c} \tag{3.9}$$

or, alternatively,

$$P(X = 1|r) = 1 - P(X = 0|r) = 1 - \frac{c}{kK(r) + c} \tag{3.10}$$

Therefore to calculate $P(X = 1|r)$ we need to find the coefficients k and c, since $K(r)$ can be obtained taking the values for r_c and r_t for every cluster in our sample provided in the Harris catalog (Harris, 1996). These two remaining coefficients, k and c, can be easily found by a least squares fit of $K(r)$ to the observed surface density of stars $f_t(r)$ (see *eq.* 3.8 and upper plots in figure 3.2). To find the observed $f_t(r)$, we need to first calculate the number of stars at a given r in our observation, and then divide it by the area coverage at a given r in our observation. The number of stars at a given r in our observation is just the probability density $\rho(r)$ of stars in our observation, multiplied by the total number of observed stars. The probability density $\rho(r)$ of stars is calculated feeding *locfit* with the radial positions of the stars and a smoothing factor with a constant bandwidth of 0.25 arcmin. The surface coverage calculation at a given r in our observation is not trivial to find, since our FOV is a square not centered in the cluster center (see figure 2.2). In order to quickly calculate this area, we create a grid of points equally spaced over our FOV, calculate the probability density $\rho(r)$ of points, and then multiply by the area of the FOV. The probability density $\rho(r)$ of points is calculated feeding *locfit* with the radial positions of the points in the grid and a smoothing factor with a constant bandwidth of 0.25 arcmin.

- The conditional probability $P(X = 1|c, m)$ can be written, using the Bayes theorem, as

$$P(X = 1|c, m) = \frac{\rho(c, m|X = 1)P(X = 1)}{\rho(c, m)} \tag{3.11}$$

For any given cluster, we do not know the true distribution in magnitude and color in our observations of genuine GC members, but we can model the distribution of the field, non-member stars. We use the model of the Galaxy described in Robin et al. (2003), from now on referred as the Besançon model, to obtain $\rho(c, m|X = 0)$. We can now rewrite *eq.* 3.11 as

$$P(X = 1|c, m) = 1 - P(X = 0|c, m) = 1 - \frac{\rho(c, m|X = 0)P(X = 0)}{\rho(c, m)} \quad (3.12)$$

where $\rho(c, m|X = 0)$ is obtained feeding *locfit* with the position in the CMD of the Galactic field stars provided by the Besançon model [2] and a smoothing factor with a nearest neighbor ratio of 0.01, $\rho(c, m)$ is obtained feeding *locfit* with the position in the CMD of the stars in our observations and a smoothing factor with a nearest neighbor ratio of 0.01, and $P(X = 0)$ is just the ratio of the total number of field, non-member, modeled stars for an area equal to the FOV of the observation, to the total number of observed stars, which include field and cluster stars. To take care of the different variation ranges in color and in magnitude for the stars in the CMD a scale (see appendix) of 1 in color to 5 in magnitude is also provided to *locfit* as an input parameter to calculate $\rho(c, m|X = 0)$ and $\rho(c, m)$. In the lower plots in figure 3.2 we can see the different $P(X = 1|c, m)$ for the stars in M62, one of the clusters in our sample. Similar methods to calculate $P(X = 1|c, m)$ have been employed by Hughes et al. (2007) based on calculations by Hughes & Wallerstein (2000) and Mighell et al. (1998), and also by Law et al. (2003) based on calculations by Odenkirchen et al. (2001) and Grillmair et al. (1995). In contrast to these other studies we do not eliminate stars based on these probabilities, but downweight them.

Given the importance of the model used to analyze the Galactic field component of our observations and calculate $\rho(c, m|X = 0)$, we describe here in more detail the input parameters that we use to build these models.

[2]These CMDs can be easily obtained via the web interface provided at: http://model.obs-besancon.fr/

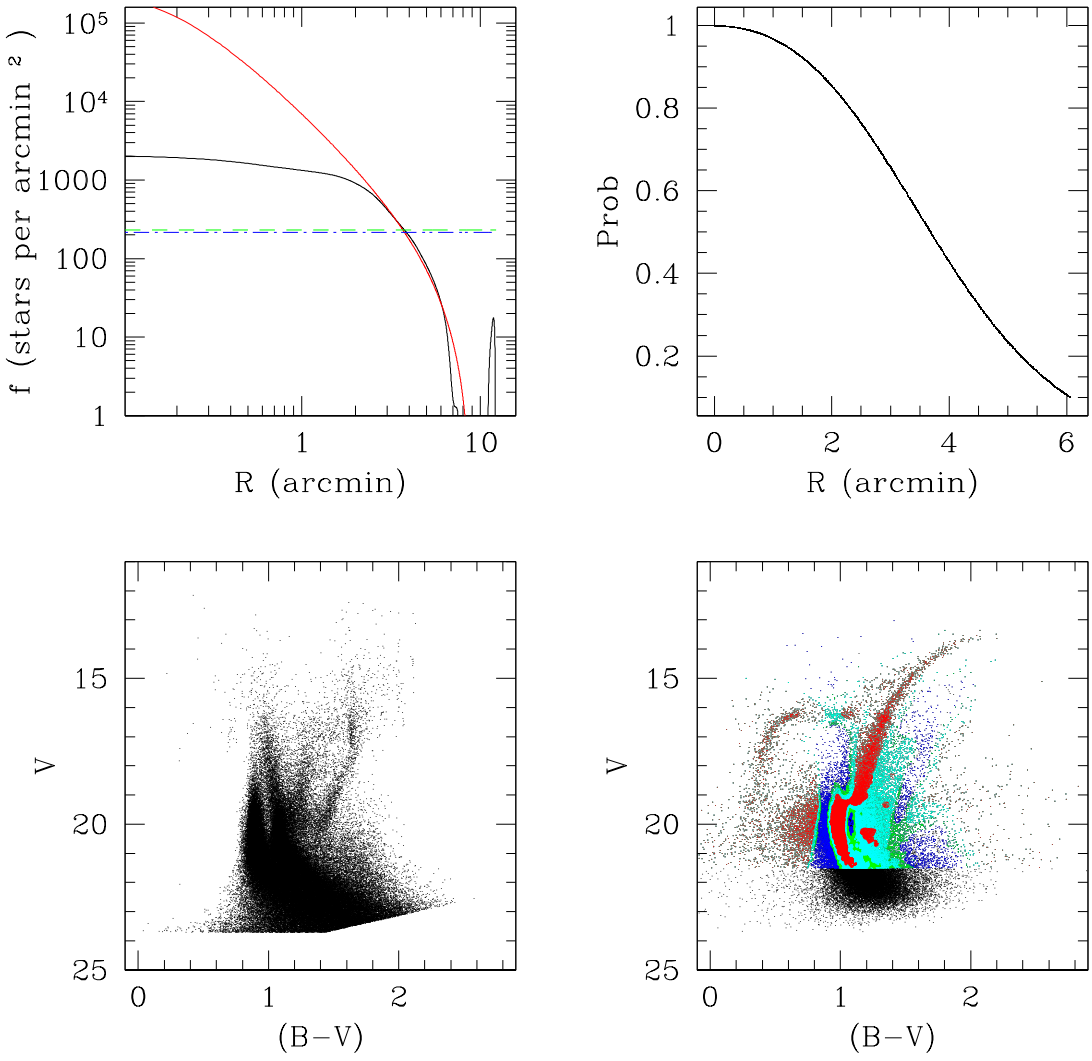

Figure 3.2. On the upper left, the density distribution per area of the stars in M62 as a function of distance to the GC center, minus the constant density distribution found for the field (dashed green line), is plotted as the solid black line, while the King model for the cluster is plotted with a red solid line, and the constant density distribution of stars in the field provided by the Besançon model is shown as a blue dashed line. On the upper right, the probability of the stars to belong to the cluster as a function of distance from the Galactic center $P(r|x = 1)$. On the lower right, CMD from the Besançon model of the Galactic stars in the field centered in the cluster position (see table 4.3 for the parameters used to build the model). On the lower right, our observed CMD, with the cluster belonging probabilities as a function of color and magnitude $P(c, m|X = 1)$ represented by the different colors of the stars: $0.1 \leq P(c, m|X = 1) < 0.25$ in blue, $0.25 \leq P(c, m|X = 1) < 0.5$ in green, $0.5 \leq P(c, m|X = 1) < 0.75$ in cyan, and $0.75 < P(c, m|X = 1) \leq 1$ in red. Notice that stars dimmer than the completeness limit ($V = 21.51$) are not compared.

- **Field of view.** We use the small field option from the web interface, in which the simulated stars are all supposed to be at the same coordinates (see table 4.3), implicitly assuming that the field star density gradient across the FOV is negligible. The same assumption was made in the calculation of $f_{non}(r)$ (see *eq*. 3.7). To obtain arbitrarily better statistical precision in the models, we can increase the selection area to obtain a larger number of stars in the model. $\rho(c, m|X = 0)$ is independent of the area and the number of stars used, since it is normalized (see *eq*. 3.5). In practice, we set this parameter to select ~ 300000 stars (see table 4.3). We have to notice though, that when calculating $P(X = 0)$ in *eq*. 3.12 we need to normalize the number of stars in the model to the FOV.

- **Extinction law.** First we choose a model without extinction. Then we make preliminary density maps for the CMDs of the models and for the CMDs from our observations, normalizing for every 1 magnitude interval. We move the density maps of the models along the reddening vectors in increments of 0.01 extinction calculating:

$$g_{ext} = \sum_{c,m} [\rho(c, m)\rho(c, m|X = 0)] \tag{3.13}$$

  The value of A_v where g_{ext} is a maximum is the value we choose for our absolute extinction. This A_v is generally equal or within a few hundredths of a magnitude to the one provided in Harris (1996). The extinction is simulated in the model as a cloud with an extinction equal to this A_v at distance of 0 pc (see table 4.3). The normalization is necessary because if we do not, we are giving more weight to regions in which there are more stars, e.g., the main sequence. This way we give a similar weight to all the regions of the CMD.

- **Characteristics of the stars used in the model.** We allow all ages, Galactic components, and spectral types provided by the model. We provide a limit only in the intervals of magnitudes equal to the ones of our observations (table 4.3). We also model our observational errors with an exponential function of the

apparent magnitude m in each band:

$$\sigma_{ph} = A + exp(Cm - B) \tag{3.14}$$

so the models will take the photometric error into account providing a more realistic approximation (see table 4.3).

Certain problems arise in this procedure, including:

- We have to take into account the completeness factor of our photometric observations. In general, completeness decreases with magnitude somewhat smoothly at the faint end, but suddenly at the saturation limit. Because of this, and since we are trying to calculate the probabilities comparing our observations with models (King profile and Besançon model) we need to find where the completeness factor starts to decrease at the faint end. Usually this is done with artificial-star tests, injecting stars in the CMD and analyzing the amount and magnitudes of the ones recovered (Piotto et al., 1999a). But our large sample and large density gradients within individual fields make artificial star tests highly inefficient, so we explore another method that is well-suited to our specific fields, and also much more efficient to implement. From the Besançon model we can calculate the number of non-member stars per area in the field that we have in a given magnitude range, and from our data we can also find the number of non-member stars per area in the field in a given magnitude range just by fitting *eq.* 3.8 in that magnitude range. So we iteratively calculate both numbers making the magnitude range smaller taking away stars in the 0.1 mag fainter end every time we do the calculation, repeating the process until we are able to get the cumulative luminosity functions (LF) for the seven fainter magnitudes for the non-member stars from everyone of our pointings. Then we can compare the modeled and observed LFs to see where the functions deviate one from the other. But this approximation proves to be not very accurate, especially in cases in which the number of non-member stars in the field is small. Instead we explore yet another approximation. We notice that

the LF in the Besançon model is always a concave function, while the observed LF of the non-member stars in the field becomes a convex function at the faint end. We can then identify the limit where the completeness factor starts to decrease as the inflexion point where the observational cumulative LF changes from concave to convex. The inflexion point is the point where the derivative of the LF has a extreme, a minimum in our cases. And the derivative is easily found using *locfit* to calculate non-parametrically the LF and its derivative (see appendix). The completeness limit is usually located in our observations at ~ 2 magnitudes from the faint end in V. In our posterior analysis we only used stars brighter than this limit.

- The completeness factor also depends on the distance to the center of the cluster, strongly so for the more crowded cases. Close to the cluster center we are not only missing stars at the faint end of the magnitude distribution, but at all magnitudes, since most of the lower completeness factor in this region is caused by masking saturated regions in DoPHOT (Schechter et al., 1993), the program used to do the photometric analysis of the images. From the calculation of the $P(X = 1|r)$, we can see that this reduced completeness factor reveals itself as a deviation from the linear model fit at distances close to the center of the cluster (see figure 3.2). If we assume that we are missing equal percentage of stars from the cluster and from the field, we can calculate its effect as the ratio between the observed and modeled $f_t(r)$. In the CMD, this lower completeness factor can lead to a miscalculation of $P(c, m|X = 1)$ if the FOV is small. However, since the area of the regions whose extinction we are able to map are much bigger than the areas where the reduced completeness factor is an issue, the comparison of our observations with the Besançon model is not significantly affected. The only appreciable consequence is that the calculated $P(X = 0)$ is a little higher than real. But this high value for $P(X = 0)$ can be corrected if when we calculate the number of stars, we take into account the deviation of the observation from the linear model as a function of the distance to the center

of the cluster, as we mentioned before.

- $P(c, m|X = 1)$ is obtained comparing a real observation with a model, where photometric errors are incorporated by mimicking the real photometric errors by the exponential function described above. In general, we observe that stars from the models tend to be a little more concentrated along the field different evolutionary sequences in the CMDs than stars from real observations. Therefore, for a given magnitude, $\rho(c, m|X = 0)$ peaks higher and decreases faster in the model than in the real observation, producing two main errors in our calculations of $P(c, m|X = 1)$. The first error is that we mistakenly assign a smaller than real probability of being in the field, and therefore a higher than real probability of being cluster members, to stars in the regions where the observed color is an extreme for a given magnitude. But since there are not many stars in these regions and they usually have higher photometric errors in color than our functions describe, they are downweighted or removed from our calculations later on (see section 3.4). More important is the second error, the case were $\rho(c, m|X = 0)$ peaks higher in the model than in reality, making the probability of the star to be a non-member in the field too high, and $P(c, m|X = 1)$ too low, lower than 0. In order to avoid these non-physical cases, and even too extreme cases that can give too low a weight value to the information coming from those stars, we put the hard limit $P(c, m|X = 1) \geq 0.1$.

3.2 Building the ridgeline

We try to model the first stages (MS, SGB and RGB) of the evolutionary path followed by the stars in a GC (see section 1.2 and figures 1.3 and 3.3) building the ridgeline for the CMDs of the GGCs, using *locfit* (see appendix) to construct a univariate non-parametric regression of the color of the stars as a function of the magnitude. This process is composed of three iterations.

- We begin this process by carrying out a non-parametric regression in the whole CMD to obtain a first estimation of the cluster ridgeline as a function of magni-

tude. We feed *locfit* with the magnitudes and colors of the stars and a smoothing parameter with a constant bandwidth of 0.2 magnitudes. Also, we give *locfit* preliminary weights for the stars

$$weight = P(X = 1|r)P(X = 1|c, m)w_{ph} \tag{3.15}$$

where $P(X = 1|r)$ and $P(X = 1|c, m)$ are the membership probabilities calculated in the previous subsection and w_{ph} is a photometric weight equal to the inverse of the square of the Poisson error of the photometric magnitude $w_{ph} = 1/\sigma_V^2$. These values have proven experimentally to be adequate for describing the MS and part of the RGB, but the regression fails to describe the SGB, and the stars in the HB create problems when trying to model the whole RGB. Still, they produce a reasonable first approximation (see upper left plot in figure 3.3) and let us identify the TO point, which we define as the bluest point of our ridgeline. We should note here that the MS is defined not to the faintest magnitude limit of the data, but to the completeness limit found in section 3.1.

- In the second iteration we try to get a less noisy whole ridgeline, along with a better defined RGB ridgeline. As a first step we divide the initial ridgeline in three regions: the MS region, where the ridgeline magnitudes are $m > m_{TO}$; the SGB region, where the ridgeline magnitudes are $m_{TO} - 1 \leq m \leq m_{TO}$; and the RGB region, where the ridgeline magnitudes are $m < m_{TO} - 1$. To smooth out any noisy part, we take the points from the ridgeline from the first iteration for every region, and smooth them using *locfit* with a nearest neighbor ratio of 0.7(*locfit* default), no preliminary weights or constant bandwidth requirements. The RGB ridgeline is still not well defined, because of the effects of stars in the HB. To calculate a better ridgeline of the RGB getting rid of the effects of the blue part of the HB, we go back to the CMD of the stars. We take only stars in the magnitude range $m < m_{TO} - 1$ and in the color range $col_{TO} < col$. We feed *locfit* with their magnitudes and colors, and a constant bandwidth of 0.2

mag and a nearest neighbor ratio of 0.1 to calculate the smoothing parameter. We use the nearest neighbor ratio because if not, the upper part of the RGB, usually scarcely populated, can become very noisy. Still, the red part of the HB, whenever present, is going to deviate the RGB ridgeline. To eliminate its effect we have to locate first where the HB is. We look for a change in the sign of the slope of the RGB. The bluest point brighter than the point where the slope sign change is, shows where the HB is. And the difference between these two points provides information about the thickness of the HB, $m_{HBthickness}$. Once the HB is located, we repeat the analysis done before for the RGB, with the same smoothing parameter and weights, but now omitting also points in the interval $m_{HB} - m_{HBthickness} \leq m \leq m_{HB} + m_{HBthickness}$. That way we have a better ridgeline for the upper and lower regions of the RGB. To get a ridgeline for the whole RGB, smoothing any noisy part, we follow a similar process to what we do in the beginning of this second iteration. We take the points in the description of the upper and lower RGB ridgeline, and use *locfit* again, but now with a nearest neighbor ratio of 0.7, no preliminary weights or constant bandwidth requirements. The ridgeline is much better now, but still we are a little off in the description of the SGB (see upper right plot in figure 3.3).

- In the third and last iteration, we try to calculate a better ridgeline for the SGB. In order to do that we follow Marín-Franch et al. (2009), where they use rotated histograms to recalculate the ridgeline for the GC in their sample, using only stars perpendicular to the ridgeline in the calculation. Although our approximation is similar, the implementation is a little different. We calculate the slope of the curve at every point of the previously calculated ridgeline using *locfit* to get the derivative of the slope at a given point of the ridgeline. Once we have this, we rotate the coordinate system of every star at every magnitude with the angle α_i of the slope of the ridgeline at that magnitude, and centered at the ridgeline. Once this is done, we can get a ridgeline in the new coordinate system using *locfit* again. This new ridgeline should be a straight line along

the Y coordinate with a value of 0 in the X coordinate. Any deviation from that will mean that the ridgeline in the original color-magnitude coordinate system requires a more accurate calculation. Notice that in order for the new coordinate system to consistently show these deviations, we need the range of both coordinates to be similar in the old coordinate system. This is not the case for the range of colors and magnitudes presented in a CMD. To try to get them to a similar scale we multiplied the color by a factor of 5 before doing the rotation. In the calculation of the ridgeline in the new coordinate system the preliminary weights and smoothing factor used for *locfit* where the same as in the first iteration. We observe that the X coordinate of the ridgeline in the new reference system does not deviate significantly from 0 in the region of the MS stars, but does so in the SGB and upper RGB region. In the RGB region it is expected due to the scarcity of the population there. We took care of that in the previous iteration, so we concentrated our attention in the SGB region. We derotated the ridgeline in that region (the part where the original magnitudes where in the range $m_{TO} - 1 < m < m_{TO}$) to get their coordinates in the color-magnitude coordinate system, and after smoothing out any noise using *locfit* with a nearest neighbor ratio of 0.7, we put together the different parts of the ridgeline (see lower left plot in figure 3.3). The new ridgeline seems to follow accurately the different evolutionary sequences present in the GCs, and is the one we use in the next calculations.

In section 3.4 we discuss how we can use stars in the HB to test the accuracy of our method. To carry this test, we need to model a ridgeline for this region too. The process to find the ridgeline here is a little more interactive than for the other regions of the CMD. First, we have to decide by visual inspection of the CMD if we are dealing with a cluster that has only blue, only red or both sections of the HB. If the cluster shows only a blue HB, we carry out a non-parametric regression on the stars bluer than the TO to obtain an estimation of the cluster HB ridgeline as a function of magnitude. We feed *locfit* with the magnitudes and colors of the HB, and a constant bandwidth of 0.2 mag and a nearest neighbor ratio of 0.1 to calculate the smoothing

parameter. If only a red HB is present instead, the non-parametric regression is performed on stars in the interval $m_{HB} - m_{HBthickness} \leq m \leq m_{HB} + m_{HBthickness}$ to obtain an estimation of the cluster HB ridgeline as a function of color. The smoothing parameter is calculated by *locfit* with the same parameters as for the blue HB. Finally, if the HB shows red and blue sections, we calculate both independently following the methods previously described, and then we smooth the result as a function of color, feeding *locfit* with the magnitudes and colors of the points in the description of the blue and red HB ridgeline, and a nearest neighbor ratio of 0.25, no preliminary weights or constant bandwidth requirements (see lower right plot in figure 3.3).

3.3 Calculating an extinction for every star

To calculate an extinction for every star we move the stars along the reddening vector until they intersect the ridgeline (see figure 3.4). The reddening vectors are described by the equations

$$A_V/E(B-V) = 3.317 \tag{3.16}$$

and

$$A_V/E(V-I) = 2.411 \tag{3.17}$$

as given in Schlegel et al. (1998), which are evaluated using the $R_V = 3.1$ extinction laws of Cardelli et al. (1989) and O'Donnell (1994).

The HB ridgeline, and therefore also stars in the range $m_{HB} - m_{HBthickness} < m < m_{HB} + m_{HBthickness}$, are not used in this calculation, since we want to use them as an independent test of the goodness of our method (see section 3.4). We do not use stars dimmer than the completeness limit found in the previous section either. These stars and stars that do not intersect with the ridgeline are given a weight 0 in the calculation of the extinction map described in next section.

To calculate the error of these shifts we follow the analysis in von Braun & Mateo (2001):

- We created an error ellipse for every star defined by the Poisson error in its color and magnitude.

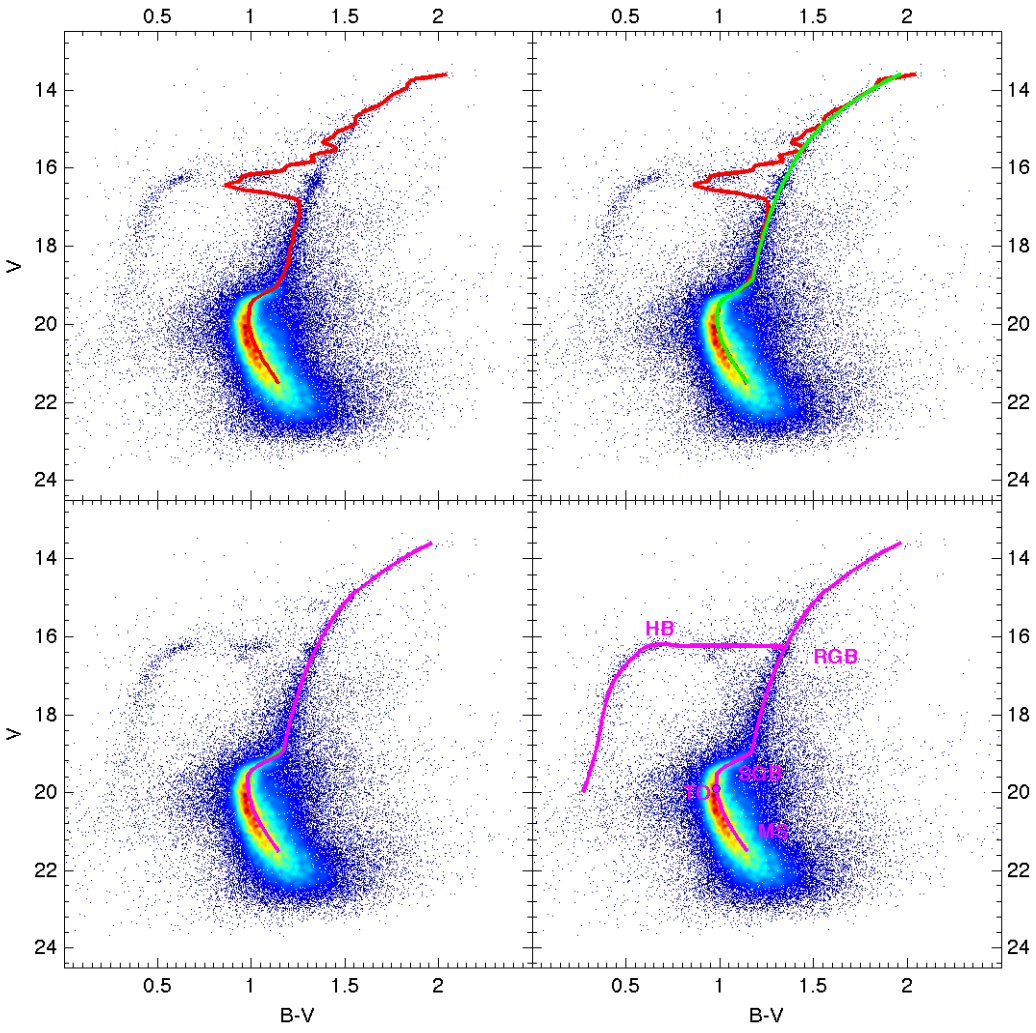

Figure 3.3. CMD of the example GC, M62 with the ridgeline provided after the first (upper left), second (upper right), and third (lower left) iterations of our method. Warmer (redder) colors mean higher density of stars in a region of the CMD. On the lower right, the HB ridgeline is also shown, along the different parts of the CMD morphology: main sequence (MS), turn-off point (TO), subgiant branch (SGB), red giant branch (RGB) and horizontal branch (HB).

- Since the color and magnitude errors are correlated, the error ellipse is tilted. The tilt angle and the length of the semi-major and semi-minor axes of the error ellipse are functions of the error in color and in magnitude.

$$\tan(2\theta) = \frac{2\sigma_{cm}}{\sigma_c^2 + \sigma_m^2} \tag{3.18}$$

$$\sigma_{c'}^2 = \frac{\sigma_c^2 + \sigma_m^2}{2} + \left[\frac{(\sigma_c^2 - \sigma_m^2)^2}{4} + \sigma_{cm}^2\right]^{1/2} \tag{3.19}$$

$$\sigma_{m'}^2 = \frac{\sigma_c^2 + \sigma_m^2}{2} - \left[\frac{(\sigma_c^2 - \sigma_m^2)^2}{4} + \sigma_{cm}^2\right]^{1/2} \tag{3.20}$$

  where θ is the tilt angle of the error ellipse, $\sigma_{c'}$ and $\sigma_{m'}$ are the semi-major and semi-minor axis of the tilted ellipse, and σ_{cm} is the covariance of the color and magnitude.

- For every star, we move the error ellipse along the reddening vector. The point of first contact (pfc), i.e., the point where the ellipse touches the ridgeline for the first time, and the point of last contact (plc), where the ellipse touches the ridgeline for the last time, represent the one-sigma-deviation points (see figure 3.4).

- Although these two contact points are not necessarily symmetric about the reddening value of the star, i.e., the center of the error ellipse, we are going to define the error in the shift as:

$$\sigma_{ellipse} = 0.5(pfc + plc) - center \tag{3.21}$$

3.4 Creating the extinction map

We now take all the color excesses for the individual stars and smooth them using *locfit* to build a bivariate non-parametric regression of the extinction as a function of the spatial coordinates right ascension and declination, up to a distance from the

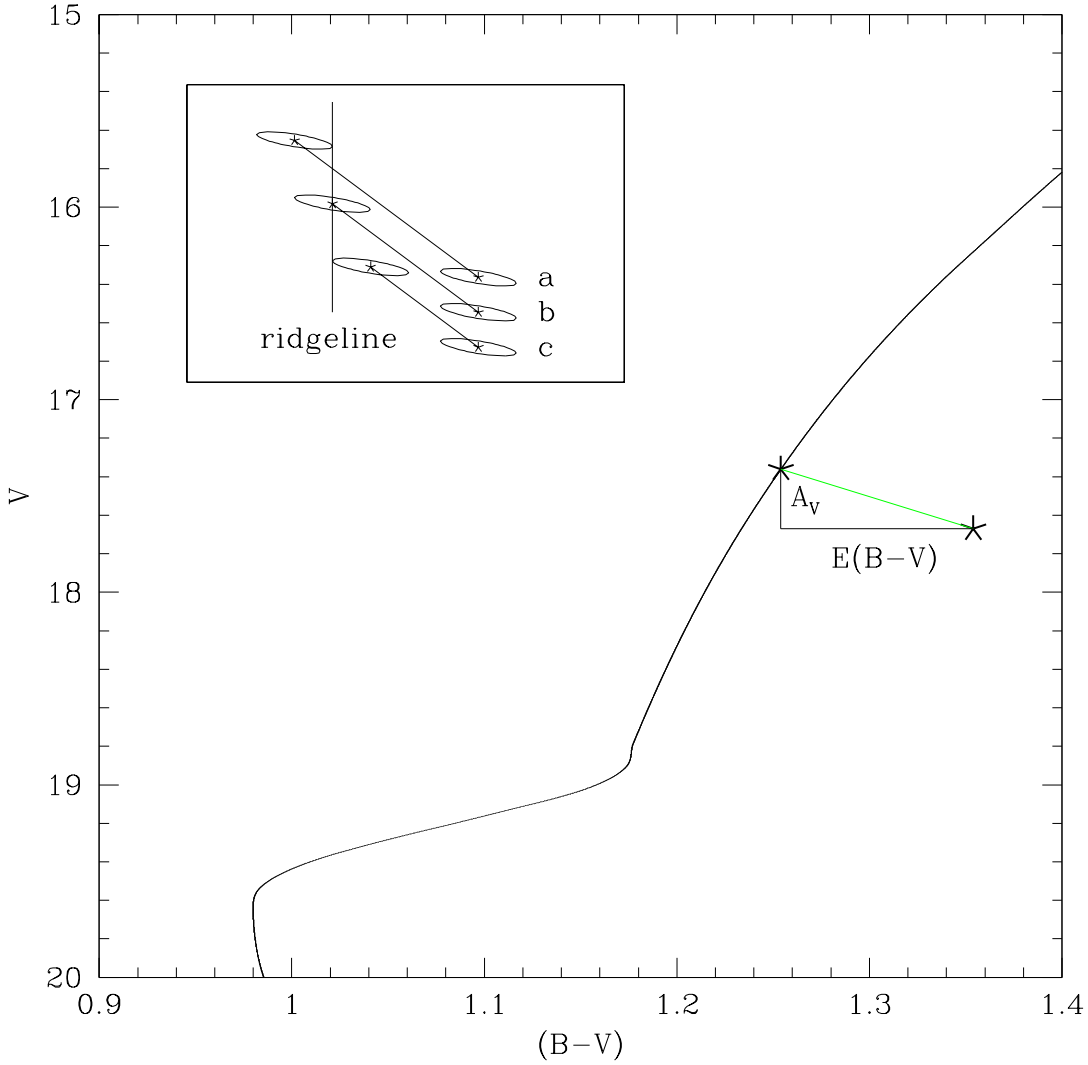

Figure 3.4. Example of how we move one of M62's star along the reddening vector (in green) until it intersect the ridgeline. From there a value for the color excess E(B-V) is obtained. In the upper left box, we schematically show how the error ellipse moves and how the error in the shift is calculated. The 'point of last contact' of the error ellipse with the ridgeline is represented in a, the shift of the original datapoint until it intersects the ridgeline is represented in b, and the 'point of first contact' of the error ellipse with the ridgeline is presented in c.

center of the cluster equal to where $P(X = 1|r) = 0.1$ or the limit of our observations, whichever comes first. This limit is employed after preliminary applying our method to the clusters in our sample with looser restrictions, and not observing an improvement in the dereddened CMDs (see section 3.5) for stars located beyond these boundaries. Stars that were given a 0 weight in the previous subsections (stars in the HB region, stars dimmer than the completeness limit, stars that do not intersect with the ridgeline after being moved along the reddening vector) are not taken into account for the calculation of the map, although after the map is built a reddening correction is applied to all of them. Preliminary weights are assigned in *locfit* to all stars as they were calculated in previous subsections, but now $w_{ph} = 1/\sigma^2_{ellipse}$. The kernel in this case has a constant bandwidth of $0.5' \times 0.5'$ or a nearest neighbor ratio of 0.03, whichever is bigger. These values for the smoothing parameter are used after experimentally checking in a few of our clusters which kernel provides us with a tighter HB, in the sense of a smaller standard deviation of the stars from the ridgeline of this region (see section 3.2), after generating the dereddened CMD (see section 3.5). This is an independent test to check the goodness of our dereddening method, since our technique does not use stars in the HB to calculate the extinction map. Since the tests were not highly conclusive on choosing a particular set of parameters, giving similar results for a range of parameters, the set used is an average of the best values obtained for the different clusters tested.

Along with the extinction map, an extinction precision map is also calculated. This is done assuming that the precision of the extinction map is a function of the spatial coordinates. That way, following Wasserman (2006), we can write

$$Y_i = r(\alpha_i, \delta_i) + \sigma(\alpha_i, \delta_i)\epsilon_i,\ \mathbb{E}(\epsilon_i) = 0,\ \mathbb{V}(\epsilon_i) = 1 \tag{3.22}$$

where Y_i is the calculated extinction for the i-th star, and $r(\alpha_i, \delta_i)$ is the value for the extinction provided by the regression function at the coordinates (α, δ) of the i-th

star. If we let $Z_i = log(Y_i - r(\alpha_i, \delta_i))^2$ and $\Delta_i = log\epsilon_i^2$, we have

$$Z_i = log\sigma^2(\alpha_i, \delta_i) + \Delta_i \tag{3.23}$$

This suggests estimating $\log\sigma^2(\alpha_i, \delta_i)$ by regressing the log squared residuals on the spatial coordinates (α, δ). We do this using *locfit* with the same weights and smoothing parameters we have used to calculate the extinction map. Once we have obtained an estimate $\hat{s}(\alpha_i, \delta_i)$ of $\log\sigma^2(\alpha_i, \delta_i)$ we get

$$\hat{\sigma}(\alpha_i, \delta_i) = \sqrt{e^{\hat{s}(\alpha_i, \delta_i)}} \tag{3.24}$$

This precision map [3] provides us with a tool to better determine our extinction map. We iteratively repeat the whole process of the calculation of extinction maps, but every time using only stars that have extinctions that are no more than 3σ away from the value that our previous extinction map gives for those coordinates. Preliminary weights and smoothing parameters are the same in every calculation. We repeat the process until it converges. This way for every cluster we are able to provide an extinction map (see top plot of figure 3.5), a precision map for this extinction map (see bottom plot of figure 3.5), and a resolution map with the bandwidth that we have use in a certain region to calculate the extinction map there (see central plot of figure 3.5).

[3] Note that the previous analysis to obtain the variance in the extinction maps is biased since Wasserman's method does not take into account that the distribution of the Δ_i have a mean $\mathbb{E}(\Delta_i) \neq 0$. We should notice that if the ϵ_i follow a normal distribution with mean $\mathbb{E}(\epsilon_i) = 0$ and variance $\mathbb{V}(\epsilon_i) = 1$, the ϵ_i^2 follow a χ^2 distribution with mean $\mathbb{E}(\epsilon_i^2) = 1$, and the $\Delta_i = log\epsilon_i^2$ follow a distribution with a mean, obtained from Monte Carlo simulations, of $\mathbb{E}(\Delta_i) = -1.27$. Hence, if we define $\eta_i = \Delta_i + 1.27$, then we could write eq. 3.23 as

$$Z_i + 1.27 = log\sigma^2(\alpha_i, \delta_i) + \eta_i \tag{3.25}$$

where $\mathbb{E}(\eta_i) = 0$, and now we need to regress not just the Z_i's, but the $Z_i + 1.27$, to obtain an estimate $\hat{s}(\alpha_i, \delta_i)$ of $\log\sigma^2(\alpha_i, \delta_i)$. Since in our analysis we follow Wasserman's method, we did not take into account this bias, and our extinction variation maps are underestimated by a factor of almost 2. Another approach would have been to regress directly the residuals, without taking the logarithms. We applied this approach to one of the clusters in our study, and obtained results for the variation estimation similar to the ones obtained from Wasserman's approach, once corrected by its bias. The extinction maps after all the iterative steps were applied did not change significantly

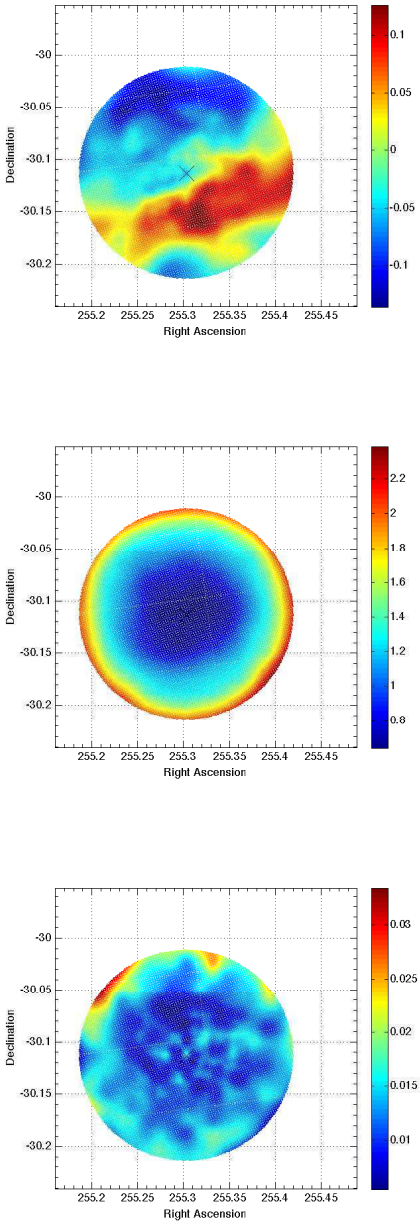

Figure 3.5. Extinction map for the M62 cluster (top), along its resolution (middle), and its precision (down), as provided by our technique. The x marks the position where the center of the cluster is. The color code gives the color excesses $E(B-V)$ for the extinction map, the bandwidths used in the resolution map, and the standard deviation σ of the color excesses in the precision maps. Notice that the extinction map provides only the differential extinction in the field, and the adopted absolute reddening zero point is defined by where our ridgeline lies, and has to be established from other methods (see text).

3.5 Creating the dereddened CMD

All the stars are given a reddening correction from the extinction map and a dereddened CMD is constructed (see figure 3.6). This dereddened photometry is the input on the next iteration to calculate the cluster membership probabilities, and to build a new improved ridgeline (see figure 3.1). Notice though that the input on the calculation of the individual reddenings to generate the extinction maps is the original photometry in every iteration (see figure 3.1).

We iteratively repeat this process until there is a convergence in the calculated ridgeline (see figure 3.1), which is going to produce a convergence in the reddening values of the extinction map. For our dataset, convergence usually occurs after just two or three iterations.

between the two approaches.

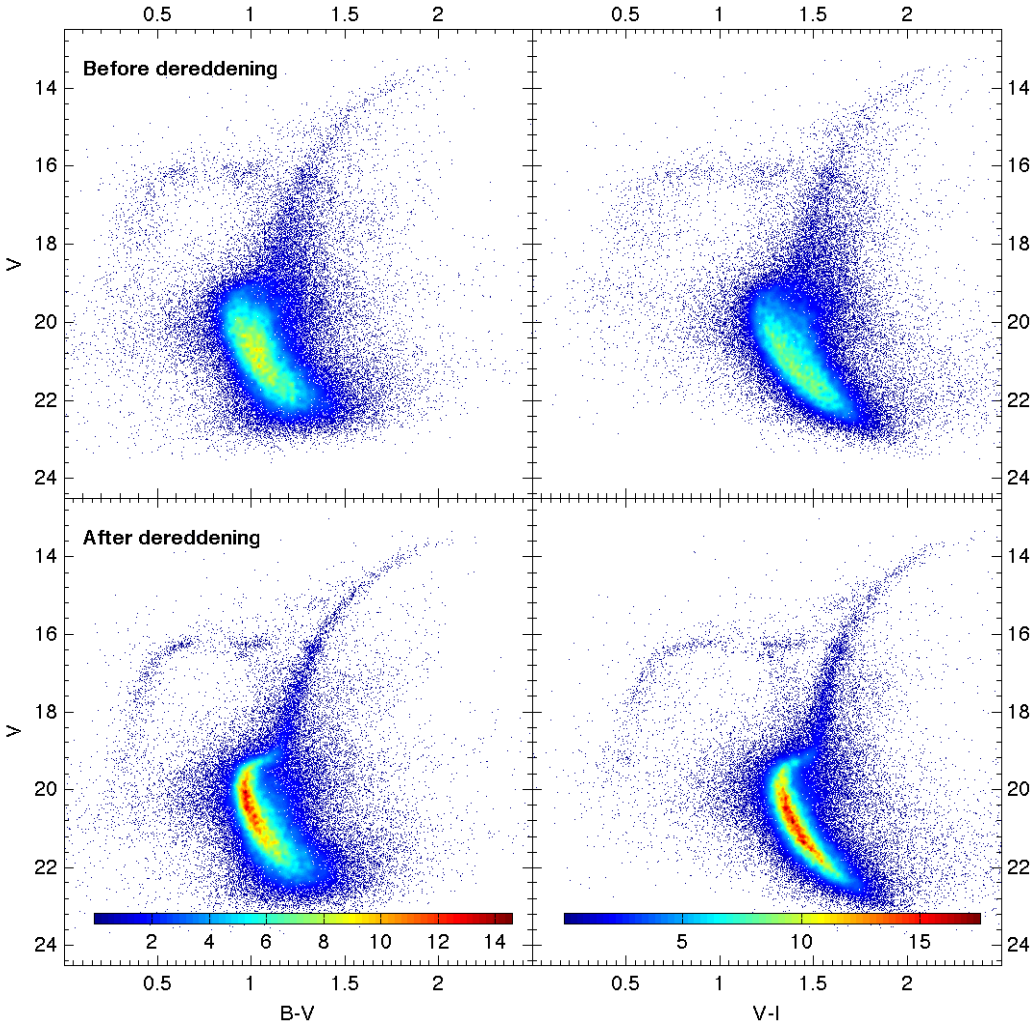

Figure 3.6. B-V vs. V (left) and V-I vs. V (right) CMDs of M62, before and after applying our dereddening technique to them. Color bars show the range in the densities of stars in the CMD ($\times 10^4$ stars per square magnitude). The color ranges are the same for a given color (B-V or V-I) in the CMD before and after applying our technique.

CHAPTER 4

Applying the technique: dereddened CMDs and extinction maps

In this chapter we present the results of applying the dereddening method described in chapter 3 to all the clusters in the sample of 25 globular clusters shown in chapter 2. We describe any improvement in the CMDs of the globular clusters. We also provide the extinction maps that the dereddening technique generates, and compare them with the extinction maps supplied by Schlegel et al. (1998), from now on referred as the SFD extinction maps.

A detailed explanation of the dereddening method is provided in chapter 3. Let us just remind here that the technique is applied independently to the two colors ($B-V$ and $V-I$), and it is only in the end of the process that the extinction maps obtained from both analysis are averaged.

The first step of our dereddening method is to calculate the probabilities $P(X = 1|r)$ and $P(X = 1|c, m)$ for the observed stars to belong to the cluster. In order to do that, we calculate the densities of the stars as functions of distance to the center of the cluster and of color and magnitude and compared them with a King profile plus constant field model (see figure 4.1) and with a Besançon model respectively. The densities of observed stars are calculated using stars down to the completeness limit of our observations (see table 4.1). The densities in the models were calculated using the parameters shown in table 4.2, for the King model, and table 4.3, for the Besançon model. Applying *eq*.3.9 and *eq*.3.12 we are able to find $P(X = 1|r)$ (see figure 4.2), and $P(X = 1|c, m)$ (see figures 4.3 and 4.4). We restrict our analysis to areas in which $P(X = 1|r) > 0.1$. There are a few cases in which we do not calculate $P(X = 1|c, m)$ in one of the colors (NGC 6144, NGC 6558, and NGC 6626 in $B-V$,

Table 4.1. Limits for the stars used in our analysis

Cluster	V_{CL} [a]	ΔV_{CL} [b]	R_{an} [c]
NGC 6121	20.69	1.9	12.26
NGC 6144	22.03	2.0	12.40
NGC 6218	21.71	1.8	12.32
NGC 6235	22.70	2.0	4.56
NGC 6254	22.07	1.9	11.92
NGC 6266	21.51	2.2	6.07
NGC 6273	21.86	2.2	8.37
NGC 6287	21.90	2.1	4.89
NGC 6304	21.69	2.9	3.90
NGC 6333	22.38	2.1	5.70
NGC 6342	22.44	2.3	4.17
NGC 6352	21.66	2.5	5.65
NGC 6355	21.98	2.2	2.39
NGC 6397	20.66	2.1	8.06
NGC 6522	20.99	3.5	2.34
NGC 6541	22.32	2.0	12.68
NGC 6553	21.42	2.3	4.07
NGC 6558	21.37	3.2	1.84
NGC 6624	21.62	2.6	3.76
NGC 6626	21.11	2.6	4.94
NGC 6637	20.99	2.2	4.34
NGC 6642	20.00	1.9	2.25
NGC 6656	20.77	2.4	12.25
NGC 6681	22.02	2.2	4.90
NGC 6809	22.17	1.7	12.16

[a] V magnitude where the completeness limit is reached.
[b] ΔV between the completeness limit and the dimmest star observed for that cluster.
[c] Distance, in arcmin, from the center of the cluster to the limit of our analysis (see text).

and NGC 6235, NGC 6342 and NGC 6355 in $V-I$), since the observed CMD of the cluster are not be calibrated in those colors, and a comparison with the Besançon models can lead to mistakes. In those cases, the only effect in the next steps of the analysis, which are not affected by any constant offset in the color calibration, is that the weights are not calculated using *eq.* 3.15, but $w = P(X = 1|r)w_{ph}$.

Once the probabilities to belong to the cluster have been calculated, we need to build the ridgeline for the CMDs of every cluster in our sample. We follow the three step recipe described in chapter 3 to obtain the ridgelines in the two available colors (see figures 4.5 and 4.6).

After that, we move the stars along the reddening vector until they intersect the ridgeline and smooth the resulting individual color excesses, obtaining an extinction map. From this map, we take the relative extinction that corresponds to every star observed. We then plot the CMD of the stars in our observation after having been corrected for the differential reddening and use it as the input for the next iteration.

Table 4.2. Parameters used to obtain and fit the King models

Cluster	r_c [a]	r_t [b]	k [c]	c_f [d]	c_B [e]
NGC 6121	0.83	32.49	2354.5	20.9	13.5
NGC 6144	0.94	33.25	642.0	11.6	30.1
NGC 6218	0.72	17.60	6055.3	2.5	7.3
NGC 6235	0.36	7.61	6857.1	59.1	80.9
NGC 6254	0.86	21.48	6758.8	4.4	12.3
NGC 6266	0.18	8.97	312264.7	226.4	216.6
NGC 6273	0.43	14.50	36115.27	155.1	153.1
NGC 6287	0.26	10.51	6907.5	55.	57.6
NGC 6304	0.21	13.25	43428.8	575.6	543.6
NGC 6333	0.58	8.16	16728.2	140.4	123.1
NGC 6342	0.05	14.86	43428.8	575.6	543.6
NGC 6352	0.83	10.51	3224.9	121.3	173.9
NGC 6355	0.05	15.18	161307.1	399.1	748.0
NGC 6397	0.05	15.81	1087398.2	46.1	35.2
NGC 6522	0.05	16.44	336785.0	918.8	1239.5
NGC 6541	0.30	29.60	47238.6	66.4	125.0
NGC 6553	0.55	8.16	5640.3	446.2	682.4
NGC 6558	0.03	10.44	360518.0	548.5	814.4
NGC 6624	0.06	20.55	218858.1	320.0	431.6
NGC 6626	0.24	11.27	61400.5	389.1	444.4
NGC 6637	0.34	8.35	9296.2	121.9	153.6
NGC 6642	0.10	10.07	5548.3	112.5	150.7
NGC 6656	1.42	28.97	4459.2	149.8	133.8
NGC 6681	0.03	7.91	1908674.5	103.3	118.6
NGC 6809	2.83	16.28	2086.6	5.0	18.9

[a] Core radius, in arcminutes, according to 2009 version of Harris catalog.
[b] Tidal radius, in arcminutes, according to 2009 version of Harris catalog.
[c] k constant, in stars per arcmin^2, from the King profile (see *eq*.3.8).
[d] Surface density of non-member field stars, in stars per arcmin^2, from the fit (see *eq*.3.8).
[e] Surface density of non-member field stars, in stars per arcmin^2, according to the Besançon model.

Table 4.3. Parameters used to obtain the Besançon model for the non-cluster stars in the observed fields.

NGC 6121	
Field of view	
Field	Small field
	l=350.97°; b=15.97°
	Solid angle=2.100 square degree
Extinction law	
Diffuse extinction	0.0 mag/kpc
Discrete clouds	A_v=1.30; Distance=0pc
Selection on	
Intervals of magnitude	$15.04 \leq B \leq 24.48$
	$14.56 \leq V \leq 22.58$
	$13.18 \leq I \leq 22.53$
Photometric errors	Error function: Exponential
	Band=B; A=0.006, B=21.75, C=0.861
	Band=V; A=0.006, B=22.24, C=0.901
	Band=I; A=0.007, B=23.66, C=0.997
NGC 6144	
Field of view	
Field	Small field
	l=351.93°; b=15.70°
	Solid angle=1.350 square degree
Extinction law	
Diffuse extinction	0.0 mag/kpc
Discrete clouds	A_v=1.88; Distance=0pc
Selection on	
Intervals of magnitude	$16.59 \leq B \leq 25.64$
	$16.05 \leq V \leq 24.13$
	$14.73 \leq I \leq 23.54$
Photometric errors	Error function: Exponential
	Band=B; A=0.005, B=23.11, C=0.864
	Band=V; A=0.005, B=24,35, C=0.938
	Band=I; A=0.009, B=25.36, C=1.043
NGC 6218	
Field of view	
Field	Small field
	l=15.72°; b=26.31°
	Solid angle=6.108 square degree
Extinction law	
Diffuse extinction	0.0 mag/kpc
Discrete clouds	A_v=0.67; Distance=0pc
Selection on	
Intervals of magnitude	$14.99 \leq B \leq 25.03$
	$14.75 \leq V \leq 23.52$
	$14.04 \leq I \leq 22.80$
Photometric errors	Error function: Exponential
	Band=B; A=0.004, B=22.20, C=0.838
	Band=V; A=0.003, B=21.25, C=0.803
	Band=I; A=0.004, B=23.20, C=0.940

continued on next page

continued from previous page

NGC 6235	
Field of view	
Field	Small field
	l=358.92°; b=13.52°
	Solid angle=0.610 square degree
Extinction law	
Diffuse extinction	0.0 mag/kpc
Discrete clouds	A_v=1.31; Distance=0pc
Selection on	
Intervals of magnitude	$17.14 \leq B \leq 26.09$
	$16.79 \leq V \leq 24.74$
	$15.70 \leq I \leq 24.05$
Photometric errors	Error function: Exponential
	Band=B; A=0.008, B=24.42, C=0.904
	Band=V; A=0.010, B=26.45, C=1.000
	Band=I; A=0.012, B=26,95, C=1.068
NGC 6254	
Field of view	
Field	Small field
	l=15.14°; b=23.08°
	Solid angle=3.910 square degree
Extinction law	
Diffuse extinction	0.0 mag/kpc
Discrete clouds	A_v=0.77; Distance=0pc
Selection on	
Intervals of magnitude	$15.50 \leq B \leq 25.29$
	$15.54 \leq V \leq 23.97$
	$14.78 \leq I \leq 23.37$
Photometric errors	Error function: Exponential
	Band=B; A=0.005, B=22.33, C=0.839
	Band=V; A=0.004, B=22.32, C=0.840
	Band=I; A=0.005, B=24.38, C=0.969
NGC 6266	
Field of view	
Field	Small field
	l=353.57°; b=7.32°
	Solid angle=0.190 square degree
Extinction law	
Diffuse extinction	0.0 mag/kpc
Discrete clouds	A_v=1.38; Distance=0pc
Selection on	
Intervals of magnitude	$15.75 \leq B \leq 25.14$
	$15.56 \leq V \leq 23.71$
	$14.75 \leq I \leq 22.44$
Photometric errors	Error function: Exponential
	Band=B; A=0.006, B=22.68, C=0.866
	Band=V; A=0.005, B=23.22, C=0.899
	Band=I; A=0.009, B=30.12, C=1.238
NGC 6273	
Field of view	
Field	Small field
	l=356.87°; b=9.38°
	Solid angle=0.280 square degree
Extinction law	
Diffuse extinction	0.0 mag/kpc
Discrete clouds	A_v=1.22; Distance=0pc
Selection on	
Intervals of magnitude	$16.38 \leq B \leq 25.59$
	$16.09 \leq V \leq 24.08$
	$15.46 \leq I \leq 23.09$
Photometric errors	Error function: Exponential
	Band=B; A=0.007, B=21.67, C=0.820
	Band=V; A=0.007, B=22.70, C=0.873
	Band=I; A=0.010, B=24.54, C=1.002

continued on next page

continued from previous page

NGC 6287	
Field of view	
Field	Small field
	l=0.13°; b=11.02°
	Solid angle=0.600 square degree
Extinction law	
Diffuse extinction	0.0 mag/kpc
Discrete clouds	A_v=2.08; Distance=0pc
Selection on	
Intervals of magnitude	$16.77 \leq B \leq 25.46$
	$16.05 \leq V \leq 24.11$
	$14.66 \leq I \leq 23.37$
Photometric errors	Error function: Exponential
	Band=B; A=0.004, B=23.65, C=0.890
	Band=V; A=0.007, B=25.91, C=0.998
	Band=I; A=0.007, B=26.72, C=1.088
NGC 6304	
Field of view	
Field	Small field
	l=355.83°; b=5.38°
	Solid angle=0.064 square degree
Extinction law	
Diffuse extinction	0.0 mag/kpc
Discrete clouds	A_v=1.80; Distance=0pc
Selection on	
Intervals of magnitude	$17.45 \leq B \leq 25.87$
	$16.78 \leq V \leq 24.56$
	$15.34 \leq I \leq 23.80$
Photometric errors	Error function: Exponential
	Band=B; A=0.005, B=22.25, C=0.826
	Band=V; A=0.010, B=26.91, C=1.019
	Band=I; A=0.010, B=26.82, C=1.084
NGC 6333	
Field of view	
Field	Small field
	l=5.54°; b=10.70°
	Solid angle=0.380 square degree
Extinction law	
Diffuse extinction	0.0 mag/kpc
Discrete clouds	A_v=1.18; Distance=0pc
Selection on	
Intervals of magnitude	$16.04 \leq B \leq 26.11$
	$15.41 \leq V \leq 24.50$
	$14.50 \leq I \leq 23.54$
Photometric errors	Error function: Exponential
	Band=B; A=0.006, B=22.93, C=0.844
	Band=V; A=0.006, B=23.22, C=0.882
	Band=I; A=0.015, B=29.32, C=1.192
NGC 6342	
Field of view	
Field	Small field
	l=4.90°; b=9.73°
	Solid angle=0.290 square degree
Extinction law	
Diffuse extinction	0.0 mag/kpc
Discrete clouds	A_v=1.64; Distance=0pc
Selection on	
Intervals of magnitude	$16.95 \leq B \leq 26.11$
	$16.31 \leq V \leq 24.73$
	$15.12 \leq I \leq 23.44$
Photometric errors	Error function: Exponential
	Band=B; A=0.006, B=24.15, C=0.890
	Band=V; A=0.007, B=25.10, C=0.956
	Band=I; A=0.012, B=27.68, C=1.113

continued on next page

continued from previous page

NGC 6352	
Field of view	
Field	Small field
	l=341.42°; b=−7.17°
	Solid angle=0.290 square degree
Extinction law	
Diffuse extinction	0.0 mag/kpc
Discrete clouds	A_v=0.94; Distance=0pc
Selection on	
Intervals of magnitude	$15.72 \leq B \leq 25.32$
	$15.18 \leq V \leq 24.20$
	$14.53 \leq I \leq 23.52$
Photometric errors	Error function: Exponential
	Band=B; A=0.005, B=22.31, C=0.837
	Band=V; A=0.006, B=24.13, C=0.915
	Band=I; A=0.008, B=25.71, C=1.033
NGC 6355	
Field of view	
Field	Small field
	l=359.58°; b=5.43°
	Solid angle=0.064 square degree
Extinction law	
Diffuse extinction	0.0 mag/kpc
Discrete clouds	A_v=2.26; Distance=0pc
Selection on	
Intervals of magnitude	$16.55 \leq B \leq 25.83$
	$15.50 \leq V \leq 24.20$
	$14.03 \leq I \leq 23.21$
Photometric errors	Error function: Exponential
	Band=B; A=0.004, B=23.31, C=0.864
	Band=V; A=0.004, B=22.92, C=0.869
	Band=I; A=0.005, B=24.39, C=0.992
NGC 6397	
Field of view	
Field	Small field
	l=338.17°; b=−11.96°
	Solid angle=1.110 square degree
Extinction law	
Diffuse extinction	0.0 mag/kpc
Discrete clouds	A_v=0.54; Distance=0pc
Selection on	
Intervals of magnitude	$13.26 \leq B \leq 24.53$
	$13.08 \leq V \leq 22.74$
	$12.77 \leq I \leq 22.82$
Photometric errors	Error function: Exponential
	Band=B; A=0.005, B=21.61, C=0.849
	Band=V; A=0.004, B=21.13, C=0.838
	Band=I; A=0.009, B=26.54, C=1.121
NGC 6522	
Field of view	
Field	Small field
	l=1.02°; b=−3.93°
	Solid angle=0.064 square degree
Extinction law	
Diffuse extinction	0.0 mag/kpc
Discrete clouds	A_v=1.61; Distance=0pc
Selection on	
Intervals of magnitude	$16.65 \leq B \leq 25.79$
	$16.23 \leq V \leq 24.47$
	$14.98 \leq I \leq 22.91$
Photometric errors	Error function: Exponential
	Band=B; A=0.006, B=21.53, C=0.796
	Band=V; A=0.008, B=22.16, C=0.840
	Band=I; A=0.014, B=25.32, C=1.032

continued on next page

continued from previous page

NGC 6541	
Field of view	
Field	Small field
	l=349.48°; b=−11.09°
	Solid angle=0.450 square degree
Extinction law	
Diffuse extinction	0.0 mag/kpc
Discrete clouds	A_v=0.63; Distance=0pc
Selection on	
Intervals of magnitude	$15.53 \leq B \leq 25.53$
	$15.18 \leq V \leq 24.30$
	$14.64 \leq I \leq 23.41$
Photometric errors	Error function: Exponential
	Band=B; A=0.006, B=22.55, C=0.841
	Band=V; A=0.005, B=22.44, C=0.848
	Band=I; A=0.005, B=22.51, C=0.898
NGC 6553	
Field of view	
Field	Small field
	l=5.25°; b=−3.03°
	Solid angle=0.064 square degree
Extinction law	
Diffuse extinction	0.0 mag/kpc
Discrete clouds	A_v=2.76; Distance=0pc
Selection on	
Intervals of magnitude	$17.08 \leq B \leq 25.31$
	$16.21 \leq V \leq 23.86$
	$14.71 \leq I \leq 22.48$
Photometric errors	Error function: Exponential
	Band=B; A=0.004, B=22.80, C=0.848
	Band=V; A=0.006, B=26.89, C=1.041
	Band=I; A=0.007, B=26.60, C=1.102
NGC 6558	
Field of view	
Field	Small field
	l=0.20°; b=−6.02°
	Solid angle=0.064 square degree
Extinction law	
Diffuse extinction	0.0 mag/kpc
Discrete clouds	A_v=1.21; Distance=0pc
Selection on	
Intervals of magnitude	$16.64 \leq B \leq 26.26$
	$15.92 \leq V \leq 24.61$
	$15.17 \leq I \leq 23.23$
Photometric errors	Error function: Exponential
	Band=B; A=0.005, B=22.21, C=0.823
	Band=V; A=0.007, B=22.81, C=0.858
	Band=I; A=0.008, B=24.07, C=0.968
NGC 6624	
Field of view	
Field	Small field
	l=2.79°; b=−7.91°
	Solid angle=0.064 square degree
Extinction law	
Diffuse extinction	0.0 mag/kpc
Discrete clouds	A_v=0.94; Distance=0pc
Selection on	
Intervals of magnitude	$16.30 \leq B \leq 25.44$
	$15.87 \leq V \leq 24.25$
	$14.73 \leq I \leq 23.31$
Photometric errors	Error function: Exponential
	Band=B; A=0.005, B=22.26, C=0.842
	Band=V; A=0.005, B=22.86, C=0.871
	Band=I; A=0.007, B=23.60, C=0.956

continued on next page

continued from previous page

NGC 6626	
Field of view	
Field	Small field
	l=7.80°; b=−5.58°
	Solid angle=0.064 square degree
Extinction law	
Diffuse extinction	0.0 mag/kpc
Discrete clouds	A_v=1.50; Distance=0pc
Selection on	
Intervals of magnitude	$16.33 \leq B \leq 25.36$
	$15.67 \leq V \leq 23.69$
	$14.63 \leq I \leq 22.79$
Photometric errors	Error function: Exponential
	Band=B; A=0.003, B=21.36, C=0.801
	Band=V; A=0.005, B=22.78, C=0.874
	Band=I; A=0.006, B=23.20, C=0.961
NGC 6637	
Field of view	
Field	Small field
	l=1.72°; b=−10.27°
	Solid angle=0.270 square degree
Extinction law	
Diffuse extinction	0.0 mag/kpc
Discrete clouds	A_v=0.68; Distance=0pc
Selection on	
Intervals of magnitude	$15.30 \leq B \leq 24.66$
	$14.76 \leq V \leq 23.16$
	$14.09 \leq I \leq 22.53$
Photometric errors	Error function: Exponential
	Band=B; A=0.004, B=22.40, C=0.861
	Band=V; A=0.003, B=21.74, C=0.852
	Band=I; A=0.004, B=23.30, C=0.956
NGC 6642	
Field of view	
Field	Small field
	l=9.81°; b=−6.44°
	Solid angle=0.194 square degree
Extinction law	
Diffuse extinction	0.0 mag/kpc
Discrete clouds	A_v=1.28; Distance=0pc
Selection on	
Intervals of magnitude	$13.96 \leq B \leq 23.38$
	$13.47 \leq V \leq 21.95$
	$12.29 \leq I \leq 20.73$
Photometric errors	Error function: Exponential
	Band=B; A=0.002, B=21.83, C=0.874
	Band=V; A=0.003, B=22.85, C=0.941
	Band=I; A=0.002, B=20.68, C=0.917

continued on next page

continued from previous page

NGC 6656	
Field of view	
Field	Small field
	l=9.89°; b=−7.55°
	Solid angle=0.190 square degree
Extinction law	
Diffuse extinction	0.0 mag/kpc
Discrete clouds	A_v=1.05; Distance=0pc
Selection on	
Intervals of magnitude	$14.69 \leq B \leq 24.35$
	$14.30 \leq V \leq 23.19$
	$13.42 \leq I \leq 22.01$
Photometric errors	Error function: Exponential
	Band=B; A=0.006, B=21.32, C=0.847
	Band=V; A=0.006, B=22.88, C=0.904
	Band=I; A=0.008, B=24.26, C=1.018
NGC 6681	
Field of view	
Field	Small field
	l=2.85°; b=−12.51°
	Solid angle=0.400 square degree
Extinction law	
Diffuse extinction	0.0 mag/kpc
Discrete clouds	A_v=0.56; Distance=0pc
Selection on	
Intervals of magnitude	$15.90 \leq B \leq 25.17$
	$15.43 \leq V \leq 24.17$
	$14.74 \leq I \leq 23.98$
Photometric errors	Error function: Exponential
	Band=B; A=0.004, B=22.00, C=0.826
	Band=V; A=0.006, B=23.99, C=0.914
	Band=I; A=0.007, B=24.79, C=0.980
NGC 6809	
Field of view	
Field	Small field
	l=8.80°; b=−23.27°
	Solid angle=2.950 square degree
Extinction law	
Diffuse extinction	0.0 mag/kpc
Discrete clouds	A_v=0.24; Distance=0pc
Selection on	
Intervals of magnitude	$14.65 \leq B \leq 25.15$
	$14.46 \leq V \leq 23.87$
	$14.19 \leq I \leq 23.03$
Photometric errors	Error function: Exponential
	Band=B; A=0.007, B=21.42, C=0.826
	Band=V; A=0.006, B=21.74, C=0.842
	Band=I; A=0.009, B=22.33, C=0.909

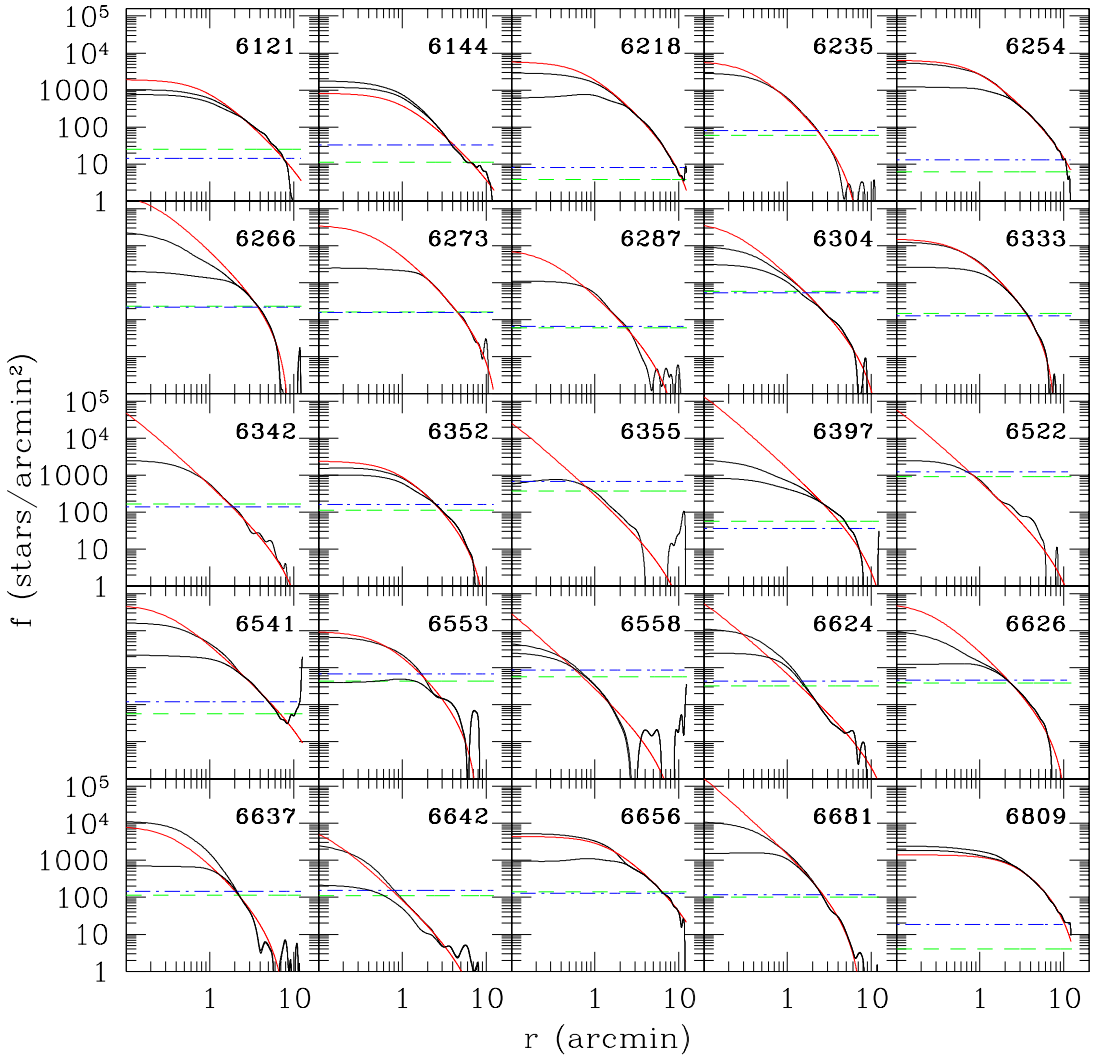

Figure 4.1. Radial surface density profile of the stars in the cluster from the observations (black) and from fitting a King profile (red), once the constant non-member field component has been substracted. The straight green dashed line show the non-member field component according to the fit. The straight blue dot-dashed line, showing the non-member field component according to the Besançon model, is plot for comparison. The general disagreement in the inner regions between observation and models is due to the lower completeness of these regions due to crowding effects.

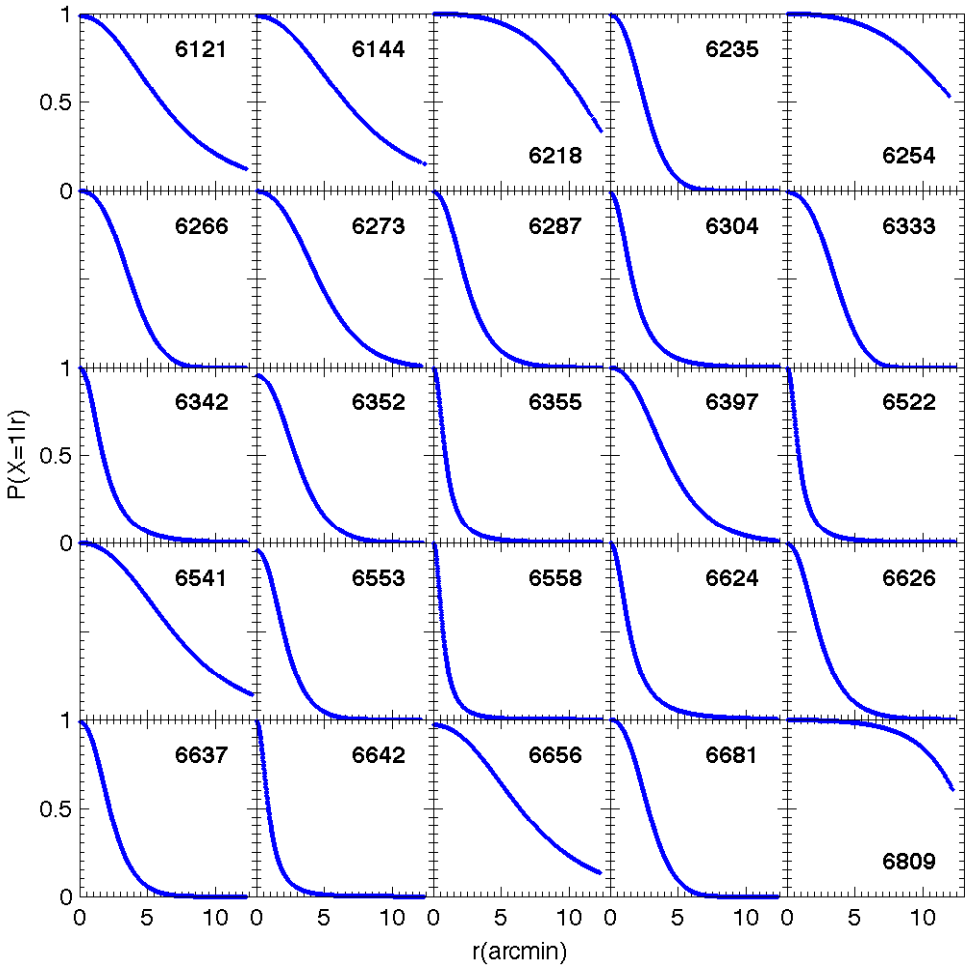

Figure 4.2. Probability to belong to the cluster as a function of distance to the center of the cluster, $P(X = 1|r)$. Notice that we restrict our analysis to distances smaller than the distance where this probability drop to 0.1

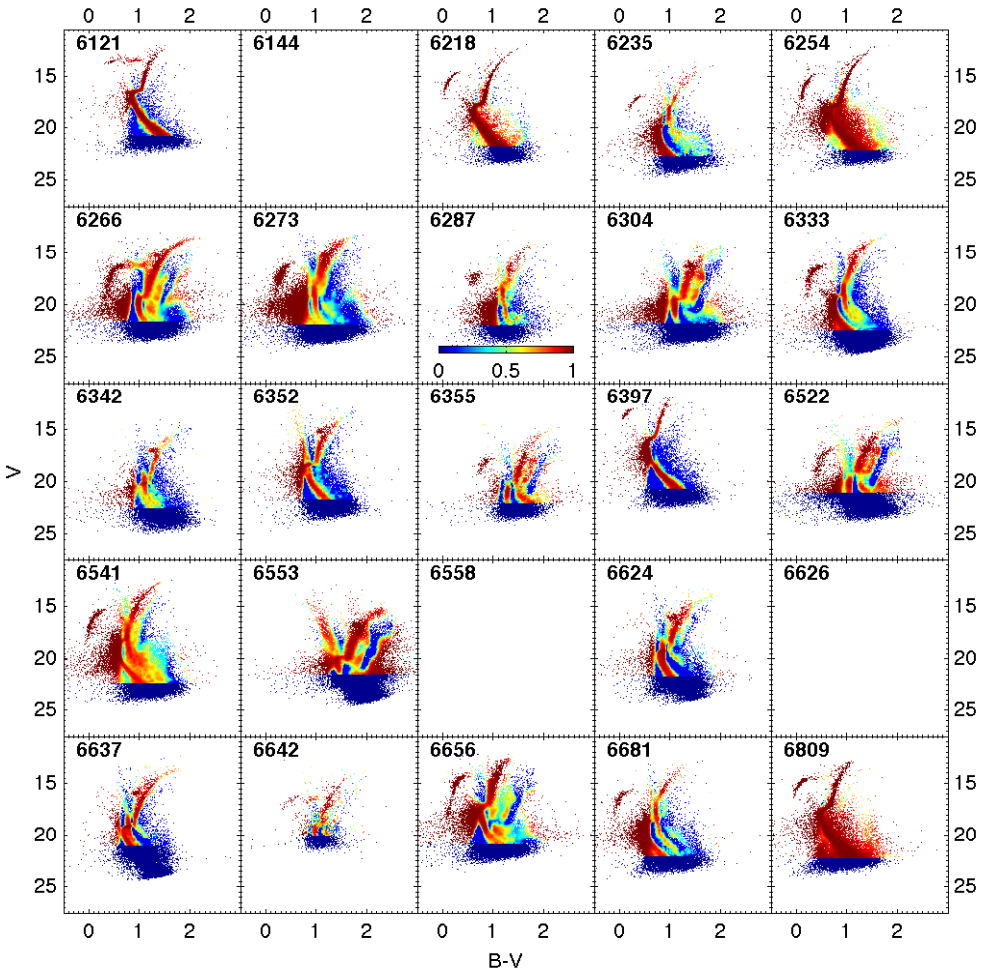

Figure 4.3. Probability to belong to the cluster as a function of magnitude V and color $(B-V)$, $P(X=1|B-V,V)$. The color code gives the different color excesses $P(X=1|c,m)$. Notice that we restrict our analysis to stars brighter than the completeness limit shown in table 4.1. NGC 6144, NGC 6558 and NGC 6626 are not included in this analysis because their CMDs have not been calibrated in this color (see table 2.5).

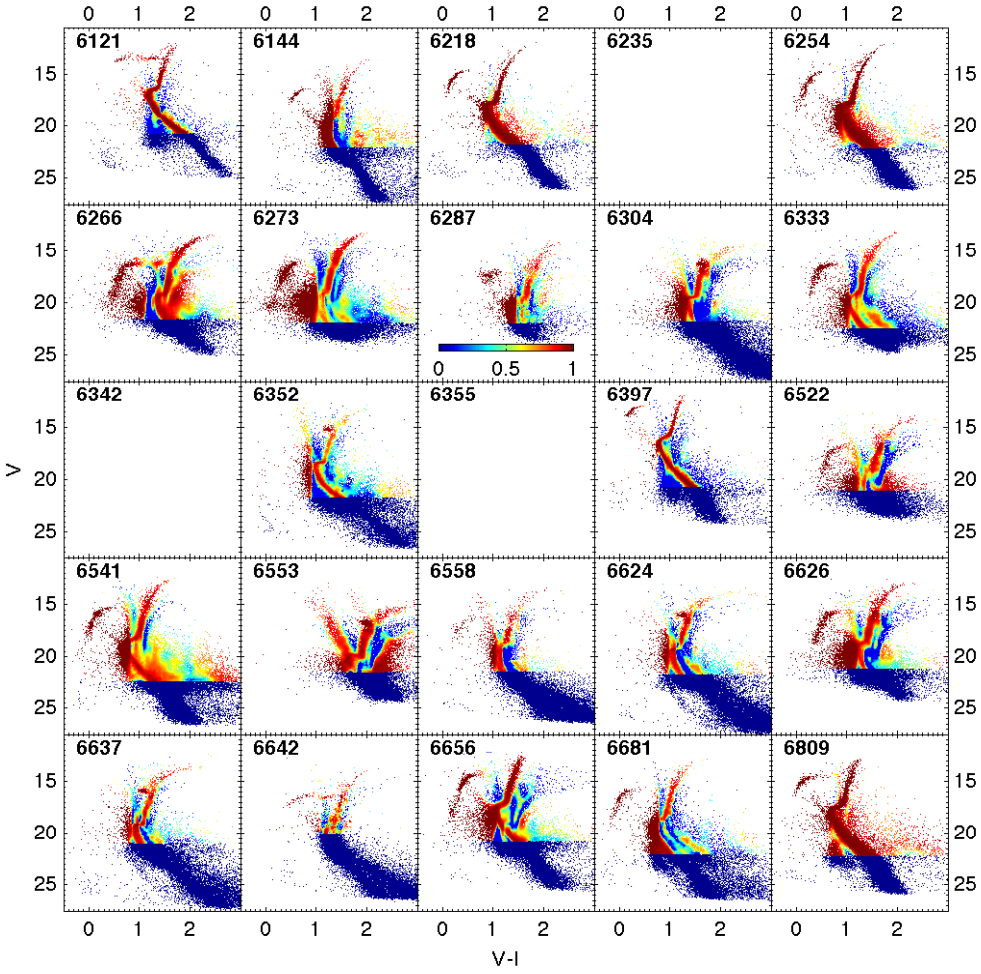

Figure 4.4. Probability to belong to the cluster as a function of magnitude V and color $(V-I)$, $P(X=1|V-I,V)$. The color code gives the different color excesses $P(X=1|c,m)$. Notice that we restrict our analysis to stars brighter than the completeness limit shown in table 4.1. NGC 6235, NGC 6342 and NGC 6355 are not included in this analysis because their CMDs have not been calibrated in this color (see table 2.5).

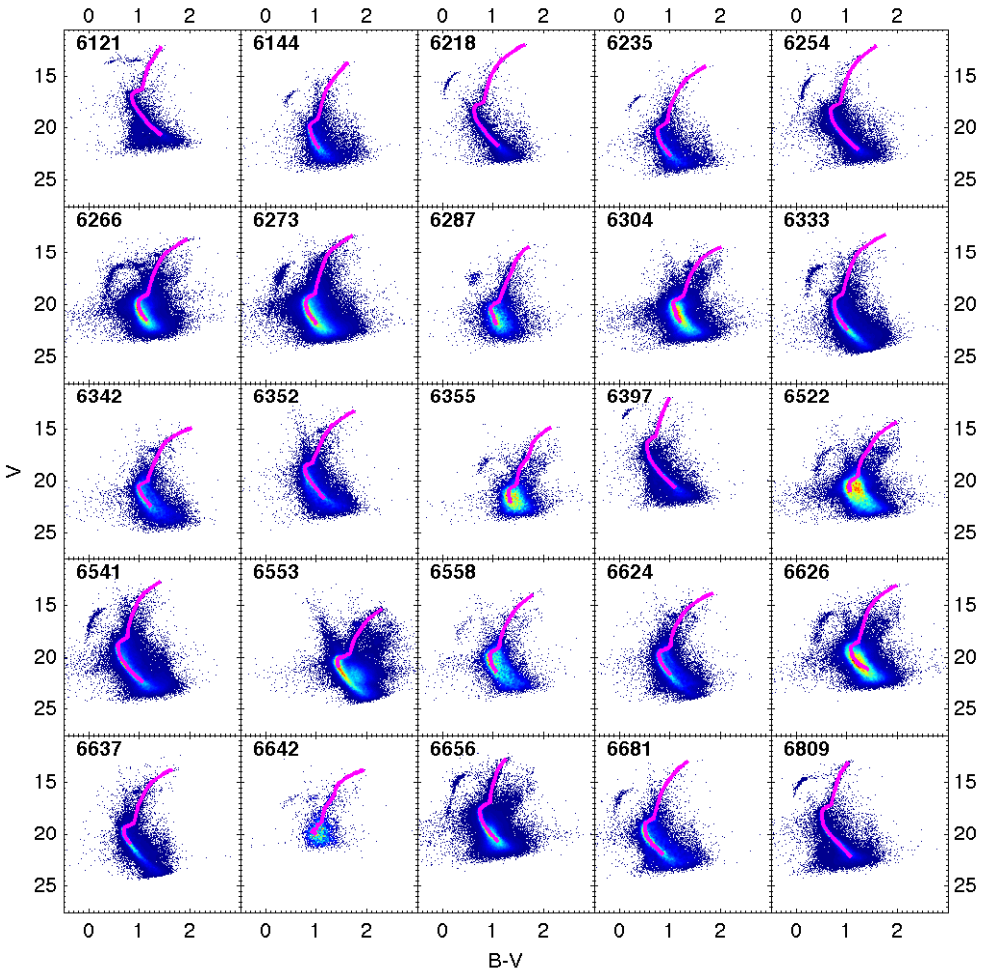

Figure 4.5. Ridgelines in the V vs. $(B-V)$ CMDs for the clusters in the sample, down to the completeness limit.

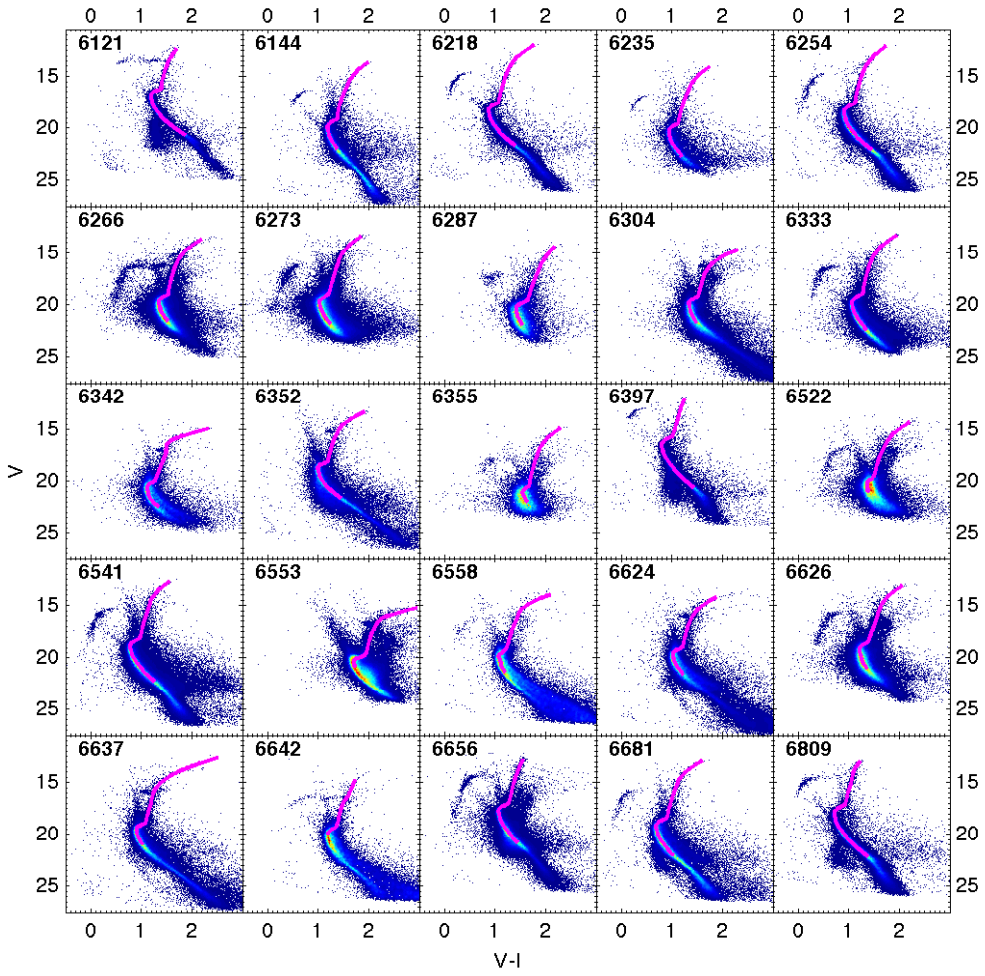

Figure 4.6. Ridgelines in the V vs. $(V-I)$ CMDs for the clusters in the sample, down to the completeness limit.

Finally, after the process converges for both colors, we average the extinction maps obtained from both colors, generating a final extinction map (e.g. figures 4.9, 4.11, 4.13), and also generating the dereddened CMDs (e.g. figures 4.8, 4.10, 4.12).

We describe now in more detail the individual cases of the different clusters in the sample. We show their CMDs, before and after being differentially dereddened, and describe any improvements. Notice that the CMDs are plotted using the merged space and ground photometries, whenever space based observations deeper than ground based observations exist, or the ground photometries in the rest of the cases. To check for improvements in the definition (decrease in the thickness) of the evolutionary sequences in the CMD, we fit Gaussian functions to the distributions of stars in color for given magnitude cuts (see figure 4.7) in the different sequences (1.5 mag above and 0.5 mag below the TO, this is, RGB and upper MS) around .

We also present the extinction maps across the field of the clusters, along their resolution and precision. We compare these maps with the SFD extinction maps. Notice that the extinction maps provided by our dereddening technique give the differential extinction in the field referred to the unknown extinction where our ridgelines lie. The comparison with the SFD maps is one of the methods that allows us to establish these absolute extinction zero-points. In order to make the comparison, we need to degrade our extinction maps to the lower resolution of the SFD maps. Since our extinction maps are described by non-parametric continuous functions, we evaluate these functions in ~ 1600 different points in every 'pixel' of the SFD maps and average the obtained values using our precision maps to calculate a weighted average that provide us with one extinction value per SFD pixel. We observe that both our maps and the SFD maps generally agree in identifying the same regions of higher and lower extinction, although our maps usually show higher variation (reaching sometimes a factor of 2) in the extinction values than the SFD maps. Whenever possible, we also compare our maps with other extinction maps available in the literature. The agreement in the few cases where these comparisons are possible is also very good.

NGC 6121 - M 4 (figures 4.8 and 4.9). The field studied in this cluster is the entire IMACS FOV. The changes in the extinction across the field are moderate

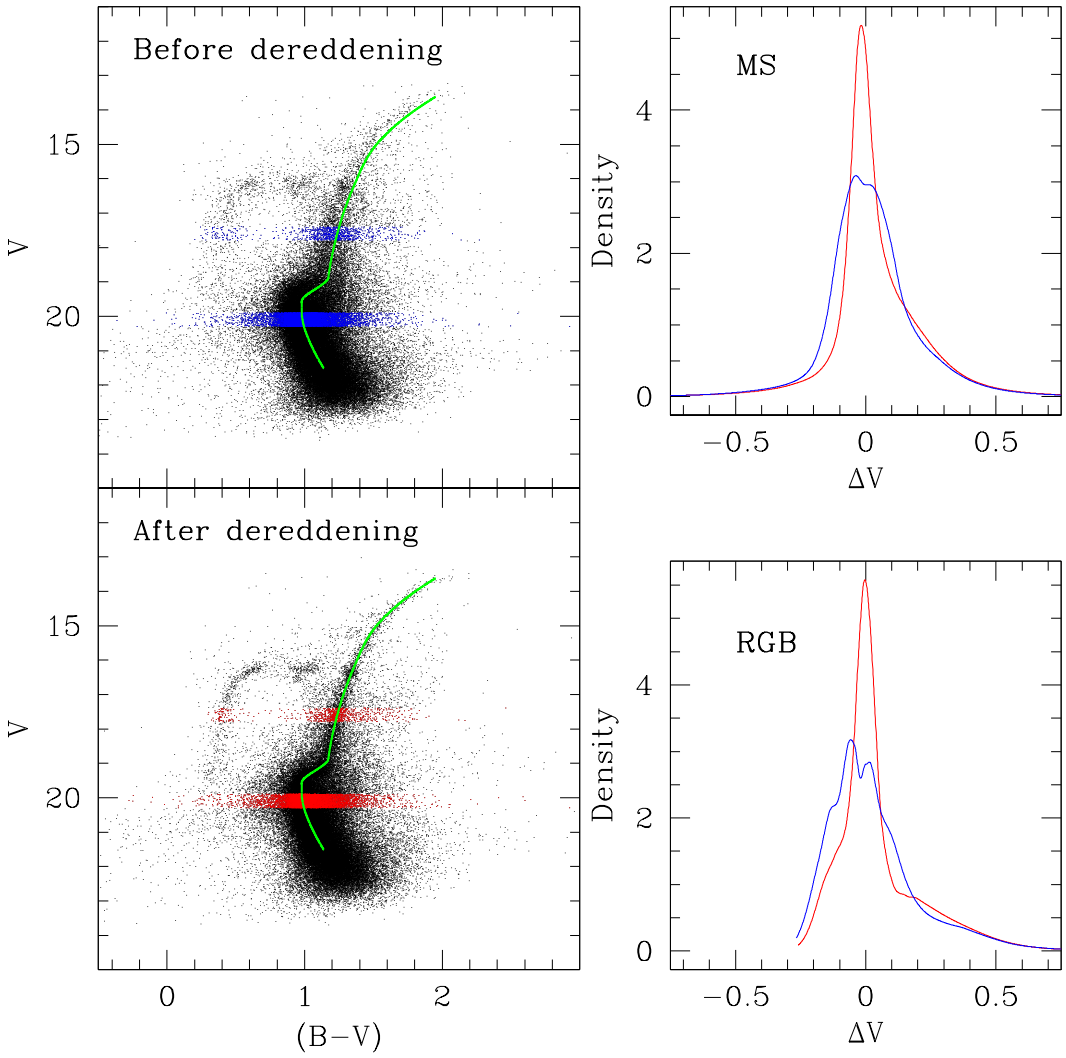

Figure 4.7. Distribution of stars in color (V-I) around the calculated ridgeline for two different magnitude cuts (1.5 mag above and 0.5 mag below the TO) for the stars in M 62, before (blue) and after (red) differentially deredden the CMD.

($\Delta E(B-V) = 0.15$). The highest extinction is located in the northeastern region of the field, while the northwestern region of the field shows the lowest. It is significant the small blob of higher extinction ($\Delta E(B-V) \sim 0.05$) ~ 0.02 deg south of the center of the cluster. The definition of the different branches in the CMD of the cluster are improved after the dereddening process, especially in the $V-I$ CMD. The upper MS and RGB get $\sim 40\%$ thinner in $V-I$, a little less in $B-V$. The absolute extinction of our zero-point reddening map is $E(B-V) = 0.50$ from comparing our map with the SFD map, which fail to show the blob of higher extinction close to the center of the cluster.

NGC 6144 (figures 4.10 and 4.11). The field studied in this cluster is the entire IMACS FOV. The variation of the extinction across the field is one of the highest shown in our sample ($\Delta E(B-V) = 0.6$). Extinction is higher in the northern region, ~ 0.1 deg from the center of the cluster, of the observed field, and peaks in the northwestern area. We can observed the different evolutionary sequences better defined in the CMD of the cluster after applying the dereddening process. The upper MS and RGB get $\sim 40\%$ thinner in $V-I$, a little less in $B-V$. The absolute extinction of our zero-point reddening map is $E(B-V) = 0.74$ from comparing our map with the SFD map. This is one of the few cases in which the differential extinction variation across the field are more important (by a factor of 2) in the SFD maps than in ours.

NGC 6218 - M 12 (figures 4.12 and 4.13). The field studied in this cluster is the entire IMACS FOV. The differential extinction across the field of this cluster is very mild ($\Delta E(B-V) \sim 0.05$). Extinction is higher in the northern region (~ 0.1 deg of the cluster center). The square structure observed close to the center is largely due to the merging of the space and ground photometries. The upper MS and RGB get $\sim 25\%$ thinner in $V-I$, a little less in $B-V$. Some of the CMD features, like the RGB (Thompson) bump are more clearly visible now. The absolute extinction of our zero-point reddening map is $E(B-V) = 0.18$ from comparing with SFD map.

NGC 6235 (figures 4.14 and 4.15). The field studied in for this cluster reach only stars located less than $4.56'$ away from the cluster center, due to the high number

of field stars relative to the GC stars. The changes in the extinction across the field are moderate ($\Delta E(B-V) \sim 0.1$), being the southwestern area of the field the region of highest extinction. The upper MS and RGB get $\sim 20\%$ thinner after being differentially dereddened. The absolute extinction of our zero-point reddening map is $E(B-V) = 0.40$ from comparing our map with the SFD map.

NGC 6254 - M 10 (figures 4.16 and 4.17). The field studied in this cluster is the entire IMACS FOV. The extinction variation across the field of this cluster is mild ($\Delta E(B-V) \sim 0.05$). Extinction is higher towards the west, peaking close ($\sim 0.02\,\mathrm{deg}$) to the cluster center. The upper MS and RGB get $\sim 20\%$ thinner after being differentially dereddened, making also features like the RGB bump more clearly visible now. The absolute extinction of our zero-point reddening map is $E(B-V) = 0.29$ from comparing our map with the SFD map.

NGC 6266 - M 62 (figures 4.18 and 4.19). The field studied in this cluster is restricted to the inner $6.07'$ of the cluster, due to the number of field stars. A band of material causing a significant increase in extinction ($\Delta E(B-V) \sim 0.25$) crosses the field in the east-west direction less than $0.02\,\mathrm{deg}$ south of the center of the cluster. The definition of the different branches in the CMD of the cluster is highly improved after the dereddening process. The upper MS and RGB get thinner by a factor of 2, and now the presence of an EBHB is clearly visible and the location of the RGB bump is more easily identifiable. The absolute extinction of our zero-point reddening map is $E(B-V) = 0.47$ from comparing our map with the SFD map. In the SFD map the presence of this band of extinction is not so clear.

NGC 6273 - M 19 (figures 4.20 and 4.21). The field studied in this cluster is restricted to the inner $8.37'$ of the cluster, due to the number of field stars. The changes in the extinction across the field are significant ($\Delta E(B-V) \sim 0.3$). Extinction is higher towards the west, and peaks in a small region located very close, less than $0.02\,\mathrm{deg}$, of the center of the cluster. The definition of the different branches in the CMD of the cluster is highly improved after the dereddening process. The upper MS and RGB get $\sim 40\%$ thinner after being differentially dereddened, and now the presence of an EBHB is clearly visible and the location of the RGB bump is

more easily identifiable. The absolute extinction of our zero-point reddening map is $E(B-V) = 0.30$ from comparing our map with the SFD map.

NGC 6287 (figures 4.22 and 4.23). The field studied in this cluster is restricted to the inner $4.89'$ of the cluster due to the number of field stars. The variation of the extinction across the field is one of the highest shown in our sample ($\Delta E(B-V) = 0.7$). Extinction is higher in the northern region. A narrow band of material causing the highest extinction in the field crosses it in the east-west direction less than 0.02 deg of the center of the cluster. The definition of the different branches in the CMD of the cluster is highly improved after the dereddening process. Now the RGB and SGB are easily identifiable, which was not the case before applying the dereddening technique. The upper MS and RGB get thinner by a factor of 2. The absolute extinction of our zero-point reddening map is $E(B-V) = 0.64$ from comparing our map with SFD map.

NGC 6304 (figures 4.24 and 4.25). The field studied in this cluster reaches only stars with distances less than $3.90'$ away from the cluster center, due to the number of field stars. The variation of the extinction across the field is moderate ($\Delta E(B-V) = 0.15$). The area located ~ 0.05 deg west of the center of the cluster is the region of highest extinction. The upper MS and RGB get $\sim 20\%$ thinner after being differentially dereddened. The absolute extinction of our zero-point reddening map is $E(B-V) = 0.51$ from comparing our map with the SFD map.

NGC 6333 -M 9 (figures 4.26 and 4.27). The field studied in this cluster is restricted to the inner $5.70'$ of the cluster due to the number of field stars. The changes in the extinction across the field are significant ($\Delta E(B-V) \sim 0.25$). The area located ~ 0.1 deg southeast of the center of the cluster is the region of highest extinction. The upper MS and RGB get $\sim 35\%$ thinner after being differentially dereddened. The absolute extinction of our zero-point reddening map is $E(B-V) = 0.41$ from comparing our map with the SFD map.

NGC 6342 (figures 4.28 and 4.29). The field studied in this cluster reach only stars with distances less than $4.17'$ away from the cluster center, due to the number of field stars. The changes in the extinction across the field are significant ($\Delta E(B-V) \sim$

0.4). The northeastern quadrant of the field, reaching the projected position of the center of the cluster, is the region of highest extinction. The definition of the different branches in the CMD of the cluster is highly improved after the dereddening process. Now the RGB and SGB are easily identifiable, which was not the case before applying the dereddening technique. The upper MS and RGB get $\sim 60\%$ thinner after being differentially dereddened. The absolute extinction of our zero-point reddening map is $E(B-V) = 0.59$ from comparing our map with the SFD map.

NGC 6352 (figures 4.30 and 4.31). The field studied in this cluster is restricted to the inner $5.65'$ of the cluster due to the number of field stars. The differential extinction variation across the field of this cluster is only moderate ($\Delta E(B-V) \sim 0.15$). Extinction is higher in the northern region of the analyzed field. The upper MS and RGB get $\sim 30\%$ thinner after being differentially dereddened. The absolute extinction of our zero-point reddening map is $E(B-V) = 0.34$ from comparing our map with the SFD map.

NGC 6355 (figures 4.32 and 4.33). The field studied in this cluster is restricted to the inner $2.39'$ of the cluster due to the number of field stars. The changes in the extinction across the field are significant ($\Delta E(B-V) \sim 0.3$). The area located $\sim 0.05\,\mathrm{deg}$ southeast of the center of the cluster is the region of highest extinction. The improvement of the CMD of this cluster is only marginal. The absolute extinction of our zero-point reddening map is $E(B-V) = 1.18$ from comparing our map with the SFD map.

NGC 6397 (figures 4.34 and 4.35). The field studied in this cluster is restricted to the inner $8.06'$ of the cluster due to the number of field stars. The differential extinction in this cluster is only mild ($\Delta E(B-V) \sim 0.05$. Extinction is not especially concentrated in any area of the field. The upper MS and RGB get $\sim 15\%$ thinner after being differentially dereddened in $V-I$, a little less in $B-V$. The absolute extinction of our zero-point reddening map is $E(B-V) = 0.18$ from comparing our map with the SFD map.

NGC 6522 (figures 4.36 and 4.37). The high number of non-cluster member stars restricts the study of this field to stars closer than $2.34'$ from the cluster center.

The differential extinction variation in this cluster is moderated ($\Delta E(B-V) = 0.1$). Extinction is higher in the southwestern region of the analyzed field. The improvement of the CMD of this cluster is only marginal. The absolute extinction of our zero-point reddening map is $E(B-V) = 0.59$ from comparing our map with SFD map.

NGC 6541 (figures 4.38 and 4.39). The field studied in this cluster is the entire IMACS FOV. The differential extinction in this cluster is moderate ($\Delta E(B-V) \sim 0.1$). Extinction is not especially concentrated in any area of the field, although there seems to be an increase in the very southwest corner of the observed field. The upper MS and RGB get $\sim 10\%$ thinner after being differentially dereddened. The absolute extinction of our zero-point reddening map is $E(B-V) = 0.16$ from comparing our map with the SFD map.

NGC 6553 (figures 4.40 and 4.41). The field studied in this cluster is restricted to the inner $4.07'$ of the cluster due to the number of field stars. There are significant changes in the extinction across the field ($\Delta E(B-V) \sim 0.25$). In our maps, the highest extinction is located in the northern region of the field, while the southeastern region of the field shows the lowest, which is not the trend shown in the SFD maps. The upper MS and RGB get $\sim 20\%$ thinner after being differentially dereddened, and the RGB bump now is more clearly identifiable. The absolute extinction of our zero-point reddening map is $E(B-V) = 1.38$ from comparing our map with the SFD map.

NGC 6558 (figures 4.42 and 4.43). The high number of non-cluster member stars restricts the study of this field to stars closer than $1.84'$ from the cluster center. The extinction variations in this cluster is significant ($\Delta E(B-V) \sim 0.2$). Extinction is a little higher in the south area of the field. The upper MS and RGB get $\sim 15\%$ thinner after being differentially dereddened. The absolute extinction of our zero-point reddening map is $E(B-V) = 0.41$ from comparing our map with the SFD map.

NGC 6624 (figures 4.44 and 4.45). The field studied in this cluster is restricted to the inner $3.76'$ of the cluster due to the number of field stars. The differential

extinction across the field is moderate ($\Delta E(B-V) \sim 0.15$). Extinction is higher in the southwestern region of the analyzed field. The improvement of the CMD of this cluster is only marginal. The absolute extinction of our zero-point reddening map is $E(B-V) = 0.25$ from comparing our map with the SFD map.

NGC 6626 - M 28 (figures 4.46 and 4.47). The field studied in this cluster is restricted to the inner $4.94'$ of the cluster due to the number of field stars. The extinction variations across the field of this cluster is significant ($\Delta E(B-V) \sim 0.2$). Extinction is lower at the projected center and southeastern region of the observed field, which is not the trend observed in the SFD maps. The upper MS and RGB get $\sim 25\%$ thinner after being differentially dereddened in $V-I$, a little less in $B-V$. The absolute extinction of our zero-point reddening map is $E(B-V) = 0.47$ from comparing our map with the SFD map.

NGC 6637 - M 69 (figures 4.48 and 4.49). The field studied in this cluster is restricted to the inner $4.34'$ of the cluster due to the number of field stars. The differential extinction across most of the observed field is moderate ($\Delta E(B-V) \sim 0.1$). Extinction is higher in the northeastern region of the observed field, which is not the trend observed in the SFD maps. The improvement of the CMD of this cluster is only marginal. The absolute extinction of our zero-point reddening map is $E(B-V) = 0.17$ from comparing our map with the SFD map.

NGC 6642 (figures 4.50 and 4.51). The high number of non-cluster member stars restricts the study of this field to stars closer than $2.25'$ from the cluster center. The differential extinction across most of the observed field is moderate ($\Delta E(B-V) \sim 0.1$). The improvement of the CMD of this cluster is only marginal. The absolute extinction of our zero-point reddening map is $E(B-V) = 0.40$ from comparing our map with the SFD map.

NGC 6656 - M 22 (figures 4.52 and 4.53). The field studied in this cluster is the entire IMACS FOV. The extinction variation across the field of this cluster is moderate ($\Delta E(B-V) \sim 0.15$. Extinction is lower in the southern area of the field, although a small region of a little higher relative extinction is located close (< 0.02 deg south) of the center of the cluster ($\Delta E(B-V) < 0.05$). The upper MS and RGB

get $\sim 30\%$ thinner in the $V-I$, a little less in $B-V$. The absolute extinction of our zero-point reddening map is $E(B-V)=0.34$ from comparing our map with the SFD map.

NGC 6681 - M 70 (figures 4.54 and 4.55). The field studied in this cluster is restricted to the inner $4.90'$ of the cluster due to the number of field stars. The differential extinction across most of the observed field is mild ($\Delta E(B-V) \sim 0.05$). Extinction is not especially concentrated in any area of the field. The improvement of the CMD of this cluster is only marginal. The absolute extinction of our zero-point reddening map is $E(B-V)=0.09$ from comparing our map with the SFD map.

NGC 6809 - M55 (figures 4.56 and 4.57). The field studied in this cluster is the entire IMACS FOV. The extinction variation across the field of this cluster is only mild ($\Delta E(B-V) \sim 0.05$). Extinction is higher in the northeastern area of the observed field. The upper MS and RGB get $\sim 10\%$ thinner after being differentially dereddened. The improvement of the CMD of this cluster is only marginal. The absolute extinction of our zero-point reddening map is $E(B-V)=0.14$ from comparing our map with the SFD map.

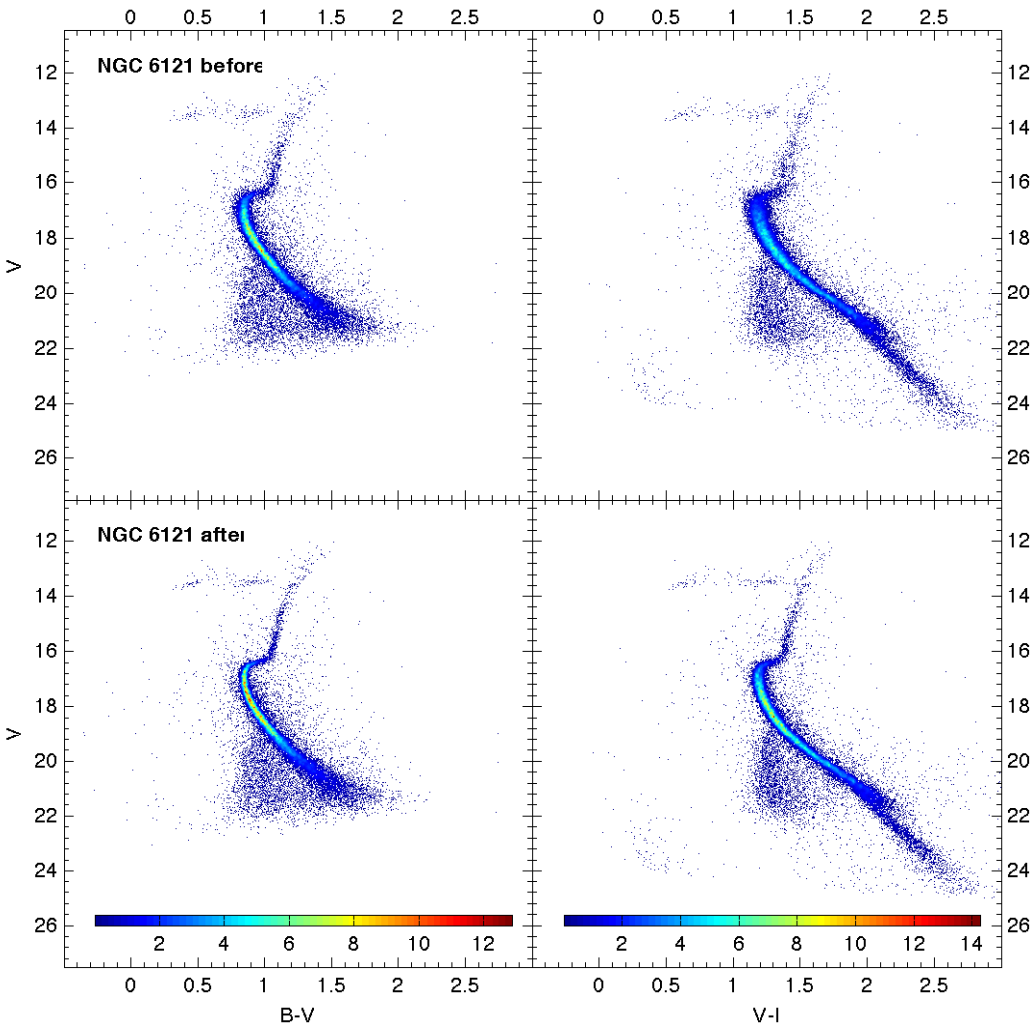

Figure 4.8. CMDs of cluster NGC 6121 - M 4, before and after being differentially dereddened. Only our Magellan photometry was used to build the $B-V$ vs. V CMD. ACS photometry (from project 10775) and Magellan photometry were used to build the V vs. $V-I$ vs. V CMD. Color bars show the range in the densities of stars in the CMD ($\times 10^4$ stars per square magnitude). The color ranges are the same for a given color (B-V or V-I) in the CMD before and after applying our technique.

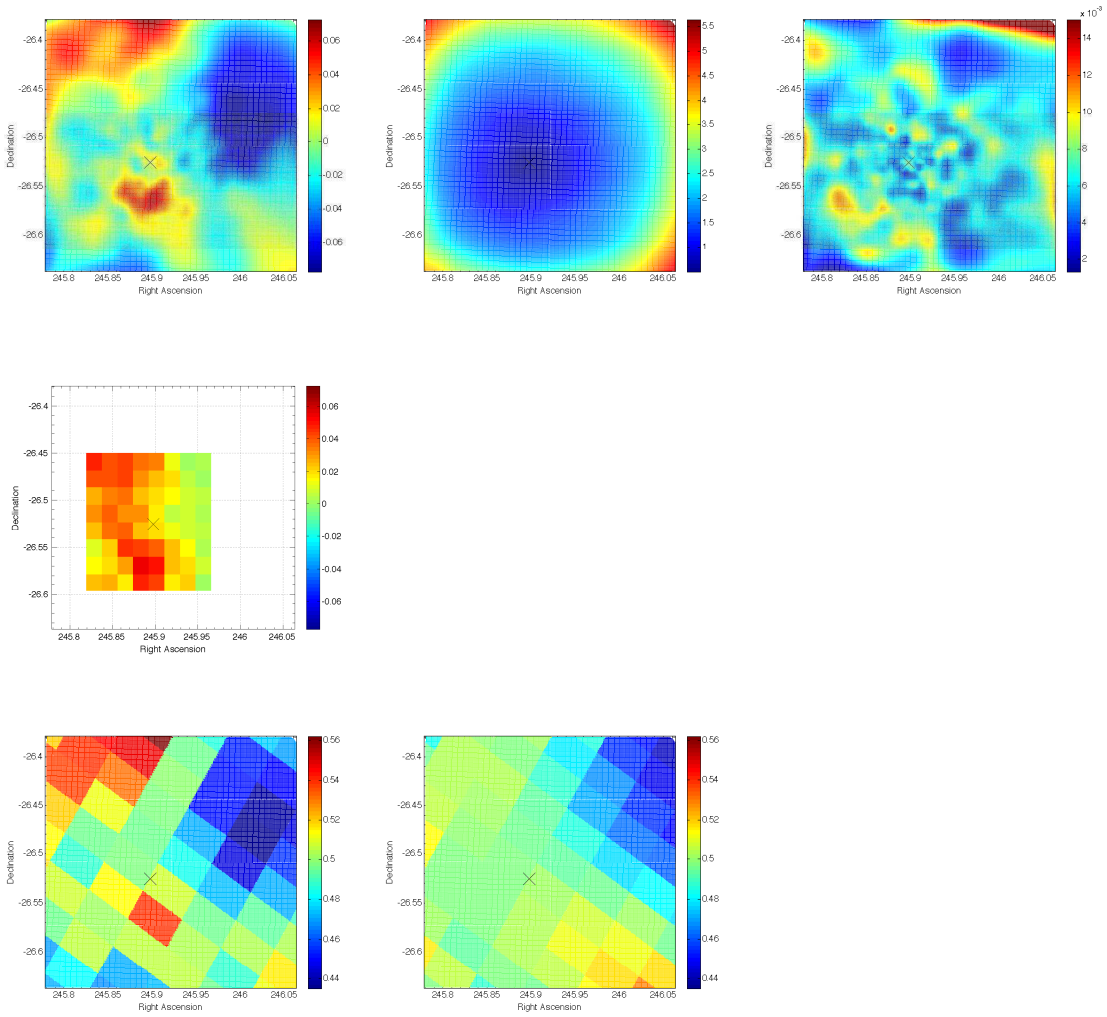

Figure 4.9. Extinction map for the cluster NGC 6121 - M 4 field (top left), along its resolution (top middle), and its precision (top right), as provided by our technique. The x marks the position where the center of the cluster is. The color code gives the color excesses $E(B-V)$ for the extinction map, the bandwidths used in the resolution map, and the standard deviation σ of the color excesses in the precision maps. On the middle, extinction map provided by Mochejska et al. (2002). The color range is the same as in our extinction map (top left) to facilitate the visual comparison between both maps, but realize that their zero point maybe different from ours. On the bottom, we have degraded (see text) our map (bottom left) to compare it with the SFD map (bottom right). From the comparison of both we have obtained a reddening zero point for our map, that we have added to facilitate the comparison.

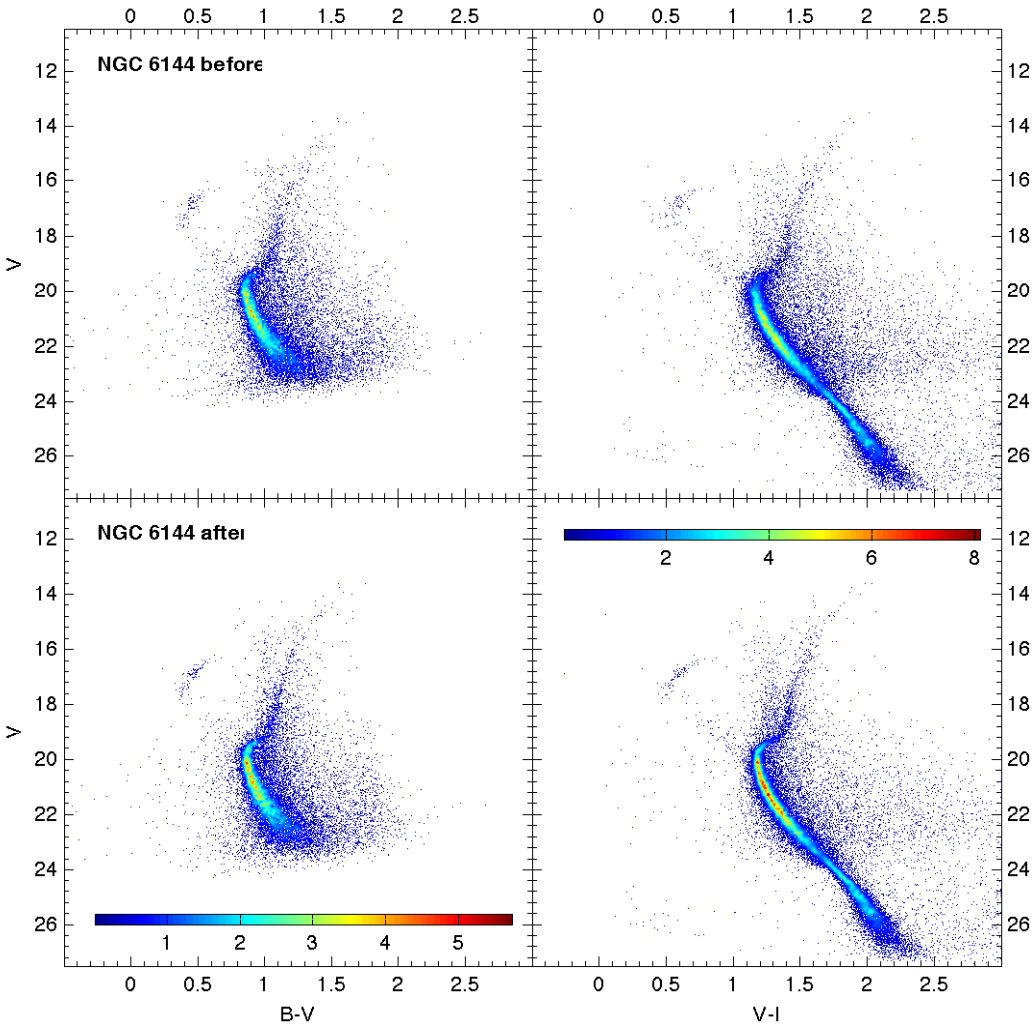

Figure 4.10. CMDs of cluster NGC 6144, before and after being differentially dereddened. Only our Magellan photometry was used to build the $B-V$ vs. V CMD. ACS photometry (from project 10775) and Magellan photometry were used to build the $V-I$ vs. V CMD. Notice that the $B-V$ vs. V CMD could not be correctly calibrated in color using the method described in the text because of the lack of calibrating data in the B filter. Color bars show the range in the densities of stars in the CMD ($\times 10^4$ stars per square magnitude). The color ranges are the same for a given color (B-V or V-I) in the CMD before and after applying our technique.

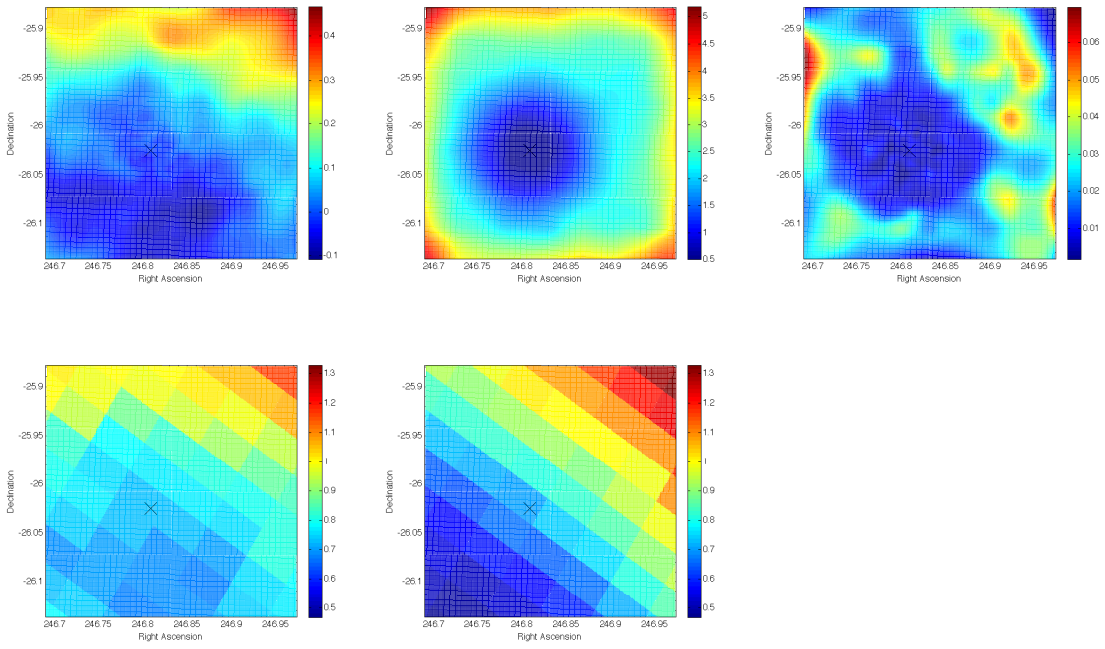

Figure 4.11. Extinction map for the cluster NGC 6144 field (top left), along its resolution (top middle), and its precision (top right), as provided by our technique. The x marks the position where the center of the cluster is. The color code gives the color excesses $E(B-V)$ for the extinction map, the bandwidths used in the resolution map, and the standard deviation σ of the color excesses in the precision maps. On the bottom, we have degraded (see text) our map (bottom left) to compare it with the SFD map (bottom right). From the comparison of both we have obtained a reddening zero point for our map, that we have added to facilitate the comparison.

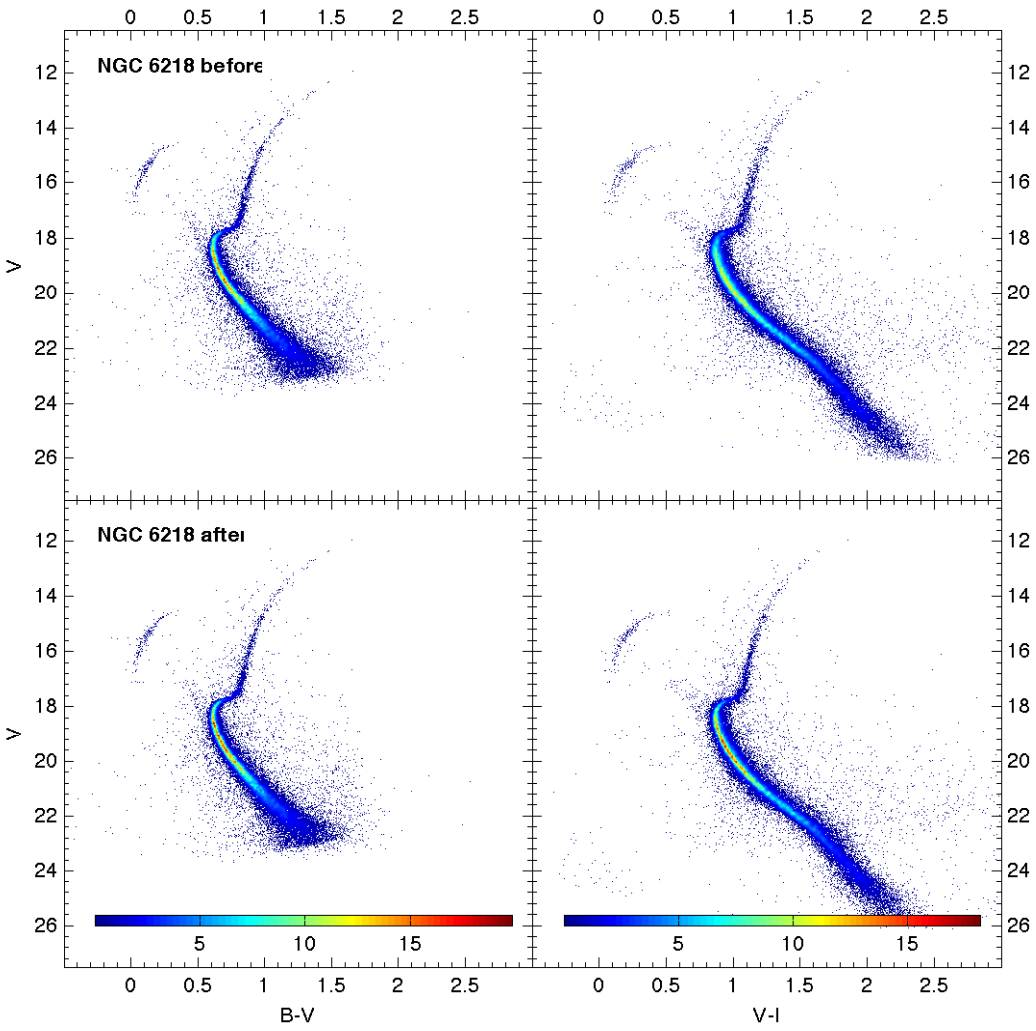

Figure 4.12. CMDs of cluster NGC 6218 - M 12, before and after being differentially dereddened. ACS photometry (from our project 10573) and Magellan photometry were used to build the $B-V$ vs. V CMD. ACS photometry (from project 10775) and Magellan photometry were used to build the $V-I$ vs. V CMD. Color bars show the range in the densities of stars in the CMD ($\times 10^4$ stars per square magnitude). The color ranges are the same for a given color (B-V or V-I) in the CMD before and after applying our technique.

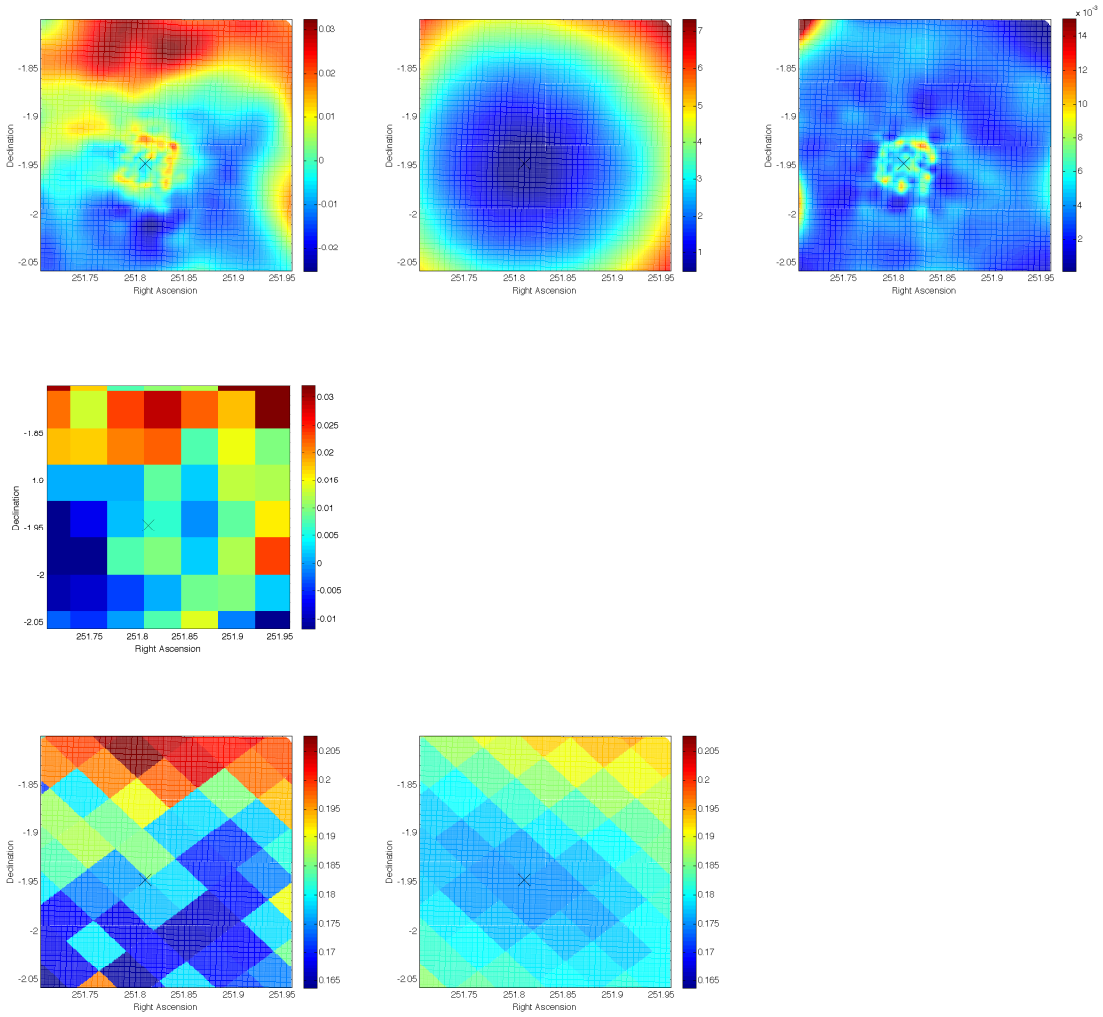

Figure 4.13. Extinction map for the cluster NGC 6218 - M 12 field (top left), along its resolution (top middle), and its precision (top right), as provided by our technique. The x marks the position where the center of the cluster is. The color code gives the color excesses $E(B-V)$ for the extinction map, the bandwidths used in the resolution map, and the standard deviation σ of the color excesses in the precision maps. On the middle, extinction map provided by von Braun et al. (2002), after transforming their E(V-I) values to E(B-V). The color range is the same as in our degraded extinction map (bottom left) to facilitate the visual comparison between maps, but with a different zero point. On the bottom, we have degraded (see text) our map (bottom left) to compare it with the SFD map (bottom right). From the comparison of both we have obtained a reddening zero point for our map, that we have added to facilitate the comparison.

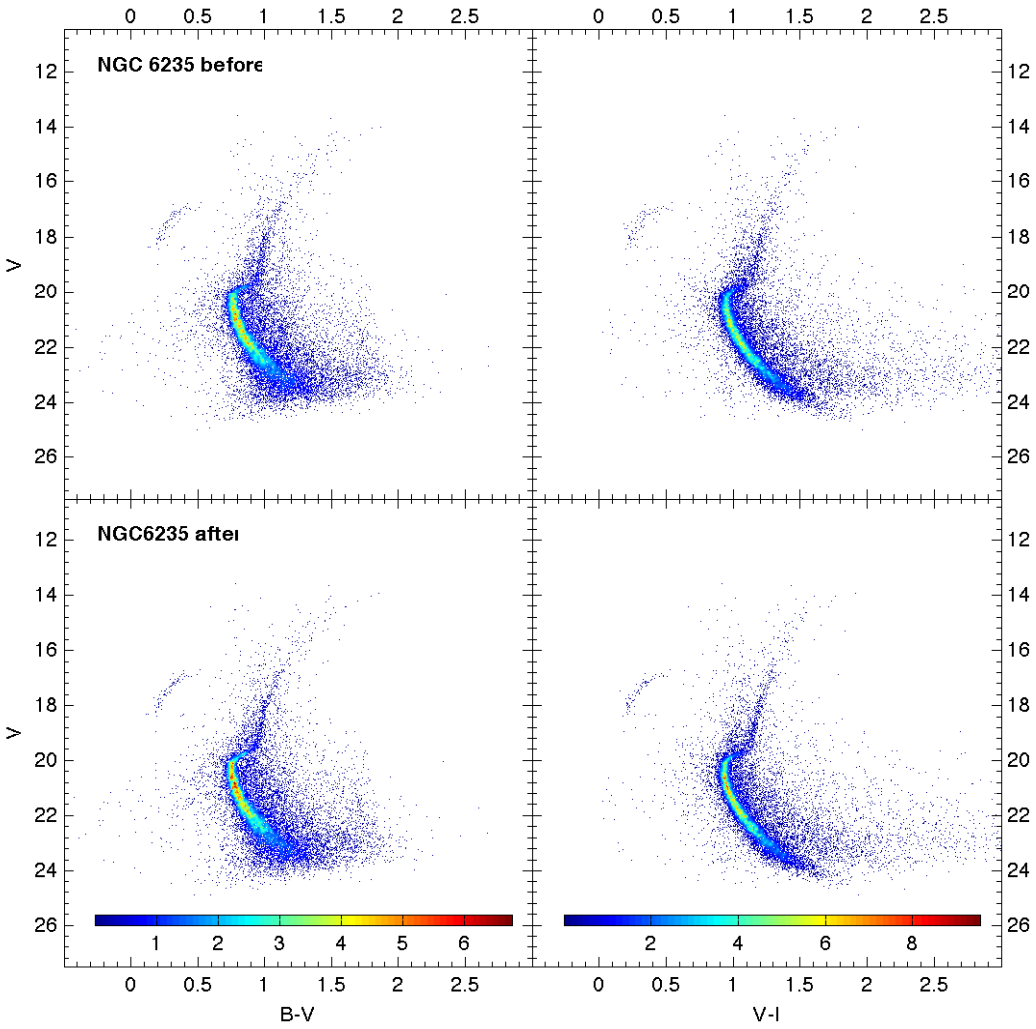

Figure 4.14. CMDs of cluster NGC 6235, before and after being differentially dereddened. Only our Magellan photometry was used to build the CMDs in both colors. Notice that the $V-I$ vs. V CMD could not be correctly calibrated in color using the method described in the text because of the lack of calibrating data in the I filter. Color bars show the range in the densities of stars in the CMD ($\times 10^4$ stars per square magnitude). The color ranges are the same for a given color (B-V or V-I) in the CMD before and after applying our technique.

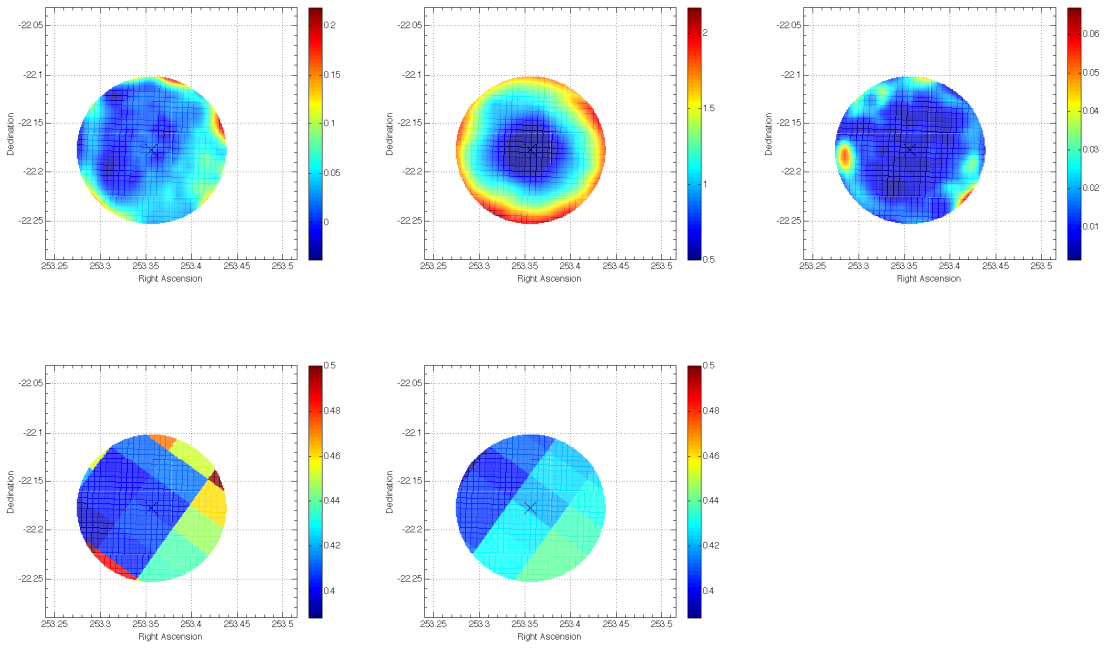

Figure 4.15. Extinction map for the cluster NGC 6235 field (top left), along its resolution (top middle), and its precision (top right), as provided by our technique. The x marks the position where the center of the cluster is. The color code gives the color excesses $E(B-V)$ for the extinction map, the bandwidths used in the resolution map, and the standard deviation σ of the color excesses in the precision maps. On the bottom, we have degraded (see text) our map (bottom left) to compare it with the SFD map (bottom right). From the comparison of both we have obtained a reddening zero point for our map, that we have added to facilitate the comparison.

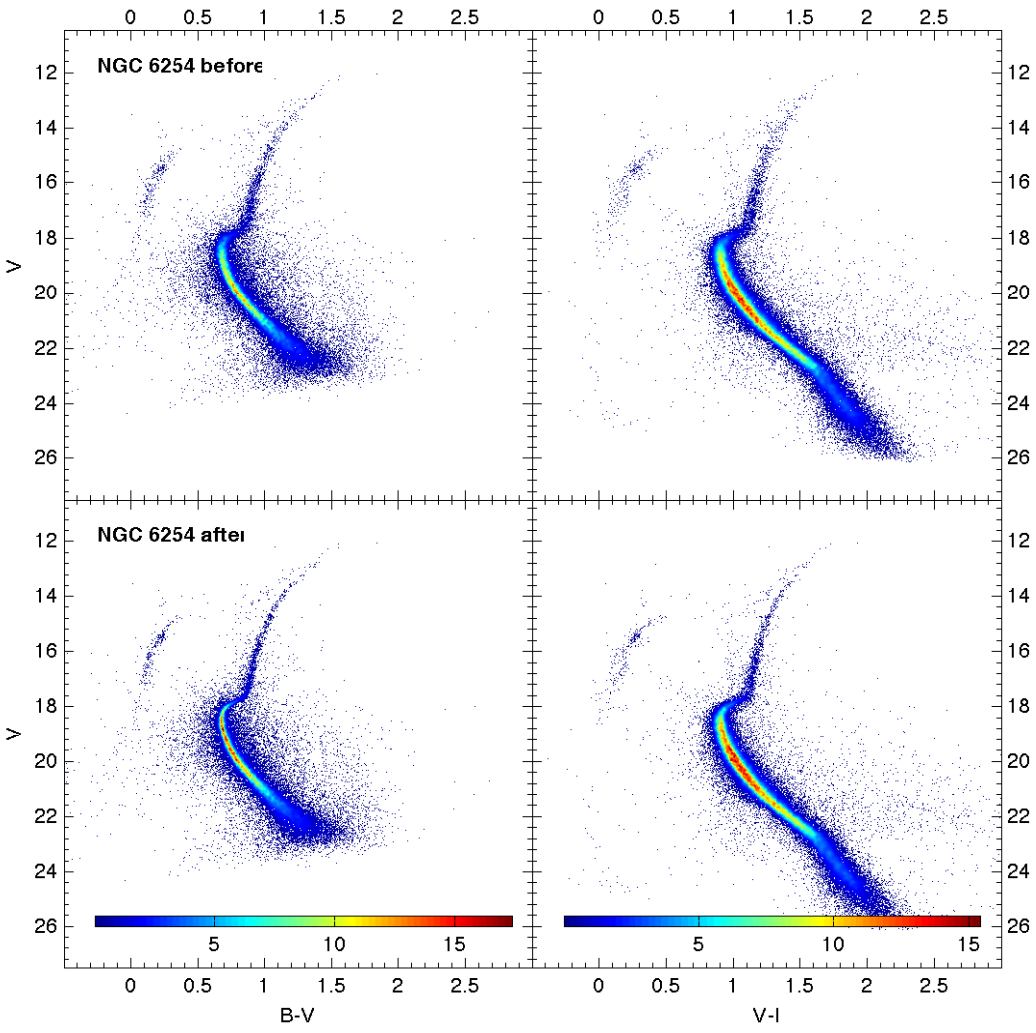

Figure 4.16. CMDs of cluster NGC 6254 - M 10, before and after being differentially dereddened. Only our Magellan photometry was used to build the $B-V$ vs. V CMD. ACS photometry (from project 10775) and Magellan photometry were used to build the $V-I$ vs. V CMD. Color bars show the range in the densities of stars in the CMD ($\times 10^4$ stars per square magnitude). The color ranges are the same for a given color (B-V or V-I) in the CMD before and after applying our technique.

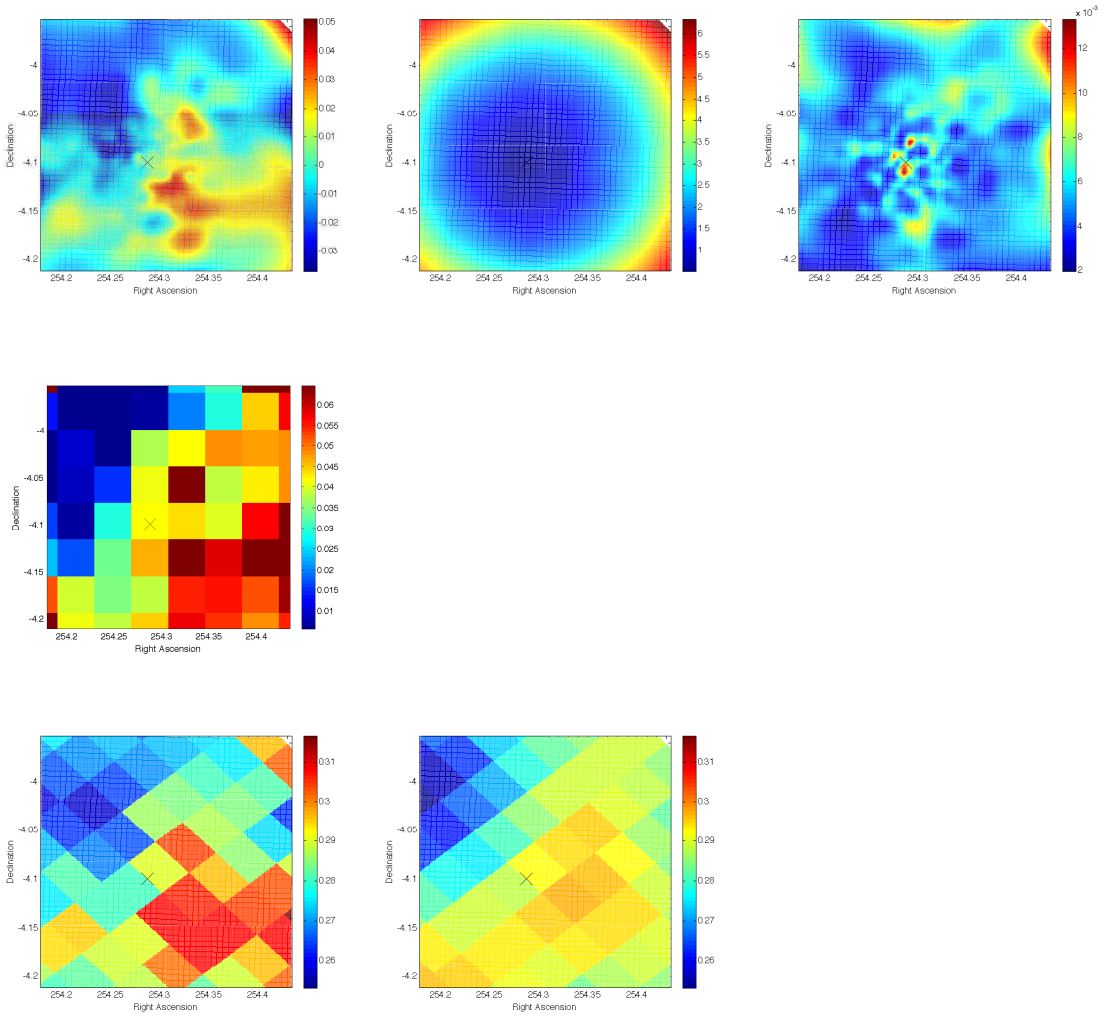

Figure 4.17. Extinction map for the cluster NGC 6254 - M 10 field (top left), along its resolution (top middle), and its precision (top right), as provided by our technique. The x marks the position where the center of the cluster is. The color code gives the color excesses $E(B-V)$ for the extinction map, the bandwidths used in the resolution map, and the standard deviation σ of the color excesses in the precision maps. On the middle, extinction map provided by von Braun et al. (2002), after transforming their E(V-I) values to E(B-V). The color range is the same as in our degraded extinction map (bottom left) to facilitate the visual comparison between maps, but with a different zero point. On the bottom, we have degraded (see text) our map (bottom left) to compare it with the SFD map (bottom right). From the comparison of both we have obtained a reddening zero point for our map, that we have added to facilitate the comparison.

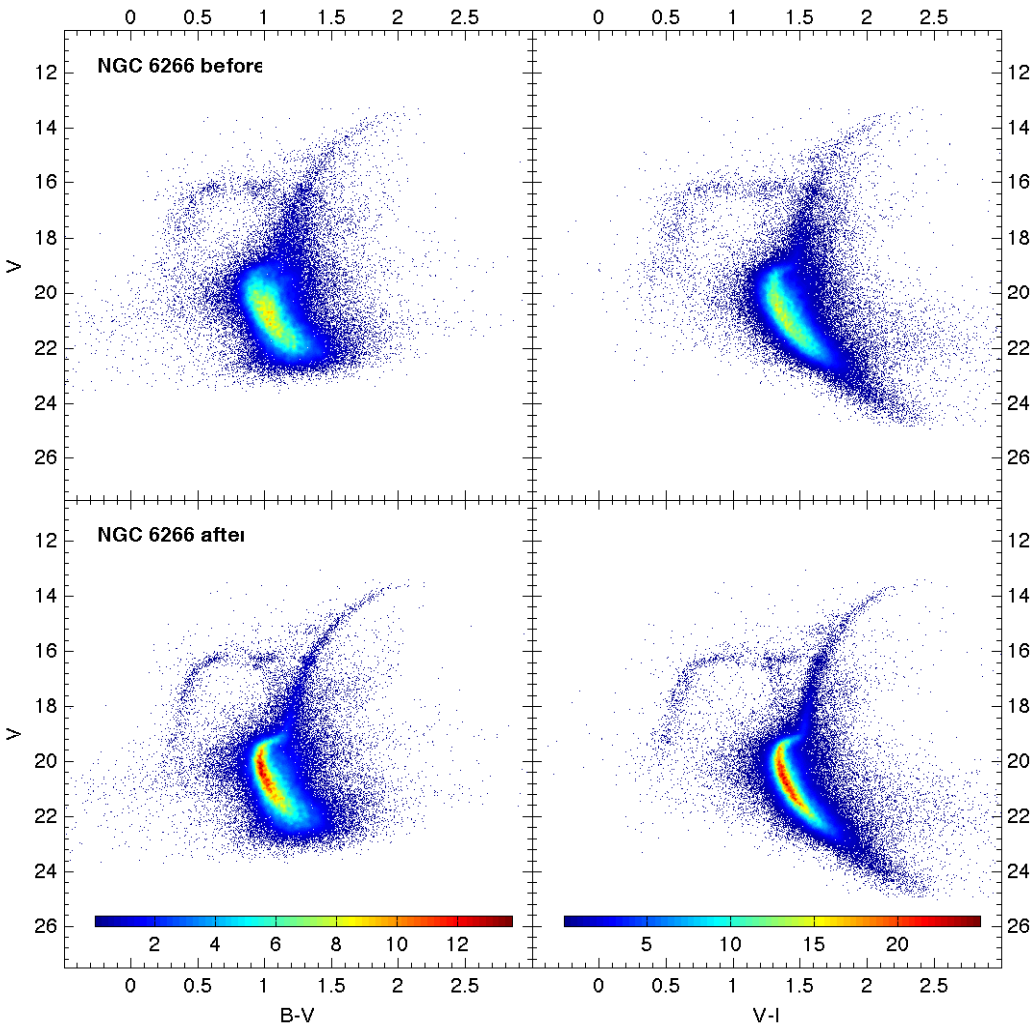

Figure 4.18. CMDs of cluster NGC 6266 - M 62, before and after being differentially dereddened. Only our Magellan photometry was used to build the $B-V$ vs. V CMD. WFPC2 photometry (from project 8709) and Magellan photometry were used to build the $V-I$ vs. V CMD. Color bars show the range in the densities of stars in the CMD ($\times 10^4$ stars per square magnitude). The color ranges are the same for a given color (B-V or V-I) in the CMD before and after applying our technique.

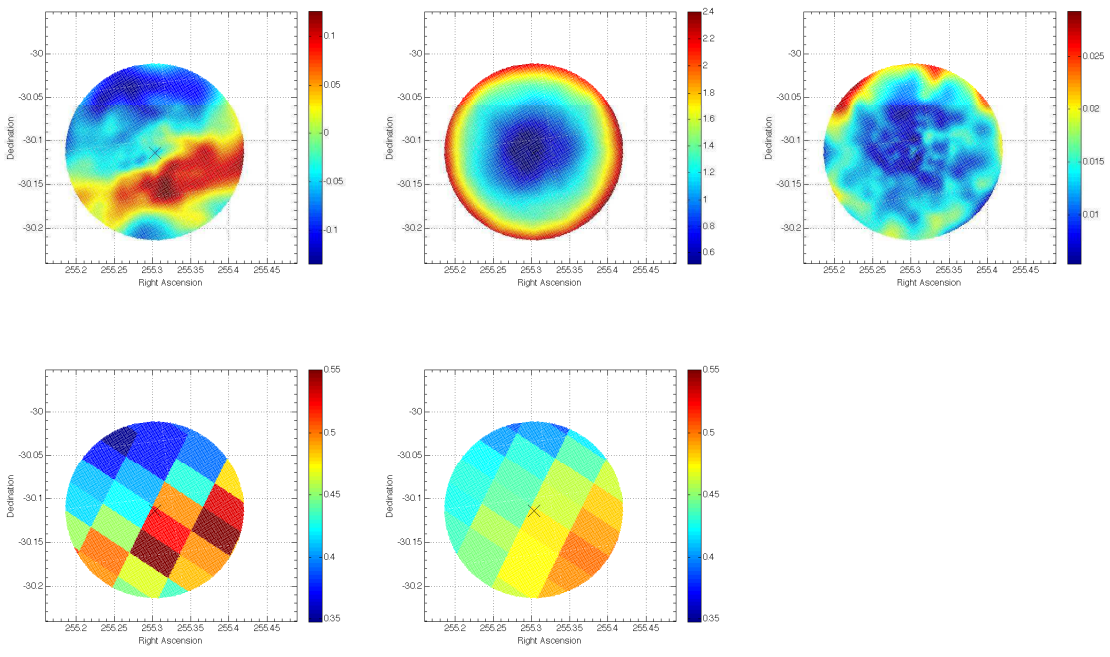

Figure 4.19. Extinction map for the cluster NGC 6266 - M 62 field (top left), along its resolution (top middle), and its precision (top right), as provided by our technique. The x marks the position where the center of the cluster is. The color code gives the color excesses $E(B-V)$ for the extinction map, the bandwidths used in the resolution map, and the standard deviation σ of the color excesses in the precision maps. On the bottom, we have degraded (see text) our map (bottom left) to compare it with the SFD map (bottom right). From the comparison of both we have obtained a reddening zero point for our map, that we have added to facilitate the comparison.

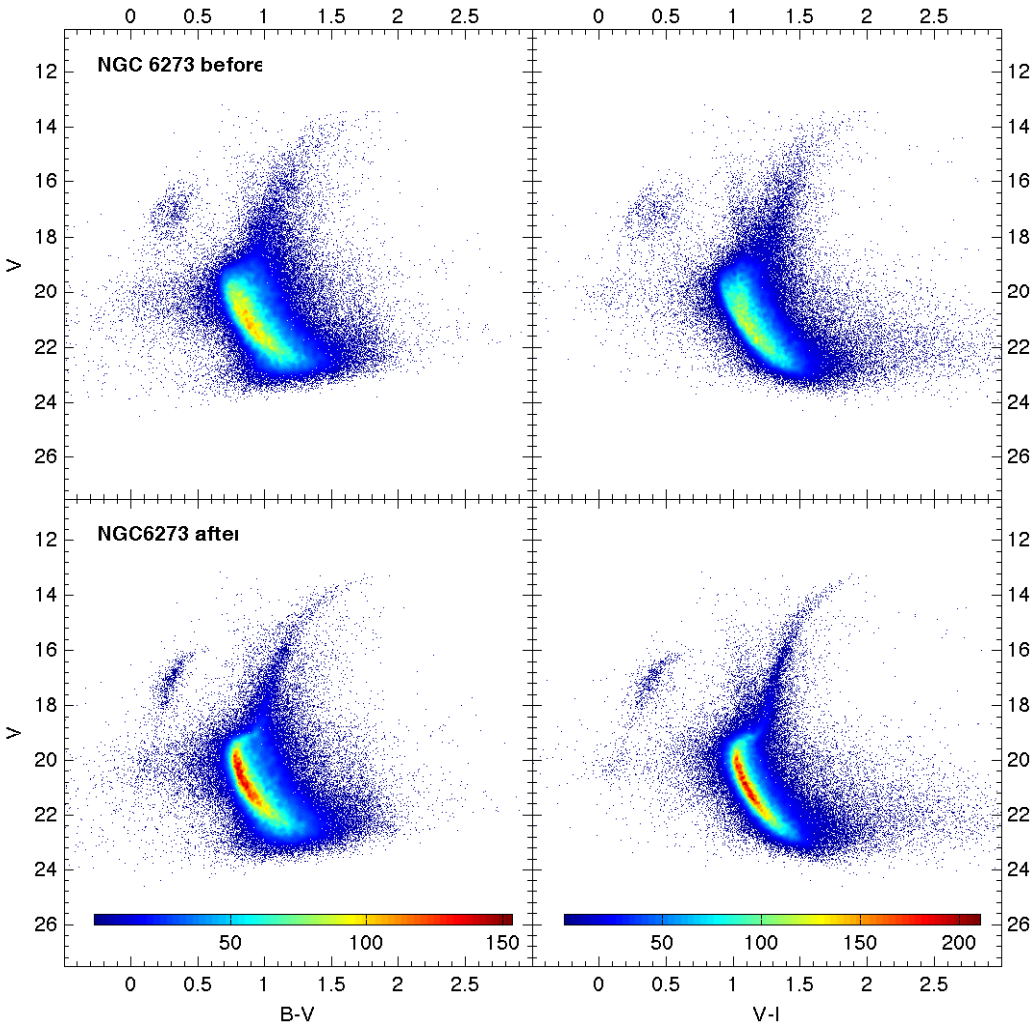

Figure 4.20. CMDs of cluster NGC 6273 - M 19, before and after being differentially dereddened. Only our Magellan photometry was used to build the CMDs in both colors. Color bars show the range in the densities of stars in the CMD ($\times 10^4$ stars per square magnitude). The color ranges are the same for a given color (B-V or V-I) in the CMD before and after applying our technique.

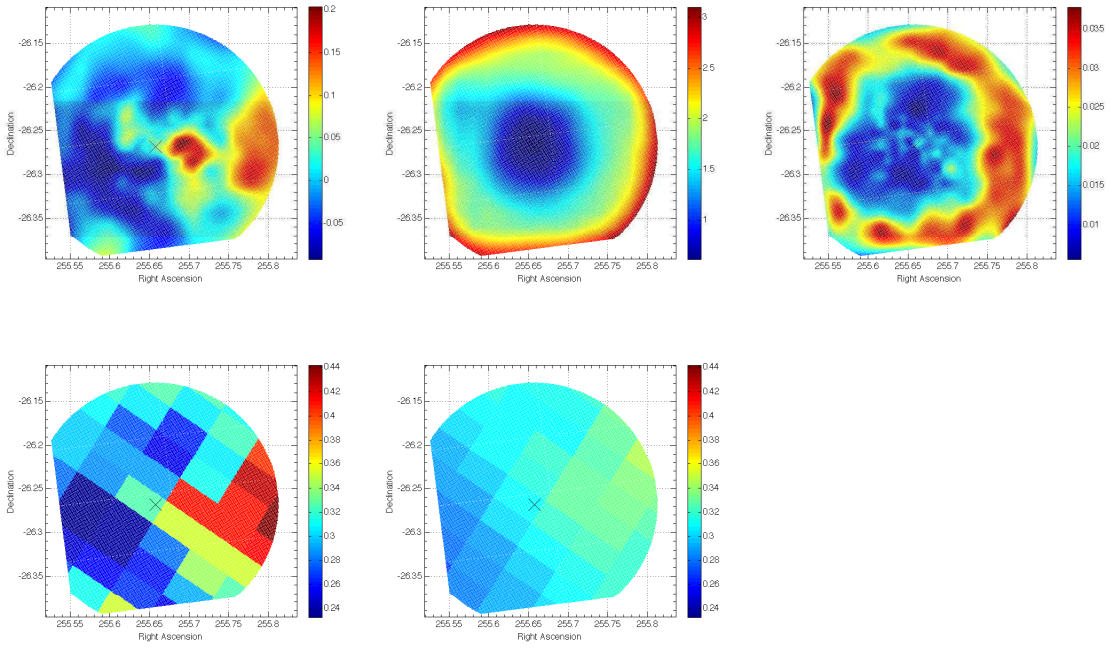

Figure 4.21. Extinction map for the cluster NGC 6273 - M 19 field (top left), along its resolution (top middle), and its precision (top right), as provided by our technique. The x marks the position where the center of the cluster is. The color code gives the color excesses $E(B-V)$ for the extinction map, the bandwidths used in the resolution map, and the standard deviation σ of the color excesses in the precision maps. On the bottom, we have degraded (see text) our map (bottom left) to compare it with the SFD map (bottom right). From the comparison of both we have obtained a reddening zero point for our map, that we have added to facilitate the comparison.

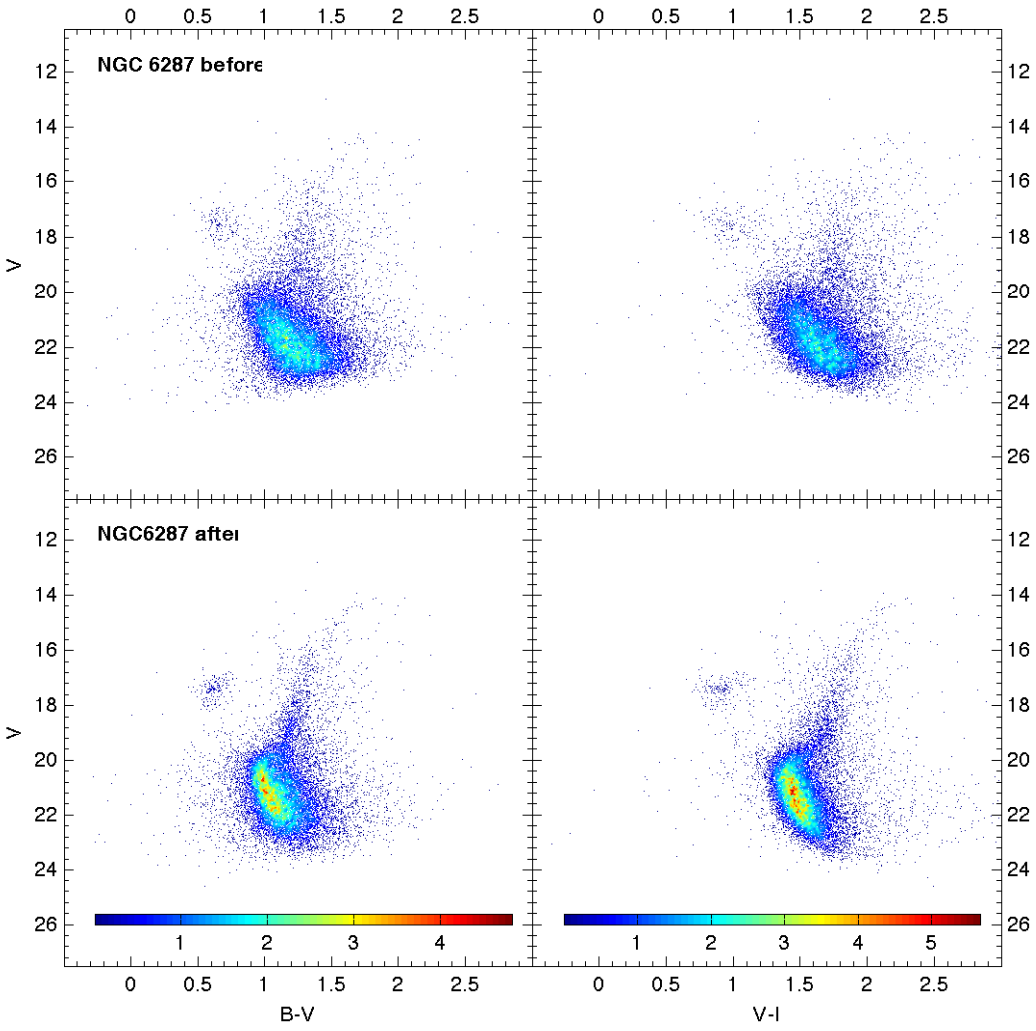

Figure 4.22. CMDs of cluster NGC 6287, before and after being differentially dereddened. Only our Magellan photometry was used to build the CMDs in both colors. Color bars show the range in the densities of stars in the CMD ($\times 10^4$ stars per square magnitude). The color ranges are the same for a given color (B-V or V-I) in the CMD before and after applying our technique.

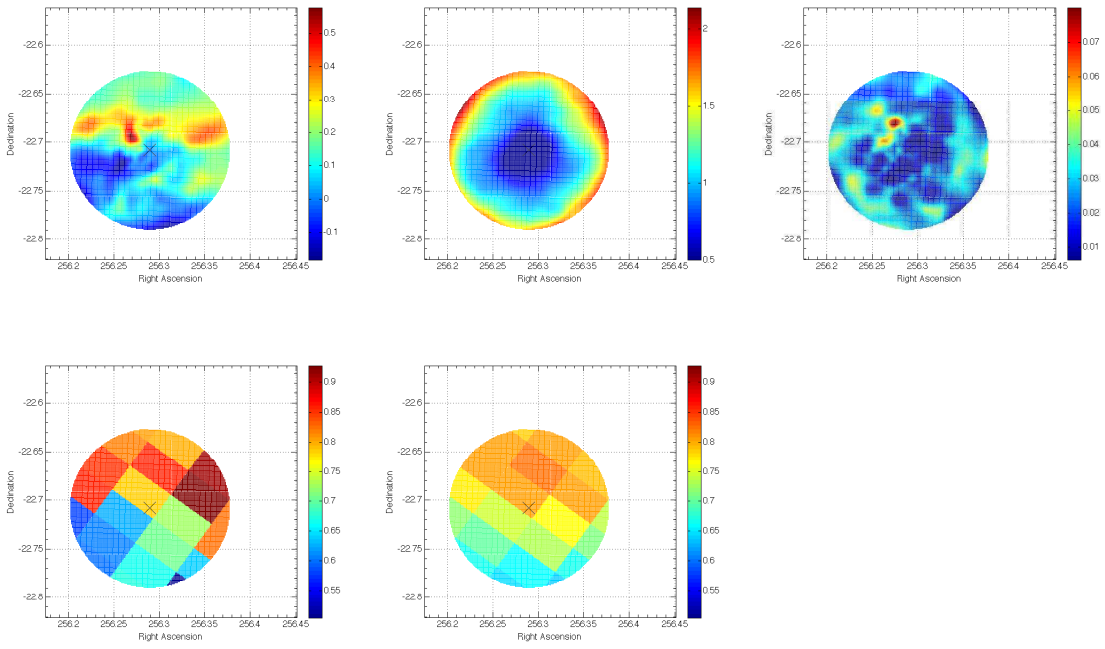

Figure 4.23. Extinction map for the cluster NGC 6287 field (top left), along its resolution (top middle), and its precision (top right), as provided by our technique. The x marks the position where the center of the cluster is. The color code gives the color excesses $E(B-V)$ for the extinction map, the bandwidths used in the resolution map, and the standard deviation σ of the color excesses in the precision maps. On the bottom, we have degraded (see text) our map (bottom left) to compare it with the SFD map (bottom right). From the comparison of both we have obtained a reddening zero point for our map, that we have added to facilitate the comparison.

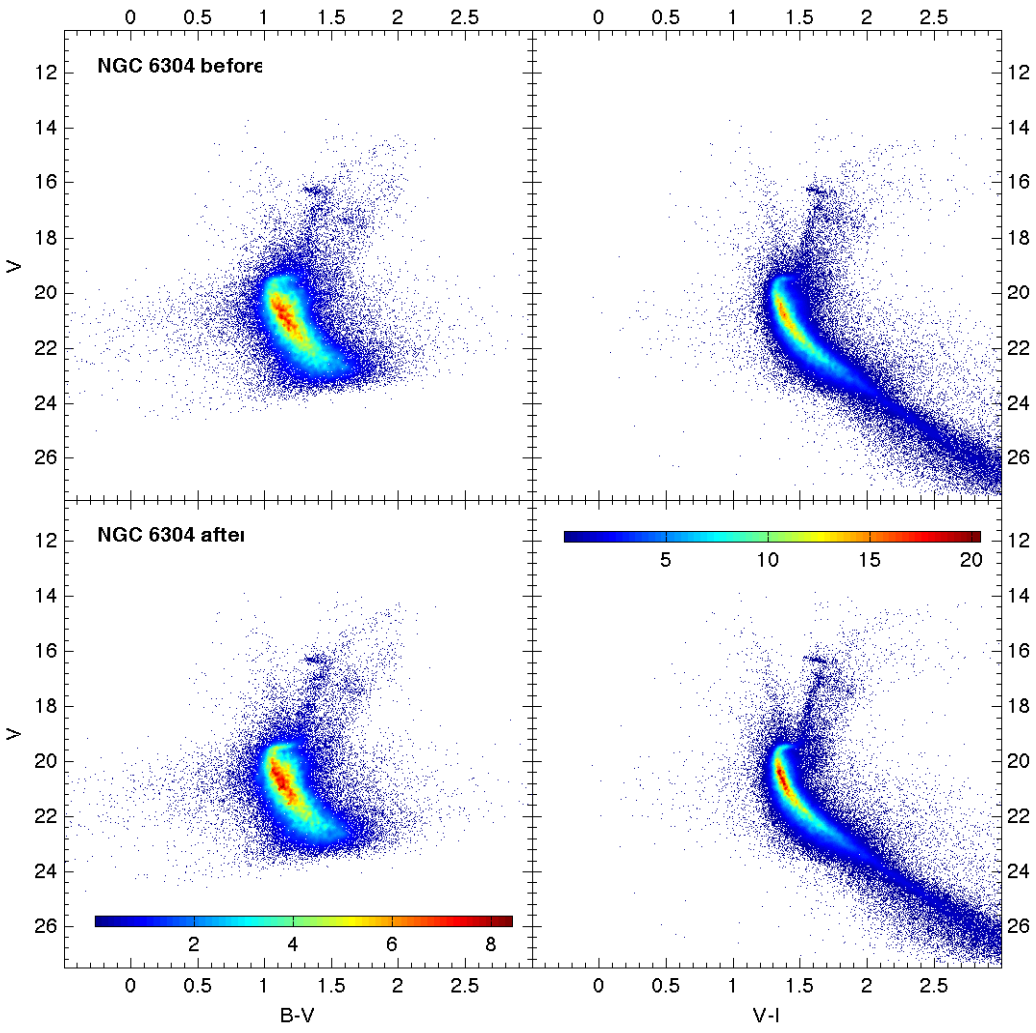

Figure 4.24. CMDs of cluster NGC 6304, before and after being differentially dereddened. Only our Magellan photometry was used to build the $B-V$ vs. V CMD. ACS photometry (from project 10775) and Magellan photometry were used to build the $V-I$ vs. V CMD. Color bars show the range in the densities of stars in the CMD ($\times 10^4$ stars per square magnitude). The color ranges are the same for a given color (B-V or V-I) in the CMD before and after applying our technique.

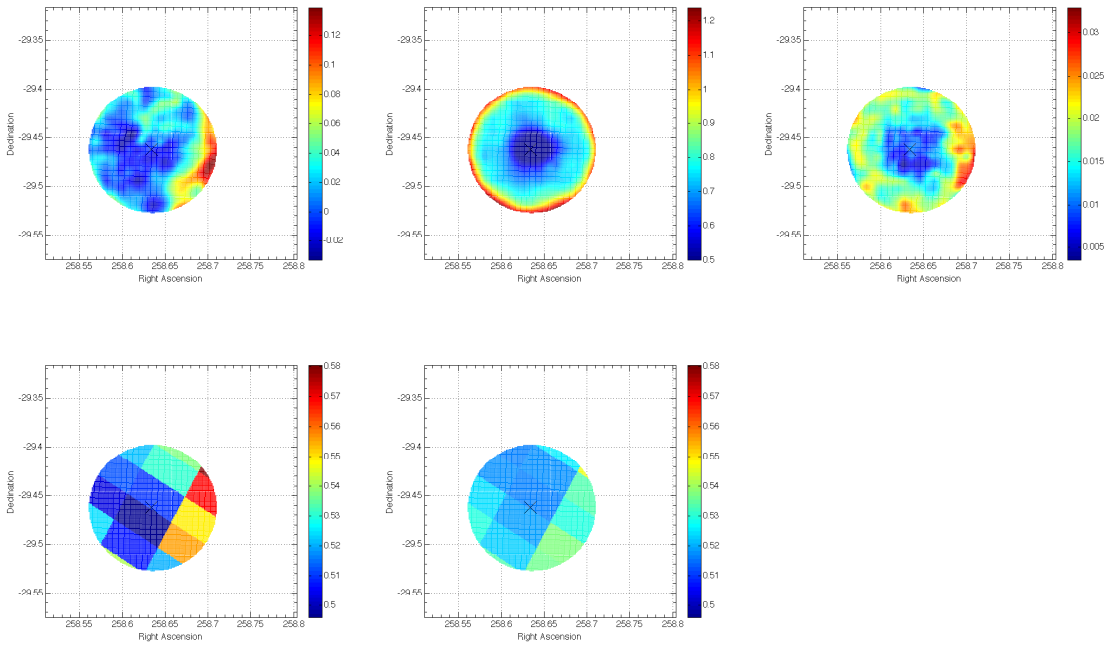

Figure 4.25. Extinction map for the cluster NGC 6304 field (top left), along its resolution (top middle), and its precision (top right), as provided by our technique. The x marks the position where the center of the cluster is. The color code gives the color excesses $E(B-V)$ for the extinction map, the bandwidths used in the resolution map, and the standard deviation σ of the color excesses in the precision maps. On the bottom, we have degraded (see text) our map (bottom left) to compare it with the SFD map (bottom right). From the comparison of both we have obtained a reddening zero point for our map, that we have added to facilitate the comparison.

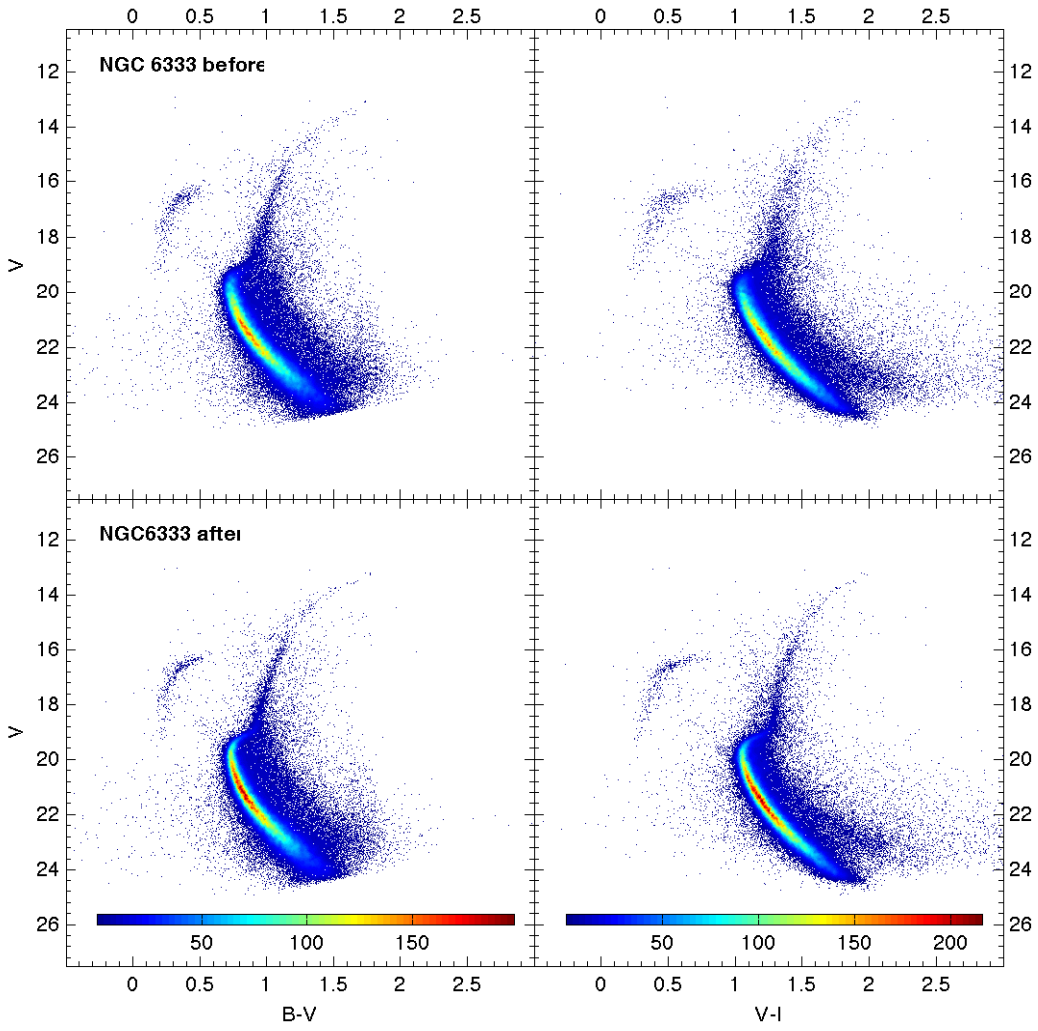

Figure 4.26. CMDs of cluster NGC 6333 - M 9, before and after being differentially dereddened. ACS photometry (from our project 10573) and our Magellan photometry were used to build the CMDs in both colors. Color bars show the range in the densities of stars in the CMD ($\times 10^4$ stars per square magnitude). The color ranges are the same for a given color (B-V or V-I) in the CMD before and after applying our technique.

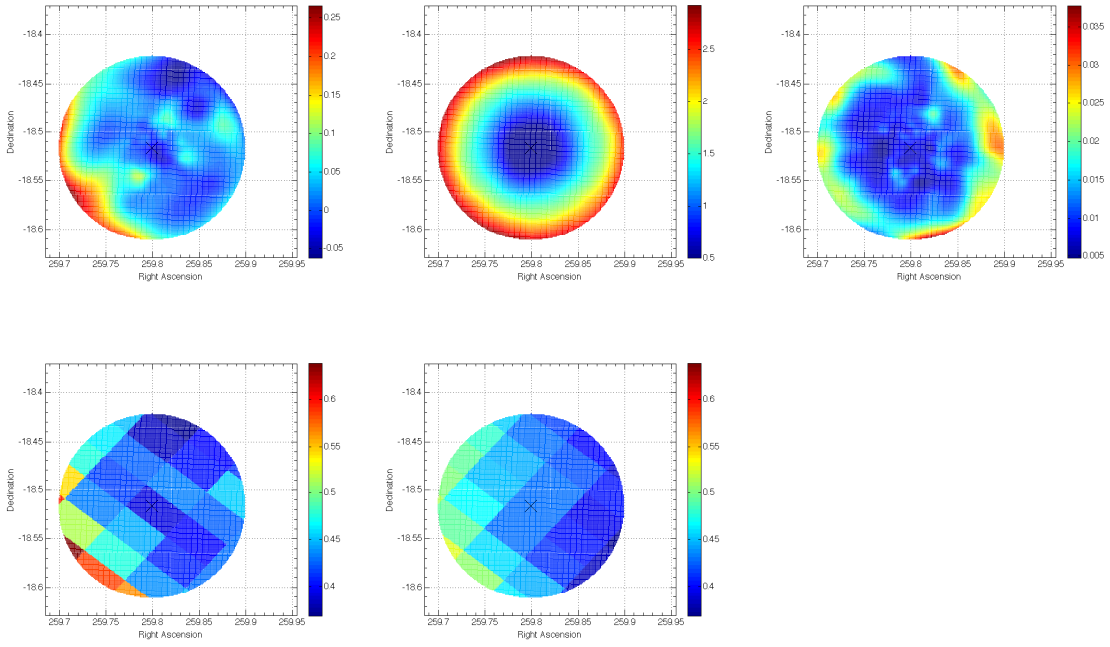

Figure 4.27. Extinction map for the cluster NGC 6333 - M 9 field (top left), along its resolution (top middle), and its precision (top right), as provided by our technique. The x marks the position where the center of the cluster is. The color code gives the color excesses $E(B-V)$ for the extinction map, the bandwidths used in the resolution map, and the standard deviation σ of the color excesses in the precision maps. On the bottom, we have degraded (see text) our map (bottom left) to compare it with the SFD map (bottom right). From the comparison of both we have obtained a reddening zero point for our map, that we have added to facilitate the comparison.

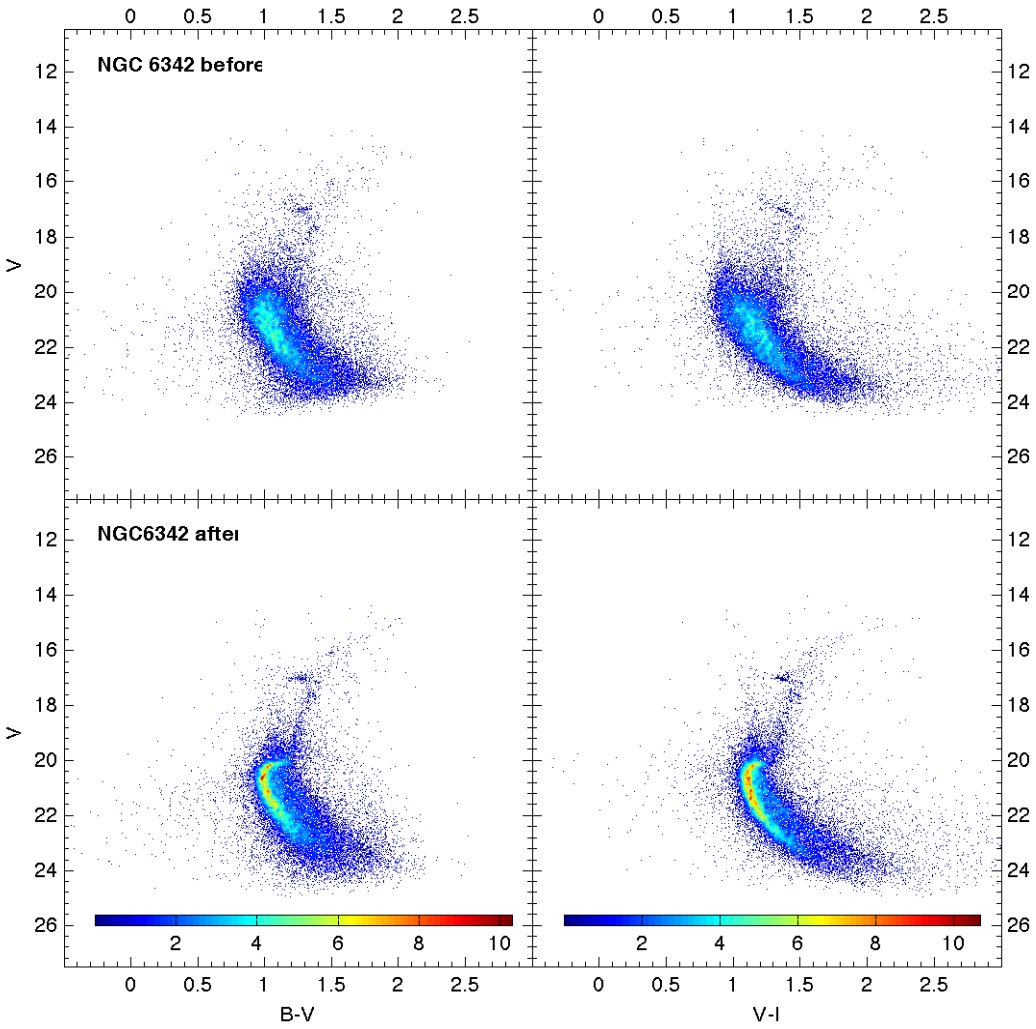

Figure 4.28. CMDs of cluster NGC 6342, before and after being differentially dereddened. Only our Magellan photometry was used to build the CMDs in both colors. Notice that the $V-I$ vs. V CMD could not be correctly calibrated in color using the method described in the text because of the lack of calibrating data in the I filter. Color bars show the range in the densities of stars in the CMD ($\times 10^4$ stars per square magnitude). The color ranges are the same for a given color (B-V or V-I) in the CMD before and after applying our technique.

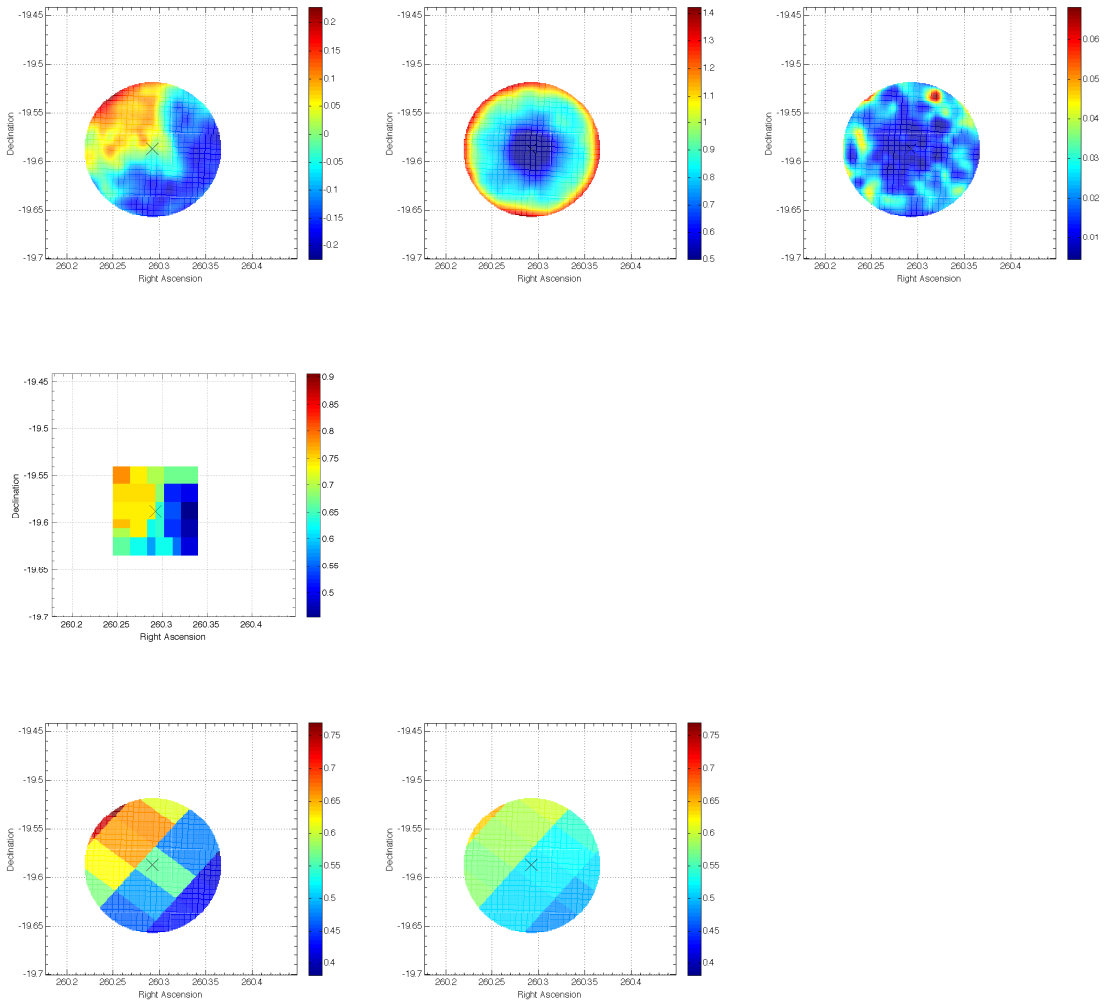

Figure 4.29. Extinction map for the cluster NGC 6342 field (top left), along its resolution (top middle), and its precision (top right), as provided by our technique. The x marks the position where the center of the cluster is. The color code gives the color excesses $E(B-V)$ for the extinction map, the bandwidths used in the resolution map, and the standard deviation σ of the color excesses in the precision maps. On the middle, extinction map provided by Heitsch & Richtler (1999). The color range is the same as in our extinction map (top left) to facilitate the visual comparison between maps, but with a different zero point. On the bottom, we have degraded (see text) our map (bottom left) to compare it with the SFD map (bottom right). From the comparison of both we have obtained a reddening zero point for our map, that we have added to facilitate the comparison.

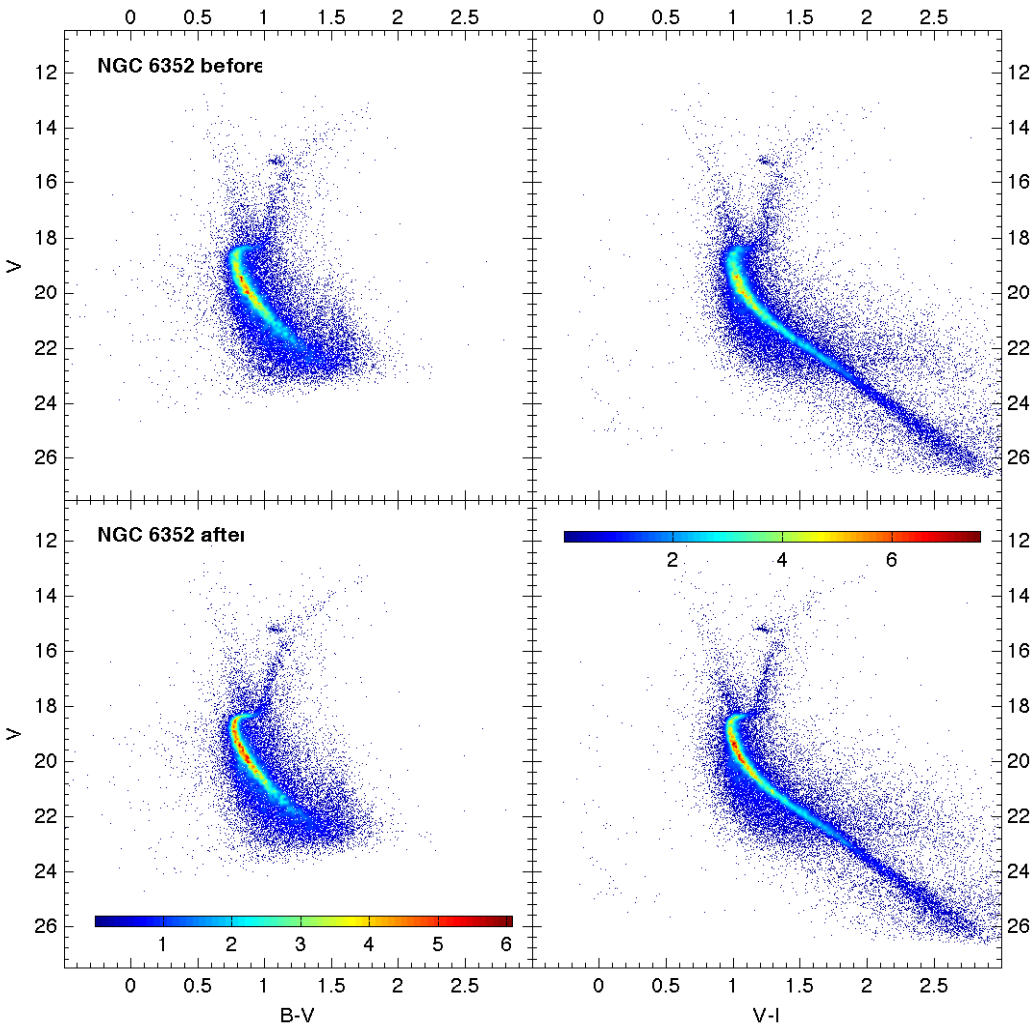

Figure 4.30. CMDs of cluster NGC 6352, before and after being differentially dereddened. Only our Magellan photometry was used to build the $B-V$ vs. V CMD. ACS photometry (from project 10775) and Magellan photometry were used to build the $V-I$ vs. V CMD. Color bars show the range in the densities of stars in the CMD ($\times 10^4$ stars per square magnitude). The color ranges are the same for a given color (B-V or V-I) in the CMD before and after applying our technique.

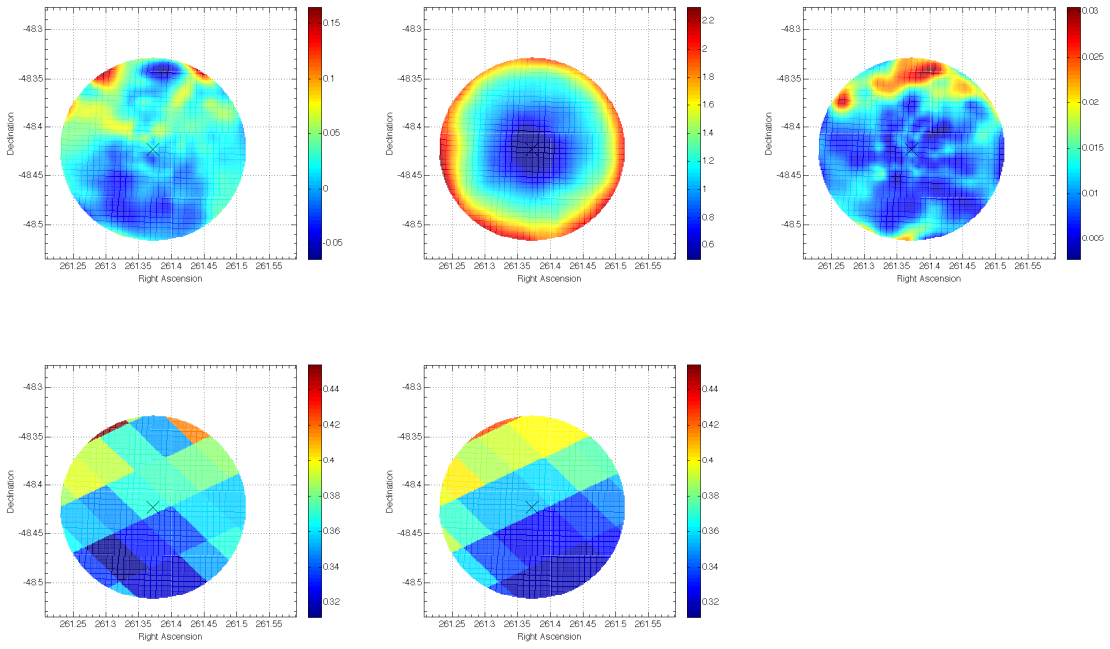

Figure 4.31. Extinction map for the cluster NGC 6352 field (top left), along its resolution (top middle), and its precision (top right), as provided by our technique. The x marks the position where the center of the cluster is. The color code gives the color excesses $E(B-V)$ for the extinction map, the bandwidths used in the resolution map, and the standard deviation σ of the color excesses in the precision maps. On the bottom, we have degraded (see text) our map (bottom left) to compare it with the SFD map (bottom right). From the comparison of both we have obtained a reddening zero point for our map, that we have added to facilitate the comparison.

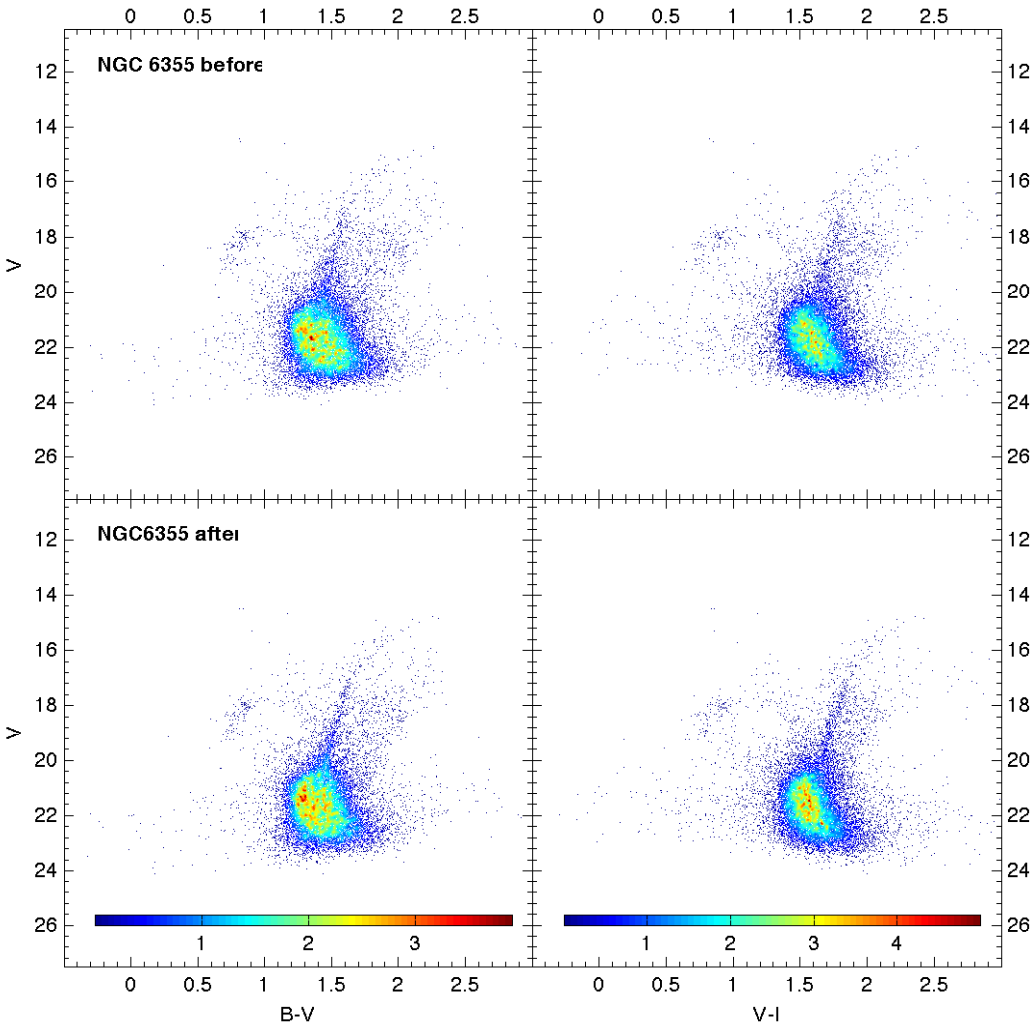

Figure 4.32. CMDs of cluster NGC 6355, before and after being differentially dereddened. Only our Magellan photometry was used to build the CMDs in both colors. Notice that the $V-I$ vs. V CMD could not be correctly calibrated in color using the method described in the text because of the lack of calibrating data in the I filter. Color bars show the range in the densities of stars in the CMD ($\times 10^4$ stars per square magnitude). The color ranges are the same for a given color (B-V or V-I) in the CMD before and after applying our technique.

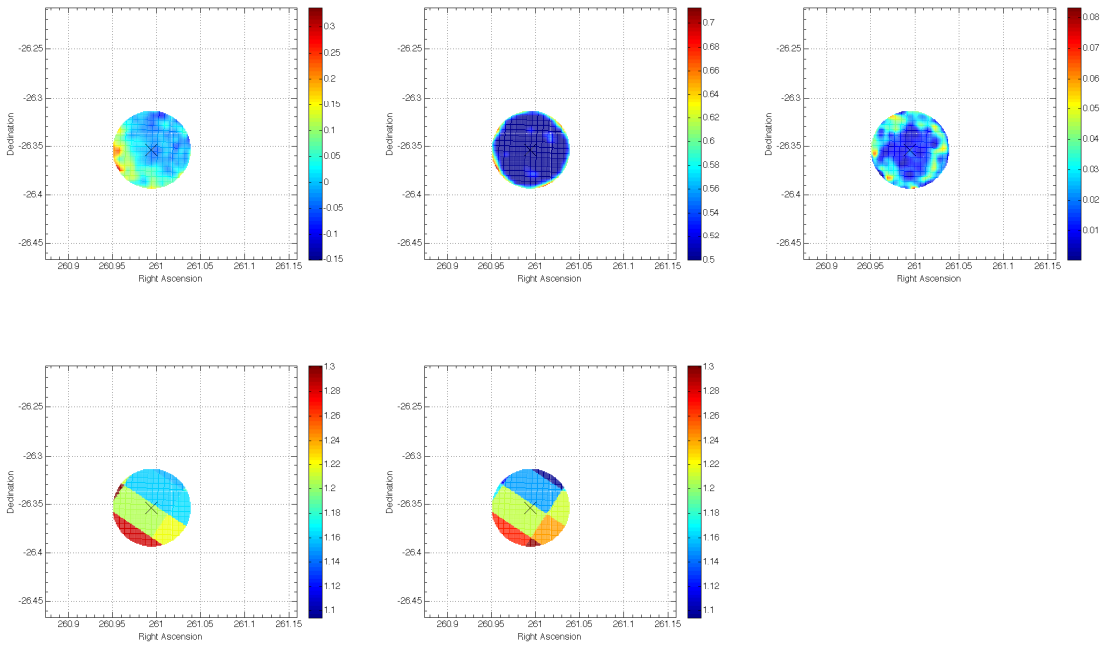

Figure 4.33. Extinction map for the cluster NGC 6355 field (top left), along its resolution (top middle), and its precision (top right), as provided by our technique. The x marks the position where the center of the cluster is. The color code gives the color excesses $E(B-V)$ for the extinction map, the bandwidths used in the resolution map, and the standard deviation σ of the color excesses in the precision maps. On the bottom, we have degraded (see text) our map (bottom left) to compare it with the SFD map (bottom right). From the comparison of both we have obtained a reddening zero point for our map, that we have added to facilitate the comparison.

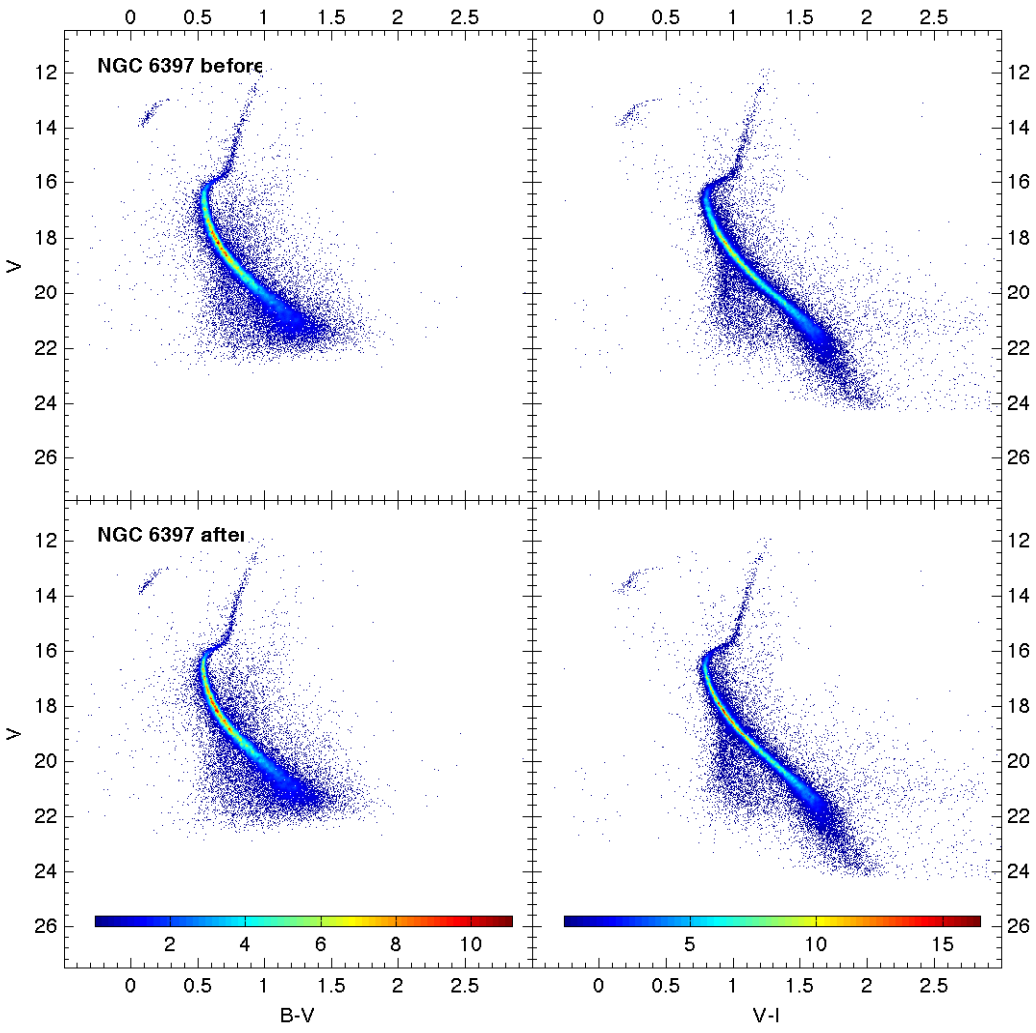

Figure 4.34. CMDs of cluster NGC 6397, before and after being differentially dereddened. Only our Magellan photometry was used to build the $B-V$ vs. V CMD. ACS photometry (from project 10775) and Magellan photometry were used to build the $V-I$ vs. V CMD. Color bars show the range in the densities of stars in the CMD ($\times 10^4$ stars per square magnitude). The color ranges are the same for a given color (B-V or V-I) in the CMD before and after applying our technique.

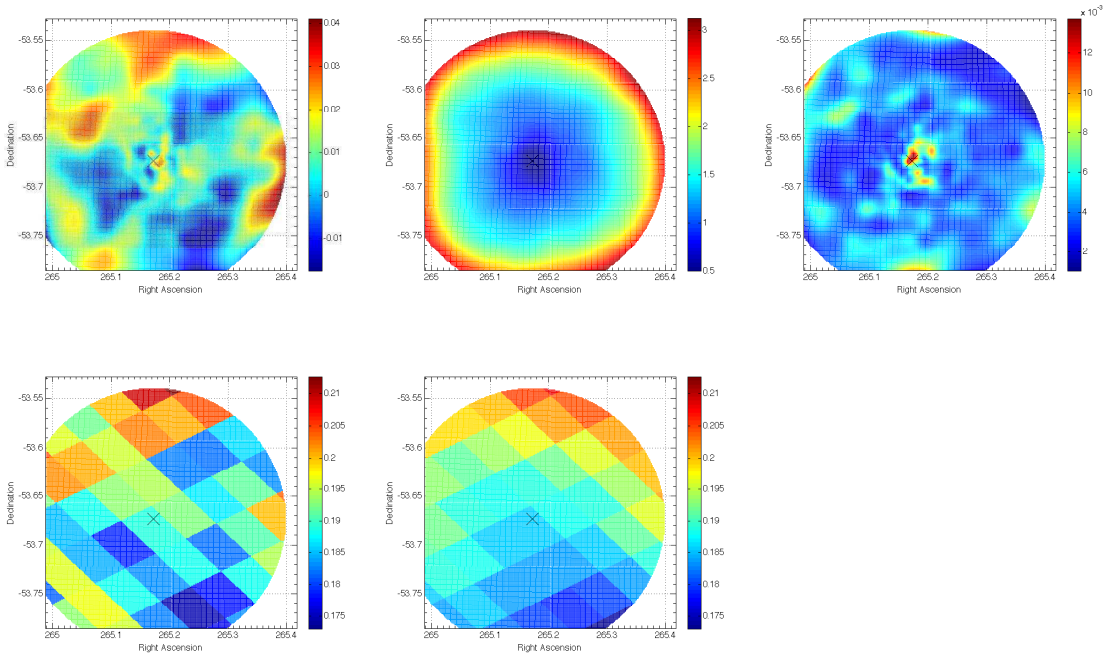

Figure 4.35. Extinction map for the cluster NGC 6397 field (top left), along its resolution (top middle), and its precision (top right), as provided by our technique. The x marks the position where the center of the cluster is. The color code gives the color excesses $E(B-V)$ for the extinction map, the bandwidths used in the resolution map, and the standard deviation σ of the color excesses in the precision maps. On the bottom, we have degraded (see text) our map (bottom left) to compare it with the SFD map (bottom right). From the comparison of both we have obtained a reddening zero point for our map, that we have added to facilitate the comparison.

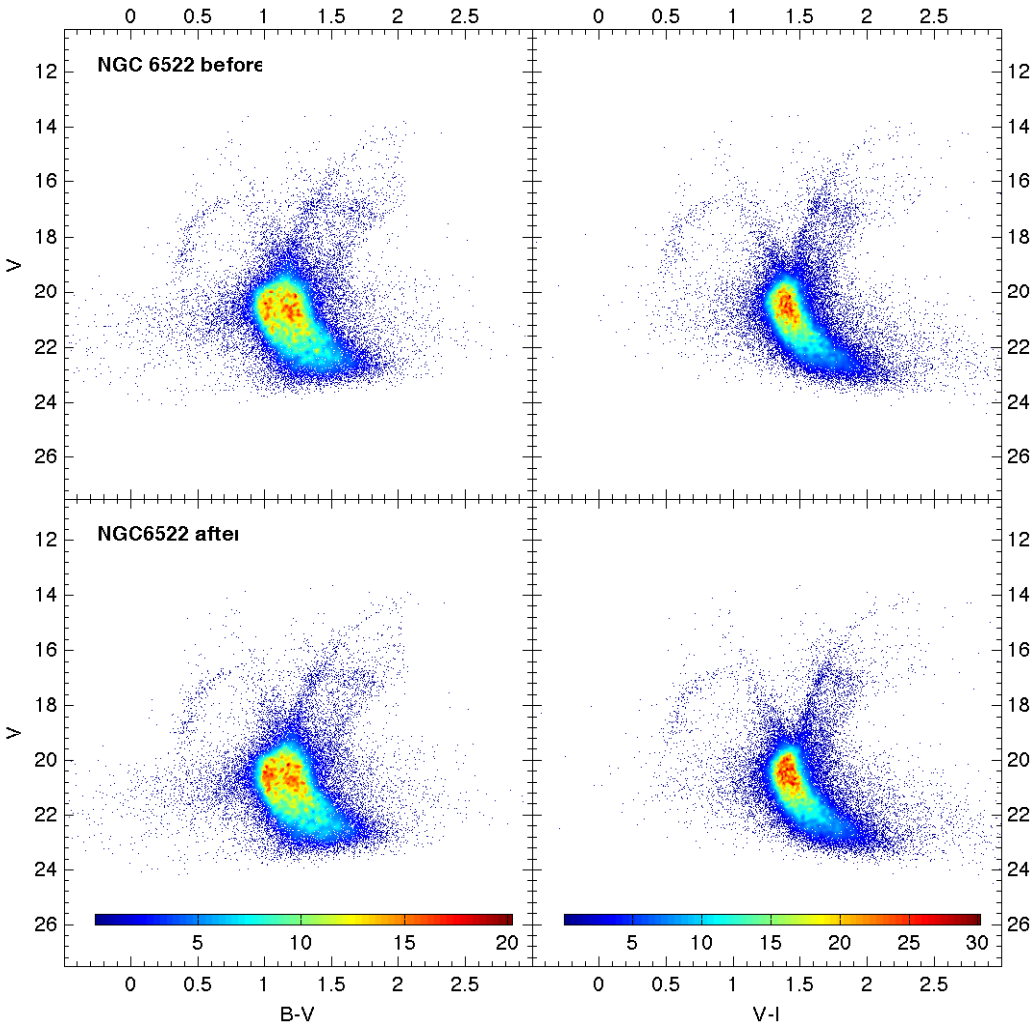

Figure 4.36. CMDs of cluster NGC 6522, before and after being differentially dereddened. Only our Magellan photometry was used to build the CMDs in both colors. Color bars show the range in the densities of stars in the CMD ($\times 10^4$ stars per square magnitude). The color ranges are the same for a given color (B-V or V-I) in the CMD before and after applying our technique.

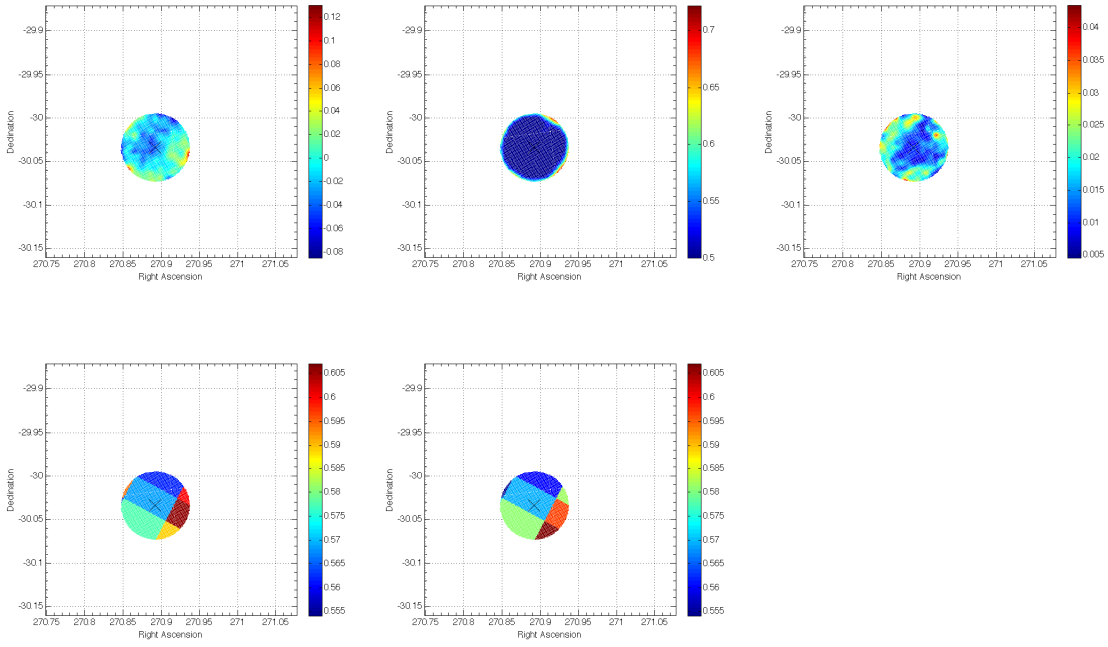

Figure 4.37. Extinction map for the cluster NGC 6522 field (top left), along its resolution (top middle), and its precision (top right), as provided by our technique. The x marks the position where the center of the cluster is. The color code gives the color excesses $E(B-V)$ for the extinction map, the bandwidths used in the resolution map, and the standard deviation σ of the color excesses in the precision maps. On the bottom, we have degraded (see text) our map (bottom left) to compare it with the SFD map (bottom right). From the comparison of both we have obtained a reddening zero point for our map, that we have added to facilitate the comparison.

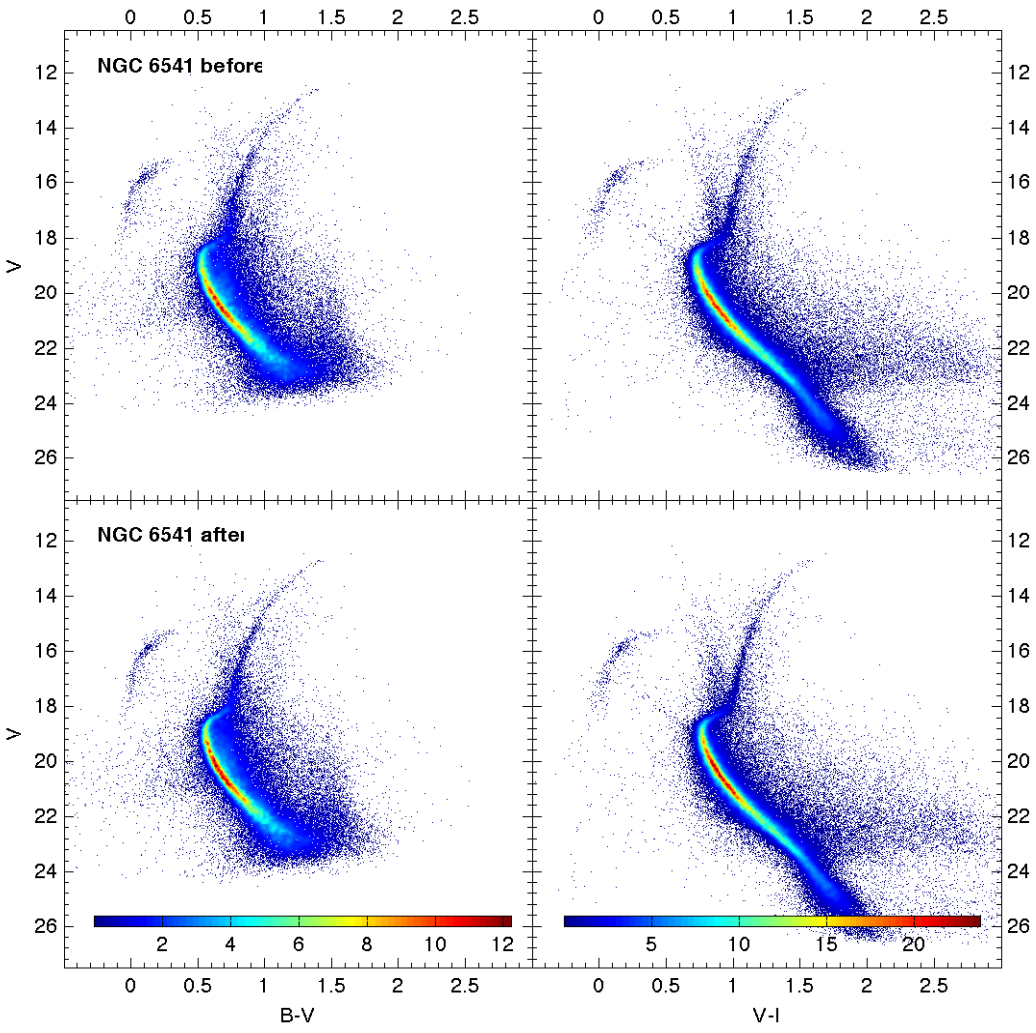

Figure 4.38. CMDs of cluster NGC 6541, before and after being differentially dereddened. Only our Magellan photometry was used to build the $B-V$ vs. V CMD. ACS photometry (from project 10775) and Magellan photometry were used to build the $V-I$ vs. V CMD. Color bars show the range in the densities of stars in the CMD ($\times 10^4$ stars per square magnitude). The color ranges are the same for a given color (B-V or V-I) in the CMD before and after applying our technique.

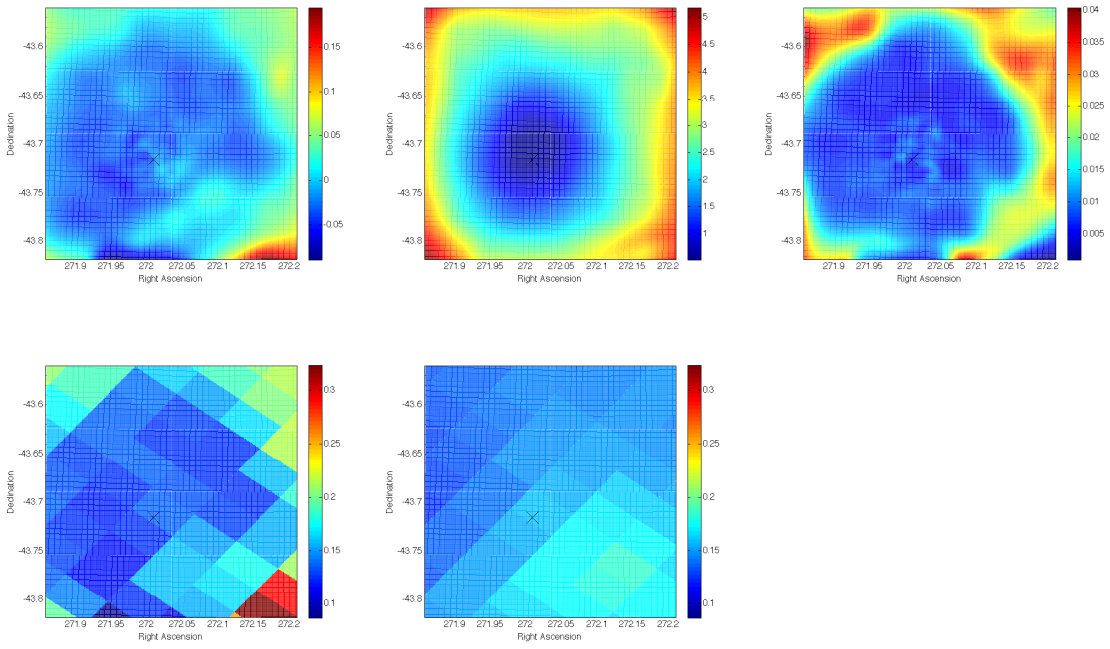

Figure 4.39. Extinction map for the cluster NGC 6541 field (top left), along its resolution (top middle), and its precision (top right), as provided by our technique. The x marks the position where the center of the cluster is. The color code gives the color excesses $E(B-V)$ for the extinction map, the bandwidths used in the resolution map, and the standard deviation σ of the color excesses in the precision maps. On the bottom, we have degraded (see text) our map (bottom left) to compare it with the SFD map (bottom right). From the comparison of both we have obtained a reddening zero point for our map, that we have added to facilitate the comparison.

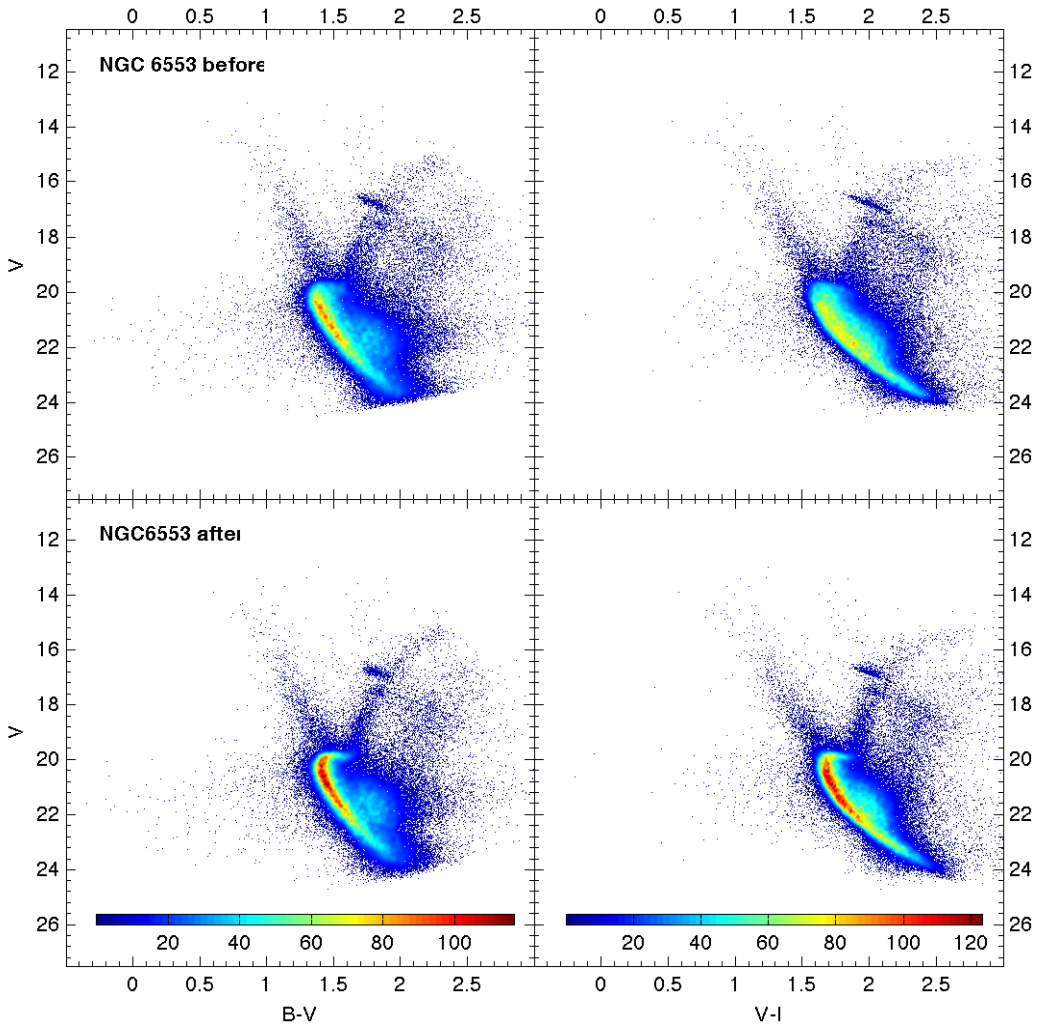

Figure 4.40. CMDs of cluster NGC 6553, before and after being differentially dereddened. ACS photometry (from our project 10573) and our Magellan photometry were used to build the CMDs in both colors. Color bars show the range in the densities of stars in the CMD ($\times 10^4$ stars per square magnitude). The color ranges are the same for a given color (B-V or V-I) in the CMD before and after applying our technique.

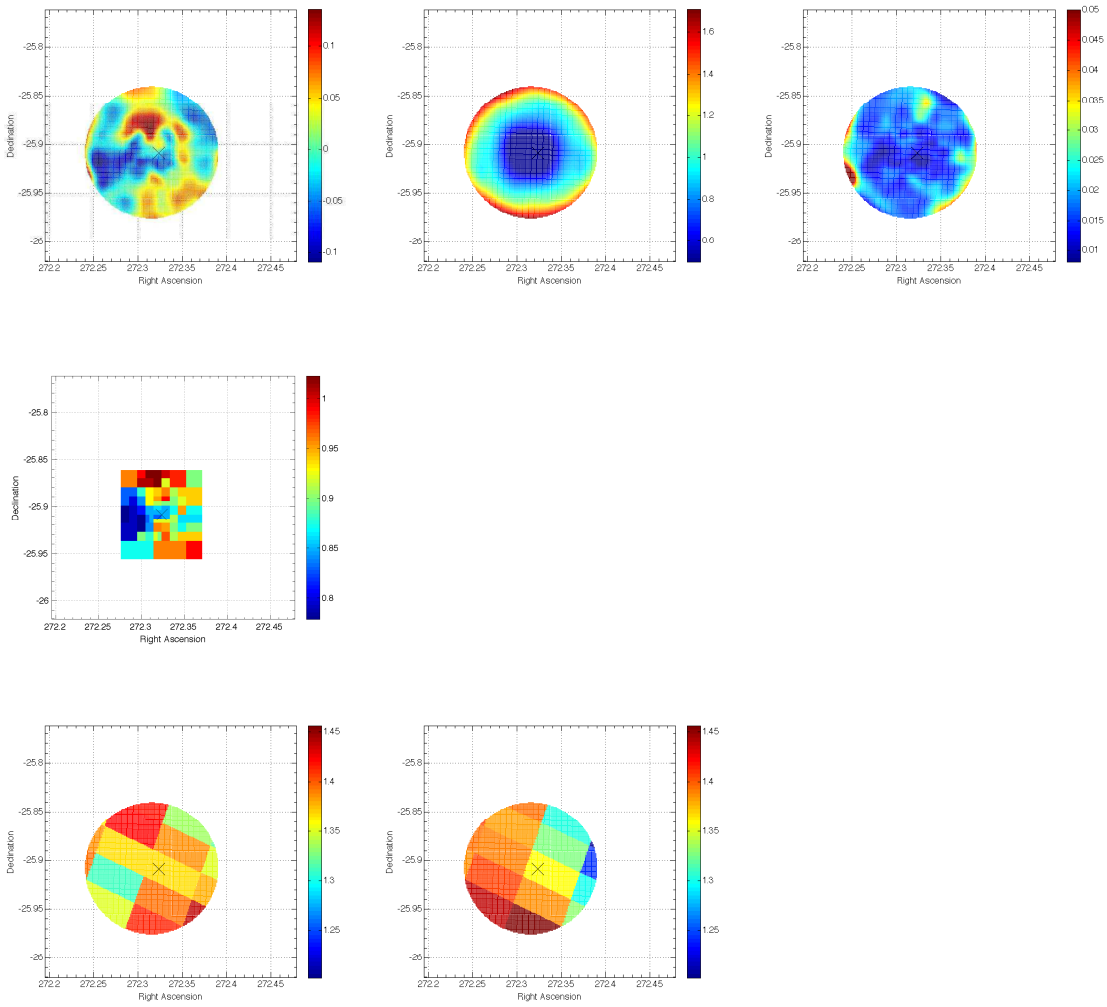

Figure 4.41. Extinction map for the cluster NGC 6553 field (top left), along its resolution (top middle), and its precision (top right), as provided by our technique. The x marks the position where the center of the cluster is. The color code gives the color excesses $E(B-V)$ for the extinction map, the bandwidths used in the resolution map, and the standard deviation σ of the color excesses in the precision maps. On the middle, extinction map provided by Heitsch & Richtler (1999). The color range is the same as in our extinction map (top left) to facilitate the visual comparison between maps, but with a different zero point. On the bottom, we have degraded (see text) our map (bottom left) to compare it with the SFD map (bottom right). From the comparison of both we have obtained a reddening zero point for our map, that we have added to facilitate the comparison.

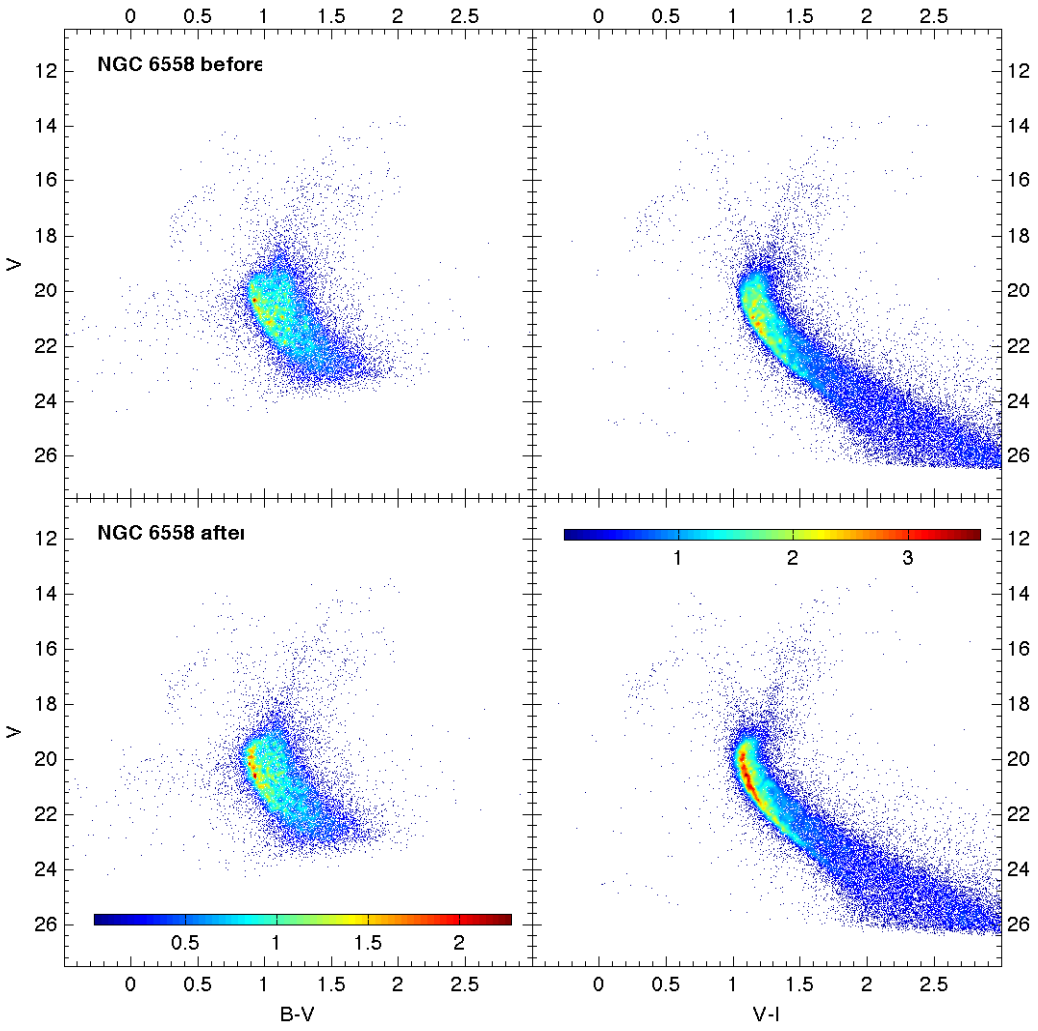

Figure 4.42. CMDs of cluster NGC 6558, before and after being differentially dereddened. Only our Magellan photometry was used to build the $B-V$ vs. V CMD. ACS photometry (from project 9799) and Magellan photometry were used to build the $V-I$ vs. V CMD. Notice that the $B-V$ vs. V CMD could not be correctly calibrated in color using the method described in the text because of the lack of calibrating data in the B filter. Color bars show the range in the densities of stars in the CMD ($\times 10^4$ stars per square magnitude). The color ranges are the same for a given color (B-V or V-I) in the CMD before and after applying our technique.

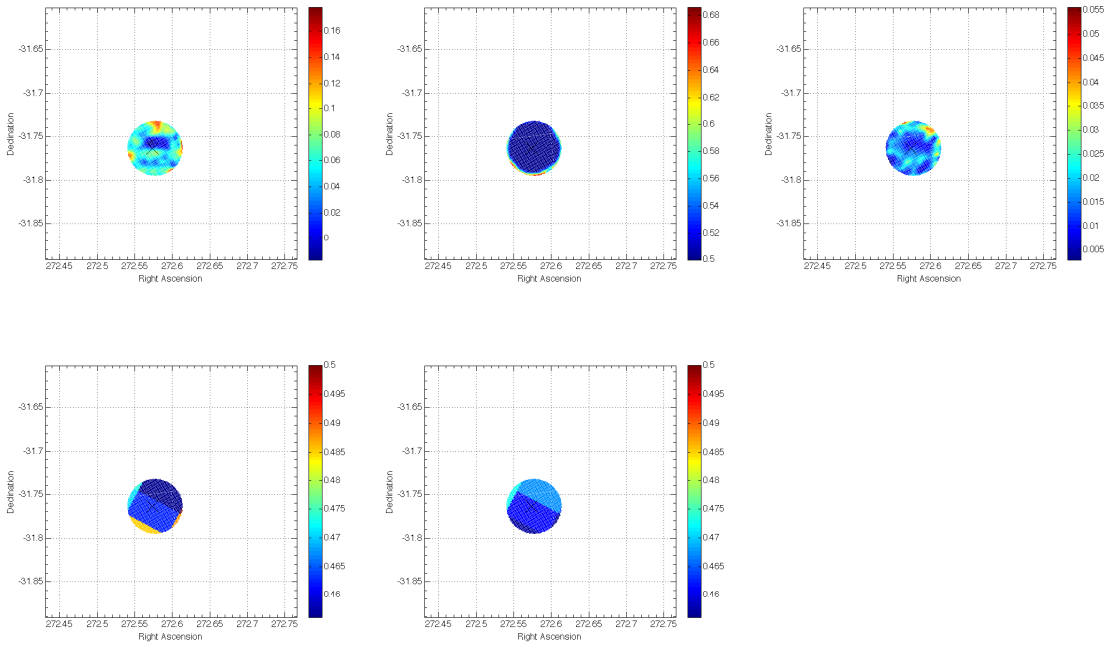

Figure 4.43. Extinction map for the cluster NGC 6558 field (top left), along its resolution (top middle), and its precision (top right), as provided by our technique. The x marks the position where the center of the cluster is. The color code gives the color excesses $E(B-V)$ for the extinction map, the bandwidths used in the resolution map, and the standard deviation σ of the color excesses in the precision maps. On the bottom, we have degraded (see text) our map (bottom left) to compare it with the SFD map (bottom right). From the comparison of both we have obtained a reddening zero point for our map, that we have added to facilitate the comparison.

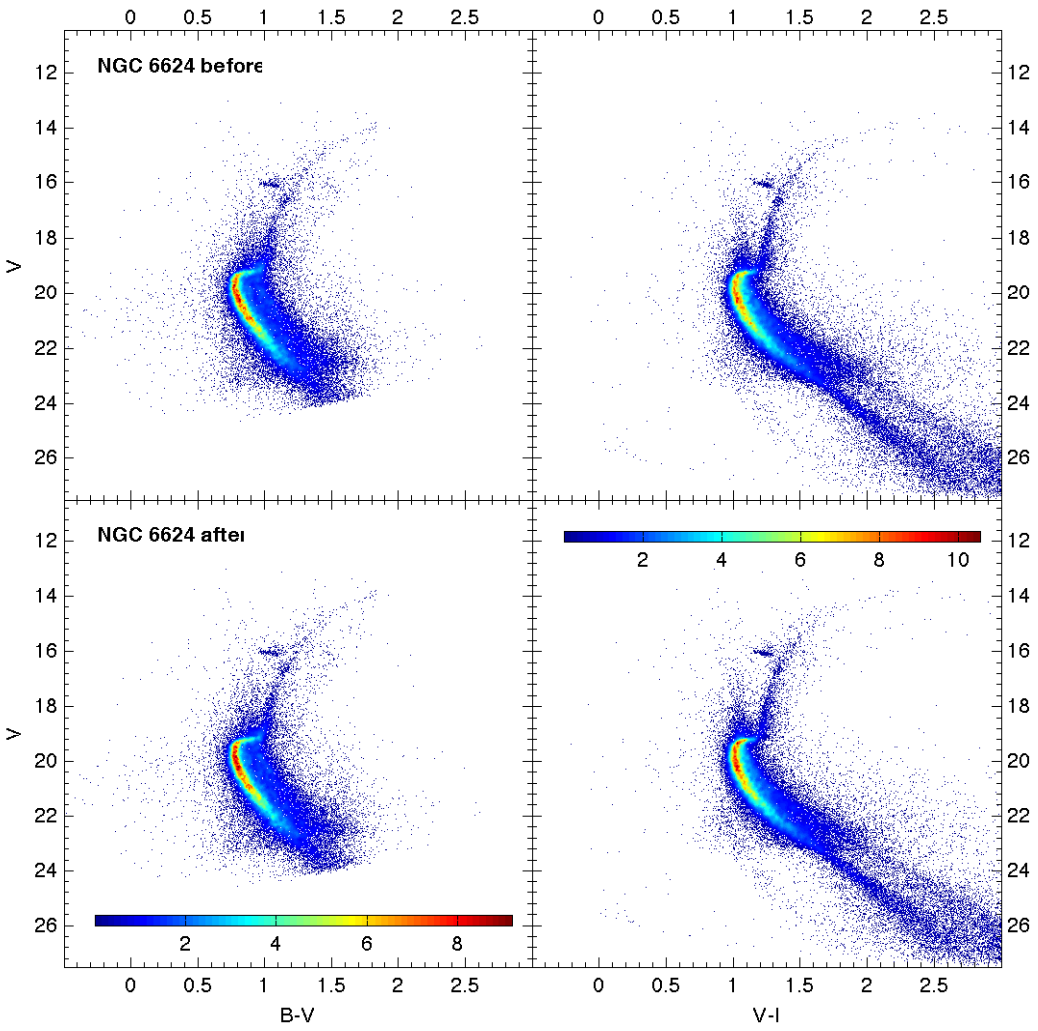

Figure 4.44. CMDs of cluster NGC 6624, before and after being differentially dereddened. ACS photometry (from our project 10573) and Magellan photometry were used to build the $B-V$ vs. V CMD. ACS photometry (from project 10775) and Magellan photometry were used to build the $V-I$ vs. V CMD. Color bars show the range in the densities of stars in the CMD ($\times 10^4$ stars per square magnitude). The color ranges are the same for a given color (B-V or V-I) in the CMD before and after applying our technique.

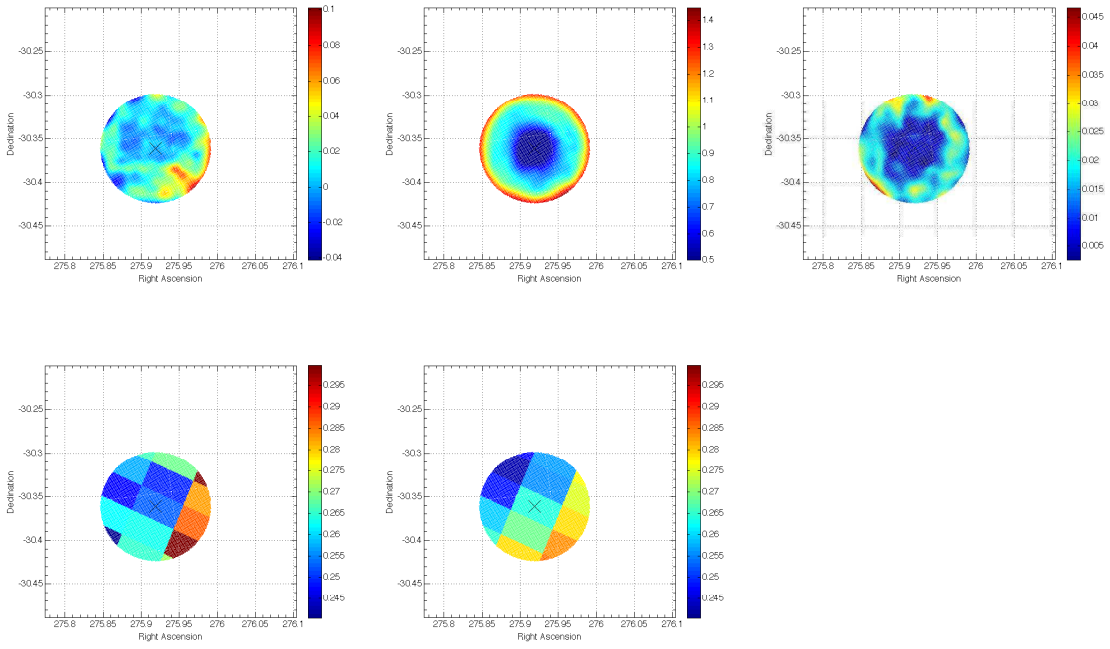

Figure 4.45. Extinction map for the cluster NGC 6624 field (top left), along its resolution (top middle), and its precision (top right), as provided by our technique. The x marks the position where the center of the cluster is. The color code gives the color excesses $E(B-V)$ for the extinction map, the bandwidths used in the resolution map, and the standard deviation σ of the color excesses in the precision maps. On the bottom, we have degraded (see text) our map (bottom left) to compare it with the SFD map (bottom right). From the comparison of both we have obtained a reddening zero point for our map, that we have added to facilitate the comparison.

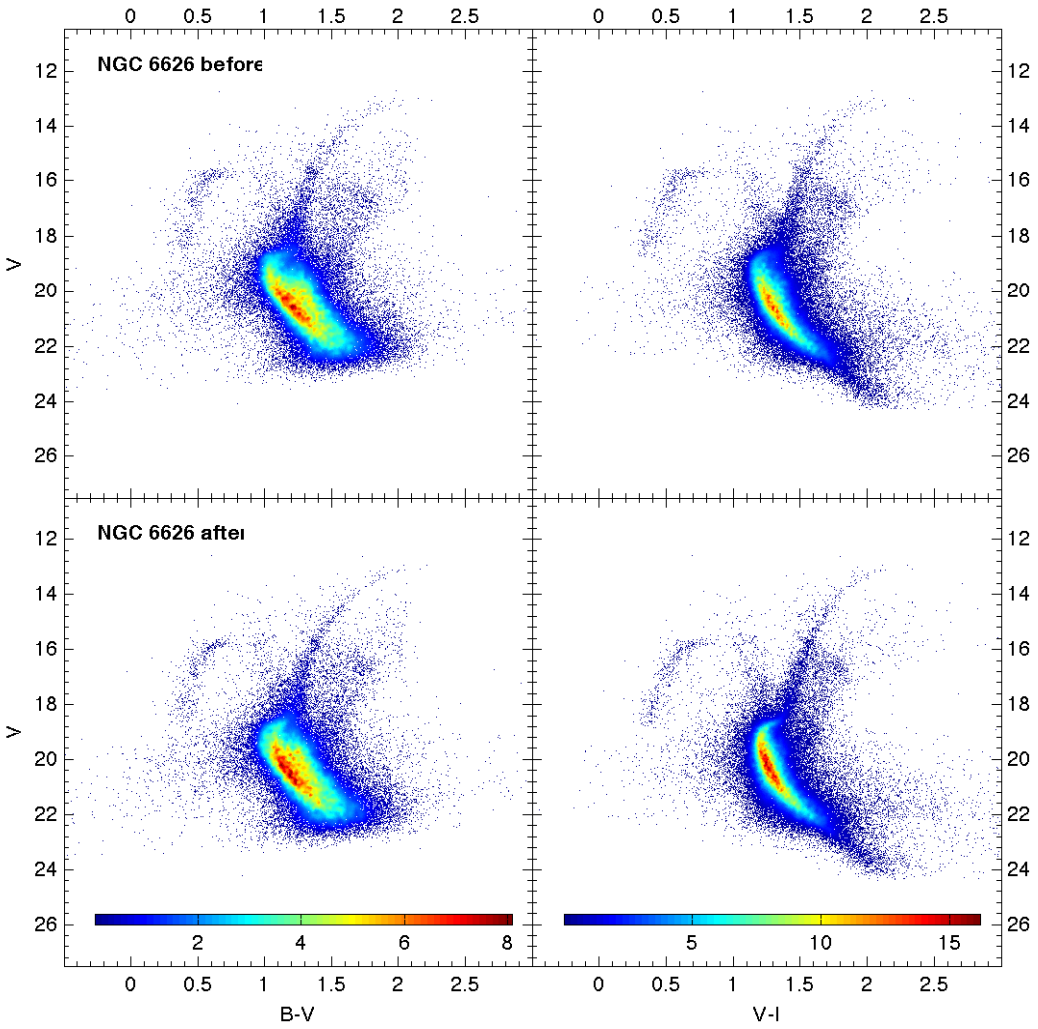

Figure 4.46. CMDs of cluster NGC 6626 - M 28, before and after being differentially dereddened. Only our Magellan photometry was used to build the $B-V$ vs. V CMD. WFPC2 photometry (from project 6779) and Magellan photometry were used to build the $V-I$ vs. V CMD. Notice that the $B-V$ vs. V CMD could not be correctly calibrated in color using the method described in the text because of the lack of calibrating data in the B filter. Color bars show the range in the densities of stars in the CMD ($\times 10^4$ stars per square magnitude). The color ranges are the same for a given color (B-V or V-I) in the CMD before and after applying our technique.

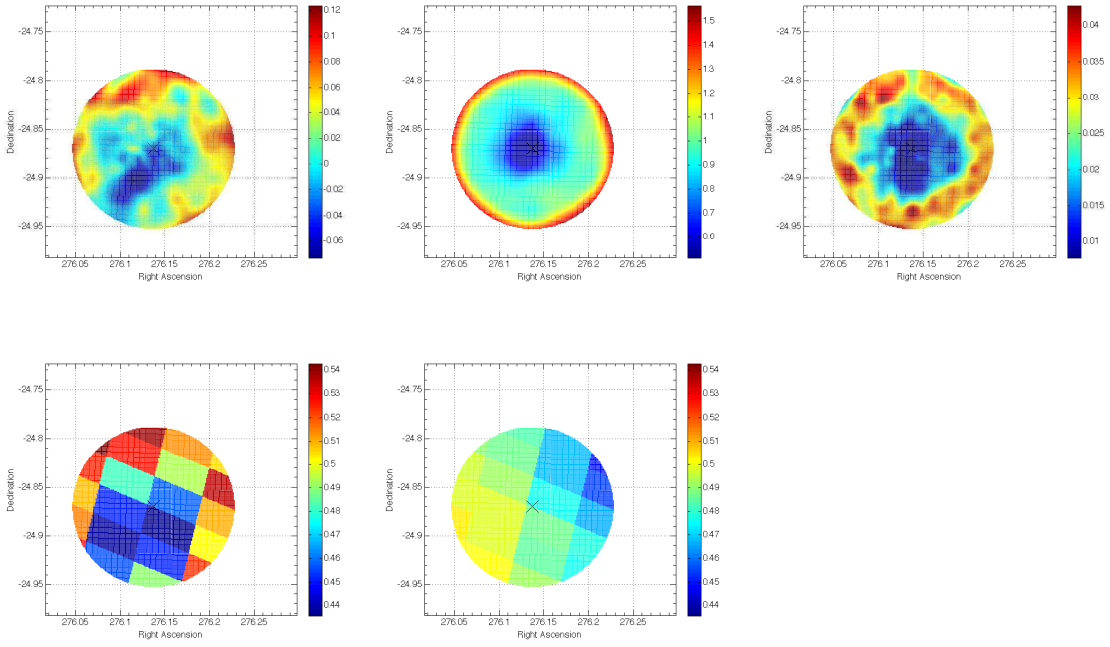

Figure 4.47. Extinction map for the cluster NGC 6626 - M 28 field (top left), along its resolution (top middle), and its precision (top right), as provided by our technique. The x marks the position where the center of the cluster is. The color code gives the color excesses $E(B-V)$ for the extinction map, the bandwidths used in the resolution map, and the standard deviation σ of the color excesses in the precision maps. On the bottom, we have degraded (see text) our map (bottom left) to compare it with the SFD map (bottom right). From the comparison of both we have obtained a reddening zero point for our map, that we have added to facilitate the comparison.

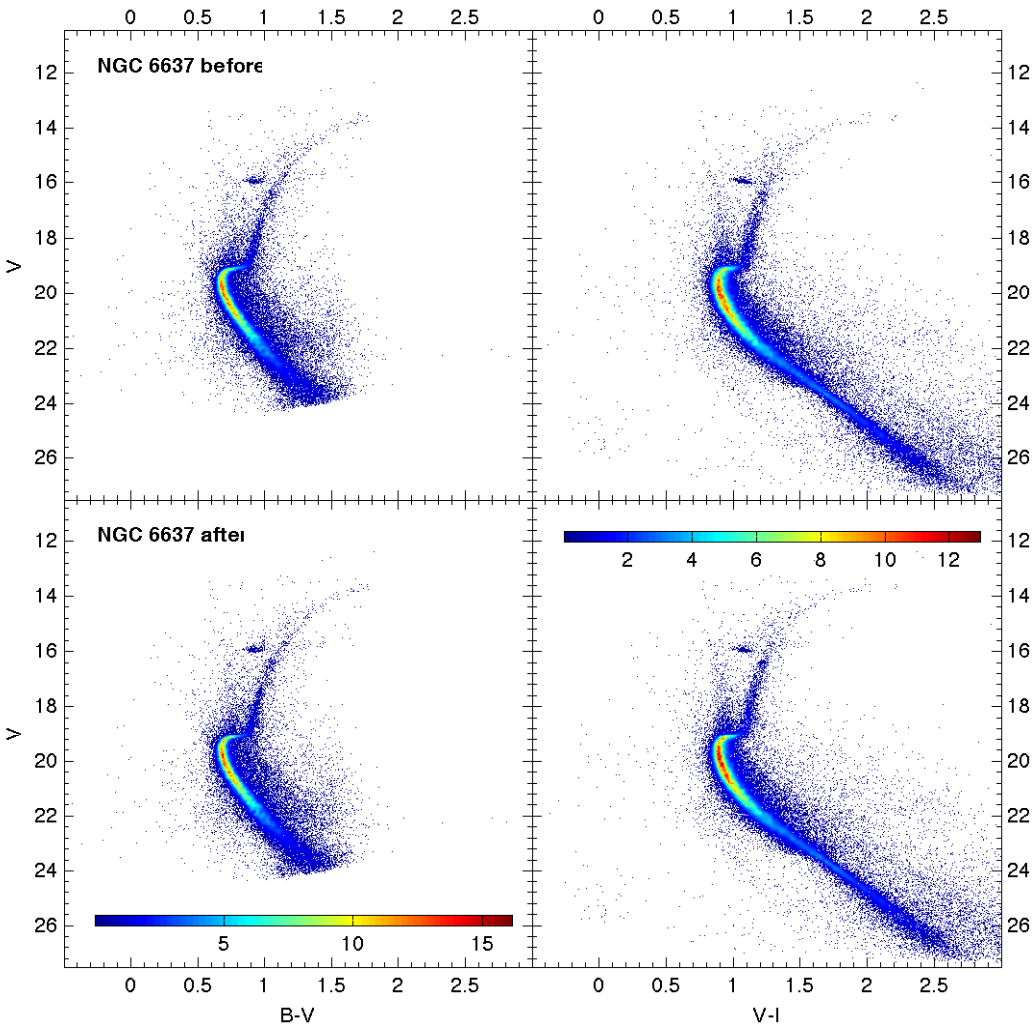

Figure 4.48. CMDs of cluster NGC 6637 - M 69, before and after being differentially dereddened. ACS photometry (from our project 10573) and Magellan photometry were used to build the $B-V$ vs. V CMD. ACS photometry (from project 10775) and Magellan photometry were used to build the $V-I$ vs. V CMD. Color bars show the range in the densities of stars in the CMD ($\times 10^4$ stars per square magnitude). The color ranges are the same for a given color (B-V or V-I) in the CMD before and after applying our technique.

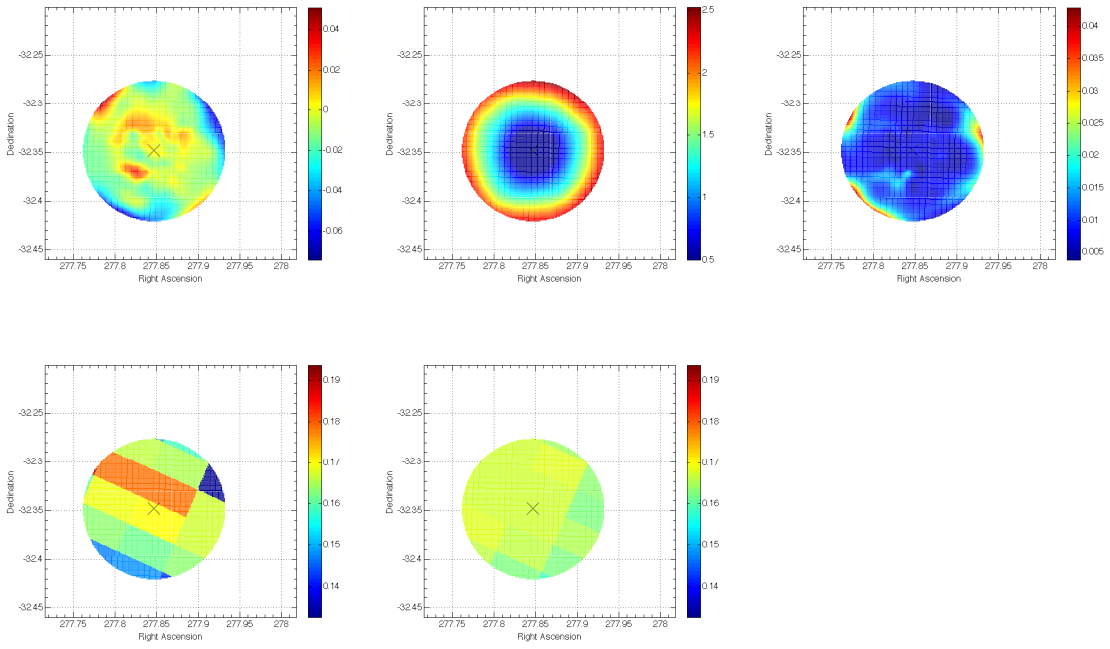

Figure 4.49. Extinction map for the cluster NGC 6637 - M 69 field (top left), along its resolution (top middle), and its precision (top right), as provided by our technique. The x marks the position where the center of the cluster is. The color code gives the color excesses $E(B-V)$ for the extinction map, the bandwidths used in the resolution map, and the standard deviation σ of the color excesses in the precision maps. On the bottom, we have degraded (see text) our map (bottom left) to compare it with the SFD map (bottom right). From the comparison of both we have obtained a reddening zero point for our map, that we have added to facilitate the comparison.

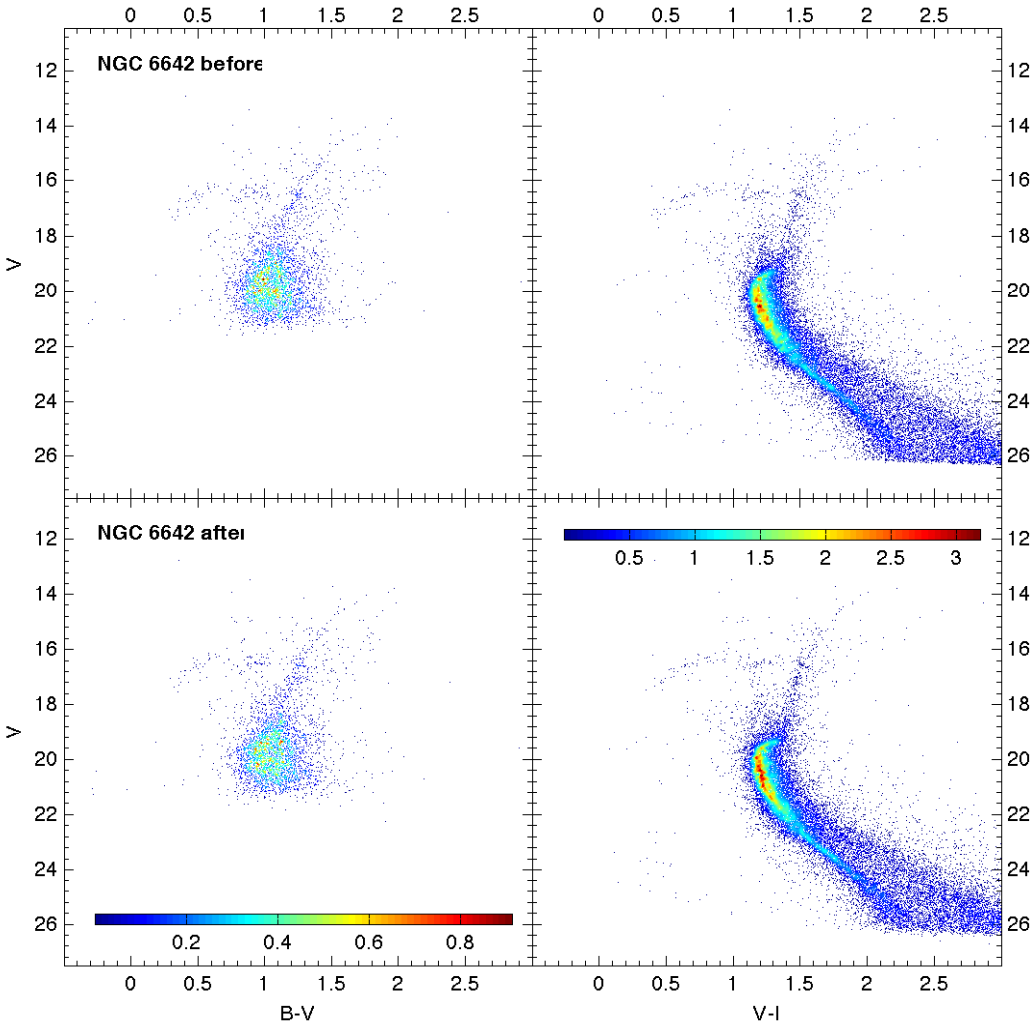

Figure 4.50. CMDs of cluster NGC 6642, before and after being differentially dereddened. Only our Magellan photometry was used to build the $B-V$ vs. V CMD. ACS photometry (from project 10775) and Magellan photometry were used to build the $V-I$ vs. V CMD. Color bars show the range in the densities of stars in the CMD ($\times 10^4$ stars per square magnitude). The color ranges are the same for a given color (B-V or V-I) in the CMD before and after applying our technique.

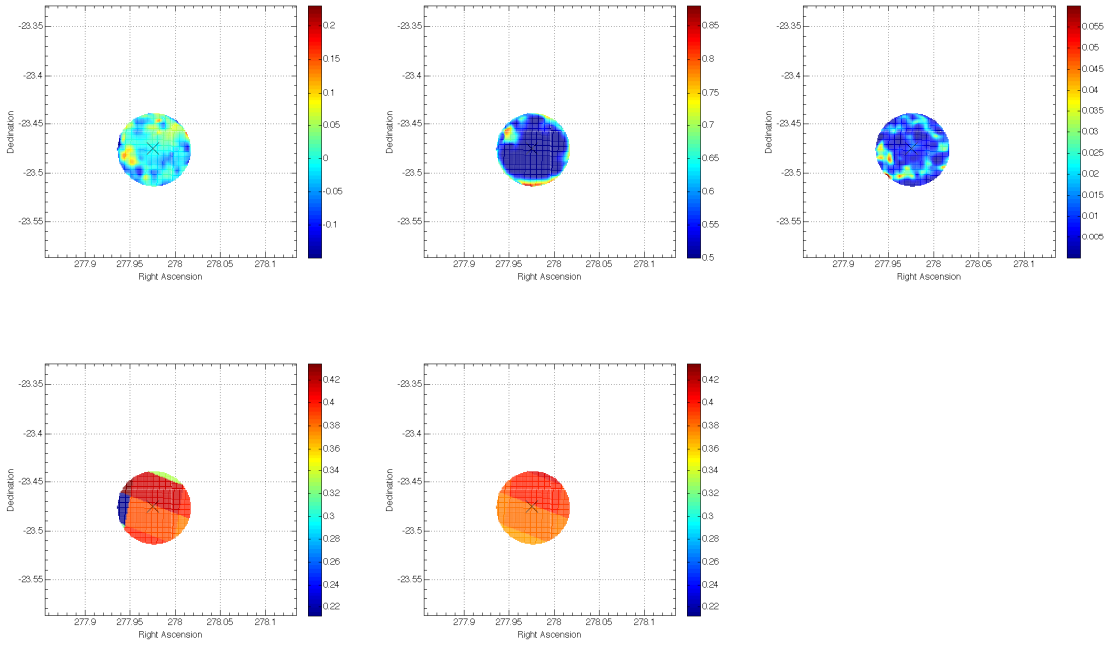

Figure 4.51. Extinction map for the cluster NGC 6642 field (top left), along its resolution (top middle), and its precision (top right), as provided by our technique. The x marks the position where the center of the cluster is. The color code gives the color excesses $E(B-V)$ for the extinction map, the bandwidths used in the resolution map, and the standard deviation σ of the color excesses in the precision maps. On the bottom, we have degraded (see text) our map (bottom left) to compare it with the SFD map (bottom right). From the comparison of both we have obtained a reddening zero point for our map, that we have added to facilitate the comparison.

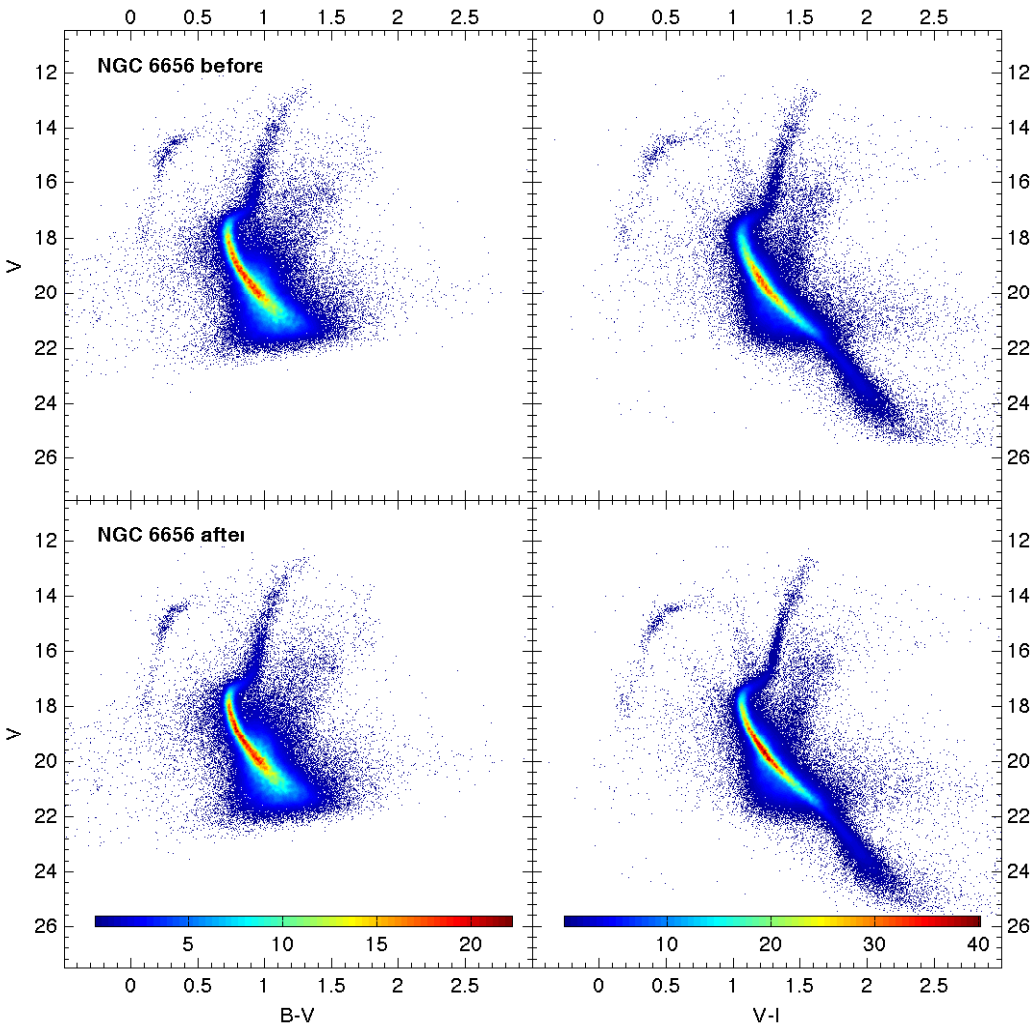

Figure 4.52. CMDs of cluster NGC 6656 - M 22, before and after being differentially dereddened. Only our Magellan photometry was used to build the $B-V$ vs. V CMD. ACS photometry (from project 10775) and Magellan photometry were used to build the $V-I$ vs. V CMD. Color bars show the range in the densities of stars in the CMD ($\times 10^4$ stars per square magnitude). The color ranges are the same for a given color (B-V or V-I) in the CMD before and after applying our technique.

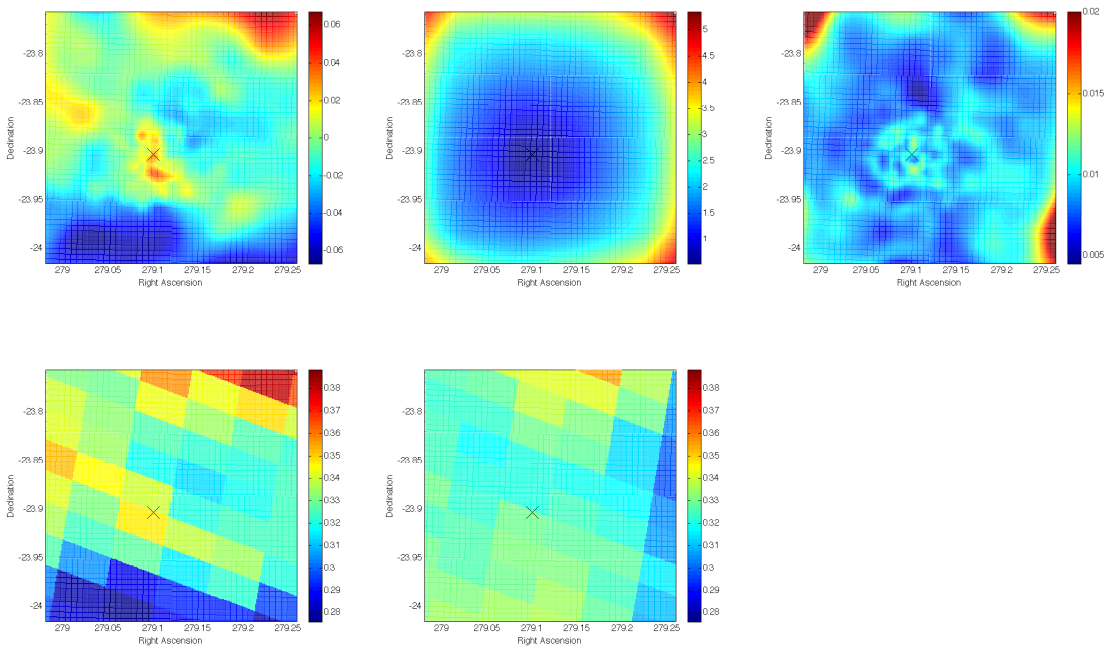

Figure 4.53. Extinction map for the cluster NGC 6656 - M 22 field (top left), along its resolution (top middle), and its precision (top right), as provided by our technique. The x marks the position where the center of the cluster is. The color code gives the color excesses $E(B-V)$ for the extinction map, the bandwidths used in the resolution map, and the standard deviation σ of the color excesses in the precision maps. On the bottom, we have degraded (see text) our map (bottom left) to compare it with the SFD map (bottom right). From the comparison of both we have obtained a reddening zero point for our map, that we have added to facilitate the comparison.

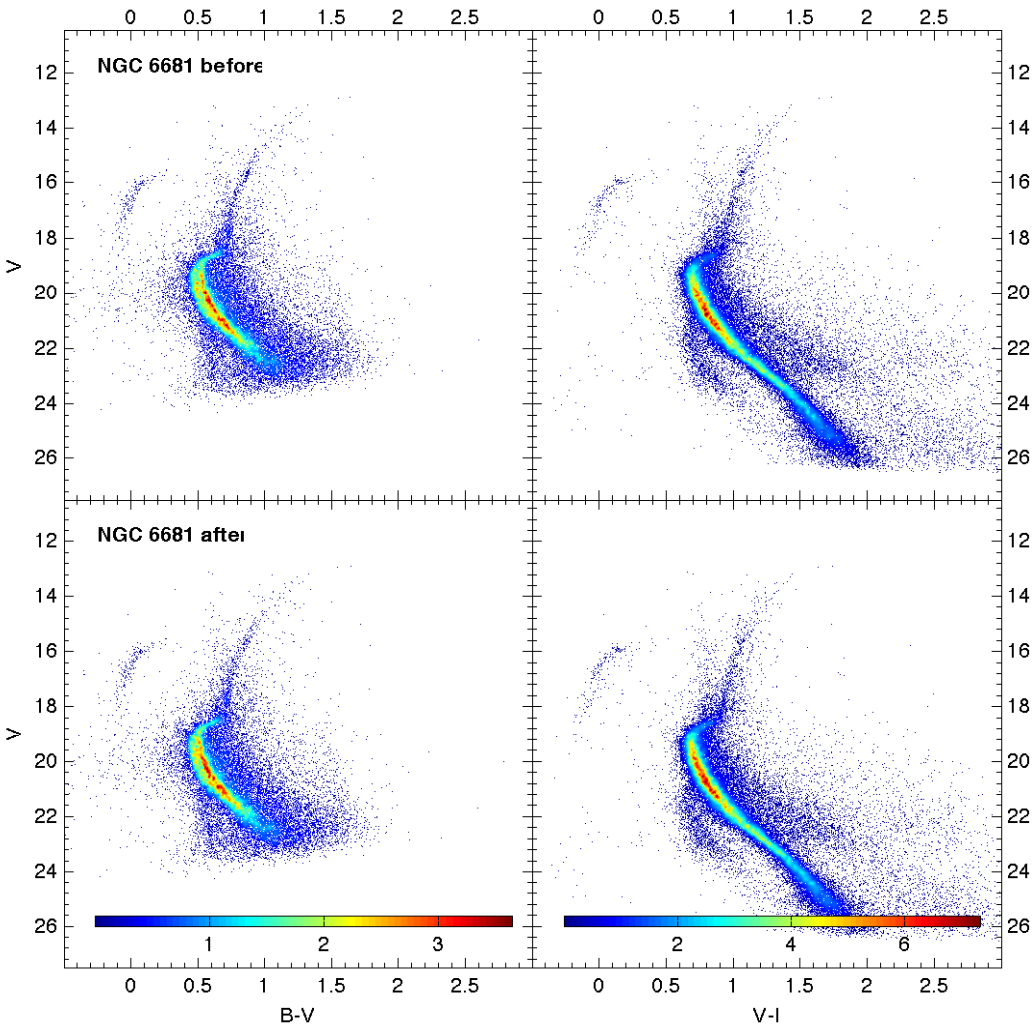

Figure 4.54. CMDs of cluster NGC 6681 - M 70, before and after being differentially dereddened. Only our Magellan photometry was used to build the $B-V$ vs. V CMD. ACS photometry (from project 10775) and Magellan photometry were used to build the $V-I$ vs. V CMD. Color bars show the range in the densities of stars in the CMD ($\times 10^4$ stars per square magnitude). The color ranges are the same for a given color (B-V or V-I) in the CMD before and after applying our technique.

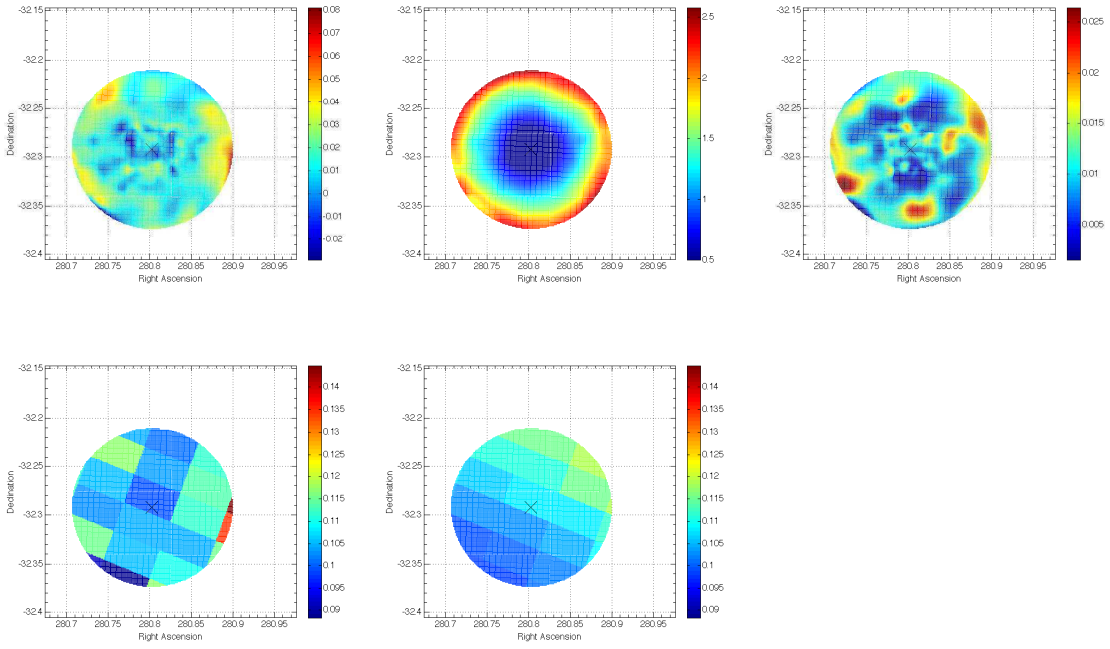

Figure 4.55. Extinction map for the cluster NGC 6681 - M 70 field (top left), along its resolution (top middle), and its precision (top right), as provided by our technique. The x marks the position where the center of the cluster is. The color code gives the color excesses $E(B-V)$ for the extinction map, the bandwidths used in the resolution map, and the standard deviation σ of the color excesses in the precision maps. On the bottom, we have degraded (see text) our map (bottom left) to compare it with the SFD map (bottom right). From the comparison of both we have obtained a reddening zero point for our map, that we have added to facilitate the comparison.

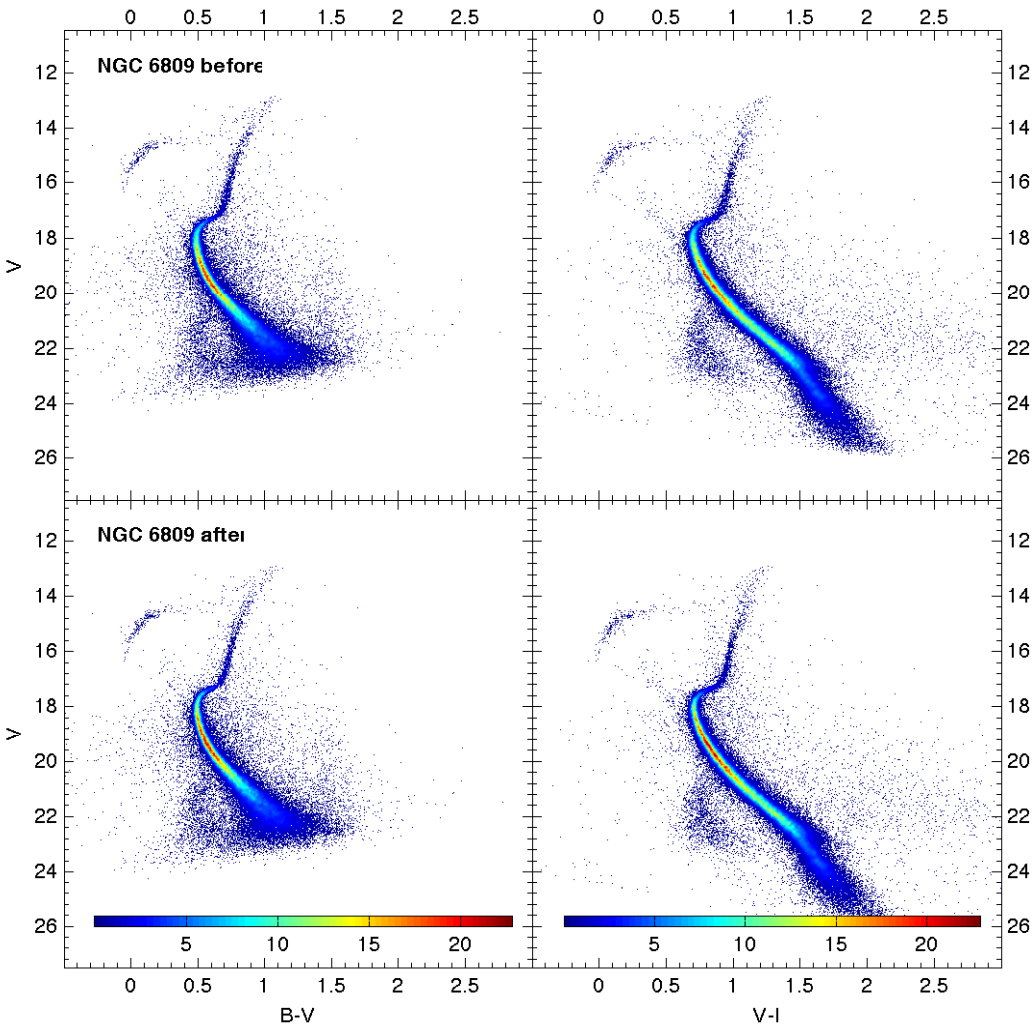

Figure 4.56. CMDs of cluster NGC 6809 - M 55, before and after being differentially dereddened. Only our Magellan photometry was used to build the $B-V$ vs. V CMD. ACS photometry (from project 10775) and Magellan photometry were used to build the $V-I$ vs. V CMD.Color bars show the range in the densities of stars in the CMD ($\times 10^4$ stars per square magnitude). The color ranges are the same for a given color (B-V or V-I) in the CMD before and after applying our technique.

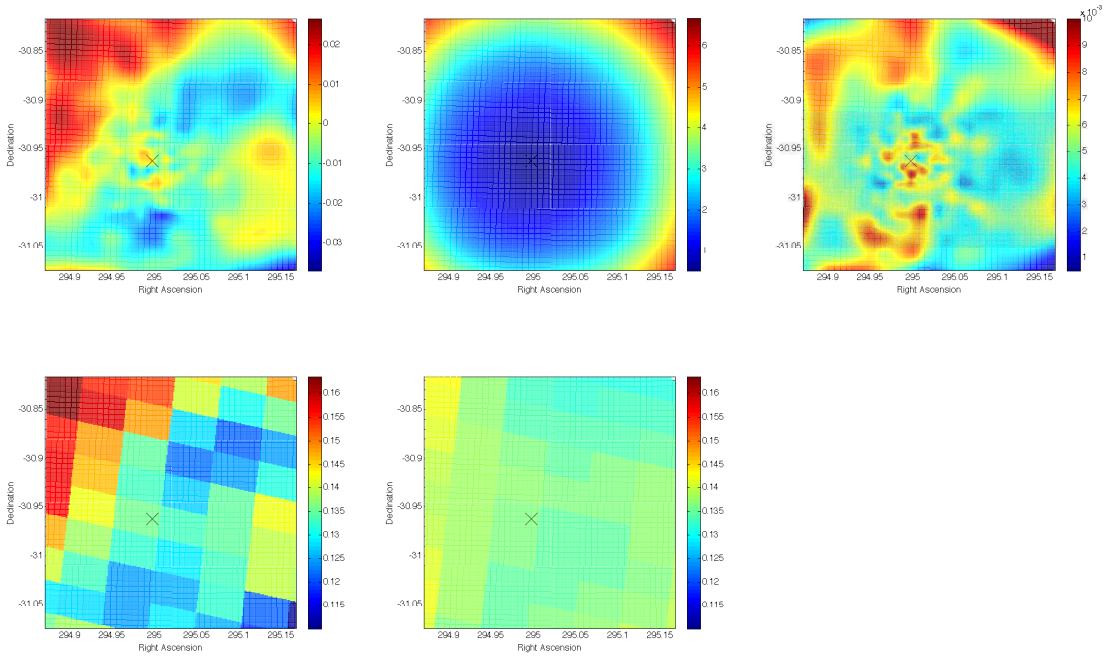

Figure 4.57. Extinction map for the cluster NGC 6809 - M 55 field (top left), along its resolution (top middle), and its precision (top right), as provided by our technique. The x marks the position where the center of the cluster is. The color code gives the color excesses $E(B-V)$ for the extinction map, the bandwidths used in the resolution map, and the standard deviation σ of the color excesses in the precision maps. On the bottom, we have degraded (see text) our map (bottom left) to compare it with the SFD map (bottom right). From the comparison of both we have obtained a reddening zero point for our map, that we have added to facilitate the comparison.

CHAPTER 5

Analysis of the stellar populations of the sampled clusters

The main goal of this thesis is the age determination of the sampled GGCs. Direct comparison between theoretical isochrones and observational CMDs of GGCs is the most natural approach to reach it. But uncertainties in the physics of the models (Cassisi, 2009) create concerns whether a global fit of all the regions in the isochrone to the model is correct (Salaris & Cassisi, 2005). This is why the calculation of relative ages in a group of clusters using some age-related features of the models whose physics are not so affected by current uncertainties has been preferred in many studies (Rosenberg et al., 2000a; Marín-Franch et al., 2009).

From the observation of a set of isochrones with different age and metallicity inputs we can obtain an idea of how these different inputs change the shape of the sequences (Salaris & Cassisi, 2005)

- The RGB and lower MS shapes are mainly affected by the metallicity of the cluster, but not by the age (see figure 5.1). Low MS stars in GGCs are still in the Zero Age Main Sequence (ZAMS) since they have not had time to evolve yet. The sequences become fainter and cooler with increasing Z due to the increment in radiative opacity. The RGB sequences become cooler and less steep with increasing Z due to the increment of the envelope opacity, which causes a more extended envelope convection zone.

- The TO location is both affected by the age and by the metallicity of the cluster (see figures 5.1 and 5.2). It becomes redder and dimmer with increasing age, since less massive stars can evolve from the MS to the RGB, and for the same

age, it is redder and dimmer with increasing metallicity.

- The brightness of the Zero Age Horizontal Branch (ZAHB) depends on metallicity, but not on age (see figure 5.1). The ZAHB becomes fainter with increasing Z due to the decrease of the mass of the He core at the He flash, and the increase of the opacity.

We should also notice here the effects produced by two other input physical parameters:

- An increase in the He content produces MS and RGB sequences brighter and hotter, and reduced evolutionary times along them, due to the decrease in opacity and increase in the mean molecular weight, which consequently produces an increase of the nuclear H-burning reaction rate. For the ZAHB we should also take into account that an increase in He content causes a decrease in the mass of the He core. Therefore for stars with low-mass envelopes (blue part of the ZAHB) this last effect dominates and the ZAHB becomes fainter, while for stars with high-mass envelopes (red part of the ZAHB) the efficient H-burning in the shell counterbalances this effect, and the tracks become brighter.

- The enhancement in α elements (i.e., the elements synthesized by nuclear α-captured reactions: O, Ne, Mg, Si, S, Ca, ...) observed in the stars in the clusters with respect to the solar mixture, produces MS sequences cooler and fainter with respect to scaled solar ones, and RGB tracks cooler and less steep, due to the increment in opacity (see figure 5.1). These effects increase as the metallicity does.

5.1 Obtaining the ages

In this thesis we calculate the ages of the sampled clusters using the ridgelines previously obtained for every GC (see figures 4.5 and 4.6), and comparing their upper MS and their SGB ($M_V^{TO} - 1.5 \leq M_V \leq M_V^{TO} + 2.0$) with modeled isochrones. We choose these two regions of the evolutionary sequence because changes in age affect them

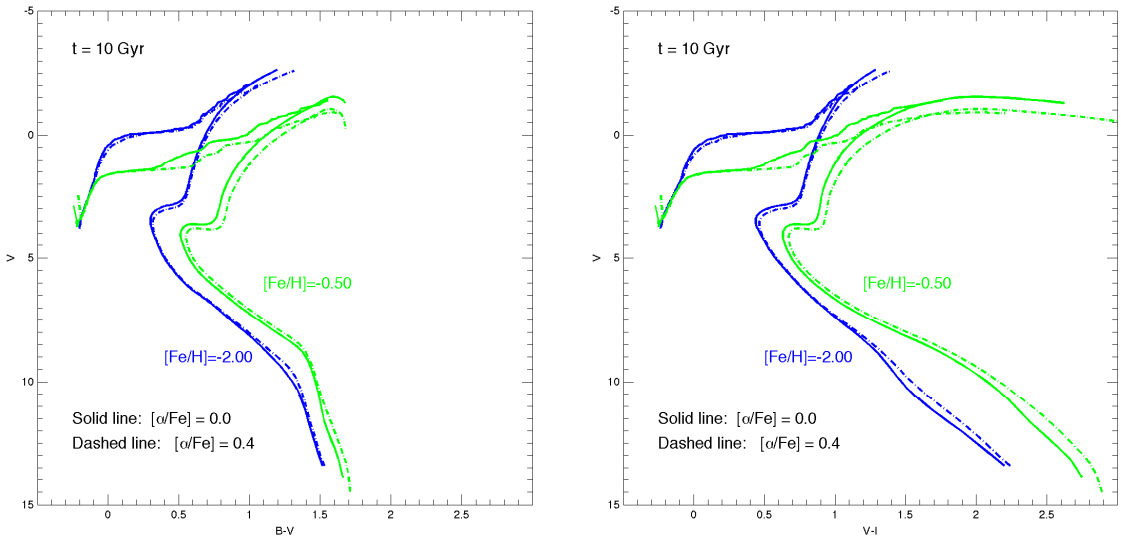

Figure 5.1. Modeled isochrones that show the effect of a change in metallicity. The main effects are redder sequences, less steep RGBs, longer in color SGBs, dimmer and redder TO points and fainter ZAHB, for increasing metallicities. Increasing abundances of alpha elements strengthen these features.

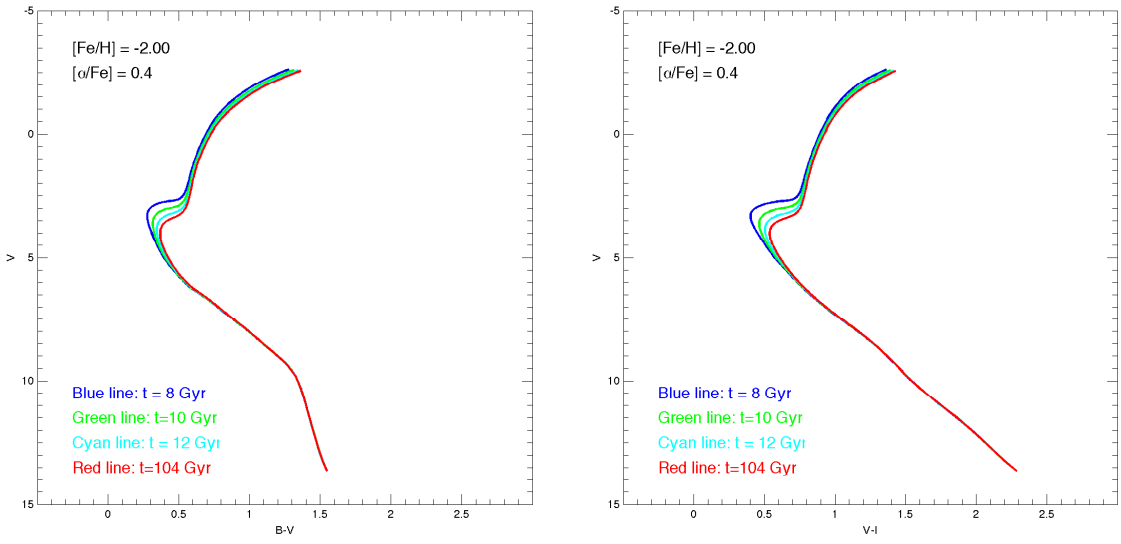

Figure 5.2. Modeled isochrones that show the effect of a change in age. The main effects are dimmer and redder TO points and shorter in colors SGBs for increasing ages.

significantly, uncertainties in the physics of the models are smaller than for other regions (Cassisi, 2009), and the ridgelines are generally well defined for them. The isochrones used are those provided by the Dartmouth group [1] (Dotter et al., 2007). Such a comparison suffers from the degeneracy between distance, absolute reddening, metallicity and age of the cluster. To simplify the analysis, we assume a metallicity for every cluster, taking the values provided in the 2009 version of the Harris catalog (Harris, 1996). We then proceed as follows:

- We obtain a set of isochrones with a metallicity equal to that of the cluster, and range in ages between 8 and 15 Gyrs using intervals of 0.5 Gyrs. The isochrones are chosen to have enhancements of $[\alpha/Fe] = 0.4$ for clusters with metallicity $[Fe/H] < -1$, and $[\alpha/Fe] = 0.2$ for clusters with metallicity $[Fe/H] > -1$. These values are chosen according to current literature estimates for the Milky Way clusters (Venn et al., 2004; Kirby et al., 2008).

- We find the observational TO point, defined as the bluest point on our ridgeline. The TO allows us to define the upper MS and SGB in the ridgeline as all the points with magnitude $M_V^{TO} - 1.5 \leq M_V \leq M_V^{TO} + 2.0$.

- We find the TO point also in the isochrones. The difference in magnitude between the TO of the isochrones and the TO point of the ridgeline provides us with a first guess of the distance modulus of the cluster [2]. In our fits, we are going to test distance moduli in the range $[\mu_V^{TO} - 1, \mu_V^{TO} + 1]$, changing in intervals of 0.01 magnitudes.

- We shift the magnitudes of the MS and SGB points of the ridgeline according to one of the test distances. Then we obtain the points in the ridgeline at the test age with magnitudes equal to those of the MS and SGB points of the ridgeline.

[1] The isochrones can be easily obtained via the web interface provided at: http://stellar.dartmouth.edu/ models/isolf.html

[2] Strictly speaking, the difference between the magnitude of the TO points gives the distance modulus μ_V^{TO} of the cluster, but the error in the TO point magnitude in the ridgeline can be significant, so it is better to take it as a first guess, and find the distance more correctly using all points in the SGB and MS

After that, we fit both isochrone and ridgeline points just by doing a color offset for every point. The mean of the color offsets obtained provides the absolute reddening, if we have the right distance and age. The standard deviation of the color offsets gives information about the goodness of the fit for a given distance and age. We represent this standard deviation in a contour map (see all contour maps in this section). These maps give a measure of the uncertainty in our approximation, and the location of the minimum value in them provides the best values of the fit for the age and distance, and consequently, also with the best absolute extinction.

To understand the significance of the standard deviation values in the mean of the color offsets as a measure of the goodness of the fit, we choose a qualitative path. We examine the case of one of the clusters in our sample, NGC 6218, and obtain the best fit using our approximation (see figure 5.3 top). We find from visual inspection that the agreement between observation and model begin to fail when we change the age by 1.5 Gyr, keeping the distance modulus and absolute reddening of our best fit model (see figure 5.3 middle), or when we change the distance modulus by 0.1, keeping the age and absolute reddening of our best fit model (see figure 5.3 bottom). In order to be consistent in our analysis, we consider now the best fit isochrone as the ridgeline of our observation, and repeat the analysis trying to fit the best isochrone. The standard deviation in the color offset for the different ages and distances tested are shown in figure 5.4. We are particularly interested in the values of the standard deviation when we change the age by 1.5 Gyr, or the distance modulus by 0.1 magnitudes. These changes translate themself in $\sigma \sim 0.016$ in the standard deviation map. We can consider this value σ_L of the standard deviation as the limit for a good fit. For clarity purposes, we are presenting from now on the standard deviation maps in the form of contour maps, and the lines will be at $0.5\sigma_L$, $1\sigma_L$, $2\sigma_L$, $3\sigma_L$, $6\sigma_L$, and $9\sigma_L$ (see fig 5.4 bottom). The colors of the lines, blue or red, provide information about which ridgeline we use for the fitting process, the one obtained from the analysis of the $B-V$ CMD, or the one obtained from the $V-I$ CMD, while the line in green is always the one located at $1\sigma_L$. We consider the best

Table 5.1. Best set of parameters obtained from the fitting of ridgelines and isochrones

Cluster	[Fe/H]	Age	μ_V	$E(B-V)$	$E(V-I)$
NGC 6121	-1.20	12.0	12.81	0.40	0.58
NGC 6144	-1.75	14.5	15.85	0.47*	0.60
NGC 6218	-1.48	13.0	14.23	0.20	0.29
NGC 6235	-1.40	13.5	16.19	0.31	0.33*
NGC 6254	-1.52	13.0	14.38	0.26	0.32
NGC 6266	-1.29	13.5	15.57	0.53	0.73
NGC 6273	-1.68	14.0	15.67	0.39	0.45
NGC 6287	-2.05	12.5	16.55	0.60	0.90
NGC 6304	-0.59	12.5	15.56	0.50	0.64
NGC 6333	-1.75	13.5	15.79	0.34	0.50
NGC 6342	-0.65	13.5	16.17	0.46	0.42*
NGC 6352	-0.70	12.5	14.45	0.24	0.32
NGC 6355	-1.50	15.0	16.84	0.86	0.90*
NGC 6397	-1.95	13.0	12.58	0.16	0.26
NGC 6522	-1.44	15.0	16.07	0.59	0.73
NGC 6541	-1.83	14.0	14.87	0.18	0.22
NGC 6553	-0.21	12.0	15.82	0.76	0.98
NGC 6558	-1.44	15.0	15.60	0.49*	0.46
NGC 6624	-0.44	12.5	15.26	0.19	0.30
NGC 6626	-1.45	14.5	15.00	0.65*	0.60
NGC 6637	-0.70	14.0	15.17	0.15	0.22
NGC 6642	-1.35	15.0	15.64	0.45	0.57
NGC 6656	-1.64	13.0	13.76	0.34	0.50
NGC 6681	-1.51	12.5	15.20	0.08	0.11
NGC 6809	-1.81	12.5	14.06	0.12	0.17

An asterisk indicates a non-calibrated color, so that color excess is not correct. That value, however, when compared with the other color excess produce by the ridgeline calculated from the other available, color-calibrated CMD, can provide a way to calibrate that color.

fit that in which the sum of standard deviation in the color offset coming from the fitting of $B-V$ and $V-I$ ridgelines reaches a minimum (see table 5.1 and figures 5.6 and following in this section). Notice that, using the Dartmouth isochrones in our sample clusters, a good fit to the upper MS and SGB also generally provides a good fit to the RGB, and a slightly worse fit to the lower MS.

Other sources of error can include a mistake in the metallicity or the $[\alpha/Fe]$ ratio selection. In figures 5.5 (top and middle) we examine the effects of changing the metallicity by $+0.3$ dex or -0.3 dex respectively. We observe that after finding the best parameters for the MS and SGB fit, the different metallicities translate to a worse fit for the RGB region. The age and distances with this change in metallicity differ from the ones obtained with the metallicity taken from the Harris catalog by ~ 0.5 Gyrs and 0.05 magnitudes in the distance modulus. Similar results happen if we change the $[\alpha/Fe]$ ratio for the clusters (see figure 5.5 (bottom), where we check the effect of using a solar scaled isochrone).

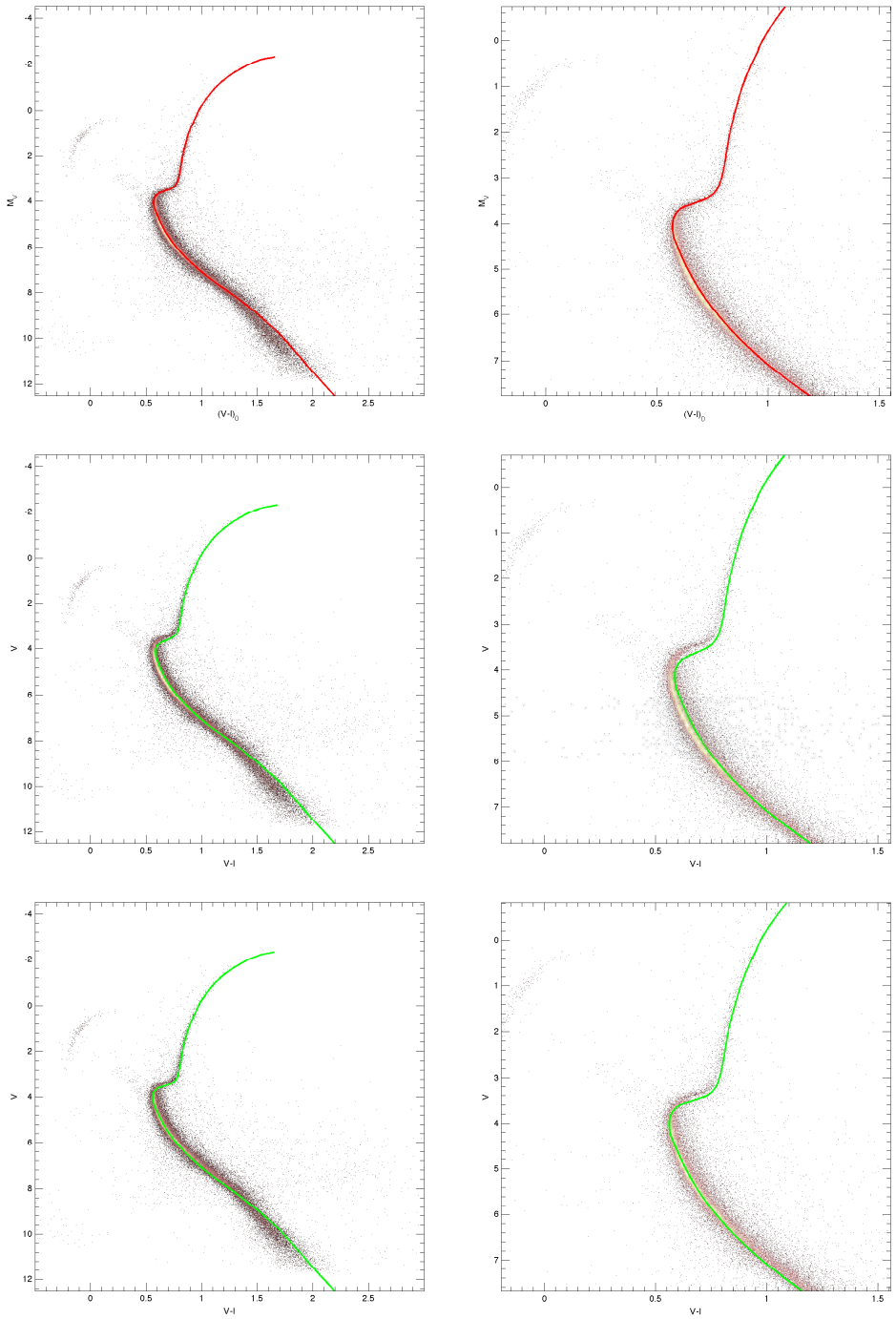

Figure 5.3. CMD of NGC 6218, corrected with the best parameters provided with the ridgeline-isochrone fit, plotted against the best fit isochrone (top, in red), an isochrone at the same distance but 1.5 Gyr older than the best fit (middle), and an isochrone of equal age but moved 0.1 magnitudes with respect to the best fit (bottom).

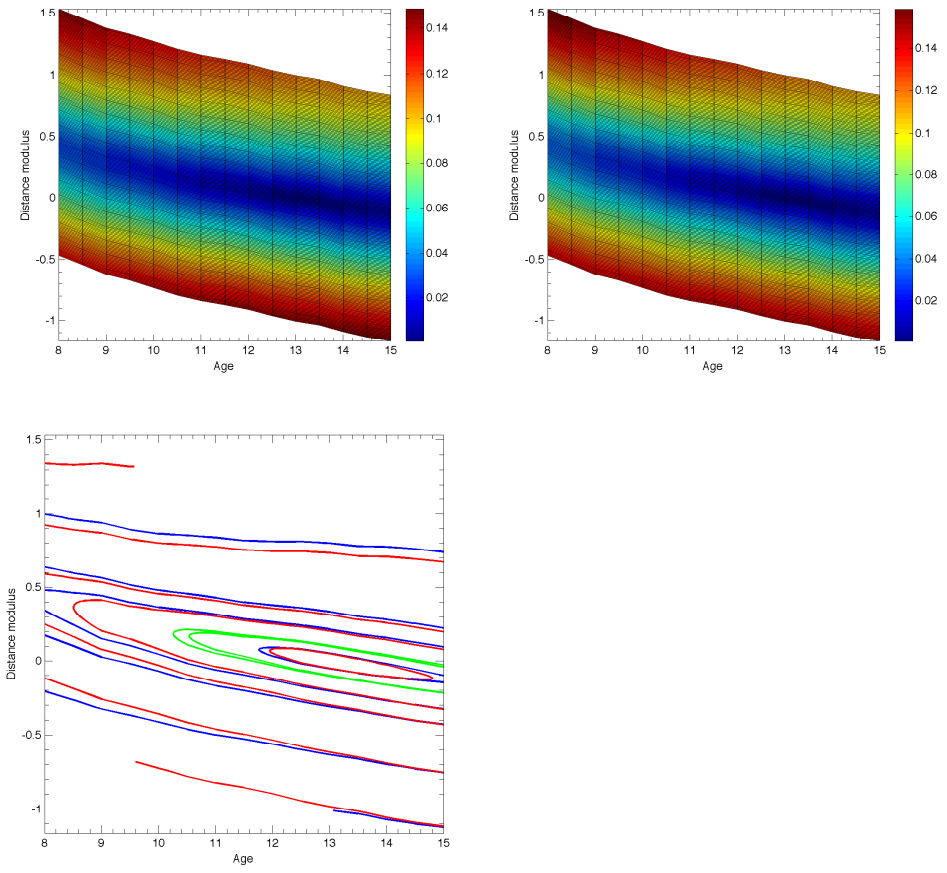

Figure 5.4. Standard deviation maps of the test case used to understand the significance of the standard deviation in the color excess to judge the goodness of the fit. The maps on the top show the standard deviation from the fitting in the $B-V$ color (left) and in the $V-I$ color (right). The contour map on the bottom is a representation of the maps on the top, with lines at $0.5\sigma_L$, $1\sigma_L$, $2\sigma_L$, $3\sigma_L$, $6\sigma_L$, and $9\sigma_L$ (see text). Blue lines are from the fitting in the $B-V$ color, and red lines are from the fitting in the $V-I$ color. The line in green is the one located at $1\sigma_L$.

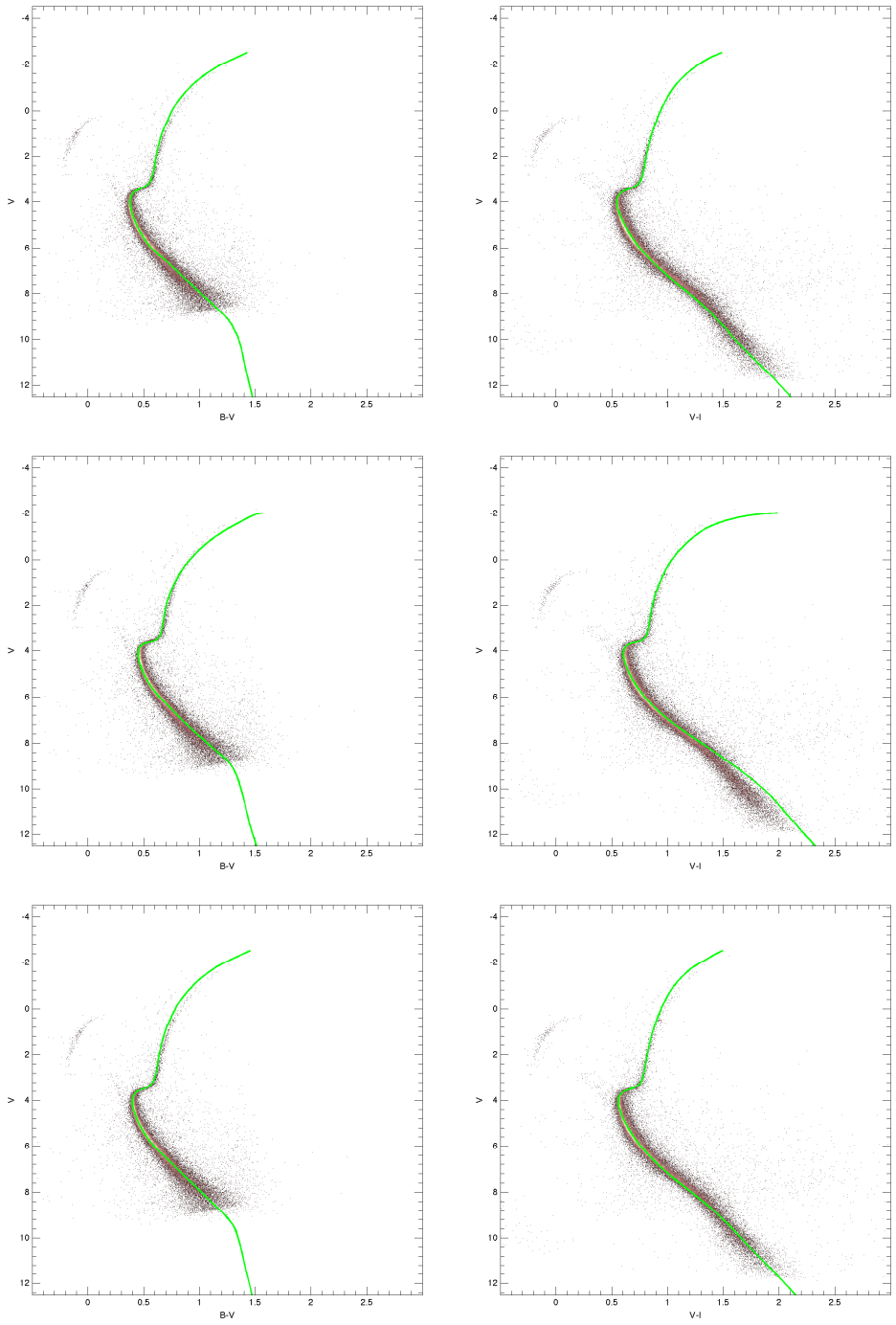

Figure 5.5. CMD of NGC 6218, corrected with the best parameters provided with the ridgeline-isochrone fit, plotted against an isochrone with an iron content -0.03 dex (top) and +0.03 dex (middle) of that specified in the Harris catalog, and with the same iron content of that specified in the Harris catalog but with a solar scaled content for the alpha elements (bottom).

In the figures in this section (see figures 5.6 and following) we show the CMDs of the clusters in our sample, corrected for the distance and absolute reddening provided by our isochrone fitting method, and plotted against the best fit isochrone. We plot the CMD instead of the ridgeline, which is what is truly compared, because, in the end, what it is desired is a good fit of the isochrone to the observational photometry results. The best values for the age, the distance, and the absolute reddening to a given cluster are presented in table 5.1. Also we provide the contour maps showing the standard deviation values for the fit for the different age and distance for the two colors available: $B - V$ and for $V - I$. As a sanity check for the goodness of the absolute reddening correction, we mark in the corrected CMDs of all the clusters with a blue HB the intrinsic location of the blue edge of the instability strip for the HB at $(B - V)_0 = 0.17$ (Mateo et al., 1995), and agree after visual inspection that this is the right position for such edge.

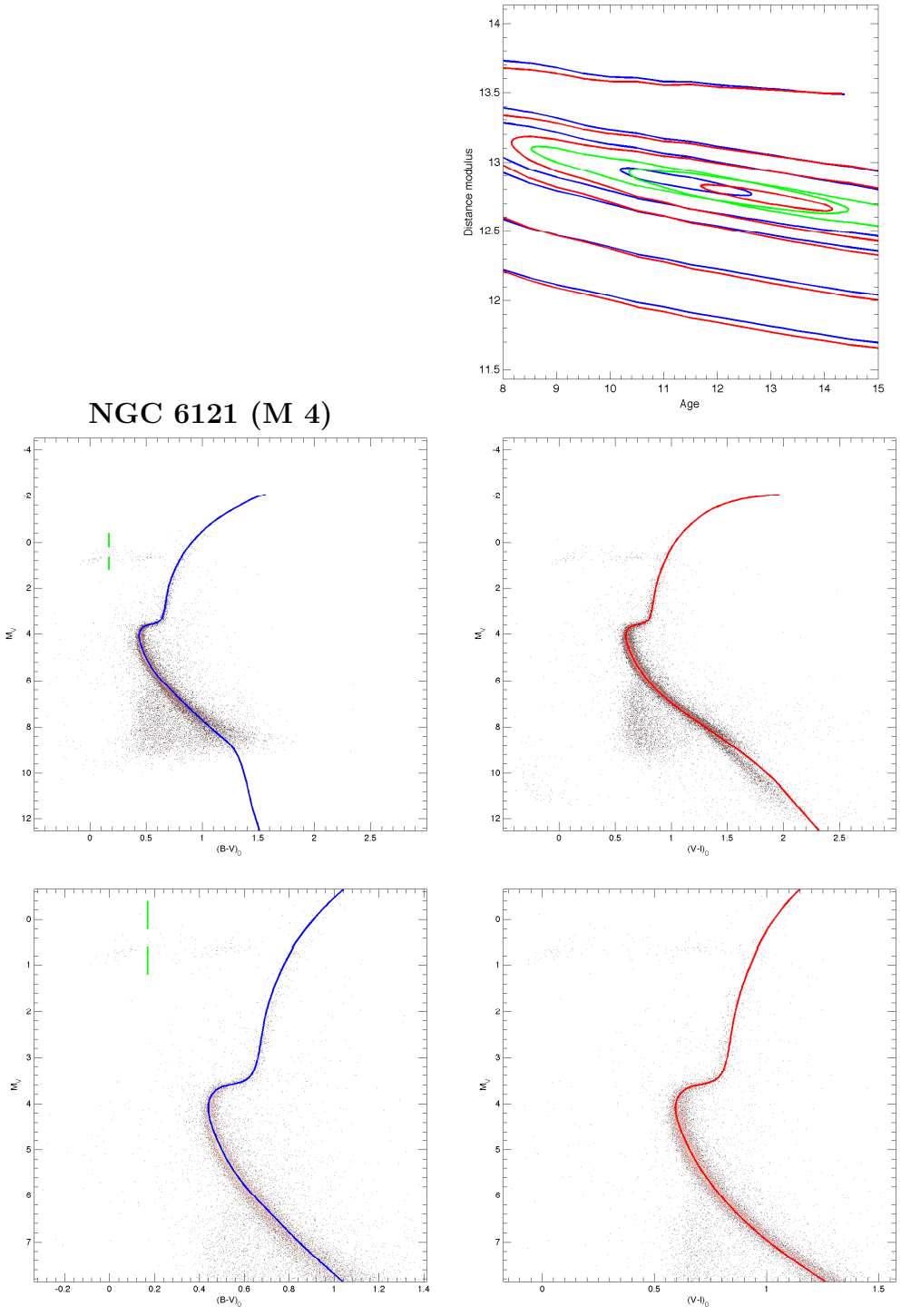

Figure 5.6. CMD of NGC 6121 (M 4), corrected for distance and absolute reddening, plotted against the best fit isochrone. The contour map represents the standard deviation values for the fit using different test ages and distances, for the two colors available: $B-V$ (in blue) and for $V-I$ (in red). The green contours are where the fit reaches $1\sigma_L$.

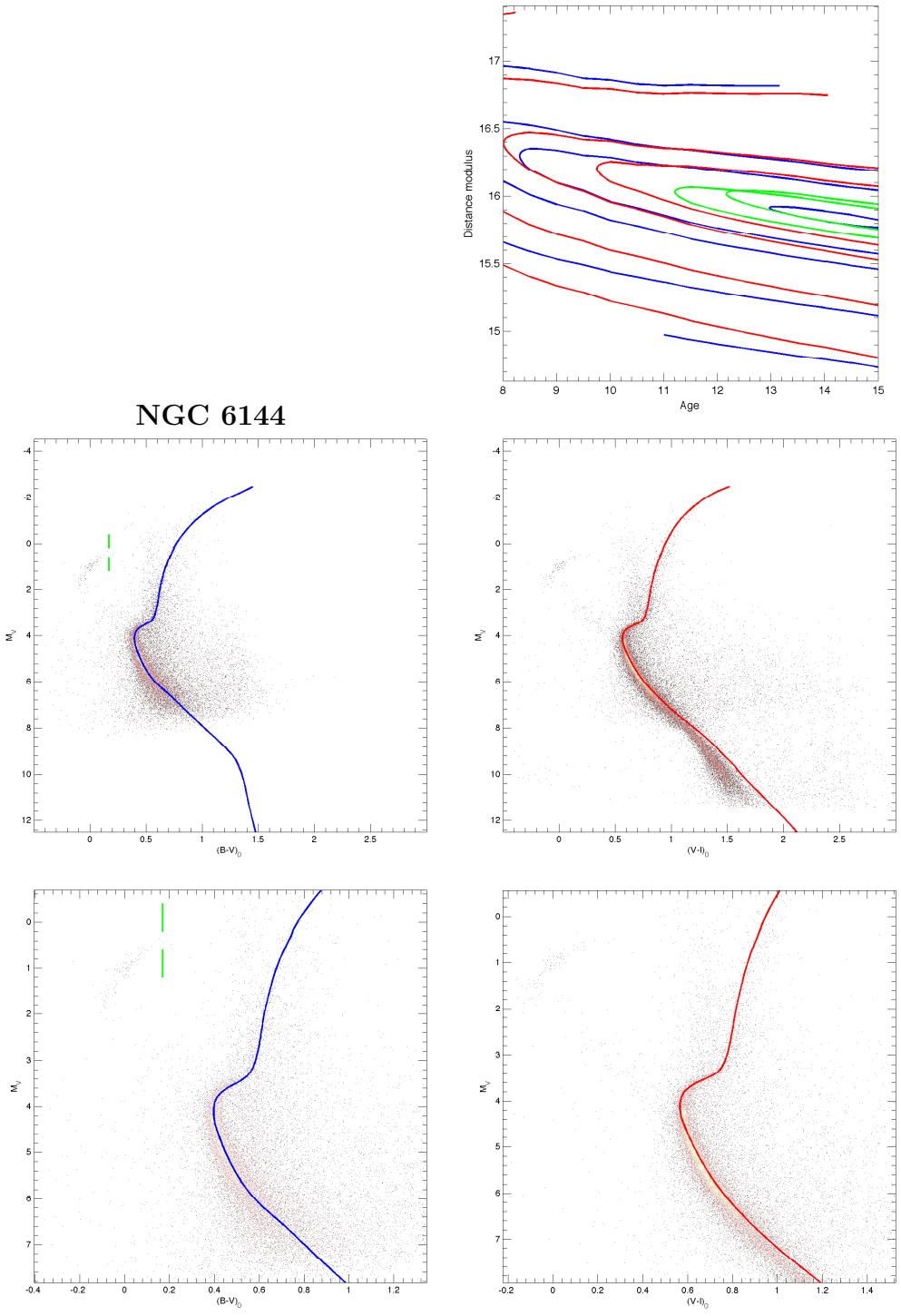

Figure 5.7. CMD of NGC 6144, corrected for distance and absolute reddening, plotted against the best fit isochrone. The contour map represents the standard deviation values for the fit using different test ages and distances, for the two colors available: $B-V$ (in blue) and for $V-I$ (in red). The green contours are where the fit reaches $1\sigma_L$.

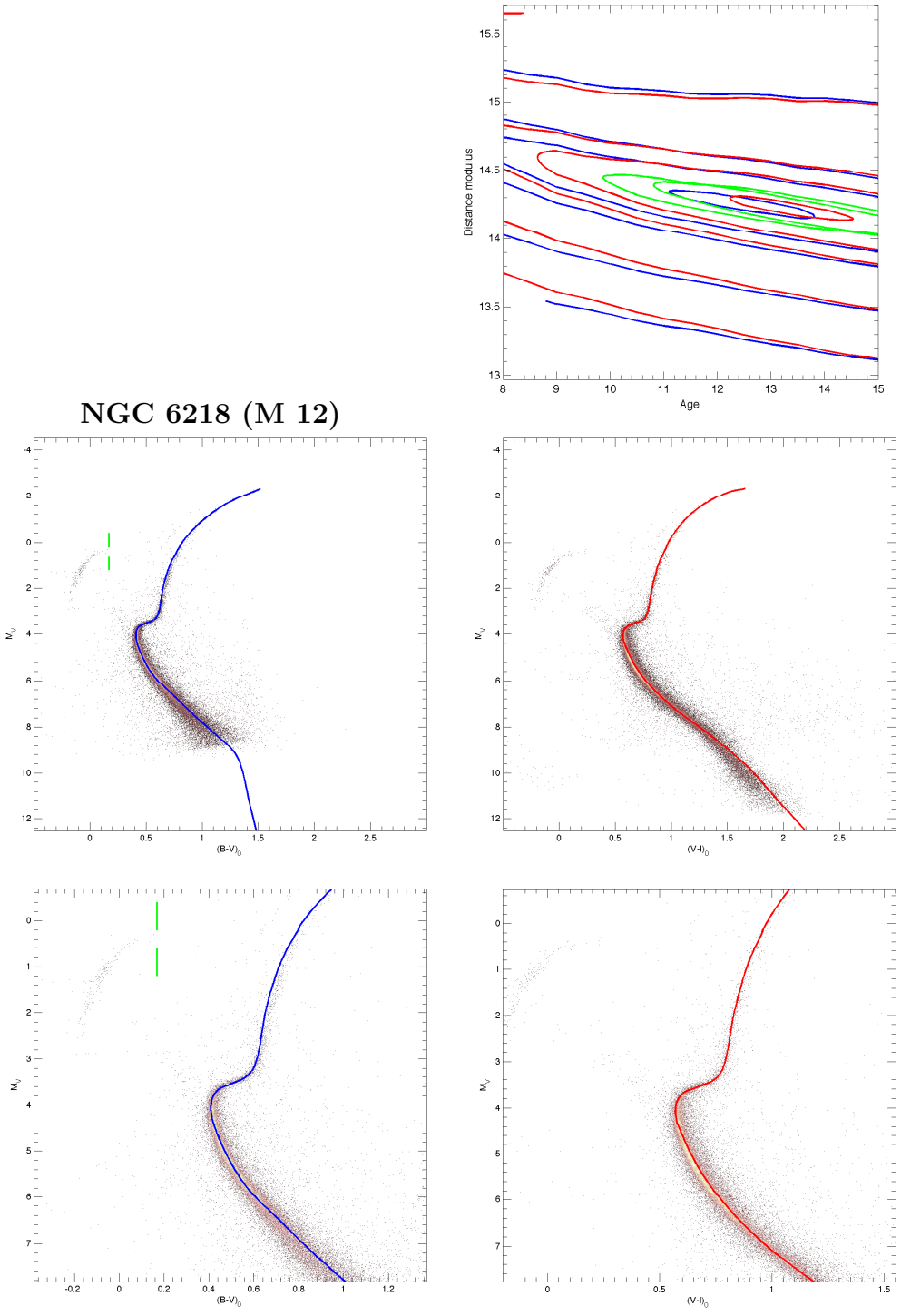

Figure 5.8. CMD of NGC 6218 (M 12), corrected for distance and absolute reddening, plotted against the best fit isochrone. The contour map represents the standard deviation values for the fit using different test ages and distances, for the two colors available: $B-V$ (in blue) and for $V-I$ (in red). The green contours are where the fit reaches $1\sigma_L$.

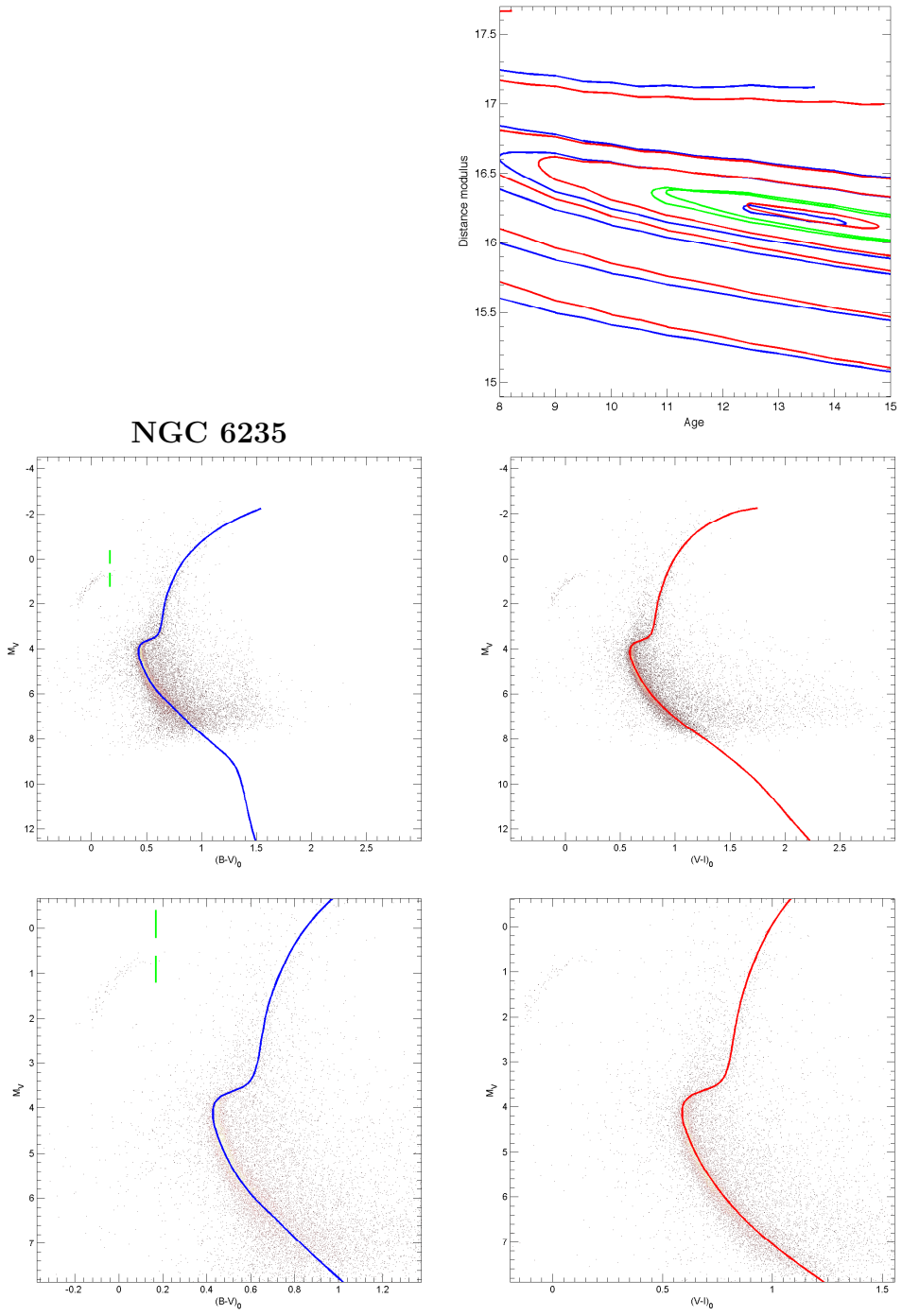

Figure 5.9. CMD of NGC 6235, corrected for distance and absolute reddening, plotted against the best fit isochrone. The contour map represents the standard deviation values for the fit using different test ages and distances, for the two colors available: $B-V$ (in blue) and for $V-I$ (in red). The green contours are where the fit reaches $1\sigma_L$.

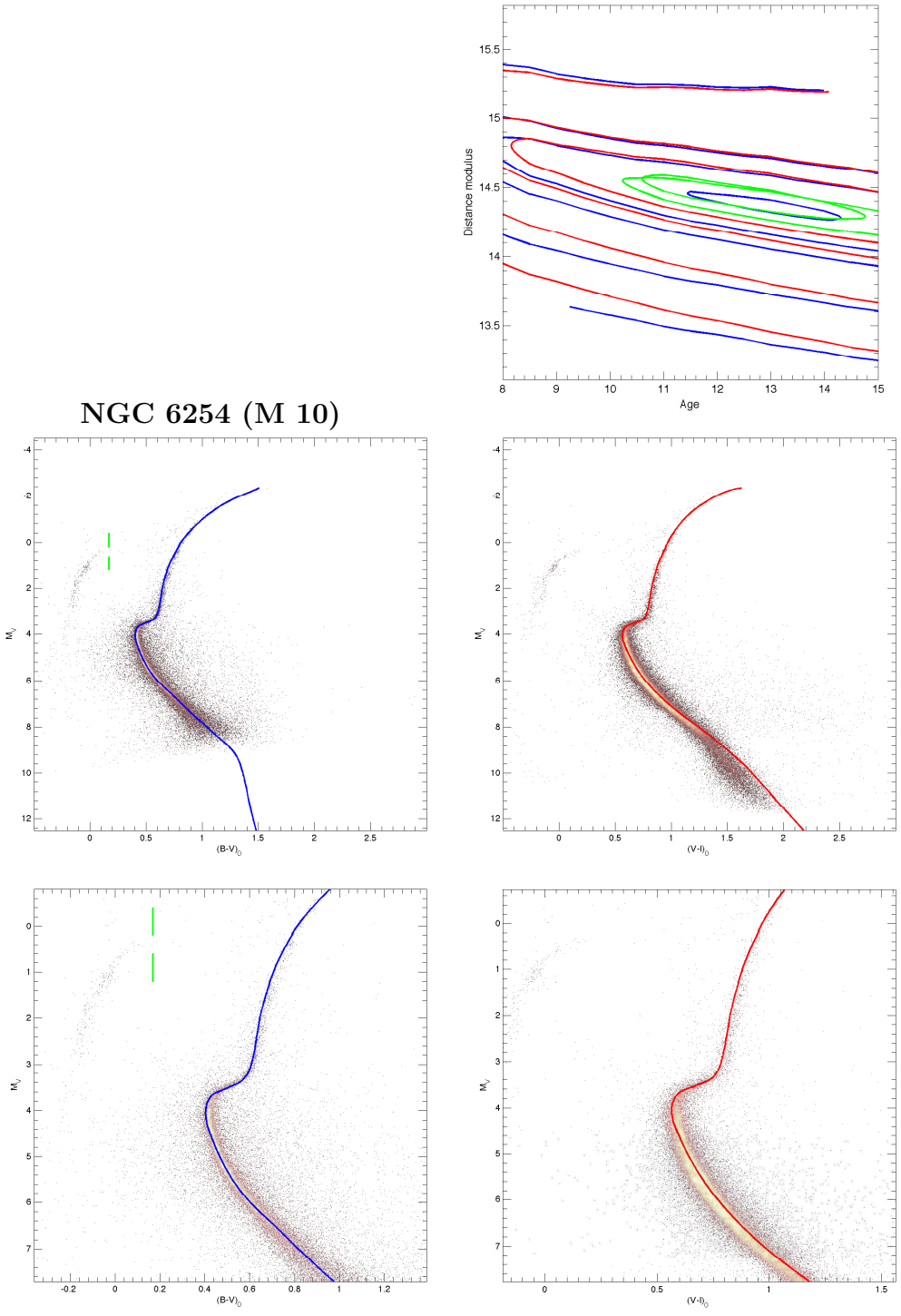

Figure 5.10. CMD of NGC 6254 (M 10), corrected for distance and absolute reddening, plotted against the best fit isochrone. The contour map represents the standard deviation values for the fit using different test ages and distances, for the two colors available: $B-V$ (in blue) and for $V-I$ (in red). The green contours are where the fit reaches $1\sigma_L$.

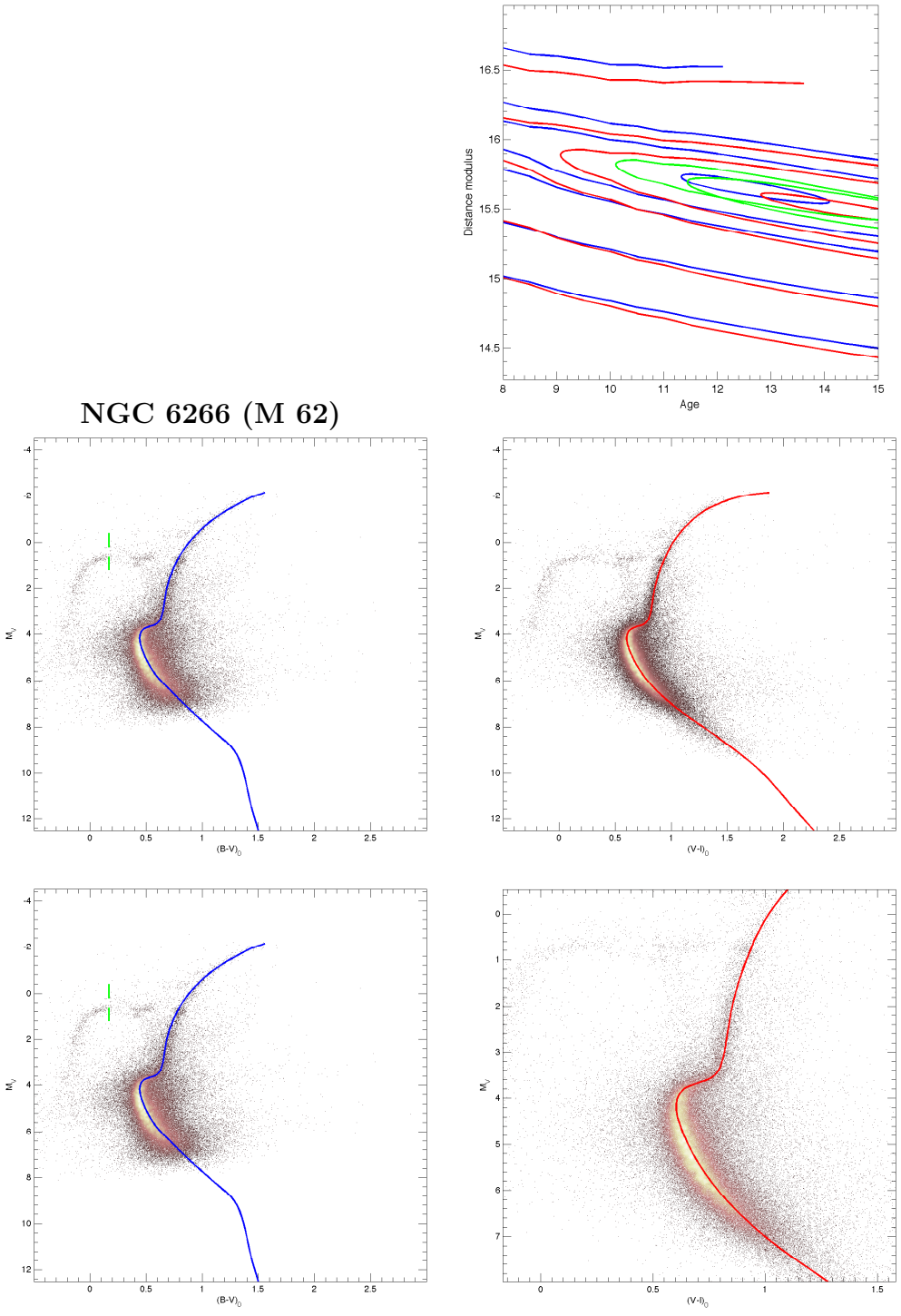

Figure 5.11. CMD of NGC 6266 (M 62), corrected for distance and absolute reddening, plotted against the best fit isochrone. The contour map represents the standard deviation values for the fit using different test ages and distances, for the two colors available: $B-V$ (in blue) and for $V-I$ (in red). The green contours are where the fit reaches $1\sigma_L$.

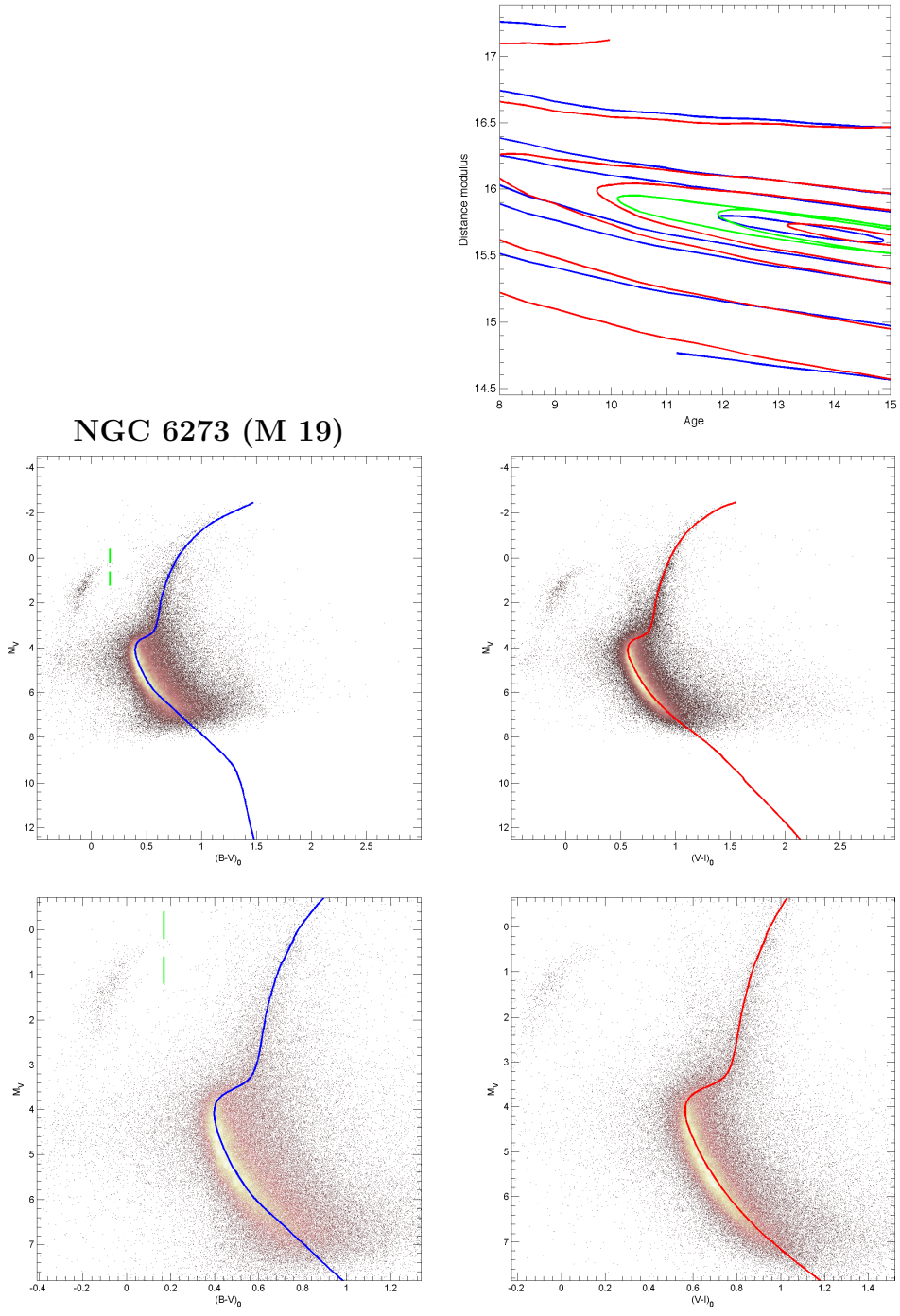

Figure 5.12. CMD of NGC 6273 (M 19), corrected for distance and absolute reddening, plotted against the best fit isochrone. The contour map represents the standard deviation values for the fit using different test ages and distances, for the two colors available: $B-V$ (in blue) and for $V-I$ (in red). The green contours are where the fit reaches $1\sigma_L$.

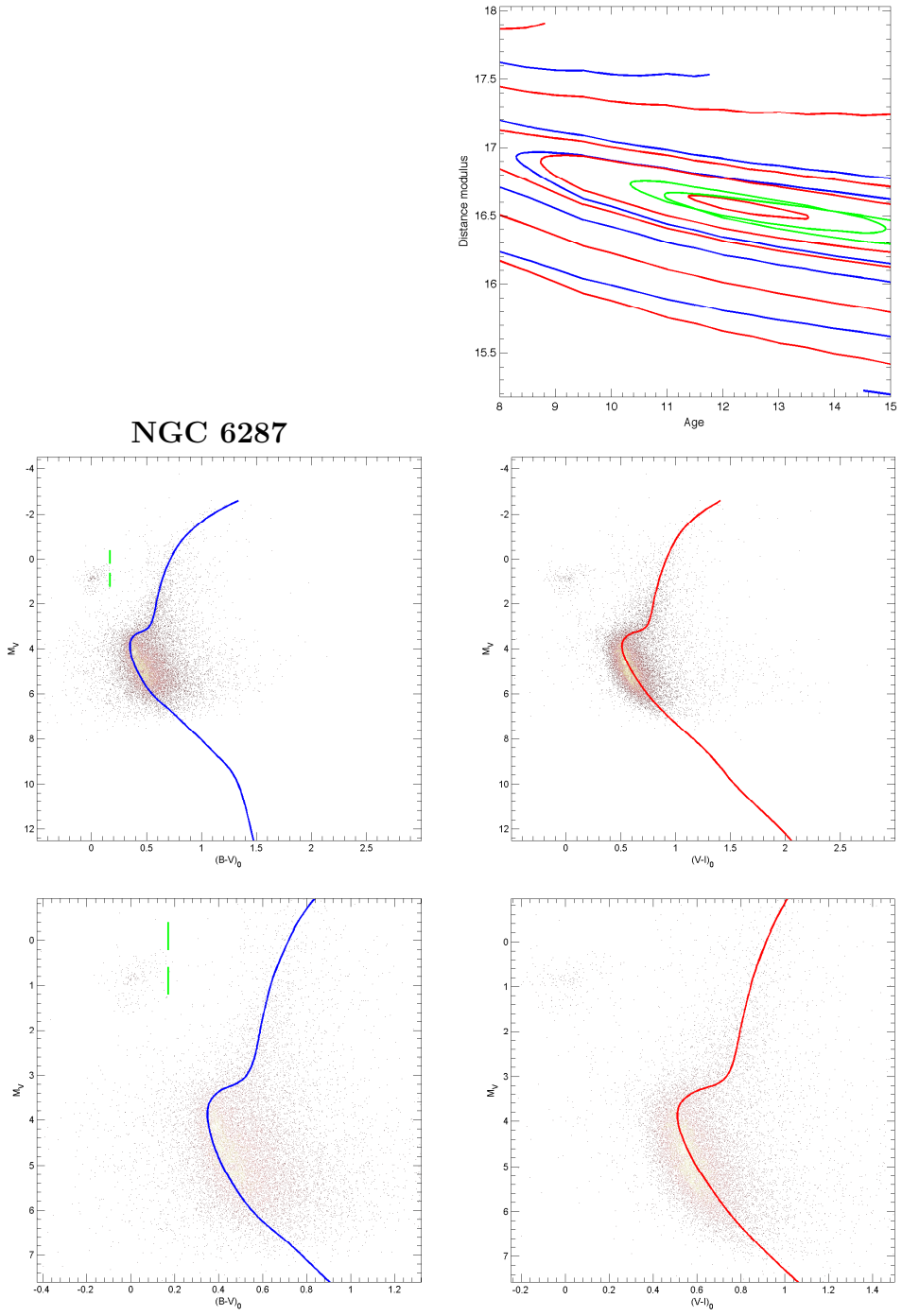

Figure 5.13. CMD of NGC 6287, corrected for distance and absolute reddening, plotted against the best fit isochrone. The contour map represents the standard deviation values for the fit using different test ages and distances, for the two colors available: $B-V$ (in blue) and for $V-I$ (in red). The green contours are where the fit reaches $1\sigma_L$.

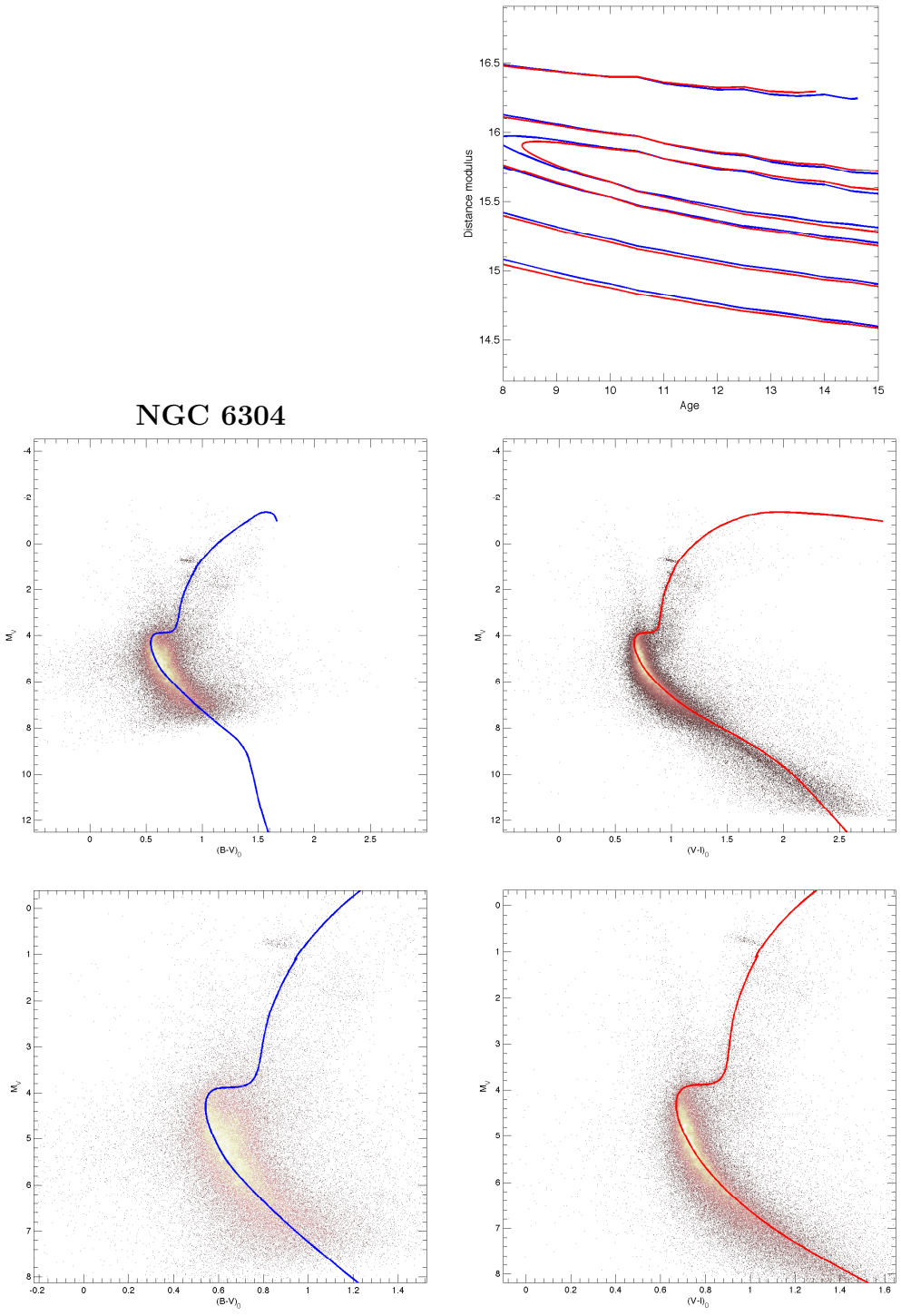

Figure 5.14. CMD of NGC 6304, corrected for distance and absolute reddening, plotted against the best fit isochrone. The contour map represents the standard deviation values for the fit using different test ages and distances, for the two colors available: $B-V$ (in blue) and for $V-I$ (in red). The green contours are where the fit reaches $1\sigma_L$.

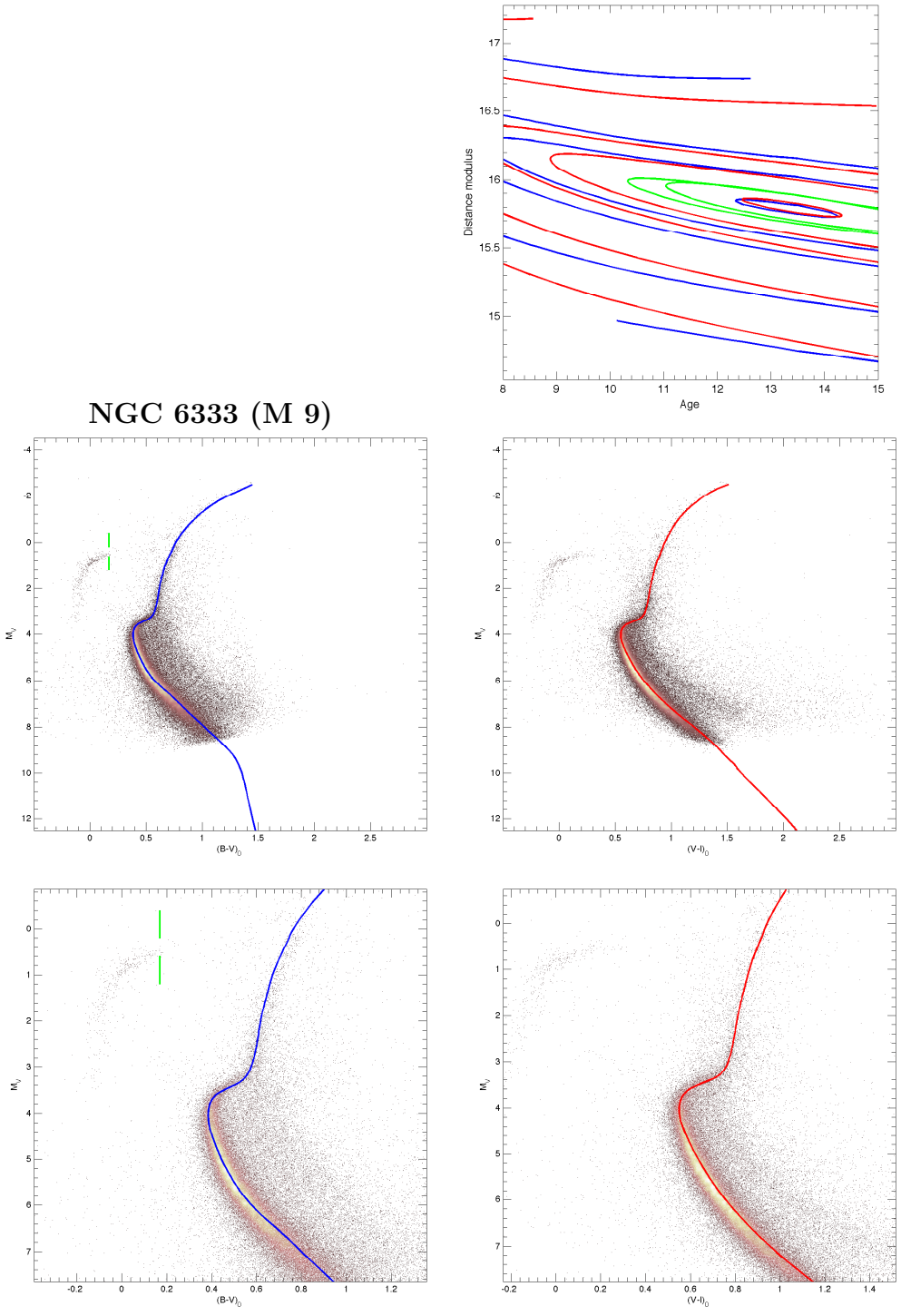

Figure 5.15. CMD of NGC 6333 (M 9), corrected for distance and absolute reddening, plotted against the best fit isochrone. The contour map represents the standard deviation values for the fit using different test ages and distances, for the two colors available: $B-V$ (in blue) and for $V-I$ (in red). The green contours are where the fit reaches $1\sigma_L$.

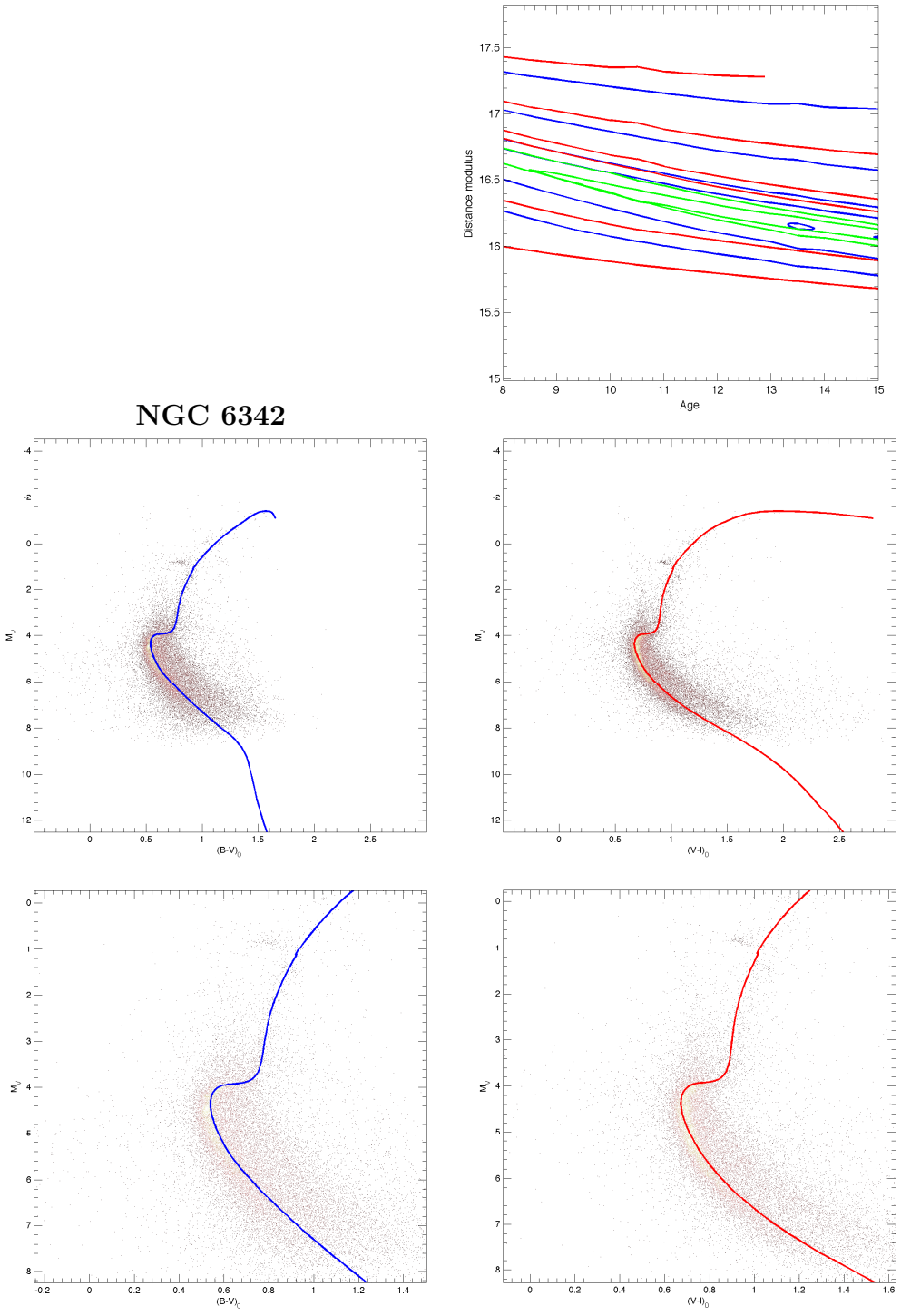

Figure 5.16. CMD of NGC 6342, corrected for distance and absolute reddening, plotted against the best fit isochrone. The contour map represents the standard deviation values for the fit using different test ages and distances, for the two colors available: $B-V$ (in blue) and for $V-I$ (in red). The green contours are where the fit reaches $1\sigma_L$.

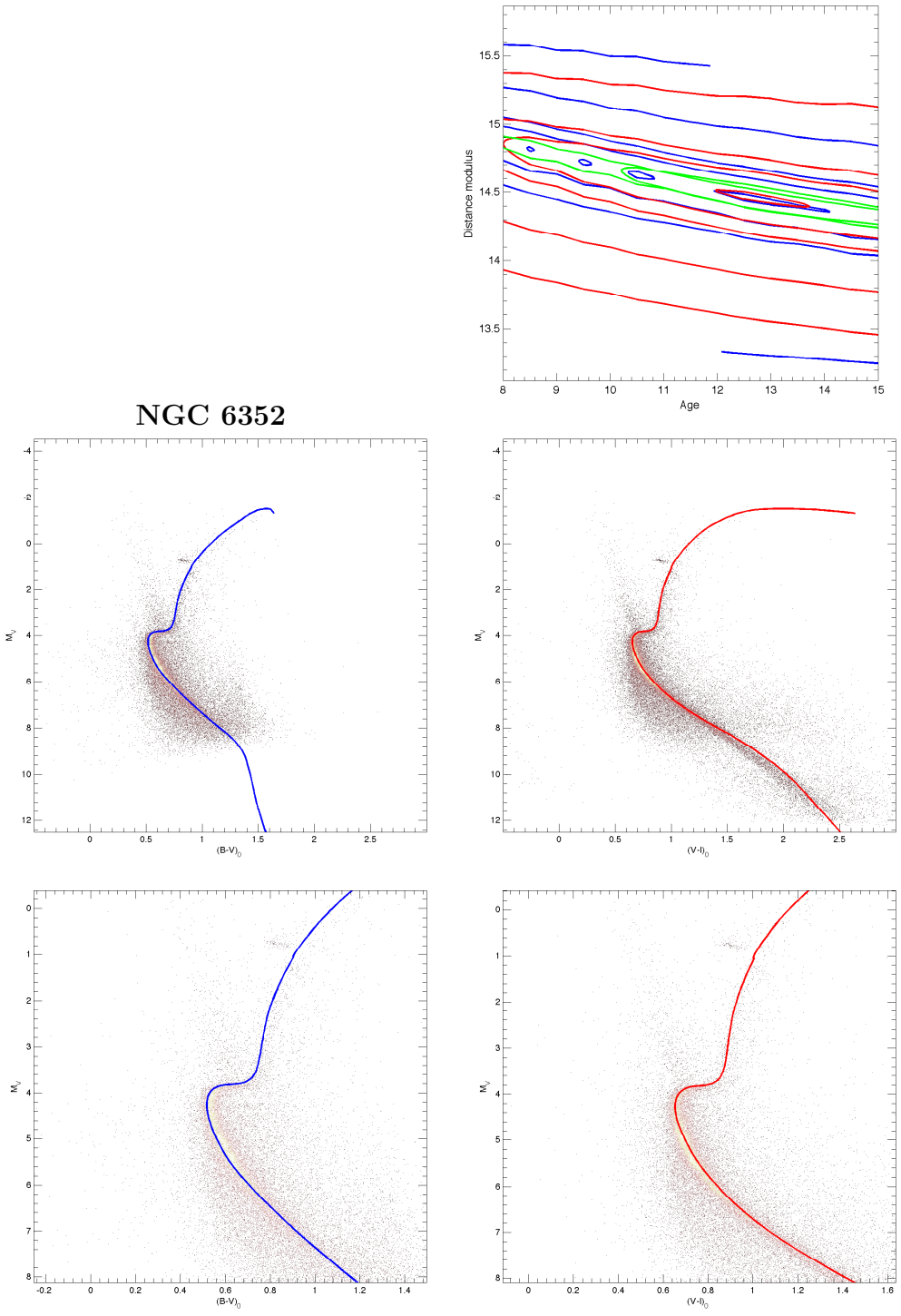

Figure 5.17. CMD of NGC 6352, corrected for distance and absolute reddening, plotted against the best fit isochrone. The contour map represents the standard deviation values for the fit using different test ages and distances, for the two colors available: $B-V$ (in blue) and for $V-I$ (in red). The green contours are where the fit reaches $1\sigma_L$.

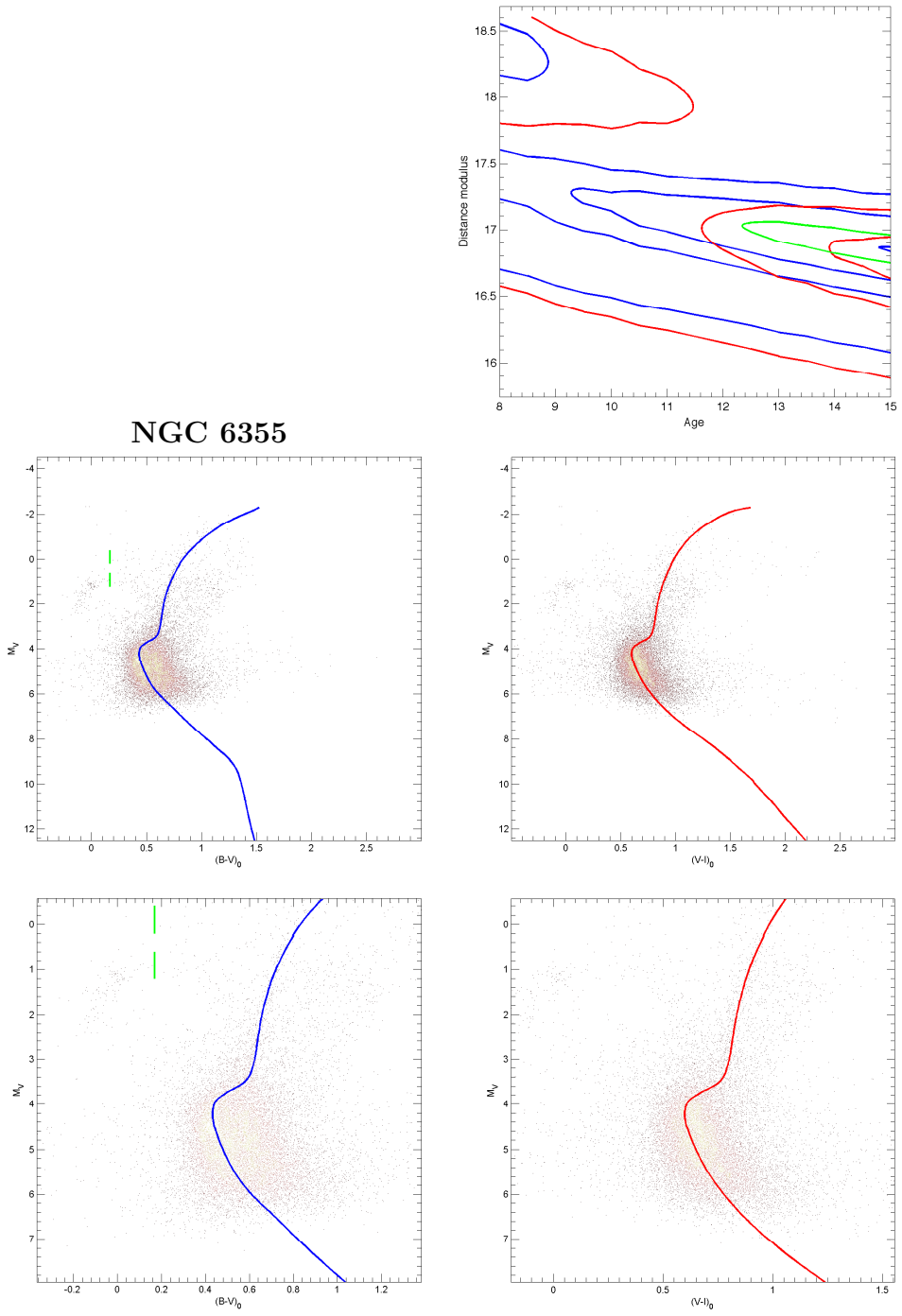

Figure 5.18. CMD of NGC 6355, corrected for distance and absolute reddening, plotted against the best fit isochrone. The contour map represents the standard deviation values for the fit using different test ages and distances, for the two colors available: $B-V$ (in blue) and for $V-I$ (in red). The green contours are where the fit reaches $1\sigma_L$.

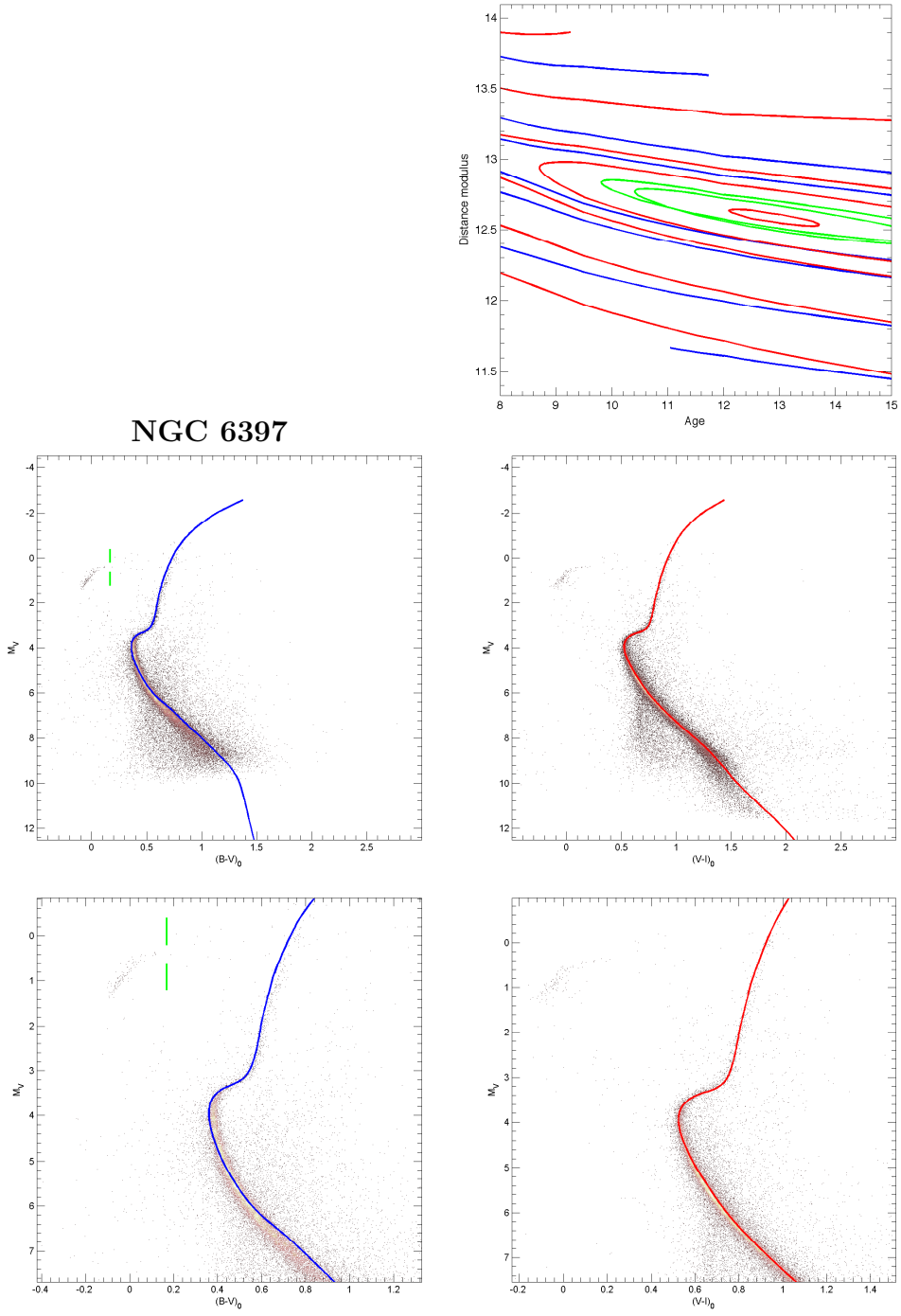

Figure 5.19. CMD of NGC 6397, corrected for distance and absolute reddening, plotted against the best fit isochrone. The contour map represents the standard deviation values for the fit using different test ages and distances, for the two colors available: $B-V$ (in blue) and for $V-I$ (in red). The green contours are where the fit reaches $1\sigma_L$.

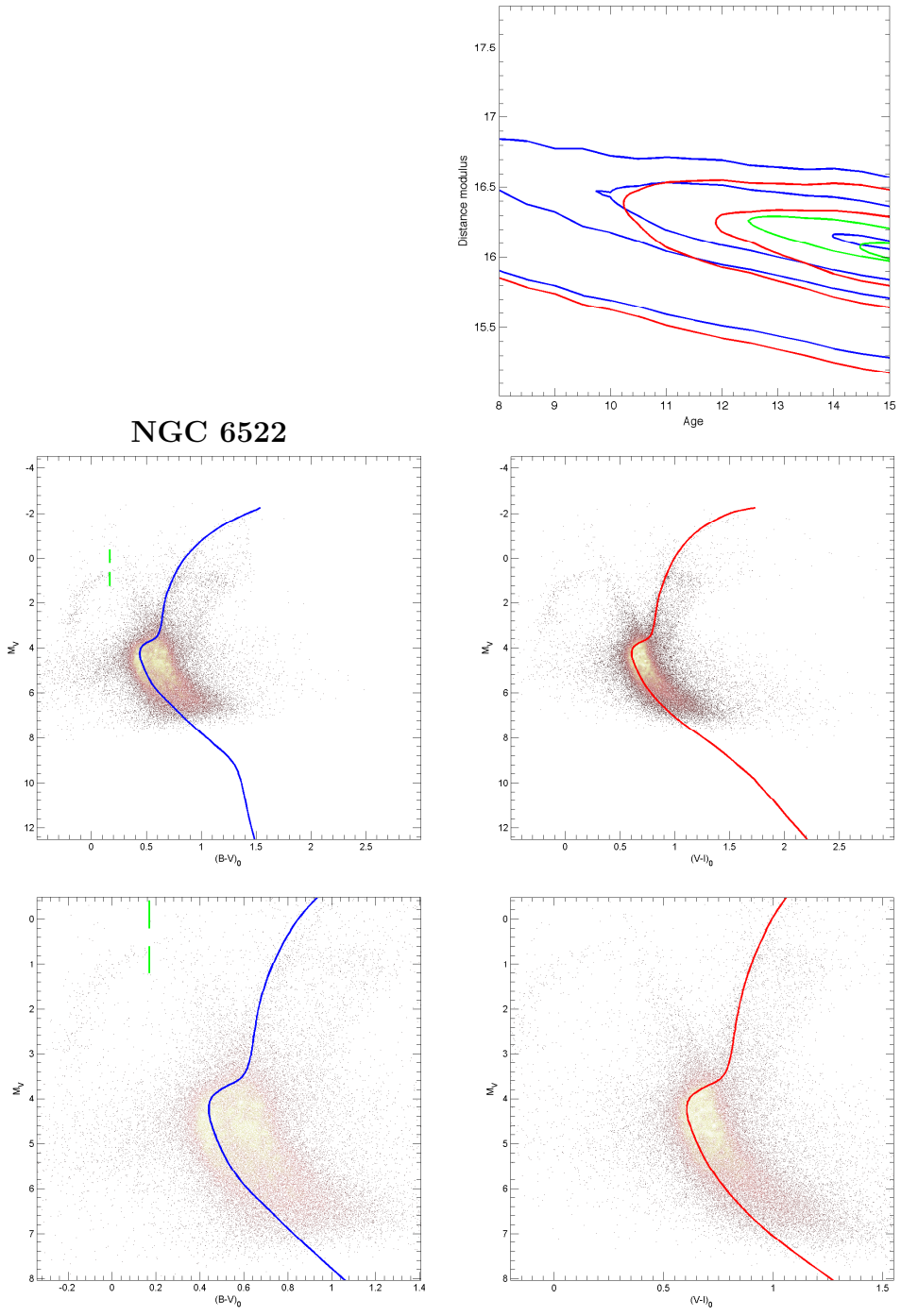

Figure 5.20. CMD of NGC 6522, corrected for distance and absolute reddening, plotted against the best fit isochrone. The contour map represents the standard deviation values for the fit using different test ages and distances, for the two colors available: $B-V$ (in blue) and for $V-I$ (in red). The green contours are where the fit reaches $1\sigma_L$.

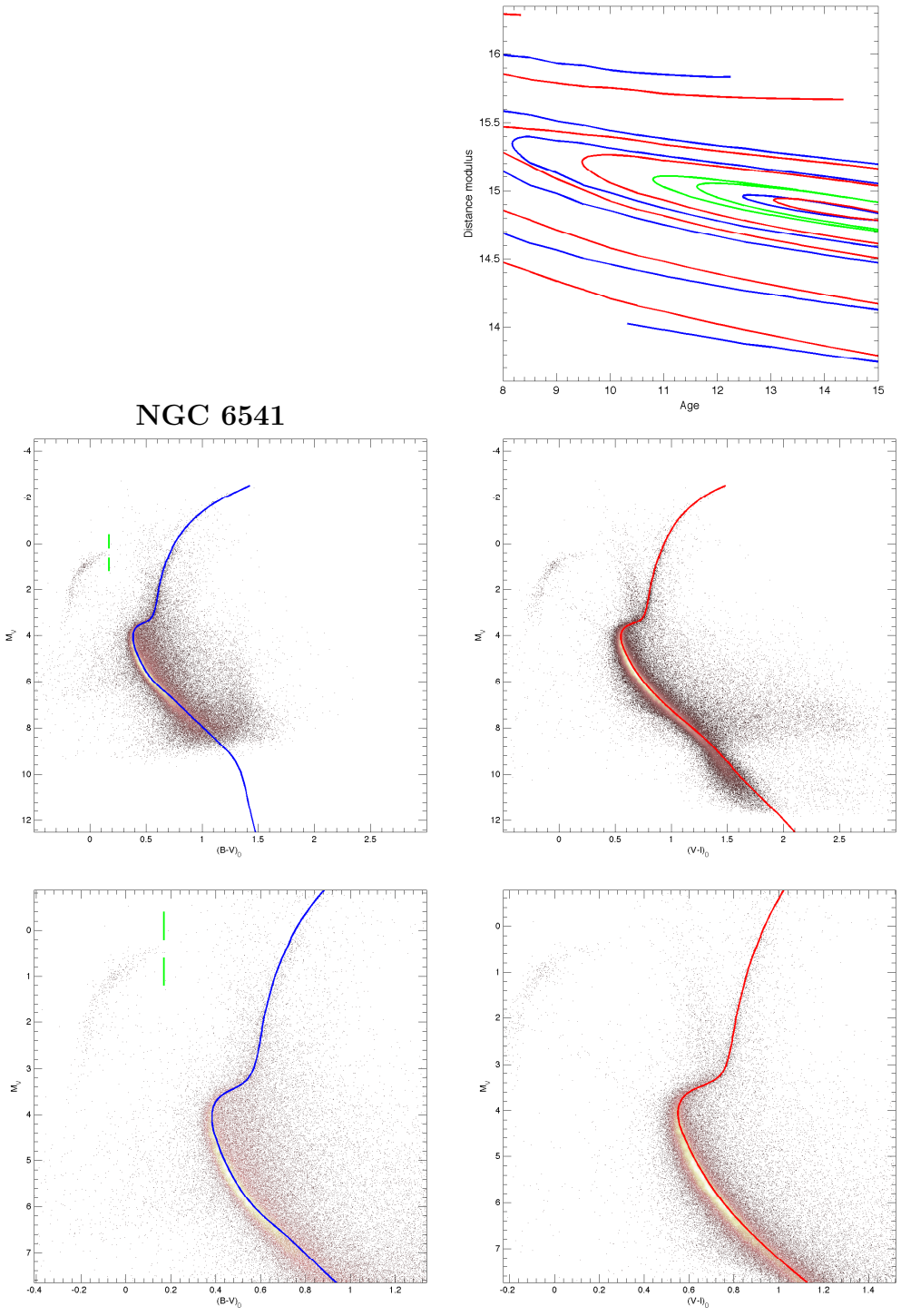

Figure 5.21. CMD of NGC 6541, corrected for distance and absolute reddening, plotted against the best fit isochrone. The contour map represents the standard deviation values for the fit using different test ages and distances, for the two colors available: $B-V$ (in blue) and for $V-I$ (in red). The green contours are where the fit reaches $1\sigma_L$.

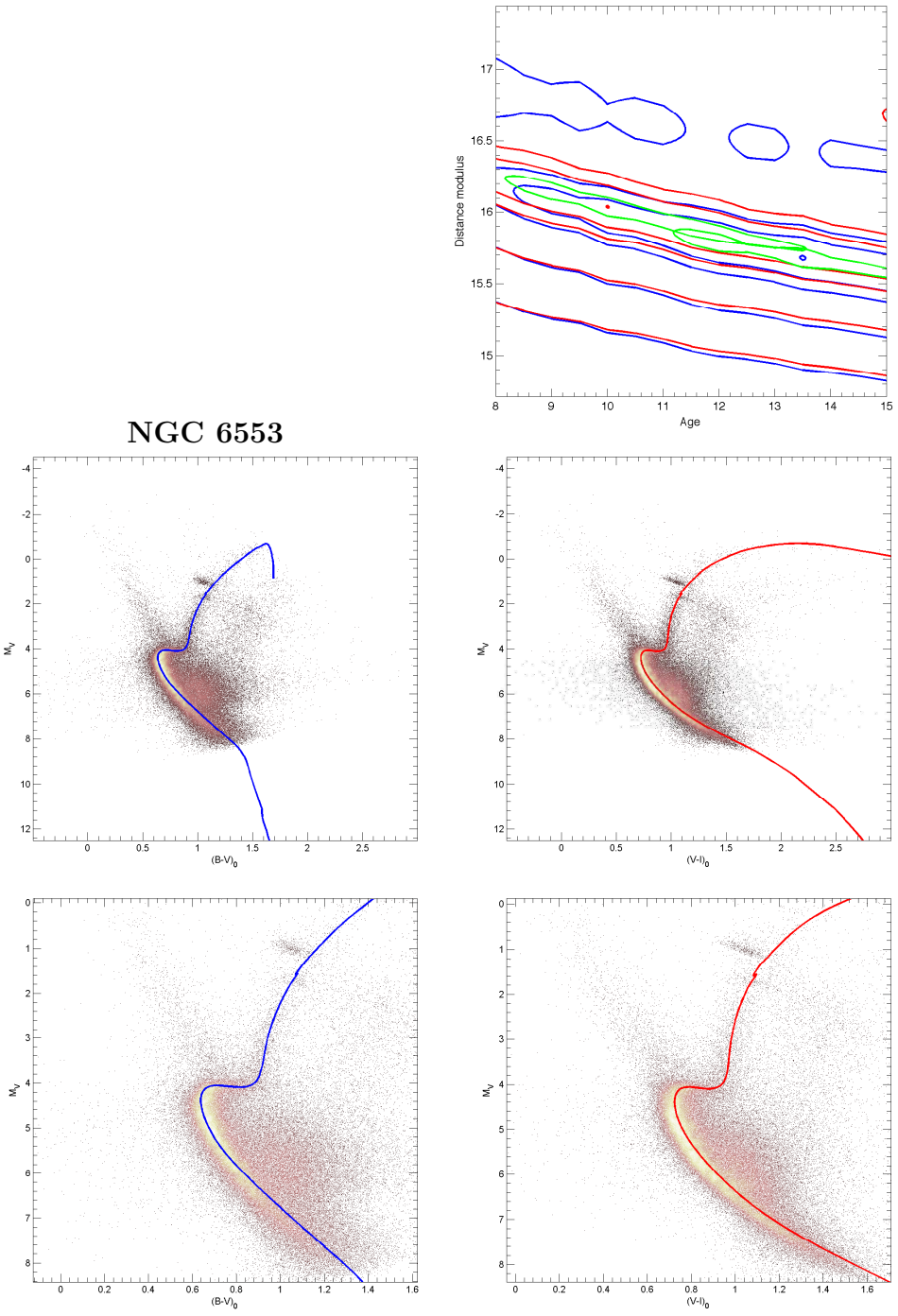

Figure 5.22. CMD of NGC 6553, corrected for distance and absolute reddening, plotted against the best fit isochrone. The contour map represents the standard deviation values for the fit using different test ages and distances, for the two colors available: $B-V$ (in blue) and for $V-I$ (in red). The green contours are where the fit reaches $1\sigma_L$.

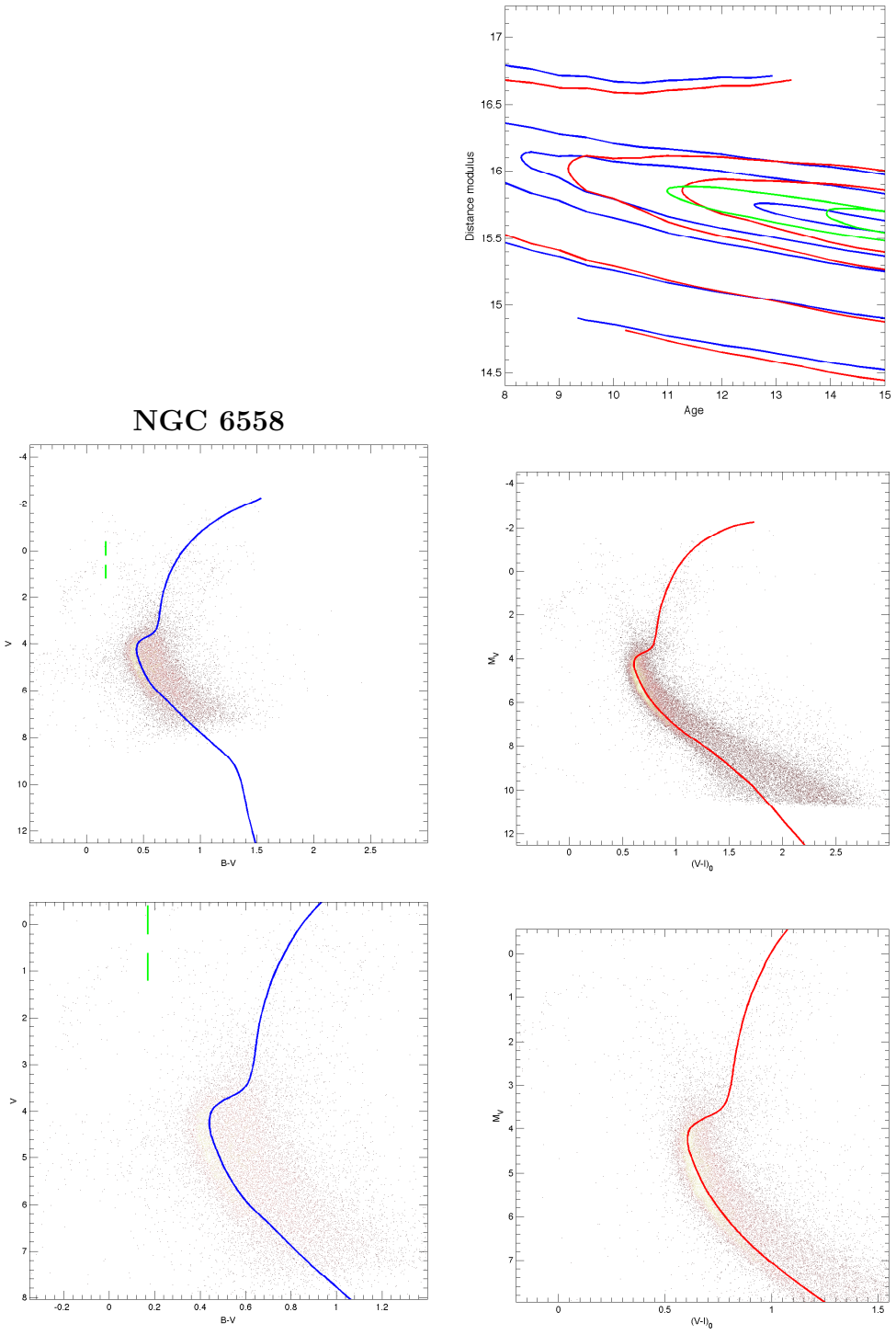

Figure 5.23. CMD of NGC 6558, corrected for distance and absolute reddening, plotted against the best fit isochrone. The contour map represents the standard deviation values for the fit using different test ages and distances, for the two colors available: $B-V$ (in blue) and for $V-I$ (in red). The green contours are where the fit reaches $1\sigma_L$.

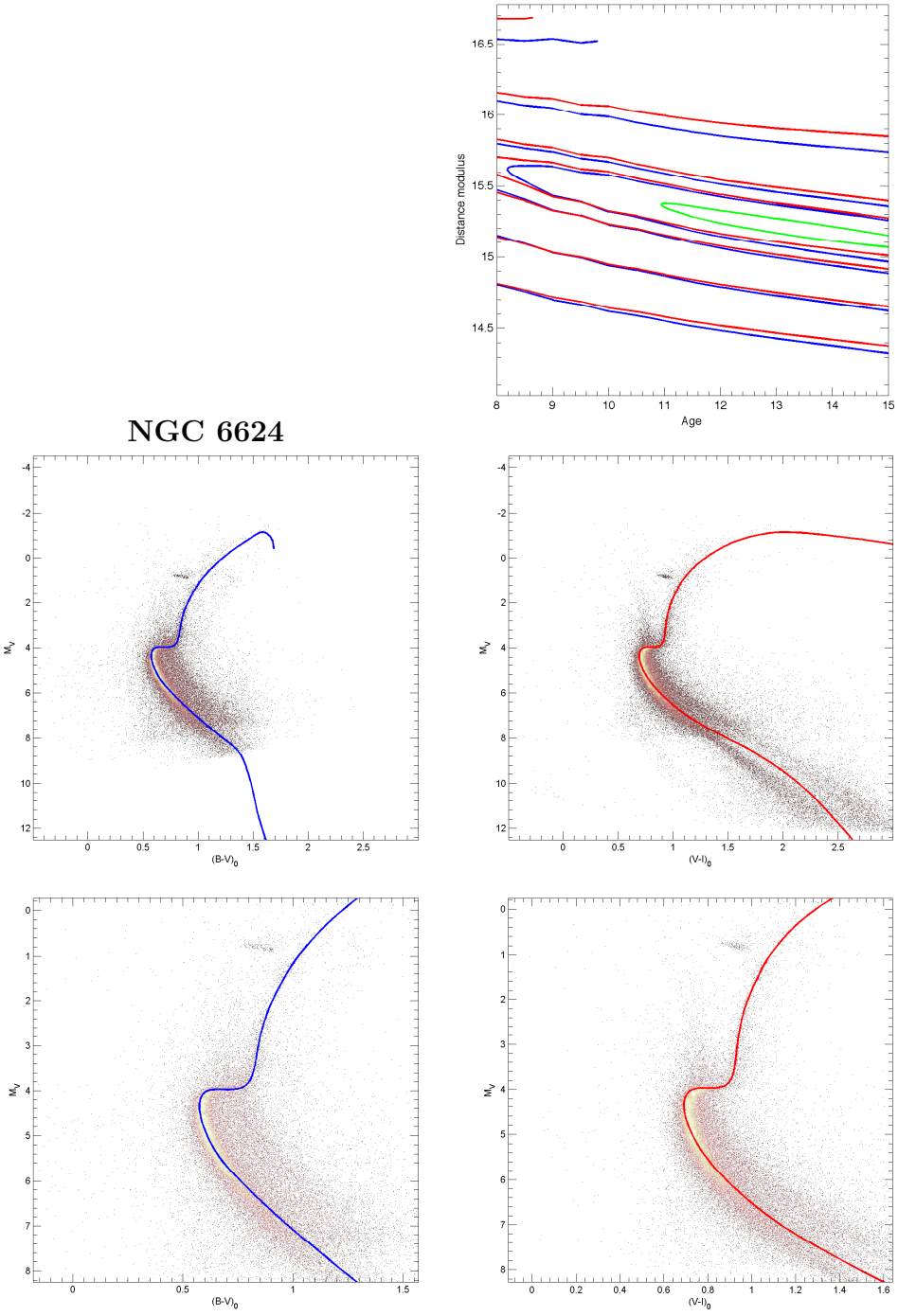

Figure 5.24. CMD of NGC 6624, corrected for distance and absolute reddening, plotted against the best fit isochrone. The contour map represents the standard deviation values for the fit using different test ages and distances, for the two colors available: $B-V$ (in blue) and for $V-I$ (in red). The green contours are where the fit reaches $1\sigma_L$.

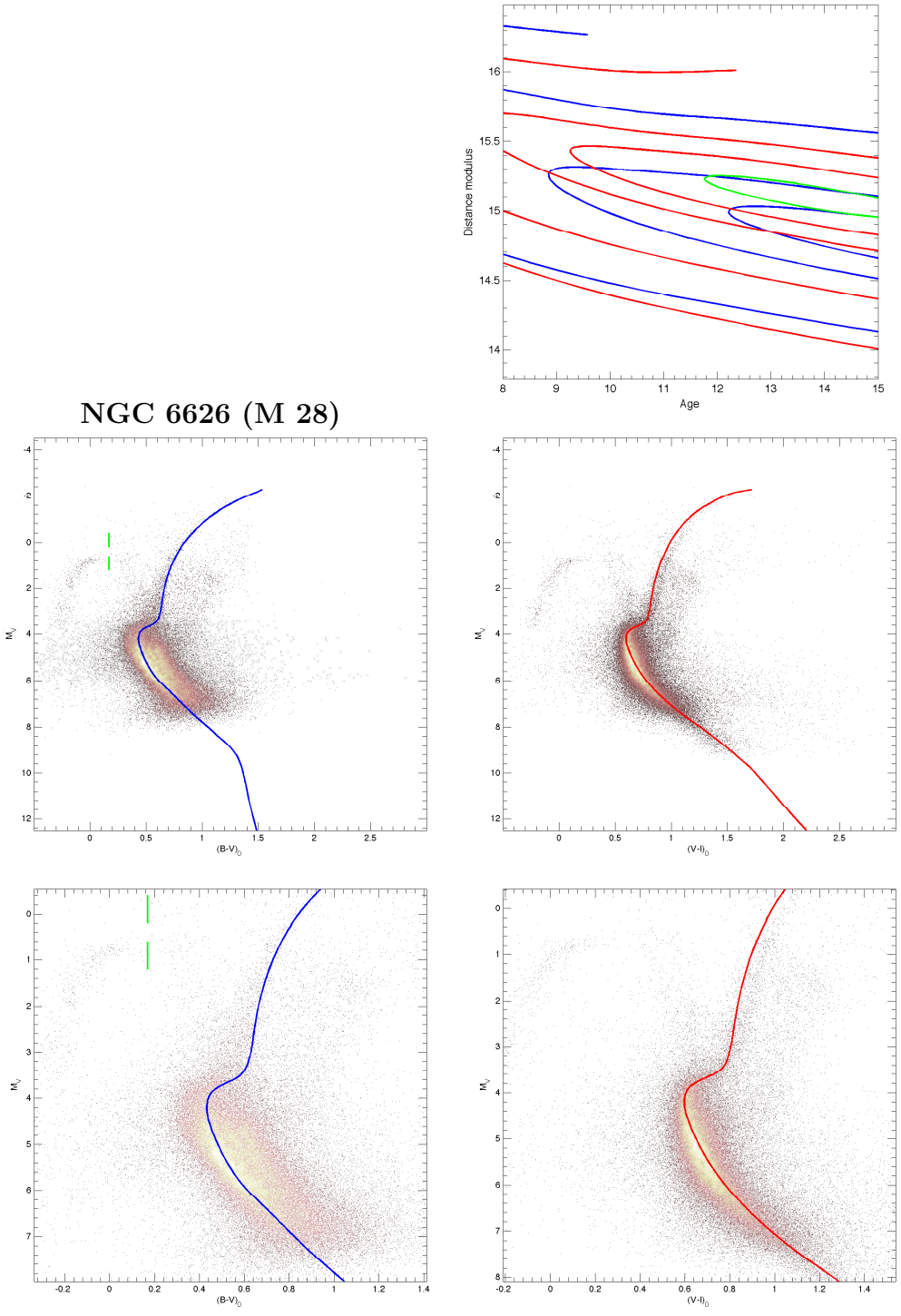

Figure 5.25. CMD of NGC 6626 (M 28), corrected for distance and absolute reddening, plotted against the best fit isochrone. The contour map represents the standard deviation values for the fit using different test ages and distances, for the two colors available: $B-V$ (in blue) and for $V-I$ (in red). The green contours are where the fit reaches $1\sigma_L$.

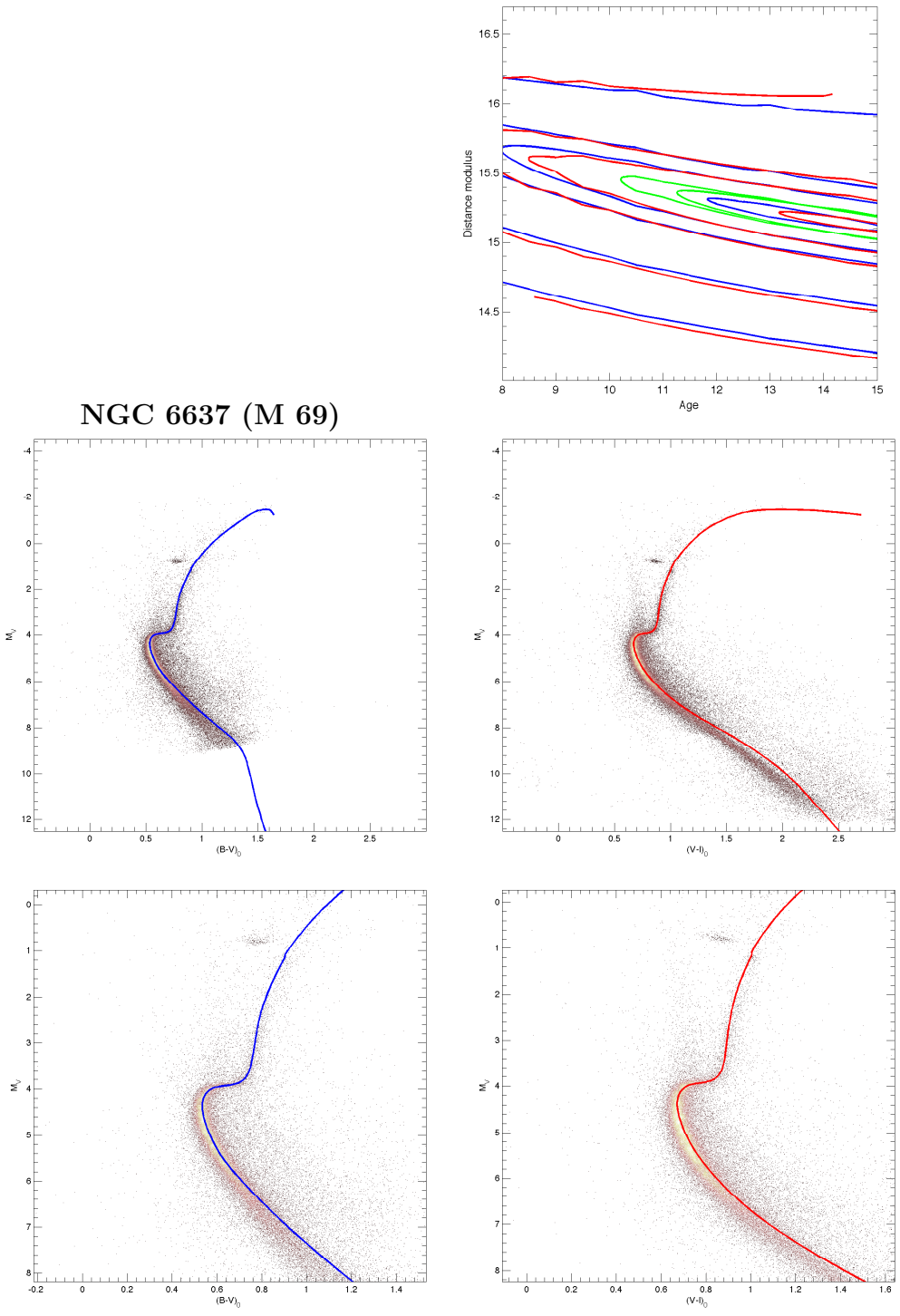

Figure 5.26. CMD of NGC 6637 (M 69), corrected for distance and absolute reddening, plotted against the best fit isochrone. The contour map represents the standard deviation values for the fit using different test ages and distances, for the two colors available: $B-V$ (in blue) and for $V-I$ (in red). The green contours are where the fit reaches $1\sigma_L$.

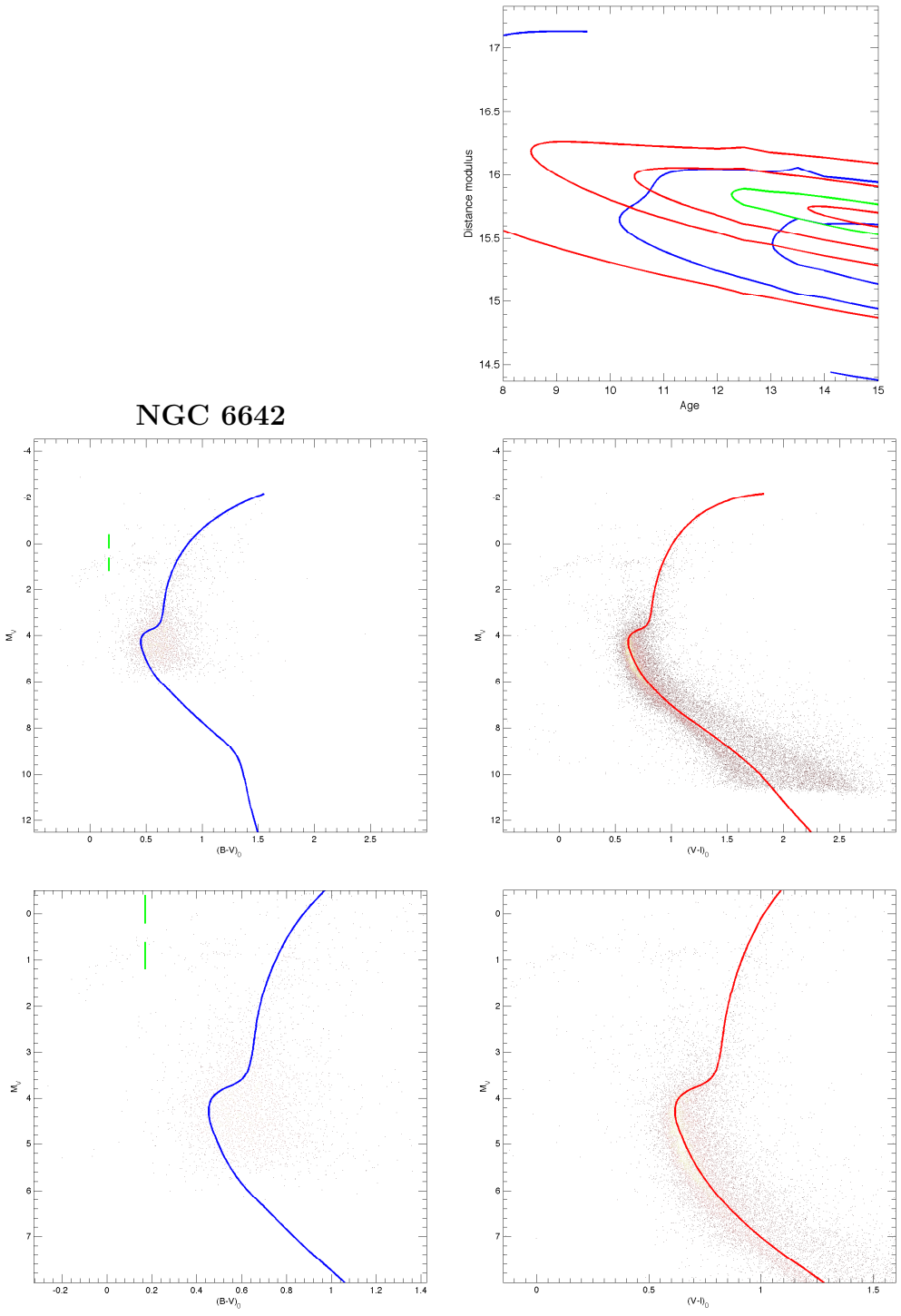

Figure 5.27. CMD of NGC 6642, corrected for distance and absolute reddening, plotted against the best fit isochrone. The contour map represents the standard deviation values for the fit using different test ages and distances, for the two colors available: $B-V$ (in blue) and for $V-I$ (in red). The green contours are where the fit reaches $1\sigma_L$.

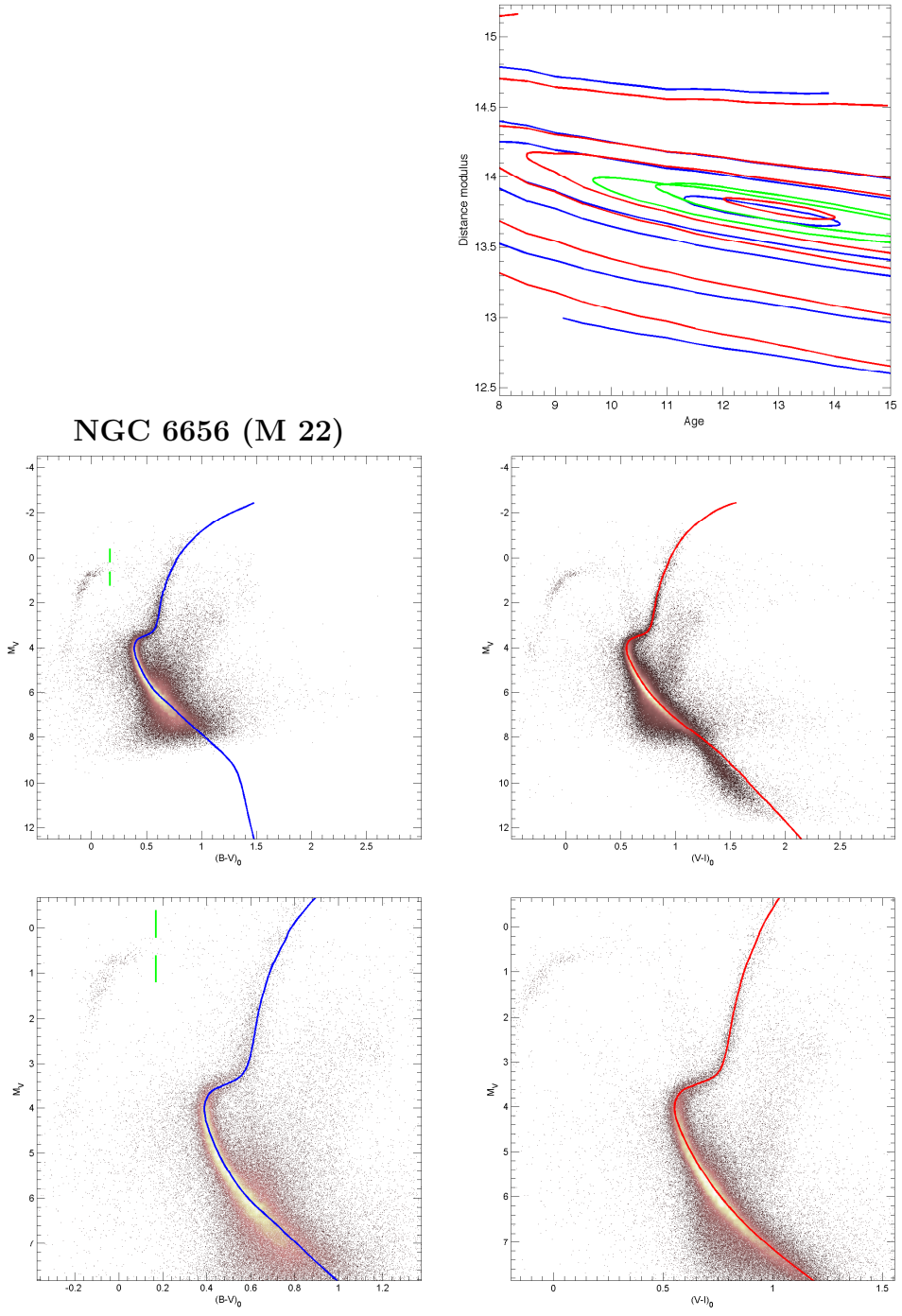

Figure 5.28. CMD of NGC 6656 (M 22), corrected for distance and absolute reddening, plotted against the best fit isochrone. The contour map represents the standard deviation values for the fit using different test ages and distances, for the two colors available: $B-V$ (in blue) and for $V-I$ (in red). The green contours are where the fit reaches $1\sigma_L$.

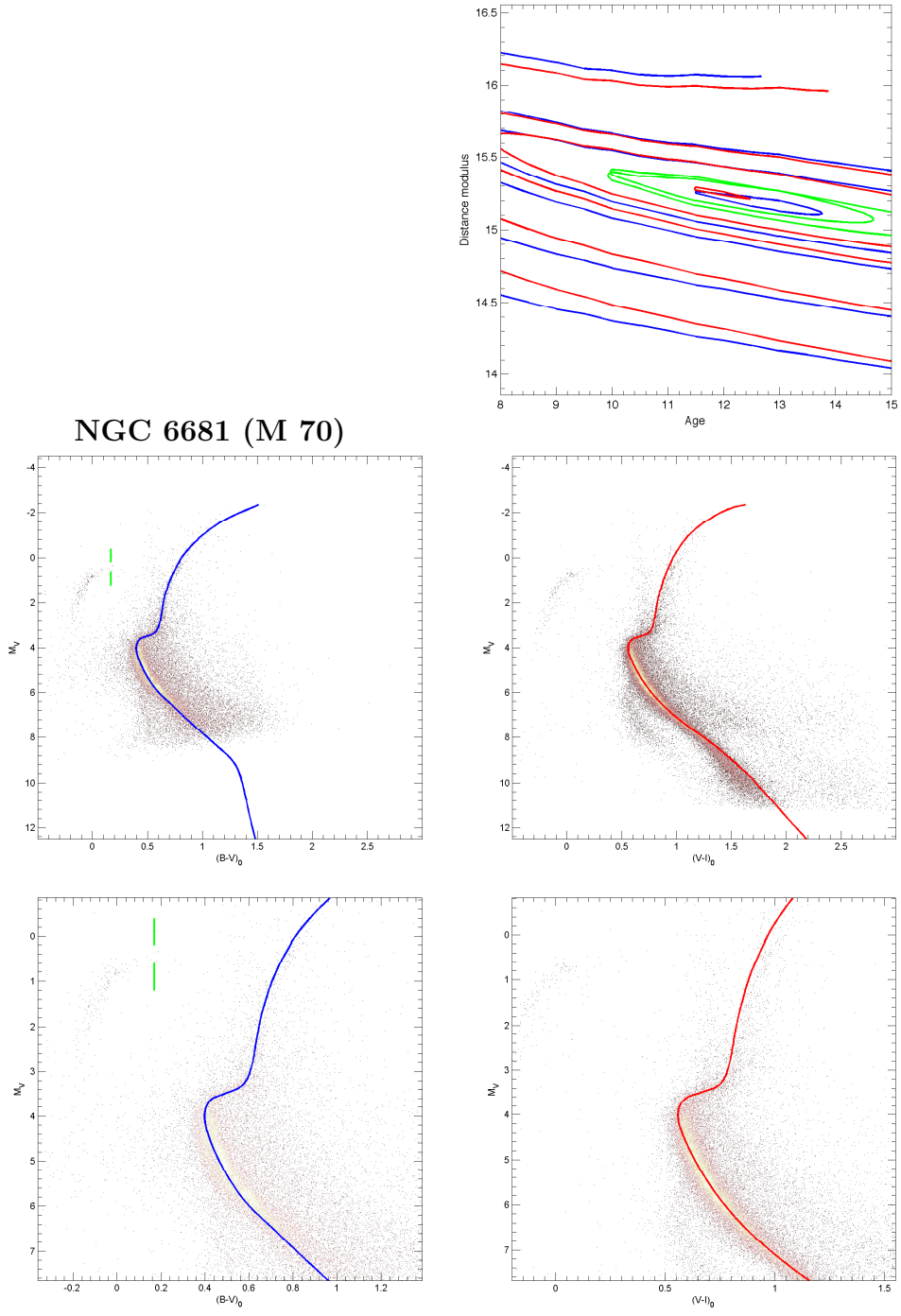

Figure 5.29. CMD of NGC 6681 (M 70), corrected for distance and absolute reddening, plotted against the best fit isochrone. The contour map represents the standard deviation values for the fit using different test ages and distances, for the two colors available: $B-V$ (in blue) and for $V-I$ (in red). The green contours are where the fit reaches $1\sigma_L$.

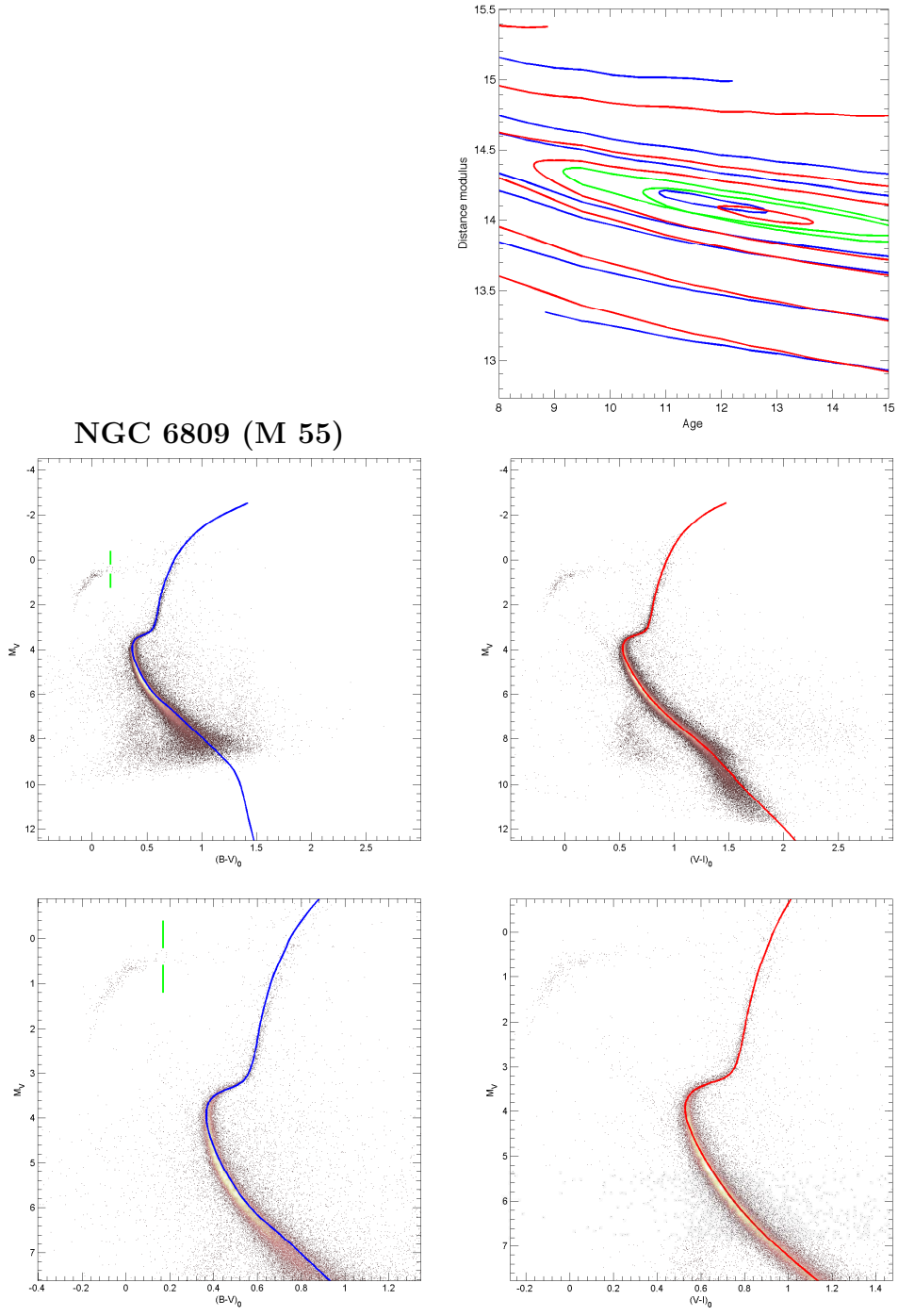

Figure 5.30. CMD of NGC 6809 (M 55), corrected for distance and absolute reddening, plotted against the best fit isochrone. The contour map represents the standard deviation values for the fit using different test ages and distances, for the two colors available: $B-V$ (in blue) and for $V-I$ (in red). The green contours are where the fit reaches $1\sigma_L$.

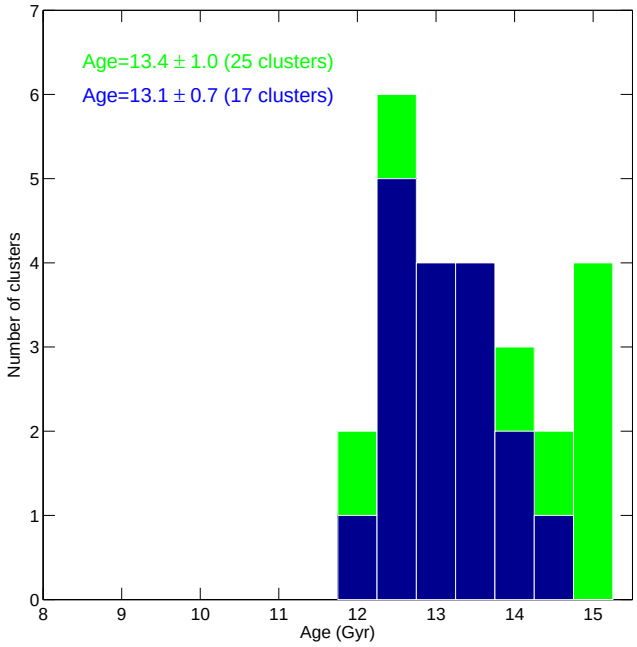

Figure 5.31. Distribution in age of the sampled clusters, with green bins showing ages obtained from unreliable fits due to the poor quality of the ridgelines

5.2 Implications from the obtained ages, distances and extinctions

In the histogram of figure 5.31 we present the distribution of ages of the clusters in our sample. The main feature of the histogram is a sharp peak at age 12.5-13 Gyrs, suggesting a very short age spread for the creation of the clusters in our sample. We should also notice a secondary peak at older ages ($\sim$ 15 Gyrs). The group of clusters with these older ages is mainly composed by clusters with poor quality, not very deep CMDs (green bins in figure 5.31). The ridgelines for these clusters do not reach 2 magnitudes below the TO point, and do not cover the whole upper MS region that we are using to do the isochrone fitting, which makes the results from this fitting to be less reliable. When this clusters are excluded, the average age of the clusters in our sample is 13.1 ± 0.7 Gyrs.

As we are interested in obtaining the ages of the Galactic bulge globular cluster population in our study, we will concentrate on clusters with galactocentric distances smaller than 3.5 kpc. Our approximation allows us to recalculate the distance to the

Table 5.2. Distances from the clusters to the Sun and to the Galactic center

Cluster	R_{GC} [a]	$R_{\odot}$ [b]	R_{GC} [c]	$R_{\odot}$ [d]
NGC 6121	6.2	1.9	5.9	2.2
NGC 6144	2.7	7.6	2.6	8.5
NGC 6218	4.6	5.1	4.5	4.9
NGC 6235	4.7	10.8	4.1	11.4
NGC 6254	4.3	5.2	4.6	4.4
NGC 6266	2.8	5.8	1.7	6.9
NGC 6273	2.6	7.9	1.6	8.6
NGC 6287	1.6	7.8	2.1	9.3
NGC 6304	2.7	6.2	2.2	6.0
NGC 6333	1.9	8.4	1.7	7.9
NGC 6342	1.7	8.5	1.7	8.6
NGC 6352	2.7	5.4	3.3	5.7
NGC 6355	3.0	6.3	1.8	9.5
NGC 6397	5.6	2.5	6.0	2.3
NGC 6522	1.2	7.0	0.6	7.8
NGC 6541	2.1	7.3	2.2	7.0
NGC 6553	3.3	4.7	2.2	6.0
NGC 6558	0.9	7.9	1.0	7.4
NGC 6624	1.3	8.3	1.2	7.9
NGC 6626	3.1	5.1	2.7	5.6
NGC 6637	1.7	8.5	1.9	9.1
NGC 6642	1.9	6.9	1.7	8.4
NGC 6656	4.8	3.3	4.9	3.2
NGC 6681	2.7	9.7	2.1	9.0
NGC 6809	4.0	5.4	3.9	5.3

[a] Galactocentric distance, in kpc, from our isochrone fit.
[b] Solar distance, in kpc, from our isochrone fit.
[c] Galactocentric distance, in kpc, from Harris catalog.
[d] Solar distance, in kpc, from Harris catalog.

sampled clusters, thanks to the values obtained for the apparent distance modulus and absolute reddening. Assuming a distance from the Sun to the center of the Milky Way of 8.0 kpc, we obtain the distances from the clusters to the Sun and to the center of the Galaxy shown in table 5.2. Using that distance information, we obtain the distribution of ages of the clusters with distances from the Galactic center $R_{GC} < 3.5$ (see figure 5.32), which shows clearly a peak at 12.5 Gyrs, and have an average of 13.3 ± 0.8 Gyrs. Most of the clusters at this peak are metal-rich ($[Fe/H] > -1$) clusters, which have long been associated with the bulge population on the grounds of sharing the kinematics, distribution and composition of bulge field stars (Minniti & Zoccali, 2008). We show a diagram of their age distribution in figure 5.33. Although small in number in our sample, it is obvious the strong concentration of the distribution at 12.5 Gyr, with almost no dispersion in age.

To build the histograms we have used the absolute minimum of our goodness of fit parameter, the standard deviation in the mean error of the color offsets, obtained for a set of ages and distances (remember that we are already assuming the metallicity,

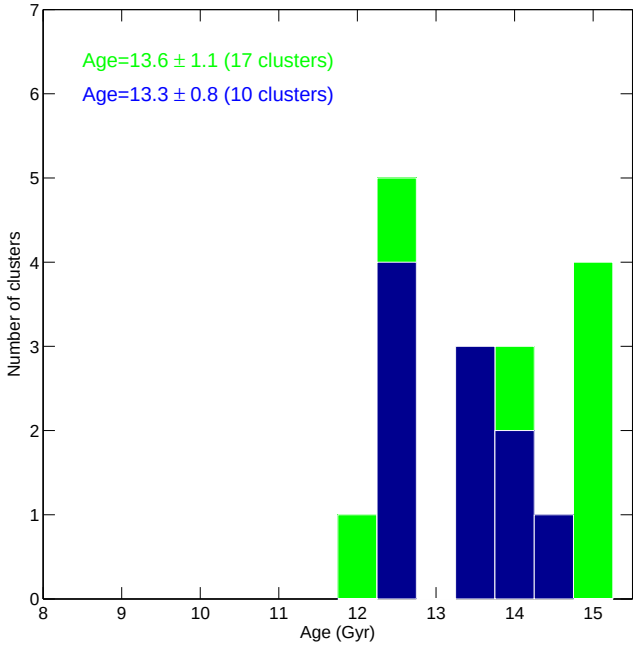

Figure 5.32. Distribution in age of the inner Galactic ($R_{GC} < 3.5$ kpc) sampled clusters, with green bins showing ages obtained from unreliable fits due to the poor quality of the ridgelines.

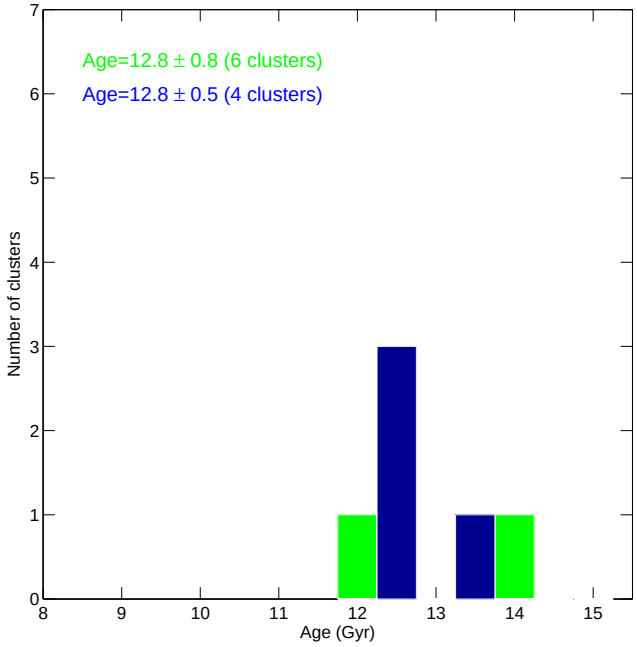

Figure 5.33. Distribution in age of the sampled metal rich ([Fe/H]> -1) clusters, with green bins showing ages obtained from unreliable fits due to the poor quality of the ridgelines.

and that the absolute reddening is a result of the fit). Therefore the histogram does not show any uncertainty in the age of the individual clusters. To get an idea of these uncertainties we proceed as follow. For every cluster, at a given age, we can easily find from examining the contour maps a distance that provides us with the minimum of the standard deviation in the mean error of the color offsets, for that given age. If we plot these minima in the standard deviation at a given age (see figure 5.34 and 5.35) we observe some interesting features:

- Young isochrones (age $\leq$ 10 Gyrs) have goodness of fit parameters $\sigma \geq 2\sigma_m$, where σ_m is the minimum standard deviation for a given cluster. These high values suggest that we can strongly rule out ages younger than 10 Gyrs for the population of inner Galactic clusters.

- Clusters that occupy the last available bin in the histograms (age = 15 Gyrs) do not seem to have reach a minimum in their goodness of fit distribution, implying that if older isochrones would be available, a better fit would be provided, making the clusters too old to be compatible with the age of the universe. We have classified all these clusters' fits as less reliable due to their poor photometry (green bins in the histograms), and the point expressed in this bullet confirms our suspicions.

- On average, clusters' fits considered less reliable due to their poor photometry (green bins in the histograms) have higher values of the standard deviation at any age, as it should be expected (see dashed lines in figure 5.34 and 5.35).

- There does not seem to be any clear tendency in the values of σ_m with apparent modulus $(m - M)_V$ or color excess $E(B - V)$.

- If we considered the possibility of a common creation time for all the inner GGCs, a change in σ_m as low as 0.005 would allow this possibility for all the clusters in our sample (with the exception of those whose σ_m assign them 15 Gyrs) at an age of $\sim$ 13 Gyrs (see figure 5.36).

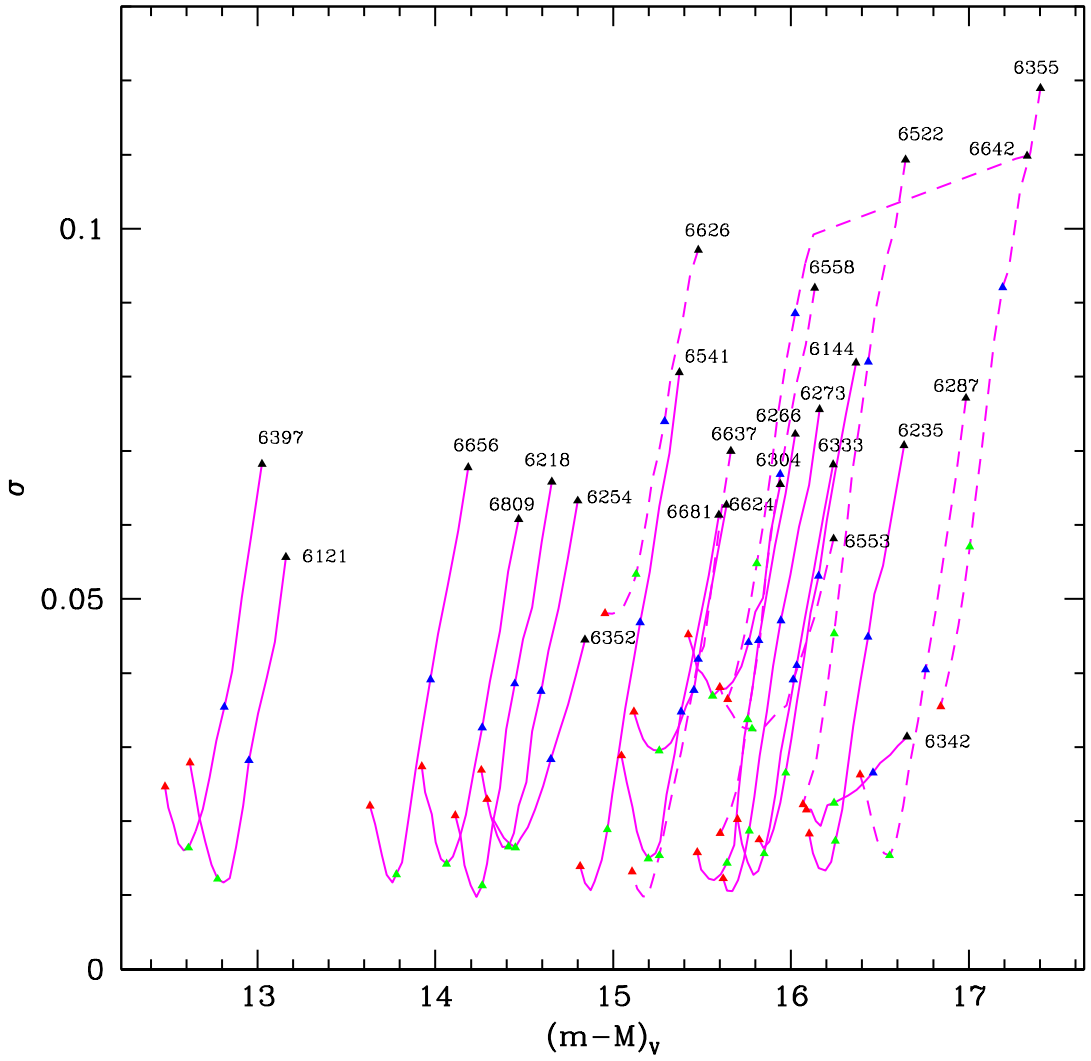

Figure 5.34. Apparent distance modulus vs. minimum of the goodness of fit parameter at a given age for the sampled clusters. The four dots in every line represent the minima for 8 (black), 10 (blue), 12.5 (green) and 15 (red) Gyrs. The dashed lines show clusters where the fit with the isochrones is considered less reliable due to a poor photometry.

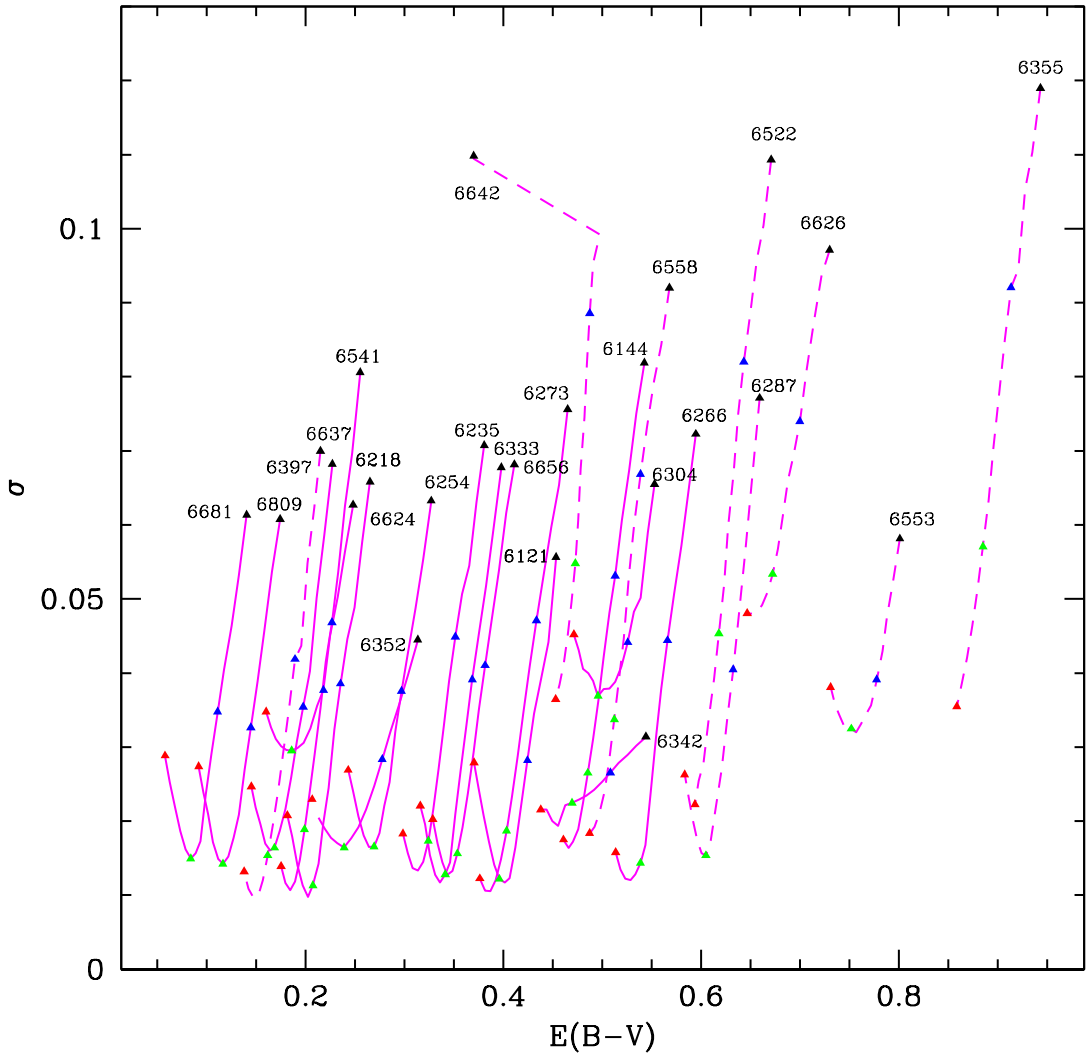

Figure 5.35. Color excess vs. minimum of the goodness of fit parameter at a given age for the sampled clusters. The four dots in every line represent the minima for 8 (black), 10 (blue), 12.5 (green) and 15 (red) Gyrs. The dashed lines show clusters where the fit with the isochrone is considered less reliable due to a poor photometry.

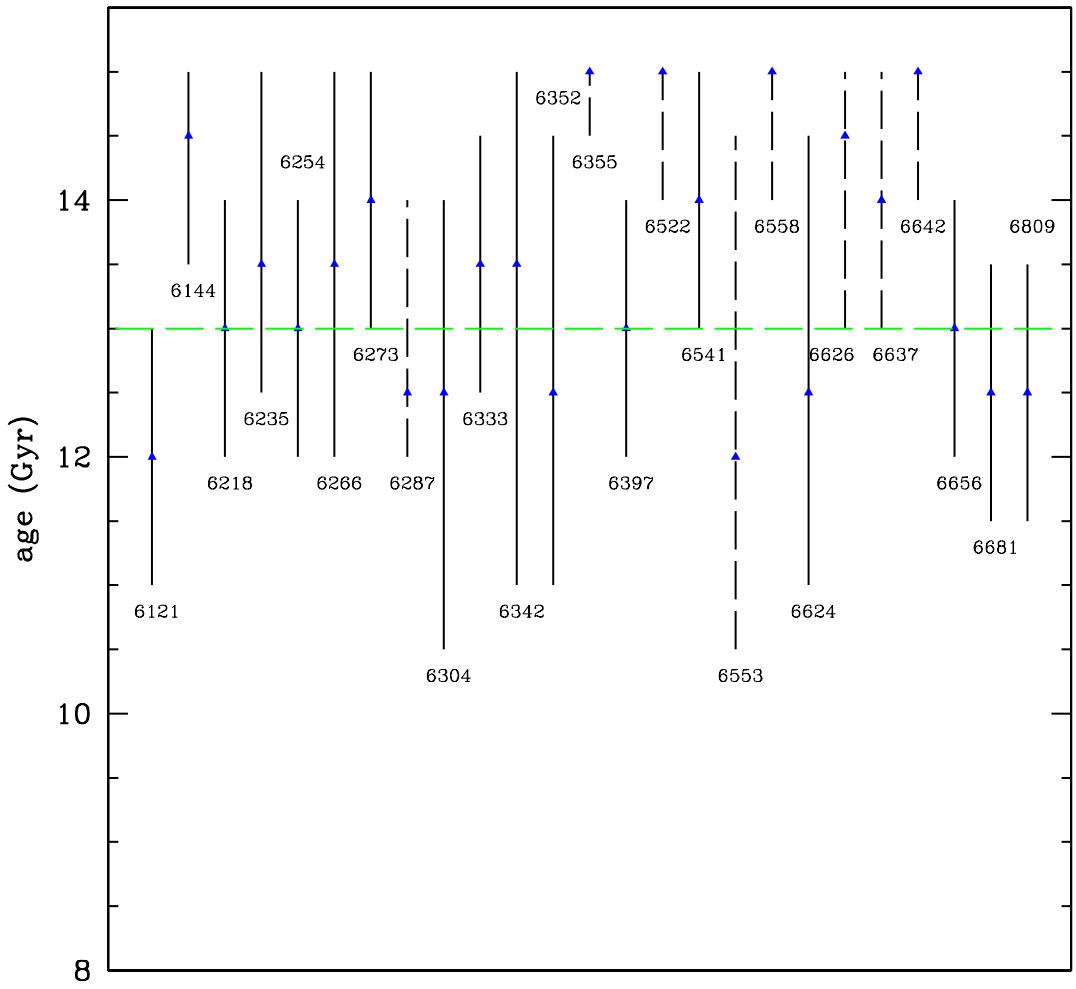

Figure 5.36. Age variation for a goodness of fit parameter of $\sigma \leq \sigma_m + 0.005$ for the sampled clusters. This small change in σ_m would allow a common creation time for all the clusters in our sample (with the exception of those whose σ_m assign them 15 Gyrs) at an age of $\sim$ 13 Gyrs. Dashed lines show ages obtained from less reliable fits due to the poor quality of the ridgelines. Notice that the cut at ages older than 15 Gyrs. is due to the lack of isochrones for these older ages.

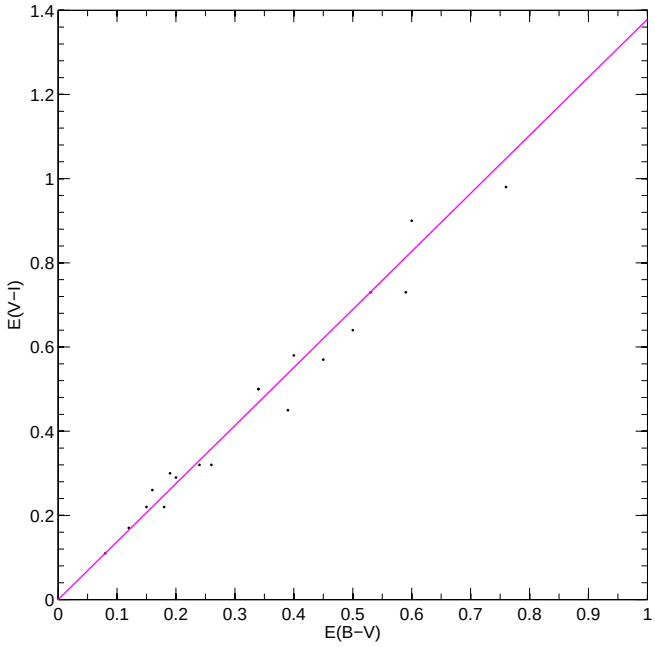

Figure 5.37. Relation between E(B-V) and E(V-I) for the clusters in our sample with calibrated colors. The straight line shows the fitted relation between them.

To finish this section, we should also mention an implication of the absolute extinction values derived from the isochrone fitting approximation. The absolute color excesses $E(B-V)$ and $E(V-I)$ in the line of sight to the sampled cluster are provided from our isochrone fit (see table 5.1). Their relation provides an independent check of the reliability of the reddening law applied all the way through the thesis ($E(V-I)/E(B-V) = 1.376$). The mean value of this ratio in our sampled clusters is $E(V-I)/E(B-V) = 1.38 \pm 0.13$, very close to the one that we use. No cluster in our sample seems to significantly deviate from this law (see figure 5.37).

CHAPTER 6

Summary, conclusions and future work

Extensive photometric studies of the globular clusters located towards the center of the Milky Way have been historically neglected. The presence of patchy differential reddening in front of these clusters has proven to be a significant obstacle to their detailed study, along with high crowding produced by very significant field star contamination in many cases.

In this thesis we carry a photometric study of a sample of 25 Galactic globular clusters located in the direction of the inner Galaxy, aiming to reliably obtain their reddenings, distances, and ages. To try to limit the effects of crowding we use the IMACS camera on the Magellan telescope and the ACS and WFPC2 onboard the HST, which provide us with the large field of views, deep photometry and low values for the seeing necessary for this kind of work. The final analyzed photometry has relative precision of 0.01-0.02 magnitudes, with absolute precision of 0.02-0.03 magnitudes in most cases. To minimize the effects of the differential reddening we have developed a technique which maps the extinction in the field of the cluster and eliminates its effects from the CMDs. This technique uses a non-parametric, star by star, approach to the determination of the differential extinction across the clusters FOV, taking the reddening information provided by stars on the MS, SGB, and RGB sequences of the CMD. The method has been applied to all the clusters in the sample, and cleaner CMDs have been generated, along with relative extinction maps.

From a comparison between our extinction maps with the SFD extinction maps, we observe a general good agreement on large-scale structure, with finer structure visible in our maps, due to the higher precision of our approximation. To obtain an absolute value for the color excess in our maps, we degraded them to the resolution

Table 6.1. E(B-V) values for the clusters in our sample obtained from different methods.

Cluster	$E(B-V)_{Harris}$ [a]	$E(B-V)_{Bes}$ [b]	$E(B-V)_{SFD}$ [c]	$E(B-V)_{isoc}$ [d]	$E(B-V)_{HB}$ [e]
NGC 6121	0.36	0.42	0.50	0.41	OK
NGC 6144	0.36	0.60	0.74	0.43	OK
NGC 6218	0.19	0.20	0.18	0.21	OK
NGC 6235	0.36	0.42	0.40	0.31	OK
NGC 6254	0.28	0.25	0.29	0.25	OK
NGC 6266	0.47	0.41	0.47	0.53	OK
NGC 6273	0.41	0.38	0.30	0.36	OK
NGC 6287	0.60	0.67	0.64	0.63	OK
NGC 6304	0.53	0.56	0.51	0.48	NA
NGC 6333	0.38	0.38	0.41	0.35	OK
NGC 6342	0.46	0.51	0.59	0.46	NA
NGC 6352	0.21	0.30	0.34	0.24	NA
NGC 6355	0.75	0.72	1.18	0.86	OK
NGC 6397	0.18	0.17	0.18	0.17	OK
NGC 6522	0.48	0.52	0.59	0.56	OK
NGC 6541	0.14	0.20	0.16	0.17	OK
NGC 6553	0.63	0.89	1.38	0.74	NA
NGC 6558	0.44	0.39	0.41	0.34	OK
NGC 6624	0.28	0.30	0.15	0.20	NA
NGC 6626	0.40	0.50	0.47	0.46	OK
NGC 6637	0.16	0.21	0.17	0.15	NA
NGC 6642	0.41	0.42	0.40	0.43	OK
NGC 6656	0.34	0.32	0.34	0.35	OK
NGC 6681	0.07	0.17	0.09	0.08	OK
NGC 6809	0.08	0.08	0.14	0.12	OK

[a] Color excess provided in the Harris catalog.
[b] Color excess from the comparison with Besançon model.
[c] Color excess from the comparison with SFD maps.
[d] Color excess from the comparison with isochrone fits.
[e] Agreement with color excess from the intrinsic location
of the blue edge of the instability strip for the HB at $(B-V)_0 = 0.17$.
E(V-I) values, whenever available, are transformed to E(B-V) using
the relation E(V-I)=1.376E(B-V), and then averaged with E(B-V) values obtained independently.

of the SFD maps. We observe that on average the color excesses variation across the map are a little higher, up to 0.1 mag in some cases, in our maps than in the SFD, even when degraded to similar resolutions. The absolute values for the color excess agree well with the values obtained from other methods and from the literature (see table 6.1), except for the clusters in our sample with the highest extinction. In those cases, the SFD maps seem to overestimate the color excesses. This tendency has been previously observed (Arce & Goodman, 1999).

The cleaner CMDs, with better defined sequences, decreasing in thickness sometimes up to a factor of 2 or better, are compared with a set of isochrones. We have already calculated the ridgelines for all the clusters as one of the steps involved in the dereddening technique application. In our approximation we fix the metallicity, using literature values for the sampled clusters, and get the best fit between the MS and SGB regions of the ridgeline and a set of isochrones. To do that, we minimize the

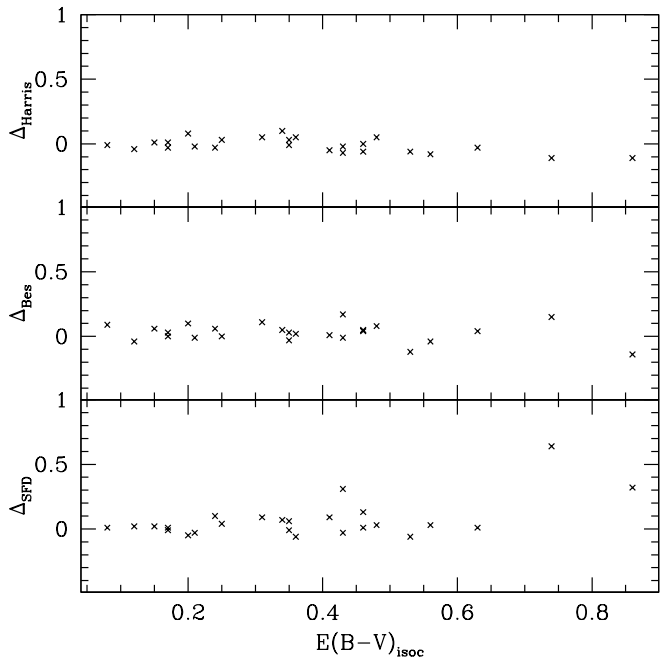

Figure 6.1. Comparison of the color excesses E(B-V) for the clusters in our sample obtained from the isochrone fitting approach with those supplied in the Harris catalog (top), obtained from the comparison with the Besançon model for the field (middle), and obtained from the SFD maps (bottom), in the sense of E(B-V) obtained from the other methods minus $E(B-V)_{isoc}$.

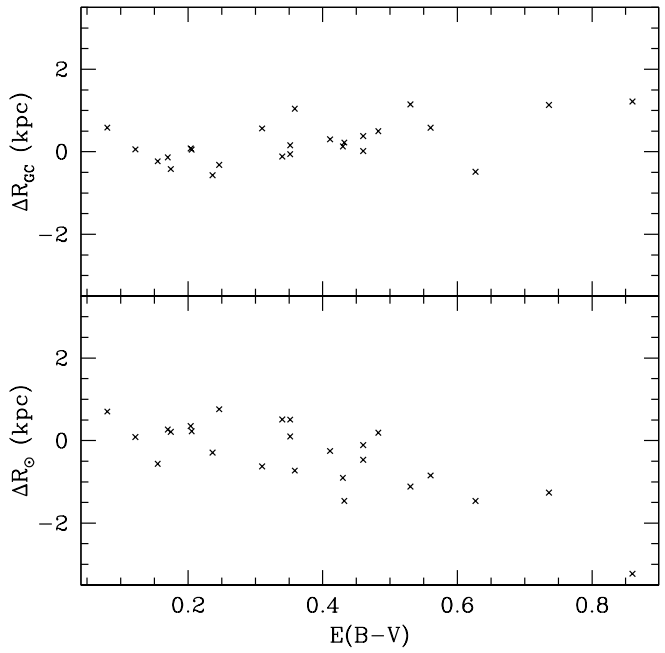

Figure 6.2. Comparison of the galactocentric distance (top) and distance to the Sun (bottom) of the clusters in our sample obtained from the isochrone fitting approach with those supplied in the Harris catalog, in the sense of R_{isoc} minus R_{Harris}.

standard deviation in the color offset between the two lines, ridgeline and isochrone, while changing the age and distance over a big range (ages from 8 to 15 Gyrs and distances over a 1 magnitude range in the distance modulus provided by the TO point). This approximation gives in the end a value for the age, distance and absolute differential reddening for every sampled cluster. From table 6.1 and figure 6.1 we observe that absolute color excesses obtained from the isochrone analysis agree well, within a few hundredths of a magnitude, with the values obtained from the literature or using other approximations in this thesis, although differences increased for higher extincted clusters. In this cases current literature values are smaller by ~ 0.1 magnitudes, while SFD maps tend to overestimate the extinction values, as we have mentioned before. A comparison of the distances to the clusters obtained from the isochrone fitting with current literature values (see table 5.2 and figure 6.2) shows in general good agreement at small extinctions, but clusters with significant absolute extinction ($E(B-V) > 0.4$) and, maybe more importantly, high differential extinction (e.g., NGC 6266, NGC 6273, NGC 6553) are ~ 1 kpc. closer to the Sun and ~ 1 kpc further from the galactic center. The distribution in age of the inner Galactic globular clusters in our sample show a clear peak at 12.5 Gyr, fundamentally due to the metal-rich fraction of clusters in our sample, which has been historically linked to the bulge on the base of sharing kinematics, distribution and composition with bulge field stars (Minniti & Zoccali, 2008). The mean value of the distribution is 13.3 ± 0.8 Gyrs, implying a short time spread in the creation of the inner clusters. This conclusion agrees with the results presented in Marín-Franch et al. (2009), in which they assign an age of 12.8 ± 0.6 for the old cluster group where all their inner Galactic clusters and many of their outer sampled clusters lie, and with results from Rosenberg et al. (2000a) which show a similar time span for the creation of the metal-rich clusters, although differently from them, we do not observe the metal-rich clusters of our sample to be significantly younger than the metal-poor group.

If the cluster population of the bulge traces back the population of field stars, this result seems to rule out the slow formation of the bulge by the secular evolution of the disk, favoring it to be a prototypical old, fast forming, spheroid rather than a

pseudo-bulge. This result agrees with current evidence that the bulge in the Milky Way is not a pseudo-bulge, evidence coming from chemical studies of their forming stars that point out the chemical differences between bulge and disk (Lecureur et al., 2007; Fulbright et al., 2007), and the presence of a metallicity gradient along the bulge minor axis (Zoccali et al., 2008).

If we consider such a scenario for the Galactic bulge formation (a rapid ($\sim$ 1.5 Gyrs) formation $\sim$ 13 Gyrs ago, which seems compatible with other studies (Ballero et al., 2007)), we can get an estimate of the star formation rate density (ρ_{SFR}) for the Galactic bulge. Since the stellar mass of the Galactic bulge is $M_{bulge} = 1.8 \times 10^{10} M_{\odot}$ (Sofue et al., 2009), the SFR density of the Galactic bulge would therefore be $\rho_{SFR} = 12 M_{\odot} year^{-1} Mpc^{-3}$ for that period. Notice that in this calculation we are only considering the region where the Galactic bulge was formed. The obtained value is more than an order of a magnitude higher than the average values that we can find when we extrapolate the values found in the literature (Le Borgne et al., 2009; Pérez-González et al., 2005) to that time ($5 \leq z \leq 10$), and certainly much higher than the values in the Universe today, $\rho_{SFR} \sim 0.01 M_{\odot} year^{-1} Mpc^{-3}$ (Le Borgne et al., 2009; Pérez-González et al., 2005). This suggests a scenario of very intense star formation activity in a very early time in the universe for spheroids such as the Galactic bulge.

It would be interesting to increase the sample of clusters to include a higher percentage of the inner GGCs. Now that we have seen that our dereddening method works in our current sample, we can easily apply it to extract the same type of information on more inner GGCs. Increasing by only 1 magnitude our observational limit, we can increase our sampled globular clusters by a factor of 2, being able to reach clusters more heavily reddened or located in the other side of the bulge.

Also, it would be interesting to apply our extinction maps and new cleaner photometry to help on spectroscopic studies. There are not many high-resolution spectroscopic studies of stars in inner Galactic GCs (see table 6.2), the main reason being the limitations set by interstellar reddening which generates uncertainties in the effective temperature and surface gravity of the stars studied. Most of the chemical abundance measurements of these inner GCs rely on only a few spectrophotometric

Table 6.2. Clusters in our sample with high-resolution spectra studies.

Cluster	Number of stars	References
NGC 6121	3	Gratton et al. (1986)
...	3	Brown & Wallerstein (1992)
...	24	Ivans et al. (1999)
...	14	Cassisi (2009)
NGC 6144	0	...
NGC 6218	1	Mishenina et al. (2003)
...	11	Cassisi (2009)
NGC 6235	0	...
NGC 6254	2	Gratton & Ortolani (1989)
...	14	Kraft et al. (1995)
...	2	Mishenina et al. (2003)
...	14	Cassisi (2009)
NGC 6266	0	...
NGC 6273	0	...
NGC 6287	2	Lee & Carney (2002)
NGC 6304	0	...
NGC 6333	0	...
NGC 6342	4	Origlia et al. (2005)
NGC 6352	3	Gratton (1987)
NGC 6355	0	...
NGC 6397	3	Gratton & Ortolani (1989)
...	2	Norris & Da Costa (1995)
...	16	Castilho et al. (2000)
...	8	James et al. (2004)
...	13	Cassisi (2009)
NGC 6522	0	...
NGC 6541	2	Lee & Carney (2002)
NGC 6553	2	Barbuy et al. (1999)
...	5	Cohen et al. (1999)
...	4	Alves-Brito et al. (2006)
NGC 6558	0	...
NGC 6624	0	...
NGC 6626	0	...
NGC 6637	0	...
NGC 6642	0	...
NGC 6656	3	Gratton & Ortolani (1989)
...	7	Brown & Wallerstein (1992)
NGC 6681	0	...
NGC 6809	2	Shetrone et al. (2003)

indices (e.g. Ca triplet) in low or mid-resolution measurements (Rutledge et al., 1997) or even just photometric indices (Zinn & West , 1984). Now we can use the extinction maps that our technique has produced and our reddening-corrected CMDs to obtain more accurate values for the temperature and surface gravity estimates of the stars in these clusters. We can this way use high-resolution spectra studies and spectral modeling to calculate directly and more reliably the metallicities and α-enhancements of the stars in the inner GGCs in our sample.

Another possible application of our work involves the extinction maps that our dereddening technique produces. These maps can be used to study the ISM along numerous low latitude lines of sight. The strength of the extinction variations in the

maps as a function of angular scale can be characterized in terms of its power spectrum. The index of this power spectrum can be used to extract valuable information about the density and temperatures of the ISM (Kiss et al. 2003).

APPENDIX

APPENDIX A

Non-parametric analysis using locfit

In our work we have extensively used non-parametric statistics to estimate probability densities and regressions.

Probability densities and regressions can be expressed in a parametric way, where the function used to describe them can be written as a mathematical formula which is fully described by a finite set of parameters that we have to find, or in a non-parametric way where we want to estimate the function directly, without reference to a specific form.

In our analysis we have used *locfit*, a local likelihood estimation software implemented in the R statistical programming language. *Locfit* is extensively explained in Loader (1999), so here we just want to give a general idea of how it works and the main tuning parameters that we have chosen in our analysis. *Locfit* does not constrain the functions globally, i.e., it is non-parametric, but assumes that locally, around a certain point x, the function can be well approximated by a member of a simple class of parametric functions. *Locfit* defines a local window around a point, weighting the observations according to their distance to that point

$$w_i(x) = \begin{cases} W(\frac{x_i - x}{h(x)}) & \text{if} \quad x_i < |x + h(x)| \\ 0 & \text{if} \quad x_i \geq |x + h(x)| \end{cases}$$

and inside this local window, the function is approximated by a polynomial, using not the usual local least square criterion but a local log likelihood criterion. We have to choose the weighting function and the order of the polynomial. For both cases we take the default given by the program: a polynomial of order 2 with a tricube weight

function $W(u) = (1 - |u|^3)^3$. Still we are left with one last argument to choose, the smoothing parameter that controls the bandwidth $h(x)$. This smoothing parameter is defined by the maximum of two elements: a bandwidth generated by a nearest neighbor fraction $0 < \alpha < 1$, and a constant bandwidth. The nearest neighbor bandwidth is computed in two steps, first computing the distances $d(x, x_i) = |x - x_i|$ for all the data points and then choosing $h(x)$ to be the kth smallest distance, where $k = [n\alpha]$.

Also the likelihood criterion can be chosen, and we choose for the regression the family *qrgauss*, which is equivalent to a local robust least squares criterion where outliers are iteratively identified and downweighted, similar to the *lowess* method (Cleveland, 1979).

If we want to give more weight to some points than others, *locfit* allows preliminary weights to be given to all observations.

A scale factor can be applied to the different variables in multivariate fitting, when variables are measured in non-comparable units, or when we want to give more importance to one of them like in the determination of the densities of stars in our CMD, where the range in color for the stars is smaller than the range in magnitudes.

In addition to calculate the non-parametric function that fit the data, *locfit* can also calculate the derivative of that function.

Finally, a word about the evaluation structures in *locfit*. *Locfit* does not perform local regression directly in every point, but selects a set of evaluation points obtaining the fit there and interpolating later elsewhere. This is done for efficiency: it is much faster to evaluate the structure in a small number of points and then interpolate for the rest. But we should make sure that we do not loose information on the process. In order to achieve this, *locfit* uses, by default, a growing adaptive tree, which is the evaluation structure that we use in our analysis. A growing adaptive tree is a grid of points. One begins by bounding the data in a rectangular box and evaluating the fit at the vertices of the box. One then recursively splits the box into two pieces, then each subbox into two pieces and so on. For this kind of structure, an edge is always split at the midpoint and the decision to split an edge is based solely on the

bandwidths at the two ends of the edge, depending on the score $\delta_{ij} = d_{ij}/min(h_i, h_j)$ where d_{ij} is the distance between the two vertices of an edge, and h_i and h_j are the bandwidths used at the vertices. Any edge whose score exceeds a critical value c ($c = 0.8$ by default) is split.

BIBLIOGRAPHY

Alcaino, G., Liller, W., Alvarado, F., Kravtsov, V., Ipatov, A., & Samus, N. 1997, AJ, 114, 2638

Alves-Brito, A., et al. 2006, A&A, 460, 269

Anderson, J., Bedin, L. R., Piotto, G., Yadav, R. S., & Bellini, A. 2006, A&A, 454, 1029

Anderson, J., Cool, A. M., & King, I. R. 2003, ApJ, 597, L137

Anderson, J., et al. 2008a, AJ, 135, 2055

Anderson, J., et al. 2008b, AJ, 135, 2114

Anthony-Twarog, B. J., Twarog, B. A., & Craig, J. 1995, PASP, 107, 32

Armandroff, T. E. 1988, AJ, 96, 588

Arce, H. G. & Goodman, A. A. 1999, ApJ, 512, L135

Athanassoula, E. 2005, MNRAS, 358, 1477

Athanassoula, E. 2008, in IAU Symposium 245, Formation and Evolution of Galaxy Bulges, ed. M. Bureau, E. Athanassoula, & B. Barbuy (Cambridge, UK: Cambridge Univ. Press), 93

Barbuy, B. 2008, in IAU Symposium 245, Formation and Evolution of Galaxy Bulges, ed. M. Bureau, E. Athanassoula, & B. Barbuy (Cambridge, UK: Cambridge Univ. Press), 459

Ballero, S. K., Matteucci, F., Origlia, L., & Rich, R. M. 2007, A&A, 467, 123

Barbuy, B., Bica, E., Ortolani, S., & Bonatto, C. 2006, A&A, 449, 1019

Barbuy, B., Ortolani, S., & Bica, E. 1994, A&A, 285, 871

Barbuy, B., Renzini, A., Ortolani, S., Bica, E., & Guarnieri, M. D. 1999, A&A, 341, 539

Barbuy, B., Zoccali, M., Ortolani, S., Minniti, D., Hill, V., Renzini, A., Bica, E., & Gómez, A. 2007, AJ, 134, 1613

Bassa, C. G., Pooley, D., Verbunt, F., Homer, L., Anderson, S. F., & Lewin, W. H. G. 2008, A&A, 488, 921

Bassa et al. 2004, ApJ, 609, 755

Beaulieu, S. F., Gilmore, G., Elson, R. A. W., Johnson, R. A., Santiago, B., Sigurdsson, S., & Tanvir, N. 2001, AJ, 121, 2618

Beccari, G., Ferraro, F. R., Possenti, A., Valenti, E., Origlia, L., & Rood, R. T. 2006, AJ, 131, 2551

Bedin, L. R., Piotto, G., Anderson, J., Cassisi, S., King, I. R., Momany, Y., & Carraro, G. 2004 ApJ, 605, L125

Benjamin, R. A., et al. 2005, ApJ, 630, L149

Bessell, M. S. 1990 PASP, 102, 1181

Binney, J., & Tremaine, S. 1994, Galactic Dynamics (Princeton: Princeton Univ. Press)

Bissantz, N., & Gerhard, O. 2002, MNRAS, 330, 591

Brocato, E., Buonanno, R., Malakhova, Y., & Piersimoni, A. M. 1996, A&A, 311, 778

Brown, J. A. & Wallerstein, G. 1992, AJ, 104, 1818

Cabrera-Lavers, A., González-Fernández, C., Garzón, F., Hammersley, P. L., López-Corredoira, M. 2008, A&A, 491, 781

Calamida, A., et al. 2005, ApJ, 634, 69

Cardelli, J. A., Clayton, G. C. & Mathis, J. S. 1989, ApJ, 345, 245

Carretta, E., et al. 2007, A&A, 464, 939

Cassisi, S. 2009, arXiv, 0909.4629C

Castilho, B. V., Pasquini, L., Allen, D. M., Barbuy, B., & Molaro, P. 2000, A&A, 361, 92

Cohen, J. G., Gratton, R. G., Behr, B. B., & Carretta, E. 1999, ApJ, 523, 739

Cho, D.-H. & Lee, S.-G. 2002, AJ, 124, 977

Cleveland, W. S. 1979, J. Amer. Statist. Assn., 74, 829

Cocozza, G., Ferraro, F.R., Possenti, A., Beccari, G., Lanzoni, B., Ransom, S., Rood, R.T., & D'Amico, N. 2008, ApJ, 679, L105

Contreras, R., Catelan, M., Smith, H. A., Pritzl, B. J., & Borissova, J. 2005, ApJ, 623, L117

D'Antona, F., & Caloi, V. 2008, MNRAS, 390, 693

Davidge, T. J. 2000, AJ, 120, 1853

Davidge, T. J. 2001, AJ, 121, 3100

Davidge, T. J. & Harris, W. E. 1996, ApJ, 462, 255

Davidge, T. J., Côté, P. & Harris, W. E. 1996, ApJ, 468, 641

Davis, D. S., Richer, H. B., Anderson, J., Brewer, J., Hurley, J., Kalirai, J. S., Rich, R. M., & Stetson, P. B. 2008, AJ, 135, 2155

de Angeli, F., Piotto, G., Cassisi, S., Busso, G., Recio-Blanco, A., Salaris, M., Aparicio, A., & Rosenberg, A. 2005, AJ, 130, 116

de Marchi, G., Paresce, F., & Pulone, L. 2000, ApJ, 530, 342

de Marchi, G., Pulone, L., & Paresce, F. 2006, A&A, 449, 161

Dolphin, A. E. 2000, PASP, 112, 1383

Dotter, A., Chaboyer, B., Jevremović, D., Baron E., Ferguson, J. W., Sarajedini, A., & Anderson, J. 2007, AJ, 134, 376

Faria, D., & Feltzing, S., 2002, in ASP Conf. Ser. 274, Observed HR Diagrams and Stellar Evolution, ed. T. Lejeune & J. Fernandes, (San Francisco, CA: ASP), 373

Ferdman et al. 2004, AJ, 127, 380

Ferraro, F. R., Fusi-Pecci, F., Guarnieri, M. D., Moneti, A., Origlia, L., & Testa, V. 1994, MNRAS, 266, 829

Ferraro, F. R., Montegriffo, P., Origlia, L., & Fusi Pecci, F. 2000, AJ, 119, 1282

Freeman, K. C. 2008, in IAU Symposium 245, Formation and Evolution of Galaxy Bulges, ed. M. Bureau, E. Athanassoula, & B. Barbuy (Cambridge, UK: Cambridge Univ. Press), 3

Fulbright, J. P., McWilliam, A., & Rich, R. M. 2007, ApJ, 661, 1152

Fullton, L. K., Carney, B. W., Olszewski, E. W., Zinn, R., Demarque, P., Janes, K. A., Da Costa, G. S., & Seitzer, P. 1995, AJ, 110, 652

Fullton, L. K., Stetson, P. B., & Carney, B. W. 1999, Ap&SS, 265, 361

Gratton, R. G. 1987, A&A, 179, 181

Gratton, R. G., Bragaglia, A., Carretta, E., Clementini, G., Desidera, S., Grundahl, F., & Lucatello, S. 2003, A&A, 408, 529

Gratton, R. G., Quarta, M. L., & Ortolani, S. 1986, A&A, 169, 208

Gratton, R. G., & Ortolani, S. 1989, A&A, 211, 41

Grillmair, C. J., Freeman, K. C., Irwin, M., & Quinn, P. J. 1995, AJ, 109, 2553

Golden, A., Butler, R. F., & Shearer, A. 2001, A&A, 371, 198

Guarnieri, M. D., Ortolani, S., Montegriffo, P., Renzini, A., Barbuy, B., Bica, E., & Moneti, A. 1998, A&A, 331, 70

Guhathakurta, P., Yanny, B., Bahcall, J. N., & Schneider, D. P. 1996, in IAU Symp. 174, Dynamical evolution of star clusters: confrontation of theory and observations, ed. P. Hut & J. Makino. (Dordrecht: Kluwer), 333

Hammersley, P. L., Garzón, F., Mahoney, T. J., López-Corredoira, M., & Torres, M. A. P. 2000, MNRAS, 317, L45

Hansen et al. 2004, ApJS, 155, 551

Harris, W.E. 1996, AJ, 112, 1487

Hargis, J. R., Sandquist, E. L., & Bolte, M. 2004, ApJ, 608, 243

Heasley, J. N., Janes, K. A., Zinn, R., Demarque, P., Da Costa, G. S., & Christian, C. A. 2000, AJ, 120, 879

Heitsch, F., & Richtler, T. 1999, A&A, 347, 455

Hernandez, X., & Valls-Gabaud, D. 2008, MNRAS, 383, 1603

Howland, R., Sarajedini, A., Tiede, G. P., Gokas, T., Djagalov, R. & Martins, D. H. 2003, AJ, 125, 801

Hughes, J., & Wallerstein, G. 2000, AJ, 119, 1225

Hughes, J., Wallerstein, G., Covarrubias, R., & Hays, N. 2007, AJ, 134, 229

Hurley, J. R., et al. 2008, AJ, 135, 2129

Ivans, I. I., Sneden, C., Kraft, R. P., Suntzeff, N. B., Smith, V. V., Langer, G. E., & Fulbright, J. P. 1999, AJ, 118, 1273

James, G., Francois, P., Bonifacio, P., Carretta, E., Gratton, R. G., & Spite, F. 2004, A&A, 427, 825

Janes, K. A. & Heasley, J. N. 1991, AJ, 101, 2097

Kaluzny, J., Thompson, I. B., Krzeminski, W., & Schwarzenberg-Czerny, A. 2006, MNRAS, 365, 548

Kaluzny, J., Pietrukowicz, P., Thompson, I. B., Krzeminski, W., Schwarzenberg-Czerny, A., Pych, W., & Stachowski, G. 2005, MNRAS, 359, 677

Kaluzny, J., & Krzeminski, W. 1993, MNRAS, 264, 785

Kaluzny, J., & Thompson, I. B. 2001, A&A, 373, 899

Kirby, E. N., Guhathakurta, P., & Sneden, C. 2008, ApJ, 682, 1217

Kim, J.-W., et al. 2006, A&A, 459, 499

King, I. 1962, AJ, 67, 471

Kiss, Cs., Ábrahám, P., Klaas, U., Lemke, D., Héraudeau, Ph., del Burgo, C., & Herbstmeier, U. 2003, A&A, 399, 177

Kraft, R. P., Sneden, C., Langer, G. E., Shetrone, M. D., & Bolte, M. 1995, AJ, 109, 2586

Lanzoni, B., Dalessandro, E., Perina, S., Ferraro, F. R., Rood, R. T., & Sollima, A. 2007, ApJ, 670,1065

Landolt, A. U. 1992, AJ, 104, 340

Law, D. R., Majewski, S. R., Skrutskie, M. F., Carpenter, J. M., & Ayub, H. F. 2003, AJ, 126, 1871

Le Borgne, D., Elbaz, D., Ocvirk, P., & Pichon, C. 2009, A&A, 504, 727

Lecureur, A., Hill, V., Zoccali, M., Barbuy, B., Gómez, A., Minniti, D., Ortolani, S., & Renzini, A. 2007, A&A, 465, 799

Lee, J.-W., Carney, B. W., Fullton, L. K., & Stetson, P. B. 2001, AJ, 122, 3136

Lee, J.-W., & Carney, B. W. 2002, AJ, 124, 1511

Lee, J.-W., & Carney, B. W. 2006, AJ, 132, 2171

Lehnert, M. D., Bell, R. A., & Cohen, J. G. 1991, ApJ, 367, 514

López-Corredoira, M., Cabrera-Lavers, A., & Gerhard, O. E. 2005, A&A, 439, 107

López-Corredoira, M., Cabrera-Lavers, A., Mahoney, T. J., Hammersley, P. L., Garzón, F., & González-Fernández, C. 2007, AJ, 133, 154

Loader, C. 1999, Local Regression and Likelihood, (New York: Springer)

Marín-Franch, A., et al. 2009, ApJ, 694, 1498

Marino, A. F., Villanova, S., Piotto, G., Milone, A. P., Momany, Y., Bedin, L. R., & Medling, A. M. 2008, A&A, 490, 625

Mateo, M. Fischer, P., & Krzeminski, W. 1995, AJ, 110, 2166

Meissner, F., & Weiss, A. 2006, A&A, 456, 1085

Melbourne, J. & Guhathakurta, P. 2004, AJ, 128, 271

Mighell, K. J., Sarajedini, A., & French, R. S. 1998, AJ, 116,2395

Minniti, D., Olszewski, E. W., & Rieke, M. 1995, AJ, 110, 1686

Minniti, D. & Zoccali, M. in IAU Symposium 245, Formation and Evolution of Galaxy Bulges, ed. M. Bureau, E. Athanassoula, & B. Barbuy (Cambridge, UK: Cambridge Univ. Press), 323

Mishenina, T. V., Panchuk, V. E., & Samus, N. N. 2003, Astron. Rep., 47, 248

Mochejska, B. J., Kaluzny, J., Thompson, I., & Pych, W. 2002, AJ, 124,1486

Monaco, L., Pancino, E., Ferraro, F. R., & Bellazzini, M. 2004, MNRAS, 349, 1278

Moretti, A., et al. 2009, A&A, 493, 539

Neely, R. K., Sarajedini, A., Martins, D. H. 2000, AJ, 119, 1793

Norris, J. E., & Da Costa, G. S. 1995, ApJ, 447, 680

Odenkirchen, M., et al. 2001, ApJ, 548, 165

O'Donnell, J. E. 1994, ApJ, 422, 1580

Origlia, L., Valenti, E., & Rich, R. M. 2005, MNRAS, 356, 1276

Ortolani, S., Momany, Y., Bica, E., & Barbuy, B. 2000, A&A, 357, 495

Ortolani, S., Bica, E., & Barbuy, B. 2003, A&A, 402, 565

Pérez-González, P. G., et al. 2005, ApJ, 630, 82

Picaud, S., Cabrera-Lavers, A., & Garzón, F. 2003, A&A, 408, 141

Piersimoni, A. M., Bono, G., & Ripepi, V. 2002, AJ, 124, 1528

Piotto, G. & Zoccali, M. 1999, A&A, 345, 485

Piotto, G., Zoccali, M., King, I. R., Djorgovski, S. G., Sosin, C., Dorman, B., Rich, R. M. & Meylan, G. 1999, AJ, 117, 264

Piotto, G., Zoccali, M., King, I. R., Djorgovski, S. G., Sosin, C., Rich, R. M., & Meylan, G. 1999, AJ, 118, 1727

Piotto, G., et al. 2002, A&A, 391, 945

Piotto, G., Bedin, L. R., Anderson, J., King, I. R., Cassisi, S., Milone, A. P., Villanova, S., Pietrinferni, A., & Renzini, A. 2007, ApJ, 661, L53

Pollard, D. L., Sandquist, E. L., Hargis, J. R., & Bolte, M. 2005, ApJ, 628, 729

Pulone, L., de Marchi, G., Covino, S., & Paresce, F. 2003, A&A, 399, 121

Pulone, L., de Marchi, G., & Paresce, F. 1999, A&A, 342, 440

Pych, W., Kaluzny, J., Krzeminski, W., Schwarzenberg-Czerny, A., & Thompson, I. B. 2001, A&A, 367, 148

Rattenbury, N. J., Mao, S., Sumi, T., & Smith, M. C. 2007, MNRAS, 378, 1064

Recio-Blanco, A., et al. 2005, A&A, 432, 851

Rich, R. M., Ortolani, S., Bica, E., & Barbuy, B. 1998, AJ, 116, 1295

Richer, H. B., et al. 2004, AJ, 127, 2771

Richer, H. B., et al. 2008, AJ, 135, 2141

Richter, P., Hilker, M., & Richtler, T. 1999, A&A, 350, 476

Richtler, T., Grebel, E. K., & Seggewiss, W. 1994, A&A, 290, 412

Robin, A. C., Reylé, C., Derrière, S., & Picaud, S. 2003, A&A, 409, 523

Rosenberg, A., Aparicio, A., Saviane, I., & Piotto, G. 2000a, A&AS, 144, 5

Rosenberg, A., Aparicio, A., Saviane, I., & Piotto, G. 2000b, A&AS, 145, 451

Rutledge, G. A., Hesser, J. E., & Stetson, P. B. 1997, PASP, 109, 907

Sagar, R., Subramaniam, A., Richtler, T., & Grebel, E. K. 1999, A&AS, 135, 391

Salaris, M. & Cassisi, S. 2005, Evolution of Stars and Stellar Populations (Chichester, England: John Wiley & Sons, Ltd.)

Sarajedini, A., & Norris, J. E. 1994, ApJS, 93, 161

Sarajedini, A., Chaboyer, B., & Demarque, P. 1997, PASP, 109, 1321

Sarajedini, A., et al. 2007, AJ, 133, 1658

Schechter, P., Mateo, M., & Saha, A. 1993, PASP, 105, 1342

Schlegel, D., Finkbeiner, D., & Davis, M. 1998, ApJ, 500, 525

Sérsic, J. L. 1968, Atlas de Galaxias Australes. Obs. Astron. Cordoba

Shara, M. M., Drissen, L., Rich, R. M., Paresce, F., King, I. R., & Meylan, G. 1998, ApJ, 495, 796

Shetrone, M., Venn, K. A., Tolstoy, E., Primas, F., Hill, V., & Kaufer, A. 2003, AJ, 125, 684

Sofue, Y., Honma, M., & Omodaka, T. 2009, PASJ, 61, 227

Sosin, C. & King, I. R. 1995, AJ, 109, 639

Stetson, P. B. 2000, PASP, 112, 925

Stetson, P. B. & West, M. J. 1994, PASP, 106, 726

Stetson, P. B., Vandenberg, D. A., & Bolte, M. 1996, PASP, 108, 560

Terndrup, D. M., & Walker, A. R. 1994, AJ, 107, 1786

Terndrup, D. M., Popowski, P., Gould, A., Rich, R. M., & Sadler, E. M. 1998, AJ, 115, 1476

Testa, V., Corsi, C. E., Andreuzzi, G., Iannicola, G., Marconi, G., Piersimoni, A. M., & Buonanno, R. 2001, AJ, 121, 916

Valenti, E., Ferraro, F. R., Perina, S., & Origlia, L. 2004a, A&A, 419, 139

Valenti, E., Ferraro, F. R., & Origlia, L. 2004b, MNRAS, 351, 1204

Valenti, E., Ferraro, F. R., & Origlia, L. 2007, AJ, 133, 1287

Valenti, E., Origlia, L., & Ferraro, F. R. 2005, MNRAS, 361, 272

Venn, K. A., Irwin, M., Shetrone, M. D., Tout, C. A., Hill, V. & Tolstoy, E. 2004, AJ, 128, 1177

von Braun, K. & Mateo, M. 2001 AJ, 121, 1522

von Braun, K., Mateo, M., Chiboucas, K., Athey, A., & Hurley-Keller, D. 2002, AJ, 124, 2067

Wasserman, L. 2006, All of Non Parametric Statistics (New York: Springer)

Webb, N. A., Serre, D., Gendre, B., Barret, D., Lasota, J.-P., & Rizzi, L. 2004, A&A, 424, 133

Zoccali, M., Renzini, A., Ortolani, S., Bica, E., & Barbuy, B. 2001, AJ, 121, 2638

Zoccali, M., Hill, V., Lecureur, A., Barbuy, B., Renzini, A., Minniti, D., Gómez, A., & Ortolani, S. 2008, A&A, 486, 177

Zinn & West, 1984 ApJS, 55, 45